# Open quantum system theory from an information perspective

**vorgelegt von**
**Master of Science**

**Oliver Kästle**

an der Fakultät II – Mathematik und Naturwissenschaften
der Technischen Universität Berlin

zur Erlangung des akademischen Grades
Doktor der Naturwissenschaften

**— Dr. rer. nat. —**

genehmigte Dissertation

**Promotionsausschuss:**

| | |
|---|---|
| Vorsitzende: | Prof. Dr. rer. nat. Ulrike Woggon, TU Berlin |
| Gutachter: | Prof. Dr. rer. nat. Andreas Knorr, TU Berlin |
| Gutachter: | Prof. Dr. rer. nat. Peter Rabl, TU Wien |

Tag der wissenschaftlichen Aussprache: 28. Juni 2021

Berlin 2021

*für Alex, den großen Komprimator*

*The first principle is that you must not fool yourself –*
*and you are the easiest person to fool.*
—R. Feynman

# Abstract

Theoretical investigations of open quantum systems have uncovered a wide variety of unique dynamical phenomena. For instance, current research in quantum information technology aims to control and utilize time-delayed system-reservoir interactions and phonon-induced dynamical dissipative processes for the design of novel chip-integrated quantum optical devices. This thesis develops and advances multiple theoretical approaches for the accurate and efficient description of open quantum systems, where a high degree of information compression is essential to extract crucial information from the open system degrees of freedom which scale exponentially with the system size. The presented methods range from correlation expansions to second-order perturbative master equations, real-time path integral formulations, numerical realizations of high-dimensional tensor networks and, based on the most recent theoretical developments, machine learning implementations in the form of artificial neural networks.

We explore all of these techniques with respect to their compression efficiency, performance and representational limits by applying them to a variety of physical setups and scenarios. Firstly, emerging non-Markovian memory effects in open quantum systems are investigated, e.g., resulting from interactions with a structured phonon environment or time-discrete coherent quantum feedback, leading to information exchange and a time-delayed dynamical interplay between system and reservoir. Examined systems range from solid state $p$-wave topological superconductors coupled to a structured phonon environment, where a memory-induced stabilization and recovery of topological properties is observed, to semiconductor quantum dot nanostructures exhibiting complete population inversion and unidirectional quantum transport as a result of dissipation-induced non-Markovian system-reservoir interactions, and quantum emitters simultaneously subjected to coherent quantum feedback and a decoherence-inducing structured phonon reservoir, leading to the formation of dynamical dissipative structures and population trapping.

Secondly, novel machine learning techniques based on artificial neural networks are investigated, enabling simulations of symmetric open quantum spin-1/2 systems with Markovian dynamics. Combining their potential for parallelization and efficient Hilbert space truncation, they facilitate unmatched degrees of information compression and numerical performance for large systems. In this thesis, we expand the representational limits of the *restricted Boltzmann machine* neural network architecture by developing novel hybrid sampling strategies for a highly customizable compression of configuration space, rendering accurate and efficient simulations of asymmetric systems feasible. Finally, the applicability of the neural network is extended beyond pure spin-1/2 systems by introducing a neural bit encoding scheme for Fock number states, facilitating high performing calculations of large hybrid open quantum systems with bosonic degrees of freedom.

# Kurzfassung

Die theoretische Beschreibung offener Quantensysteme erschließt ein weites Feld einzigartiger physikalischer Phänomene und ermöglicht die Erforschung neuartiger Anwendungen von zeitretardierten System-Bad-Wechselwirkungen und phononinduzierten dissipativen Prozessen im Bereich der Quanteninformationstechnologie. In dieser Arbeit werden verschiedene theoretische Methoden zur Beschreibung offener Quantensysteme analysiert, angewandt und weiterentwickelt, für die ein hoher Grad an Informationskompression entscheidend ist, um effizient relevante Information aus den Systemfreiheitsgraden zu extrahieren, die mit wachsender Systemgröße exponentiell skalieren. Die dargelegten Ansätze umfassen Korrelationsentwicklungen, Mastergleichungen in zweiter Ordnung Störungstheorie, Pfadintegralformalismen, numerische Implementierungen hochdimensionaler Tensornetzwerke sowie Anwendungen künstlicher Intelligenz auf Basis neuronaler Netzwerke.

Die Techniken werden bezüglich ihrer Kompressions- und Leistungsfähigkeit sowie repräsentativer Limitationen beleuchtet. Zunächst werden dazu nicht-Markoffsche Gedächtniseffekte in offenen Quantensystemen untersucht, die durch zeitretardierte Interaktionen zwischen dem betrachteten System und seiner Umgebung entstehen können, etwa in Form von Wechselwirkungen mit einem strukturierten Phononreservoir oder kohärentem Quantenfeedback. Die untersuchten Systeme umfassen hierbei einen topologischen Supraleiter, der mit einem strukturierten Phononreservoir interagiert. Es zeigt sich, dass auftretende dissipative Gedächtniseffekte zu einer Stabilisierung und Verstärkung topologischer Eigenschaften führen können. Weiterhin werden Quantenpunktsysteme untersucht, in denen phonon-induzierte nicht-Markoffsche Wechselwirkungen zu vollständiger Populationsinversion und unidirektionalem Quantentransport führen können. Zuletzt wird ein Quantenemitter gleichzeitig einem strukturierten Phononreservoir und kohärentem Quantenfeedback ausgesetzt, woraus die Formation von dynamisch-dissipativen Strukturen mit stabilisierter angeregter Systembesetzung resultiert.

Weiterhin kommen in dieser Arbeit neuartige neuronale Netzwerke zur Beschreibung offener und symmetrischer Spin-1/2 Quantensysteme mit Markoffscher Dynamik zum Einsatz. Ihre unbegrenzte Parallelisierbarkeit und effiziente Hilbertraumtrunkierung ermöglichen hohe Grade an Informationskompression und hochperformante Simulationen großer Systeme. Konkret werden neuartige Hybridmethoden zur approximativen Hilbertraumabtastung entwickelt, womit präzise Simulationen asymmetrischer Spin-1/2 Systeme auf Basis der *restricted Boltzmann machine* Architektur erstmals möglich werden. Zudem wird ein neuronales Bitkodierungsformat für Fockzustände entwickelt, wodurch eine hocheffiziente Beschreibung offener Hybridsysteme mit bosonischen Freiheitsgraden auf Basis neuronaler Netzwerke ermöglicht wird.

# Publications

- **O. Kaestle**, Y. Sun, Y. Hu, and A. Carmele, "Memory-critical dynamical buildup of phonon-dressed Majorana fermions," Phys. Rev. B **102**, 245115 (2020).
- **O. Kaestle**, E. V. Denning, J. Mørk, A. Knorr, and A. Carmele, "Unidirectional quantum transport in optically driven V-type quantum dot chains," Phys. Rev. B **103**, 115418 (2021).
- **O. Kaestle**, R. Finsterhoelzl, A. Knorr, and A. Carmele, "Continuous and time-discrete non-Markovian system-reservoir interactions: Dissipative coherent quantum feedback in Liouville space," Phys. Rev. Research **3**, 023168 (2021).
- **O. Kaestle** and A. Carmele, "Sampling asymmetric open quantum systems for artificial neural networks," Phys. Rev. B **103**, 195420 (2021).
- **O. Kaestle** and A. Carmele, "Efficient bit encoding of neural networks for Fock states," Phys. Rev. A **103**, 062409 (2021).

# Contents

# Acronyms

| | |
|---|---|
| **1D** | One-dimensional |
| **2D** | Two-dimensional |
| **3D** | Three-dimensional |
| **MPS** | Matrix product state |
| **MPO** | Matrix product operator |

# 1 Introduction

## 1.1 Motivation

In contrast to isolated systems thoroughly decoupled from their environment, open quantum systems denote setups featuring crucial interactions with their surroundings, resulting in unique dynamical phenomena [1–3]. Current research aims to control and utilize such dynamical system-reservoir interactions for the design and development of novel quantum optical devices and quantum information technology [4–10]. In particular, phonon-assisted dynamical dissipative processes arising in semiconductor nanostructures are promising candidates for potential chip-integrated applications [11–24]. Since the environmental degress of freedom are often times unknown and comprise a potentially infinite number of elements, the precise description of open quantum systems constitutes an immense theoretical challenge [25–27]: For increasing numbers of system elements, the dimension of the corresponding Hilbert space scales exponentially in size. In consequence, the crucial information contained in the system of interest and its surrounding environment must be extracted and efficiently compressed to allow for an accessible theoretical description.

Multiple theoretical methods and numerical approaches have been fathomed to derive the most efficient representation of a wide variety of open quantum systems without losing crucial information on the dynamical interplay between system and environment. They include correlation expansions of the Heisenberg equations of motion [28, 29], a variety of second-order perturbative master equations based on numerous theoretical assumptions and approximations [1–3], real-time path integral formulations [30–38], numerical realizations of high-dimensional tensor networks [39–45] and, in recent developments, machine learning implementations based on artificial neural networks [46–59]. All of these techniques facilitate varying degrees of information compression based on specific assumptions about the investigated open quantum system. Depending on the underlying approach, they each have individual advantages and shortcomings with respect to the achievable compression efficiency, numerical performance and scalability, and representational limits. In this thesis, we review and compare all of the aforementioned approaches from an information perspective and apply them to a variety of physical setups and scenarios.

While a quantum system is never completely isolated from its environment, often times the interplay with an external reservoir merely results in constant dissipative processes such as decoherence or thermal loss of system excitation. The time evolution dynamics of such systems is considered *Markovian*, i.e., a system memory is not required for its accurate depiction, drastically decreasing the complexity of the system-reservoir interaction. This is not the case if the considered system and its environment evolve on similar time scales. There, the theoretical description must incorporate a system memory

to accurately capture the unfolding *non-Markovian* dynamical interplay between system and reservoir. We explore emerging dissipation-based non-Markovian memory effects induced, e.g., by system-reservoir interactions with a structured phonon environment or time-discrete coherent photonic quantum feedback, resulting in time-delayed dynamical information exchange between system and environment [60–68]. Our investigations range from $p$-wave topological superconductors coupled to a structured phonon environment, where a memory-induced stabilization and recovery of topological properties is observed [69], to semiconductor quantum dot nanostructures exhibiting complete population inversion and unidirectional quantum transport as a result of dissipation-induced non-Markovian excitation transfer [70], and quantum optical systems exposed to both coherent quantum feedback and phonon-induced decoherence, leading to the formation of dynamical dissipative structures and population trapping [71].

In terms of achievable information compression, machine learning applications in the form of artificial neural networks have recently emerged as a novel technique for the approximate description of open quantum systems, offering high performing simulations of Markovian scenarios with a potential impact on all physical research fields [46–59]. Combining their boundless capacity for parallelization with precise and customizable Hilbert space compression via Metropolis sampling algorithms, very large system sizes become accessible. In this thesis, we specifically investigate and advance the *restricted Boltzmann machine* architecture, representing a natural and highly efficient neural network realization of the density matrix of symmetric open spin-1/2 systems. We extend the representational limits of the established neural network by developing novel adaptive sampling strategies for a highly tailored compression of configuration space, enabling accurate simulations of asymmetric systems [72]. Furthermore, we push the representational power of the restricted Boltzmann machine architecture beyond spin-1/2 systems by introducing a neural bit encoding scheme for Fock number states, facilitating supremely efficient calculations of hybrid systems with bosonic degrees of freedom [73].

## 1.2 Structure of the thesis

The thesis is divided into three main parts. The first part comprises the foundation of all employed theoretical approaches and numerical techniques: In Chapter 2, we introduce the basic concepts of open quantum systems and density matrix theory. Chapter 3 provides details and derivations for the most important Markovian and non-Markovian master equations. In Chapter 4, we discuss the concepts of real-time path integrals as an alternative approach to quantum mechanics and derive the path integral description for a continuously driven quantum emitter subjected to a structured continuous reservoir of harmonic oscillators, known as the *spin-boson model*. Lastly, we introduce the core ideas of artificial neural networks and derive theoretical descriptions and numerical techniques to enable neural network calculations of the stationary states and time evolution dynamics of open quantum systems in Chapter 5.

In the second part of this thesis, we investigate the emergence of dissipative non-Markovian phenomena in open quantum systems. In Chapter 6, we employ the polaron master equa-

tion for the description of a topological $p$-wave superconductor surrounded by a structured phonon environment and demonstrate a memory-induced recovery and long-term stabilization of topological properties. In Chapter 7, both a Heisenberg correlation expansion and the polaron master equation are used to investigate optically driven $V$-type quantum dots interacting with a structured phonon reservoir. We predict the occurrence of a non-reciprocal phonon-assisted energy transfer in a single emitter, resulting in complete population inversion. Moreover, when combining multiple quantum dots to a chain-like spatial distribution, this mechanism is shown to facilitate non-Markovian undirectional quantum transport. Lastly, in Chapter 8 we develop a numerically exact tensor network-based approach to describe two non-Markovian processes with continuous and time-discrete retardation effects simultaneously, supporting both interactions with and without energy exchange between system and reservoir. Here, the implementation of the continuous reservoir is based on a real-time path integral approach. As an example application of the presented method, we consider a two-level quantum emitter featuring a time-discrete quantum memory via coherent quantum feedback and simultaneously coupled to a structured reservoir of independent oscillators. The resulting non-Markovian interplay between the two structured reservoirs leads to a dynamical protection of coherence against destructive interference processes, facilitating dynamical population trapping in the system.

The third part of this thesis is focused on the development and investigation of artificial neural networks to achieve highly efficient information compression in open quantum systems. In Chapter 9, we present an adjustment to the commonly employed Metropolis algorithm for the approximate sampling of configuration space and derive a novel hybrid sampling approach, facilitating accurate neural network simulations of asymmetric open spin-1/2 quantum systems. As an example application, we calculate the stationary state of a boundary-driven isotropic Heisenberg chain without symmetries of translational invariance. In Chapter 10, the representational capabilities of the restricted Boltzmann machine architecture are further advanced via a neural bit encoding scheme for Fock number states, allowing for the simulation of open hybrid systems comprising bosonic degrees of freedom. We confirm the accuracy, scalability and supreme compression efficiency of the presented method, outperforming even maximally optimized density matrix approaches.

Finally, we briefly summarize our findings in Chapter 11 and give an outlook on possible future investigations.

# Part I

# Theoretical background

# 2 Open quantum systems

In the simplest theoretical conception of a quantum system, it is assumed that the system of interest is completely isolated from its environment. Without external perturbations such as noise or decoherence processes, the system state remains pure for all times and the corresponding Hilbert space dimension depends only on the system degrees of freedom. However, in most conceivable quantum optical scenarios the system of interest interacts with its environment, e.g., via thermal dissipation processes or by performing measurements on the system, influencing the dynamical system state and resulting in information loss. In open quantum system theory, environmental influences are explicitly taken into account for the description of the system. Since we are only interested in a clearly defined subsystem and the environmental degrees of freedom usually remain undetermined, we differentiate between the relevant and irrelevant components of the *open system*. The irrelevant part is then compressed or partly disregarded, resulting in a mixed state representation and allowing for an efficient and accurate description of the open system potentially comprising an infinite number of degrees of freedom.

From a theoretical perspective, we declare the relevant components of the open system as the *system* and all remaining parts are collectively described as the *environment*. The Hamiltonian describing such an open system consists of freely evolving contributions $H_0$ and a coupling term $H_I$ accounting for the interactions between system and environment [1],

$$H = H_0 + H_I. \tag{2.1}$$

A schematic of a generic open quantum system is shown in Fig. 2.1. The main challenge for the description of open quantum systems is the fact that the corresponding Hilbert space dimension scales exponentially with the number of involved particles. While this issue of course also limits the theoretical accessibility of large isolated systems, in case of open systems the number of contributing environmental degrees of freedom is often undetermined. Hence, for system-reservoir interactions with a continuum of environmental modes, e.g., arising in a harmonic structured reservoir of independent oscillators, an exact analytical description is unavailable in most cases, even for small systems consisting of a single particle [74].

In order to address the exponential scaling of the Hilbert space dimension and to render the description of open quantum systems feasible, multiple analytical truncation-based approaches and novel numerical compression schemes have been developed. In the course of this thesis, we will explore and apply the most important state-of-the-art methods for the description of open quantum systems: Analytical techniques based on perturbation theory range from correlation expansions [28, 29] to second-order perturbative master equations [1–3], which exploit the fact that the environment is usually large compared

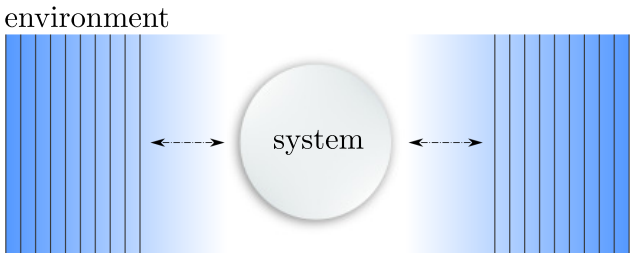


*Figure 2.1:* Sketch of an open quantum system, consisting of a system interacting with an environment.

to the system of interest. Hence, when assuming a weak system-reservoir coupling, the environment is mostly unperturbed by the system and remains in its initial state throughout the open system time evolution. In consequence, it is often sufficient to trace out the reservoir degrees of freedom for an effective reduced system description. The numerically exact real-time path integral formalism represents an alternative approach [30–38] and has been efficiently implemented using high-dimensional tensor networks, allowing for on-the-fly compression [39, 75–77]. In most recent developments, machine learning applications based on artificial neural networks have been employed for the description of symmetric open spin-1/2 quantum systems [46, 47, 51, 56–59, 78, 79], achieving vast performance gains via an efficient compression of configuration space and the required degrees of freedom.

Depending on the investigated open system and the architecture employed for its description, time-delayed information backflow between system and reservoir may occur, resulting in an effective system memory and unfolding non-Markovian dynamics [1–3, 60–66, 80]. Utilizing and controlling such non-Markovian memory effects has emerged as a major field of research, with a broad range of potential applications in the fields of quantum optical devices and quantum information technology [4–10], and represents the field of research of the second part of this work.

## 2.1 Density matrix theory

A pure quantum state is described by a state vector $|\psi(t)\rangle$, with its time evolution provided by the Schrödinger equation. In case parts of the considered system are deemed irrelevant and disregarded from the description, the system is no longer in a pure state. Rather, the system takes on a mixed state which can be represented in terms of the density matrix $\rho$, defined by [1, 81, 82]

$$\rho(t) = \sum_{i,j} \rho_{ij}(0) \, |\psi_i(t)\rangle \, \langle\psi_j(t)| \, . \tag{2.2}$$

Here, diagonal elements $\rho_{ii}(0) \, |\psi_i(t)\rangle \, \langle\psi_i(t)|$ denote system state densities and off-diagonal elements describe coherences. We distinguish between three perspectives: Firstly, the density matrix allows for a many-body ensemble description of mixed states. Here, it is unknown in which possible realization the current system manifests itself, rendering a

superposition of diagonal state spaces necessary. For instance, in a thermal ensemble of a continuum of modes $\boldsymbol{k}$,

$$\rho_B(T) = \frac{1}{Z} \exp\left(-\frac{1}{k_B T} \int \mathrm{d}^3k \; \hbar\omega_k r_{\boldsymbol{k}}^\dagger r_{\boldsymbol{k}}\right), \tag{2.3}$$

with bosonic creation and annihilation operators $r_{\boldsymbol{k}}^\dagger$, $r_{\boldsymbol{k}}$ of modes at frequencies $\omega_k = c|\boldsymbol{k}|$ and obeying the commutation relation $[r_{\boldsymbol{k}}, r_{\boldsymbol{k}'}^\dagger] = \delta(\boldsymbol{k} - \boldsymbol{k}')$, with $c$ the mode propagation velocity, $Z$ the partition function and $k_B$ the Boltzmann constant, many realizations must be considered to define a temperature $T$. Secondly, when considering a system without an ensemble description, the density matrix still constitutes a more general representation than the corresponding pure state, as it allows for the description of purely thermalized states without off-diagonal elements [1], and is therefore the least restrictive available ansatz for the description of arbitrary quantum states. Lastly, from a statistical reasoning perspective the density matrix is the most general foundation of the probability amplitude for a certain measurement outcome: Using techniques such as quantum state tomography, it is possible to reconstruct the shape of the density matrix from experimental measurements on a quantum system [83–85], allowing to deduce an underlying pure state via quantum state estimates. On the other hand, it is not possible to reconstruct a pure system state *directly* from experimental measurements, since the pure state representation compresses the outcome of many measurements of system observables $\langle\psi(0)|\,\hat{A}(t)\,|\psi(0)\rangle$ and therefore can only be obtained *after* the fact.

The density matrix is self-adjoint and trace-preserving,

$$\rho^\dagger(t) = \rho(t), \tag{2.4a}$$
$$\mathrm{tr}\{\rho(t)\} = 1, \tag{2.4b}$$
$$\mathrm{tr}\{\rho^2(t)\} \leq 1, \tag{2.4c}$$

and the equal sign in Eq. (2.4c) holds true if the respective density matrix describes a pure state. Since the eigenvalues of a matrix are invariant under unitary transformations, the choice of basis is arbitrary as long as it is complete [1]. Therefore, a density matrix with more than one eigenvalue varying from zero cannot be described as a state vector and thus represents a mixed state. To calculate the expectation value of arbitrary Hermitian quantum operators $\hat{A}$, the trace over the operator product of $\hat{A}$ and $\rho(t)$ is taken,

$$\langle\hat{A}(t)\rangle = \mathrm{tr}\left\{\hat{A}\rho(t)\right\}. \tag{2.5}$$

The time evolution of the density matrix is governed by the von Neumann equation, which is derived next.

### 2.1.1 Von Neumann equation

The time evolution of a pure state is provided by the Schrödinger equation

$$i\hbar\frac{\mathrm{d}}{\mathrm{d}t}\,|\psi(t)\rangle = H(t)\,|\psi(t)\rangle\,, \tag{2.6}$$

with $H(t)$ denoting an arbitrary system Hamiltonian. To calculate the time evolution of the density matrix, we replace the state vector in the Schrödinger equation by $\rho(t)$, yielding

$$\begin{aligned} i\hbar\frac{\mathrm{d}}{\mathrm{d}t}\rho(t) &= i\hbar\frac{\mathrm{d}}{\mathrm{d}t}\left[\sum_{i,j}\rho_{ij}(0)\left|\psi_i(t)\right\rangle\left\langle\psi_j(t)\right|\right] \\ &= i\hbar\sum_{i,j}\rho_{ij}(0)\left[\left|\dot{\psi}_i(t)\right\rangle\left\langle\psi_j(t)\right| + \left|\psi_i(t)\right\rangle\left\langle\dot{\psi}_j(t)\right|\right] \\ &= \sum_{i,j}\rho_{ij}(0)\left[H(t)\left|\psi_i(t)\right\rangle\left\langle\psi_j(t)\right| - \left|\psi_i(t)\right\rangle\left\langle\psi_j(t)\right|H(t)\right] \\ &= H(t)\rho(t) - \rho(t)H(t) \\ &= \left[H(t),\rho(t)\right]. \end{aligned} \tag{2.7}$$

Rewriting Eq. (2.7) results in the von Neumann equation

$$\frac{\mathrm{d}}{\mathrm{d}t}\rho(t) = -\frac{i}{\hbar}\left[H(t),\rho(t)\right], \tag{2.8}$$

providing the time evolution dynamics of the density matrix. Alternatively, the density matrix can be propagated in time by application of the time evolution operator $U(t,0) = \exp[-i/\hbar\int_0^t d\tau H(\tau)]$ via [1, 82]

$$\rho(t) = U(t,0)\rho(0)U^\dagger(t,0). \tag{2.9}$$

## 2.2 Interaction picture

For the calculation of open system time evolution dynamics, it is often advantageous to transform into the interaction picture. This is performed via the unitary transformation matrix $U_0(t,0) = \exp(-iH_0t/\hbar)$,

$$\tilde{\rho}(t) = U_0^\dagger(t,0)\rho(t)U_0(t,0), \tag{2.10}$$

with $H_0$ denoting an arbitrary element of $H$. To obtain the interaction picture representation, it is chosen as the freely evolving contribution $H_0 = H - H_I$ of the open system, excluding system-reservoir interactions $H_I$. To derive the equation of motion governing the time evolution of $\tilde{\rho}(t)$, we take the time derivative of the density operator,

$$\begin{aligned} &\frac{\mathrm{d}}{\mathrm{d}t}\rho(t) = \frac{\mathrm{d}}{\mathrm{d}t}\left[U_0(t,0)U_0^\dagger(t,0)\rho(t)U_0(t,0)U_0^\dagger(t,0)\right] \\ &= \dot{U}_0(t,0)\tilde{\rho}(t)U_0^\dagger(t,0) + U_0(t,0)\dot{\tilde{\rho}}(t)U_0^\dagger(t,0) + U_0(t,0)\tilde{\rho}\dot{U}_0^\dagger(t,0) \\ &= U_0(t,0)\dot{\tilde{\rho}}(t)U_0^\dagger(t,0) - \frac{i}{\hbar}\left[H_0U_0(t,0)\tilde{\rho}(t)U_0^\dagger(t,0) - U_0(t,0)\tilde{\rho}(t)U_0^\dagger(t,0)H_0\right]. \end{aligned} \tag{2.11}$$

Applying $U_0^\dagger(t,0)$ from the left and $U_0(t,0)$ from the right of Eq. (2.11) results in

$$U_0^\dagger(t,0)\dot{\rho}(t)U_0(t,0) = \dot{\tilde{\rho}}(t) - \frac{i}{\hbar}\left[\tilde{H}_0(t),\tilde{\rho}(t)\right], \tag{2.12}$$

with $\tilde{H}_0(t) = U_0^\dagger(t,0) H_0 U_0(t,0)$.

Next, the von Neumann Eq. (2.8) is employed. Again, we apply $U_0^\dagger(t,0)$ from the left and $U_0(t,0)$ from the right, yielding

$$U_0^\dagger(t,0)\dot{\rho}(t)U_0(t,0) = -\frac{i}{\hbar}\left[\tilde{H}(t), \tilde{\rho}(t)\right], \tag{2.13}$$

with $\tilde{H}(t) = U_0^\dagger(t,0) H U_0(t,0)$. Finally, equating Eqs. (2.12) and (2.13) results in the equation of motion for the interaction picture density matrix,

$$\begin{aligned}\frac{\mathrm{d}}{\mathrm{d}t}\tilde{\rho}(t) &= -\frac{i}{\hbar}\left\{\left[\tilde{H}(t), \tilde{\rho}(t)\right] - \left[\tilde{H}_0(t), \tilde{\rho}(t)\right]\right\} \\ &= -\frac{i}{\hbar}\left[\tilde{H}_I(t), \tilde{\rho}(t)\right]. \end{aligned} \tag{2.14}$$

To conclude, in the interaction picture representation the time evolution dynamics of the density operator is solely provided by the interaction Hamiltonian $\tilde{H}_I(t)$ of the open quantum system. It is noted, however, that the transformation must be reversed for the calculation of expectation values, since in general $\langle \hat{A}(t) \rangle = \mathrm{tr}\{\hat{A}\rho(t)\} \neq \mathrm{tr}\{\hat{A}\tilde{\rho}(t)\}$.

# 3 Master equation theory

Master equations denote differential equations to describe the time evolution dynamics of open quantum systems in terms of the density matrix. They are derived in second-order perturbation theory and under the application of numerous assumptions with regard to the environmental state, the system-reservoir coupling and the history of the system. Depending on the extent of applied truncations, different forms of master equations can be derived, each with their own advantages and limitations.

In this Chapter, we outline the concepts of master equation theory and derive the most common Markovian and non-Markovian master equations. Using second-order perturbation theory, the non-Markovian Redfield master equation is derived in Sec. 3.1. Advantages and shortcomings of the Redfield form are discussed, before additional approximations are applied to derive the Markovian Lindblad form in Sec. 3.2. While the mathematical structure of the Lindblad master equation is probability conserving under all conditions, it fails to capture memory effects with potential impact on the system evolution. In Sec. 3.3, the polaron transformation is introduced and applied to reshape the Redfield equation into the non-Markovian polaron master equation. In Sec. 3.4, we discuss the Franck-Condon renormalization, a routinely applied renormalization of the open system Hamiltonian to simplify the structure of the master equation. Lastly, Sec. 3.5 provides details on the numerical implementation of the presented master equations.

## 3.1 Redfield master equation

The exponential scaling of the Hilbert space dimension for increasing system degrees of freedom represents the key challenge for the accurate description of open quantum systems (see Ch. 2). Master equation theory tackles this problem from an analytical perspective to obtain a compressed and efficient representation of the considered system. Any master equation must maintain the mathematical properties of the density matrix [Eq. (2.4)] throughout the entire time evolution. Moreover, conservation laws apply when excitation is transferred between the system and reservoir. In the density matrix formalism (see Sec. 2.1) this translates to trace conservation of the full open system density operator for all times, $\mathrm{tr}\{\rho(t)\} = 1 \; \forall t$.

We start in the interaction picture (see Sec. 2.2) and formally solve the von Neumann Eq. (2.14) by formal integration,

$$\tilde{\rho}(t) = \tilde{\rho}(0) - \frac{i}{\hbar} \int_0^t \mathrm{d}t' \; \left[\tilde{H}_I(t'), \tilde{\rho}(t')\right]. \tag{3.1}$$

For a second-order perturbative treatment, Eq. (3.1) is reinserted once more into the von Neumann equation, yielding

$$\frac{\mathrm{d}}{\mathrm{d}t}\tilde{\rho}(t) = -\frac{i}{\hbar}\left[\tilde{H}_I(t), \tilde{\rho}(0)\right] - \frac{1}{\hbar^2}\int_0^t \mathrm{d}t' \ \left[\tilde{H}_I(t), \left[\tilde{H}_I(t'), \tilde{\rho}(t')\right]\right]. \tag{3.2}$$

The first term in Eq. (3.2) is renormalized to zero by application of a Franck-Condon renormalization of the full open system Hamiltonian (see Sec. 3.4). In the second term, the integration variable is substituted by $\tau = t - t'$, resulting in

$$\frac{\mathrm{d}}{\mathrm{d}t}\tilde{\rho}(t) = -\frac{1}{\hbar^2}\int_0^t \mathrm{d}\tau \ \left[\tilde{H}_I(t), \left[\tilde{H}_I(t-\tau), \tilde{\rho}(t-\tau)\right]\right]. \tag{3.3}$$

The structure of Eq. (3.3) uncovers the influence of the past $\tau = 0, \ldots, t$ on the present state and the evolution of the open system. Due to the time retardation of $\tilde{H}_I$ and $\tilde{\rho}$ in the integrand, the evaluation of Eq. (3.3) in its current form becomes increasingly expensive for each incremental time step, drastically limiting the accessible time scales. Hence, as a next step several approximations are applied to Eq. (3.3) to obtain a more accessible representation.

### 3.1.1 Bath assumption and Born approximation

The first approximation to simplify Eq. (3.3) is based on the assumption that the environment is large compared to the system and initially in a thermal equilibrium state, often referred to as the *bath assumption*. Under these conditions the *Born approximation* is applied, assuming a weak system-reservoir interaction. In consequence of a weak coupling between system and environment, the latter is not perturbed by excitation transfer from the system or re-equilibrates on a much faster time scale than the time for the system to evolve from $\tilde{\rho}(t) \to \tilde{\rho}(t + \Delta t)$. Hence, it remains in its initial equilibrium state for all times, $\tilde{\rho}_B(t) \approx \tilde{\rho}_B(0)$, and the density matrix factorizes [1]:

$$\tilde{\rho}(t-\tau) \approx \tilde{\rho}_S(t-\tau) \otimes \tilde{\rho}_B(0). \tag{3.4}$$

As a result, Eq. (3.3) takes the form

$$\frac{\mathrm{d}}{\mathrm{d}t}\tilde{\rho}(t) = -\frac{1}{\hbar^2}\int_0^t \mathrm{d}\tau \ \left[\tilde{H}_I(t), \left[\tilde{H}_I(t-\tau), \tilde{\rho}_S(t-\tau) \otimes \tilde{\rho}_B(0)\right]\right]. \tag{3.5}$$

### 3.1.2 First Markov approximation

As a next step, the *first Markov approximation* is applied. It states that the time evolution of the system is mainly affected by its present state rather than by its past. Thus, the history of the system state is disregarded in the integrand,

$$\tilde{\rho}_S(t-\tau) \approx \tilde{\rho}_S(t), \tag{3.6}$$

resulting in

$$\frac{\mathrm{d}}{\mathrm{d}t}\tilde{\rho}(t) = -\frac{1}{\hbar^2}\int_0^t \mathrm{d}\tau \ \left[\tilde{H}_I(t), \left[\tilde{H}_I(t-\tau), \tilde{\rho}_S(t)\otimes\tilde{\rho}_B(0)\right]\right], \tag{3.7}$$

which can of course be wrong to an arbitrary degree, e.g., when considering feedback effects. Eq. (3.7) is transformed back into the Schrödinger picture by application of the transformation matrix $U_0(t,0)$ from the left and $U_0^\dagger(t,0)$ from the right (see Sec. 2.2). Moreover, since we are only interested in the dynamics of the system $S$, the reservoir contributions $B$ are traced out from the equation. Therefore, Eq. (3.7) takes the form

$$\begin{aligned}\frac{\mathrm{d}}{\mathrm{d}t}\mathrm{tr}_B\{\rho(t)\} =& -\frac{i}{\hbar}\mathrm{tr}_B\{[H_0, \rho_S(t)\otimes\rho_B(0)]\} \\ & -\frac{1}{\hbar^2}\int_0^t \mathrm{d}\tau \ \mathrm{tr}_B\{[H_I, [H_I(-\tau), \rho_S(t)\otimes\rho_B(0)]]\},\end{aligned} \tag{3.8}$$

and we arrive at the *Redfield master equation* [1–3]

$$\frac{\mathrm{d}}{\mathrm{d}t}\rho_S(t) = -\frac{i}{\hbar}[H_S, \rho_S(t)] - \frac{1}{\hbar^2}\int_0^t \mathrm{d}\tau \ \mathrm{tr}_B\{[H_I, [H_I(-\tau), \rho_S(t)\otimes\rho_B(0)]]\}, \tag{3.9}$$

where $H_S$ denotes the free evolution contribution of the system with traced out reservoir degrees of freedom.

The second term in Eq. (3.9) is referred to as the systems' *memory kernel*, representing system-reservoir interactions of past times $H_I(-\tau)$ and their effect on the current system state. Hence, the Redfield equation is of a *non-Markovian* nature, allowing for the description of environment-induced memory effects. Its validity and applicability is limited by the assumptions made in this Section. However, it is noted that mathematical issues may arise from the structure of the Redfield equation. While the trace of $\rho_S(t)$ is preserved under all conditions, the density matrix is no longer necessarily positive-semidefinite. In consequence, unphysical behavior such as negative densities may occur in the course of the time evolution, specifically depending on the parameter regime of the system-reservoir interaction strength [86], restricting the accessible parameter range to the weak coupling limit. To overcome this problem and to ensure physical results under all conditions, additional approximations can be performed. The master equation resulting from this treatment is the so-called Lindblad form, which is derived next. However, enforcing a positive-semidefinite density matrix comes at a cost: The Lindblad master equation is of a *Markovian* nature, i.e., in contrast to the Redfield equation memory effects arising from time-delayed system-reservoir backaction are no longer encompassed.

## 3.2 Lindblad master equation

Provided that the system observables evolve on much larger time scales than the bath correlations, memory effects arising from system-reservoir interactions become insignificantly small and can be neglected for a more efficient formalism. Hence, for a wide variety of scenarios a Markovian description suffices for an accurate representation of the considered

system. In this Section, the most successful and commonly applied Markovian master equation in quantum optics is derived: The Lindblad form [1].

We start from the Redfield Eq. (3.9) and assume generic fermionic system operators of the form $J^{(\dagger)}(t)$, where we differentiate between two cases,

$$(i)\ J(t) = J^\dagger(t), \tag{3.10a}$$

$$(ii)\ J(t) \neq J^\dagger(t). \tag{3.10b}$$

Provided that the operator $J$ represents a *single* operator rather than a sum of operators and under application of the rotating wave approximation, a generic system-reservoir interaction Hamiltonian featuring a structured 3D reservoir is given by

$$H_I(t) = \hbar \int \mathrm{d}^3k \ \left[ g_{\boldsymbol{k}} r_{\boldsymbol{k}} J^\dagger(t) e^{-i\omega_k t} + \mathrm{H.c.} \right], \tag{3.11}$$

with bosonic creation and annihilation operators $r^\dagger_{\boldsymbol{k}}$, $r_{\boldsymbol{k}}$ of reservoir modes at frequencies $\omega_k = c_s|\boldsymbol{k}|$, with $c_s$ denoting the propagation velocity in a given material, and mode-dependent system-reservoir coupling elements $g_{\boldsymbol{k}}$. Defining collective bosonic operators

$$R(t) = \int \mathrm{d}^3k \ g_{\boldsymbol{k}} e^{-i\omega_k t} r_{\boldsymbol{k}}(0), \tag{3.12}$$

Eq. (3.11) takes the form

$$H_I(t) = \hbar \left[ R^\dagger(t) J(t) + R(t) J^\dagger(t) \right]. \tag{3.13}$$

Eq. (3.13) is inserted into the integrand of the Redfield Eq. (3.9). The evaluation of the double commutator yields

$$\begin{aligned} \frac{\mathrm{d}}{\mathrm{d}t}\rho_S(t) = &-\frac{i}{\hbar}\left[H_S, \rho_S(t)\right] \\ &- \frac{1}{\hbar^2}\int_0^t \mathrm{d}\tau \ \Big\{ \langle R^\dagger R(-\tau)\rangle \left[ J J^\dagger(-\tau)\rho_S(t) - J^\dagger(-\tau)\rho_S(t) J \right] \\ &+ \langle R(-\tau) R^\dagger\rangle \left[ -J\rho_S(t) J^\dagger(-\tau) + \rho_S(t) J^\dagger(-\tau) J \right] \\ &+ \langle R R^\dagger(-\tau)\rangle \left[ J^\dagger J(-\tau)\rho_S(t) - J(-\tau)\rho_S(t) J^\dagger \right] \\ &+ \langle R^\dagger(-\tau) R\rangle \left[ -J^\dagger \rho_S(t) J(-\tau) + \rho_S(t) J(-\tau) J^\dagger \right] \Big\}, \end{aligned} \tag{3.14}$$

with $\langle \ldots \rangle = \mathrm{tr}_B(\ldots \rho_B)$. Under the bath assumption (see Sec. 3.1) the reservoir is modeled as a thermal ensemble,

$$\rho_B = \frac{1}{Z} \exp\left( -\frac{1}{k_B T} \int \mathrm{d}^3k \ \hbar\omega_k r^\dagger_{\boldsymbol{k}} r_{\boldsymbol{k}} \right), \tag{3.15}$$

with $Z$ the partition function, $k_B$ the Boltzmann constant and $T$ the reservoir temperature. With this, the reservoir correlations occurring in Eq. (3.14) can be calculated explicitly.

For the simplest conceivable case of an unstructured 1D reservoir in a vacuum state, i.e., $g_k \approx g_0$ and $T = 0\,\mathrm{K}$, no further approximations must be applied for the derivation of the Lindblad form. In vacuum, it is $\langle r_{\boldsymbol{k}}^\dagger r_{\boldsymbol{k}}\rangle = 0$ and calculating, e.g., $\langle RR^\dagger(-\tau)\rangle$ yields

$$\begin{aligned}\langle RR^\dagger(-\tau)\rangle &= \int_0^\infty \mathrm{d}k \int_0^\infty \mathrm{d}k'\; g_0 g_0^* e^{-i\omega_{k'}\tau}\,\langle r_k r_{k'}^\dagger\rangle \\ &= \int_0^\infty \mathrm{d}k\; |g_0|^2 e^{-ic_s k\tau} \\ &= \frac{\pi|g_0|^2}{c_s}\delta(\tau) - iP\left(\frac{1}{c_s\tau}\right),\end{aligned} \tag{3.16}$$

where $P(\ldots)$ denotes the Cauchy principal value [1] which leads to a phase shift and renormalization of the systems' transition frequencies. However, since the transition frequencies can be chosen freely and are not crucial for our investigations, the contribution from the Cauchy principle value is omitted in the following. Under these presumptions, we get $\langle R(-\tau)R^\dagger\rangle = \langle RR^\dagger(-\tau)\rangle$ and $\langle R^\dagger R(-\tau)\rangle = \langle R^\dagger(-\tau)R\rangle = 0$. Defining a constant damping rate $\pi|g_0|^2/(\hbar^2 c_s) =: \gamma$ and inserting the evaluated bath correlations into Eq. (3.14) immediately results in the *Lindblad master equation*,

$$\frac{\mathrm{d}}{\mathrm{d}t}\rho_S(t) = -\frac{i}{\hbar}\left[H_S, \rho_S(t)\right] + \gamma\left[2J\rho_S(t)J^\dagger - J^\dagger J\rho_S(t) - \rho_S(t)J^\dagger J\right]. \tag{3.17}$$

To conclude, for an unstructured 1D reservoir with energy-conserving interactions in a vacuum state ($T = 0\,\mathrm{K}$), only the Born approximation is required for the derivation of the Lindblad form. The delta function arising from the bath correlations renders the first Markov approximation unnecessary.

### 3.2.1 Second Markov approximation

Next, we consider the non-vacuum case $T > 0\,\mathrm{K}$ and a structured reservoir. Under these conditions, the bath correlations are evaluated as

$$\langle R(-\tau)R^\dagger\rangle = \int_0^\infty \mathrm{d}^3k\; |g_{\boldsymbol{k}}|^2 e^{i\omega_k\tau}\,(n_k+1)\,, \tag{3.18a}$$

$$\langle RR^\dagger(-\tau)\rangle = \int_0^\infty \mathrm{d}^3k\; |g_{\boldsymbol{k}}|^2 e^{-i\omega_k\tau}\,(n_k+1)\,, \tag{3.18b}$$

$$\langle R^\dagger(-\tau)R\rangle = \int_0^\infty \mathrm{d}^3k\; |g_{\boldsymbol{k}}|^2 e^{-i\omega_k\tau} n_k, \tag{3.18c}$$

$$\langle R^\dagger R(-\tau)\rangle = \int_0^\infty \mathrm{d}^3k\; |g_{\boldsymbol{k}}|^2 e^{i\omega_k\tau} n_k, \tag{3.18d}$$

with the mean boson number modeled by a Bose distribution,

$$n_k = \langle r_{\boldsymbol{k}}^\dagger r_{\boldsymbol{k}}\rangle \approx \left[\exp\left(\frac{\hbar\omega_k}{k_B T}\right) - 1\right]^{-1}. \tag{3.19}$$

Inserting these expressions into Eq. (3.14) results in terms containing both integrals over $\tau$ and $\boldsymbol{k}$,

$$\begin{aligned}\frac{\mathrm{d}}{\mathrm{d}t}\rho_S(t) = &-\frac{i}{\hbar}\left[H_S, \rho_S(t)\right] \\ &- \int_0^t \mathrm{d}\tau \int_0^\infty \mathrm{d}^3k\ |g_{\boldsymbol{k}}|^2 \Big\{ e^{i\omega_k\tau} n_k \left[JJ^\dagger(-\tau)\rho_S(t) - J^\dagger(-\tau)\rho_S(t)J\right] \\ &+ e^{i\omega_k\tau}\,(n_k+1)\left[-J\rho_S(t)J^\dagger(-\tau) + \rho_S(t)J^\dagger(-\tau)J\right] \\ &+ e^{-i\omega_k\tau}\,(n_k+1)\left[J^\dagger J(-\tau)\rho_S(t) - J(-\tau)\rho_S(t)J^\dagger\right] \\ &+ e^{-i\omega_k\tau} n_k \left[-J^\dagger\rho_S(t)J(-\tau) + \rho_S(t)J(-\tau)J^\dagger\right] \Big\}. \end{aligned} \tag{3.20}$$

Due to non-vanishing reservoir occupation numbers, in this case the *second Markov approximation* must be applied to obtain a simplified description. It states that the system-reservoir interaction is independent of its past, $H_I(-\tau) \approx H_I$. In consequence, the system operators lose their time dependence, $J^{(\dagger)}(-\tau) \approx J^{(\dagger)}$, and the time integration to the present time $t$ can be expanded to all future times,

$$\int_0^t \mathrm{d}\tau(\ldots) \approx \int_0^\infty \mathrm{d}\tau(\ldots). \tag{3.21}$$

The second Markov approximation is valid if the open system effectively has no memory, meaning that its time evolution dynamics is invariant against its history. The assumption made in Eq. (3.21) is only justified if the integrand decays sufficiently fast for times $\tau > t$. Therefore, the second Markov approximation is acceptable if the time scales on which the system observables vary are large compared to the decay time of the reservoir correlations [1]. The application of the full set of approximations made so far, i.e., the bath assumption, Born approximation and first and second Markov approximation, is commonly referred to as the *Born-Markov approximation*. Using the identity $\int_0^\infty \mathrm{d}\tau\ e^{-i\omega_k\tau} = \pi/c_s\delta(k) - iP\ (1/\omega_k)$, the time integral can be explicitly evaluated and Eq. (3.20) takes the form

$$\begin{aligned}\frac{\mathrm{d}}{\mathrm{d}t}\rho_S(t) = &-\frac{i}{\hbar}\left[H_S, \rho_S(t)\right] \\ &- \frac{\pi}{c_s}\int_0^\infty \mathrm{d}^3k\ |g_{\boldsymbol{k}}|^2 \Big\{ \delta(k) n_k \left[JJ^\dagger(-\tau)\rho_S(t) - J^\dagger(-\tau)\rho_S(t)J\right] \\ &+ \delta(k)\,(n_k+1)\left[-J\rho_S(t)J^\dagger(-\tau) + \rho_S(t)J^\dagger(-\tau)J\right] \\ &+ \delta(k)\,(n_k+1)\left[J^\dagger J(-\tau)\rho_S(t) - J(-\tau)\rho_S(t)J^\dagger\right] \\ &+ \delta(k) n_k \left[-J^\dagger\rho_S(t)J(-\tau) + \rho_S(t)J(-\tau)J^\dagger\right] \Big\}. \end{aligned} \tag{3.22}$$

Again, we first consider the case of a 1D reservoir, $\boldsymbol{k} = k$. Evaluation of the delta function

results in a generalized Lindblad form

$$\begin{aligned}\frac{\mathrm{d}}{\mathrm{d}t}\rho_S(t) = &-\frac{i}{\hbar}\left[H_S, \rho_S(t)\right] \\ &+ \gamma\left(n_0+1\right)\left[2J\rho_S(t)J^\dagger - J^\dagger J\rho_S(t) - \rho_S(t)J^\dagger J\right] \\ &+ \gamma n_0\left[2J^\dagger\rho_S(t)J - JJ^\dagger\rho_S(t) - \rho_S(t)JJ^\dagger\right],\end{aligned} \tag{3.23}$$

with $\gamma = \pi|g_0|^2/c_s$. Setting $n_0 = 0$ recreates the Lindblad equation for the vacuum case [Eq. (3.17)]. Secondly, Eq. (3.22) is evaluated for a structured 3D reservoir. Spherical coordinates are employed,

$$\int_{-\infty}^{\infty}\mathrm{d}^3k = 4\pi\int_0^\infty \mathrm{d}k\; k^2, \tag{3.24}$$

and to obtain a nontrivial result, the factor $k^2$ arising from the functional determinant must be compensated by the coupling element. Hence, we must assume a super-Ohmic system-reservoir coupling element, $g_{\boldsymbol{k}} \sim k^{-1}$, and define $\tilde{g}_{\boldsymbol{k}} := g_{\boldsymbol{k}}/k$. With this presumption, Eq. (3.23) can be reproduced for the 3D reservoir case at $\gamma = 4\pi^2|\tilde{g}_0|^2/(\hbar^2 c_s)$. To conclude, when considering a structured reservoir at $T > 0\,\mathrm{K}$, the second Markov approximation is required for the derivation of a Markovian Lindblad form.

## 3.3 Polaron master equation

We conclude the discussion of master equations with the non-Markovian polaron master equation. While the Lindblad and Redfield equations can for instance also be applied to photonic reservoirs to model processes such as spontaneous emission, the polaron master equation is exclusively employed for the description of systems coupled to harmonic phonon reservoirs featuring a diagonal system-reservoir coupling without energy exchange between them [1, 14, 80, 87–92]. In these scenarios, the diagonal system-reservoir coupling Hamiltonian describes decoherence processes caused by interactions with an environment of independent harmonic oscillators. For the case of diagonal 3D fermion-phonon interaction it is of the general form [93–96]

$$H_I = \int \mathrm{d}^3r\; g(\boldsymbol{r})\left\langle\psi(\boldsymbol{r})\right|\varphi(\boldsymbol{r})\left|\psi(\boldsymbol{r})\right\rangle, \tag{3.25}$$

where $|\psi(\boldsymbol{r})\rangle$ denotes the fermionic field vector, $\varphi(\boldsymbol{r})$ is the phonon field and $g(\boldsymbol{r})$ refers to the microscopic fermion-phonon coupling coefficient, respectively. In typical quantum optical setups, the fermionic particles are assumed distinguishable and located at fixed positions in space, such that the field intensity can be modeled as $\langle\psi(\boldsymbol{r})|\psi(\boldsymbol{r})\rangle = \sum_{l=1}^N c_l^\dagger c_l\delta(\boldsymbol{r}-\boldsymbol{r}_l)$ with $c_l^{(\dagger)}$ denoting fermionic creation and annihilation operators acting on the $l$-th particle at position $\boldsymbol{r}_l$. A generic 3D phonon field is given by [95]

$$\varphi(\boldsymbol{r}) = \int \mathrm{d}^3k\,\sqrt{\frac{c_s k}{2}}\left(r_{\boldsymbol{k}}^\dagger e^{-i\boldsymbol{k}\cdot\boldsymbol{r}} + \mathrm{H.c.}\right), \tag{3.26}$$

with $r_{\boldsymbol{k}}^{(\dagger)}$ again denoting bosonic annihilation (creation) operators of phonon modes at frequencies $\omega_k = c_s|\boldsymbol{k}|$, with $c_s$ the speed of sound for a given material [97, 98]. Inserting these identities into Eq. (3.25) and defining

$$g_{\boldsymbol{k}} := \sqrt{\frac{c_s k}{2}} \int \mathrm{d}^3 r \; g(\boldsymbol{r}) e^{-i\boldsymbol{k}\cdot\boldsymbol{r}} \delta(\boldsymbol{r} - \boldsymbol{r}_l), \tag{3.27}$$

the fermion-phonon interaction Hamiltonian for a set of $N$ distinguishable and localized fermionic particles takes the form

$$H_I = \sum_{l=1}^{N} \int \mathrm{d}^3 k \; c_l^\dagger c_l \left( g_{\boldsymbol{k}} r_{\boldsymbol{k}}^\dagger + \mathrm{H.c.} \right). \tag{3.28}$$

It is noted that when considering closely localized particles, the spatial dependence of the fermion-phonon coupling element $g_{\boldsymbol{k}}$ is commonly disregarded, i.e., $g(\boldsymbol{r}_l) = g(\boldsymbol{r}_0)\ \forall l$, together with phonon-induced momentum transfer. The main objective of the polaron master equation approach is to include as much information about the electron-phonon interaction as possible while still remaining in a reduced density matrix description in second-order perturbation theory [1, 14, 80, 87–92, 99, 100]. For the derivation of the polaron master equation, the open system Hamiltonian of the investigated system is transformed into the polaron picture.

### 3.3.1 Polaron transformation

A polaronic state describes a fermion in interaction with a harmonic phonon continuum, resulting in a self-reorganization of the collective ground state energy. Using collective bosonic operators $R^{(\dagger)} = \int \mathrm{d}\boldsymbol{k} \; (g_{\boldsymbol{k}}/\omega_k) r_{\boldsymbol{k}}^{(\dagger)}$, we apply the unitary polaron transformation to the full open system Hamiltonian $H = H_0 + H_I$,

$$H_p = U_p H U_p^{-1}, \tag{3.29}$$

with

$$U_p = \exp\left[ \sum_{l=1}^{N} c_l^\dagger c_l (R^\dagger - R) \right], \tag{3.30}$$

representing an exact and reversible transformation explicitly carried out via the Baker-Campbell-Hausdorff formula

$$e^X Y e^{-X} = \sum_{n=0}^{\infty} \frac{1}{n!} [X, Y]_n \,, \tag{3.31a}$$

$$[X, Y]_n = \Big[ X, [X, Y]_{n-1} \Big] \,, \tag{3.31b}$$

$$[X, Y]_0 = Y. \tag{3.31c}$$

The resulting polaron Hamiltonian $H_p = H_{p,0} + H_{p,I}$ is inserted into the Redfield Eq. (3.9), yielding the polaron master equation.

## 3.4 Franck-Condon renormalization

During the derivation of the Redfield Eq. (3.9), we have assumed throughout that

$$\mathrm{tr}_B\{[H_I, \rho(t)]\} = 0 \ \forall t, \tag{3.32}$$

such that the first term of the master equation only contains the freely evolving contribution of the open system Hamiltonian, restraining contributions from the system-reservoir interaction Hamiltonian solely to the memory kernel and significantly simplifying the structure of the equation. However, in general Eq. (3.32) does not hold true for arbitrary Hamiltonians. To ensure its validity, a *Franck-Condon renormalization* is commonly performed on the considered open system Hamiltonian, where the equilibrium position is shifted according to the interaction strength: First, the interaction Hamiltonian $H_I$ is modified by subtracting an artificial term $H_{FC}$, such that Eq. (3.32) is fulfilled. To compensate the artificial term, it is in turn added to the free Hamiltonian $H_0$. As a result, the full open system Hamiltonian $H = H_0 + H_I = (H_0 + H_{FC}) + (H_I - H_{FC})$ remains unchanged.

## 3.5 Numerical evaluation

The non-Markovian master equations derived in this Chapter represent regular integro-differential equations and can be numerically evaluated using two nested fourth order Runge Kutta algorithms, where the full system-reservoir memory kernel is evaluated iteratively during each time step. In case of the Markovian Lindblad master equation, only a single fourth order Runge Kutta algorithm is required.

Non-Markovian master equations feature a memory kernel, i.e., an integral over all past times with time-dependent system and bath operators [see Eq. (3.9)]. It is in general possible to derive analytical expressions for the time-dependent reservoir correlations. Analytical solutions of time-dependent system correlations $X(-\tau)$, consisting of combinations of system operators $J^{(\dagger)}(-\tau)$, are available in some elementary models such as the *spin-boson model* [74, 80]. Aside from these special cases, the system correlations must be evaluated numerically. For the inclusion of the full memory kernel featuring both time-dependent system and reservoir operators, the time evolution of the system correlations $X(-\tau)$ is determined by a closed set of differential equations depending only on the free evolution contribution $H_0$. Using the time evolution operator $U_0(t, 0) = \exp(-iH_0 t/\hbar)$,

we get for a specific matrix element

$$\begin{aligned}
\langle m|\, X(-\tau)\,|n\rangle &= \langle m|\, U_0^\dagger(-\tau,0) X U_0(-\tau,0)\,|n\rangle \\
&= \langle m|\, U_0(\tau,0) X U_0^\dagger(\tau,0)\,|n\rangle \\
&= \sum_{\{s\}} \langle m|\, U_0(\tau,0) X\,|s\rangle\,\langle s|\, U_0^\dagger(\tau,0)\,|n\rangle \\
&= \sum_{\{s\}} \langle s|\, U_0^\dagger(\tau,0)\, \underbrace{|n\rangle\,\langle m|}_{=:\rho_c(0)} U_0(\tau,0) X\,|s\rangle \\
&= \sum_{\{s\}} \langle s|\, \underbrace{U_0^\dagger(\tau,0)\rho_c(0)U_0(\tau,0)}_{=\rho_c(-\tau)}\, X\,|s\rangle \\
&= \mathrm{tr}\{\rho_c(-\tau) X\}. \qquad (3.33)
\end{aligned}$$

Here we introduced the *conditional density matrix* $\rho_c(-\tau)$ whose time evolution dynamics is prescribed by the free energy contribution, $\dot{\rho}_c(t) = -i/\hbar[H_{p,0}, \rho_c(t)]$, and must be determined for all possible initial conditions $\rho_c(0) = |n\rangle\langle m|$, i.e., $\langle n|\,\rho_c(0)\,|m\rangle = 1$ and all other entries set to zero. It is noted that in difference to the system density matrix, $\rho_c$ does not necessarily obey conservation laws, $\mathrm{tr}\{\rho_c(t)\} \neq 1\ \forall t$.

For the numerical solution of non-Markovian master equations, we first solve and store $\rho_c(-\tau)$ for all possible initial conditions using a fourth order Runge Kutta implementation. In a second step, the conditional density matrix is employed to calculate the system correlation elements $\langle m|\, X(-\tau)\,|n\rangle$ to evaluate the integrand during each time step. Afterwards, the integral contributions are iteratively summed up over all time steps and supplied to a second fourth order Runge Kutta algorithm to solve the time evolution dynamics of the system density matrix $\rho_S(t)$.

# 4 Real-time path integrals

The real-time path integral formalism, first developed by Richard P. Feynman [30], constitutes an alternative approach to the description of quantum mechanical phenomena. Here, the key concept is to apply the principle of least action to the quantum realm, following from the idea that classical statistical mechanics may arise as a natural limit of quantum mechanics. As a core advantage over established techniques, the path integral formalism allows for a numerically exact description of open quantum systems by taking into account the usually finite time-resolved system-reservoir correlations of the respective open system [28, 31–38]. In recent developments of novel tensor network-based descriptions for time-discrete path integrals, highly efficient and numerically exact calculations of such systems have become feasible [75–77].

In this Chapter, we introduce the core concepts of the path integral formalism. Sec. 4.1 motivates the transition from the principle of least action in classical mechanics to determining the time-evolving state of a quantum mechanical system. As an example application, Sec. 4.2 provides a detailed derivation of the time-discrete path integral representation for the *spin-boson model* [74], which has been established as a proving ground for open system methods. We conclude this Chapter by introducing the numerically exact tensor network representation for discrete path integrals in Sec. 4.3.

## 4.1 From classical action to quantum mechanics

As a motivation for the path integral approach, we start from classical mechanics where the trajectory of a particle in principle can be determined to arbitrary precision. This is no longer the case for the description of quantum mechanical particles: Here, a complex probability amplitude serves as the most accurate available description of the system state. Based on the concept of superposition, these amplitudes can be calculated by taking the integral over all possible trajectories or paths during finite time steps. In the following, we derive a general path integral description by applying the principle of least action to the quantum realm.

### 4.1.1 Principle of least action

In the Lagrangian approach to classical mechanics, the trajectory of a particle is determined by the principle of least action. The action of a particle traversing space on an

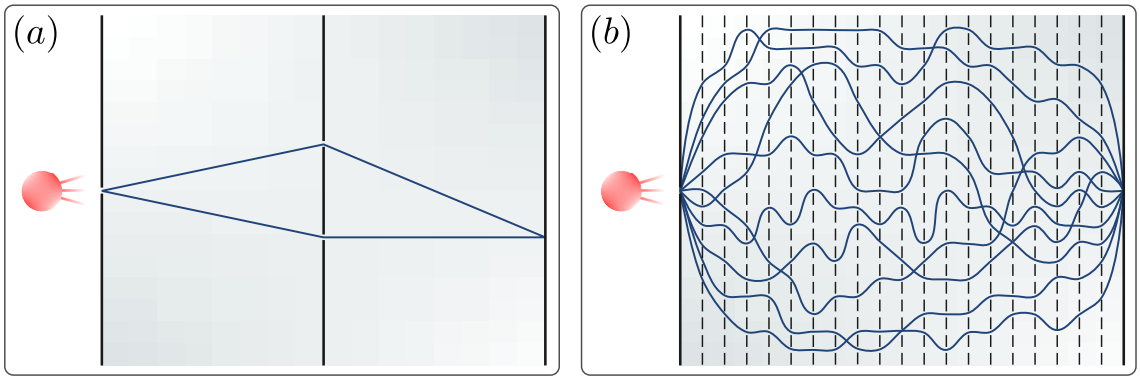


*Figure 4.1:* (a) Sketch of the double-slit experiment. A quantum mechanical particle emitted by a source (red shape) traverses through a double-slit plane, going through either the first or the second hole and is detected on a screen located at a distance behind it. (b) Extension of the double-slit setup with multiple screens in between source and detector plane, each of them featuring many holes. A particle emitted from the source may take one of many paths (blue lines) to arrive at the detector, each of them associated with its own probability amplitude.

arbitrary trajectory from an initial time $t_a$ to time $t_b$ is calculated via [30]

$$S = \int_{t_a}^{t_b} \mathrm{d}t \; L(\dot{\boldsymbol{r}}, \boldsymbol{r}, t), \tag{4.1}$$

with $L(\dot{\boldsymbol{r}}, \boldsymbol{r}, t)$ denoting the Lagrangian of the considered system and $\boldsymbol{r}(t) = [r_x(t), r_y(t), r_z(t)]^T$ the particles' position at a given time $t$. Now, the physical trajectory or *extremum path* $\bar{\boldsymbol{r}}(t)$ is calculated by application of the variational principle: Assuming fixed start and end positions, $\delta\boldsymbol{r}(t_a) = \delta\boldsymbol{r}(t_b) = 0$, the principle of least action states that the extremum path $\bar{\boldsymbol{r}}(t)$ minimizes the action, i.e.,

$$\delta S = S\left[\bar{\boldsymbol{r}}(t) - \delta\boldsymbol{r}(t)\right] - S\left[\bar{\boldsymbol{r}}(t)\right] = 0, \tag{4.2}$$

for a small variation $\delta\boldsymbol{r}(t)$. Evaluation of Eq. (4.2) yields the classical Euler-Lagrange equation of motion ($i = \{x, y, z\}$),

$$\frac{\mathrm{d}}{\mathrm{d}t}\left(\frac{\partial L}{\partial \dot{r}_i}\right) - \frac{\partial L}{\partial r_i} = 0, \tag{4.3}$$

determining the time-resolved physical trajectory $\bar{\boldsymbol{r}}(t)$ of a classical particle for a given initial condition.

### 4.1.2 Probability amplitude

In difference to classical mechanics, the trajectory of a quantum mechanical particle cannot be determined to arbitrary precision, as described by the uncertainty principle. Rather, following the Kopenhagen interpretation of quantum mechanics, since the particles' time-resolved trajectory is affected by the measurement process itself, only its averaged detection at a fixed time and position in space is deterministic [101]. Thus, many measurements

of the same event must be performed to calculate a *probability amplitude* $\psi(\boldsymbol{r}, t)$, denoting the probability of the particle to be detected at position $\boldsymbol{r}$ at time $t$.

The famous double-slit experiment constitutes a prime example of this fact [see Fig. 4.1(a)]: A source of quantum mechanical particles, e.g., electrons or photons, emits in all directions towards a double-slit screen. Positioned at a distance behind it, a detector plane measures incoming particles. If the detector has a high sensitivity and the intensity of the source is low, individual particles will be measured in the form of time-resolved pulses. Measuring the mean number of pulses at a given position in the detector plane determines the relative probability $P(\boldsymbol{r})$ for a particle to follow the path from its source to the detector location. Since the electrons or photons can be measured individually and therefore behave like particles, one might assume that they traverse either the first or the second hole of the double-slit plane on their way to the detector. Following this argument, the probability of arrival at position $\boldsymbol{r}$ would be given by the sum $P(\boldsymbol{r}) = P_1(\boldsymbol{r}) + P_2(\boldsymbol{r})$ of probabilities to go through either the first or the second hole while the respective other hole is closed. However, experimental realizations of this setup have proven otherwise [30, 101]: The measured probability $P(\boldsymbol{r})$ for the arrival of a particle in the detector plane is given by an interference pattern, as it would be expected for a wave passing through the double slit. The simplest representation of a wave amplitude is constituted by complex numbers. Thus, to correctly describe the probability distribution $P(\boldsymbol{r})$ we assume a complex *probability amplitude* $\psi(\boldsymbol{r}) = \psi_1(\boldsymbol{r}) + \psi_2(\boldsymbol{r})$ consisting of the amplitudes for passing through either hole 1 or 2, and the correct probability distribution is given by the wave intensity

$$P(\boldsymbol{r}) = |\psi(\boldsymbol{r})|^2. \tag{4.4}$$

In other words, quantum mechanical phenomena are described by a statistical theory with complex numbers, allowing to describe interference effects between measurement events. The probability amplitude or wave function $\psi(\boldsymbol{r}, t)$ is a representation of many deterministic measurements, assessing all possible outcomes and giving the most accurate description available for the time-resolved trajectory of a quantum mechanical ensemble. Following the principle of superposition, the complete probability amplitude is determined by summation over the amplitudes of all possible paths.

### 4.1.3 Path integral formalism

With the fundamental properties of the probability amplitude established, we extend the double-slit setup by considering multiple screens in between the source and the detector, each of them featuring numerous holes [see Fig. 4.1(b)]. In this scenario, a particle emitted from the source (red shape) can take one of many paths to arrive at the detector plane (blue lines), each of them associated with its own amplitude. As a result of the superposition principle, the total probability amplitude is again given by the sum of the amplitudes of all possible paths. Going one step further, we imagine infinitely many screens in between source and detector plane, each perforated by an increasing amount of holes until they consist of nothing but holes. In consequence, a single path from the source to the detector becomes a continuous function of space and time. The resulting probability amplitude

as a sum of amplitudes of all possible paths is then determined by integration over all possible paths [30]. This concept is the foundation of the path integral formalism. In the following, we explore its application in detail.

While all possible paths contribute to the full probability amplitude by the same magnitude, they differ in phases: The phase of a specific path is determined by the action $S$ in units of the quantum of action $\hbar$ [30]. In the classical limit, $S$ is much larger than $\hbar$, such that the phase contribution $S/\hbar$ is a large angle which oscillates rapidly when perturbing the path by a small amount $\delta\boldsymbol{r}$ on a classical scale. As a result, a small change in $S$ is accompanied by a drastic change of the phase, whose total contribution will average to zero. On a quantum scale, however, the phase only slightly changes by perturbation of $S \sim \hbar$ and crucially determines the contribution of a respective path to the full probability amplitude. The path integral to calculate the probability amplitude of a particle traversing from point $\boldsymbol{r}_a$ to point $\boldsymbol{r}_b$ is given by [30]

$$\psi(\boldsymbol{r}_b, t_b) = \int_{\boldsymbol{r}_a}^{\boldsymbol{r}_b} e^{(i/\hbar)S[\boldsymbol{r}_b,\boldsymbol{r}_a]}\psi(\boldsymbol{r}_a, t_a)\mathcal{D}\boldsymbol{r}(t), \tag{4.5}$$

with $\int \mathcal{D}\boldsymbol{r}(t) = \int\int \ldots \int \mathrm{d}\boldsymbol{r}_1(t)\mathrm{d}\boldsymbol{r}_2(t)\ldots\mathrm{d}\boldsymbol{r}_{N-1}(t)$ denoting the integration over all possible paths traversing points $\boldsymbol{r}_i(t)$ between the fixed start and end points $\boldsymbol{r}_a$ and $\boldsymbol{r}_b$ [see Fig. 4.1(b)]. Analogous to classical mechanics, the action is given by

$$S[\boldsymbol{r}_b, \boldsymbol{r}_a] = \int_{t_a}^{t_b} \mathrm{d}t\ L(\dot{\boldsymbol{r}}, \boldsymbol{r}, t). \tag{4.6}$$

While the form of Eq. (4.5) in principle allows to calculate the wave function, depending on the considered system it is not always the most viable representation: If all variables of the action $S$ appear only up to second order, the path integral can be described by considering the deviation from the classical trajectory prescribed by the extremum action [30]. Importantly, this condition applies to a harmonic bath of independent oscillators. Here, rather than calculating the path integral for a finite number of points $\boldsymbol{r}_i(t)$ explicitly, we minimize the action once more, introducing $S_{cl}[\boldsymbol{r}_b, \boldsymbol{r}_a] := S[\bar{\boldsymbol{r}}(t)]$. As a result, the integrals in Eq. (4.5) take the form of Gaussian integrals and can be carried out explicitly, resulting in a much simpler expression

$$\psi(\boldsymbol{r}_b, t_b) = e^{(i/\hbar)S_{cl}[\boldsymbol{r}_b,\boldsymbol{r}_a]}F(t_b, t_a)\psi(\boldsymbol{r}_a, t_a), \tag{4.7}$$

with a new function $F(t_b, t_a)$ arising from the integrations, whose specific form depends on the investigated system. Notably, in this representation the spatial dependence $\boldsymbol{r}$ has been carried out completely.

## 4.2 Path integral formulation of the spin-boson model

### 4.2.1 Spin-boson model

Despite its seemingly simple structure, the *spin-boson model* has been shown to exhibit a rich variety of physical phenomena [74, 75] and has been established as a common testing

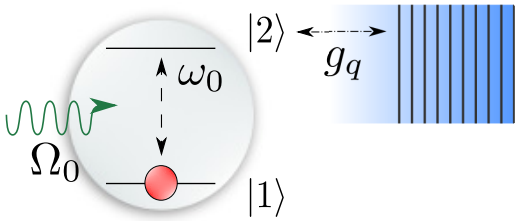


*Figure 4.2:* Sketch of the spin-boson model. A two-level emitter with a single electron (red shape) and transition frequency $\omega_0$ between ground and excited state is continuously driven by an incoming light field at Rabi frequency $\Omega_0$. The excited state $|2\rangle$ is subject to decoherence processes by diagonal coupling to a structured harmonic reservoir of independent oscillators, with a mode ($\boldsymbol{q}$)-dependent coupling element $g_{\boldsymbol{q}}$.

ground for open system methods. The spin-boson model is shown schematically in Fig. 4.2: It consists of a two-level quantum emitter with a single electron, featuring a transition frequency $\omega_0$ between ground and excited state and continuously driven by an external laser field. The excited state features diagonal coupling to a structured harmonic reservoir of independent oscillators such as phonons, resulting in decoherence processes without affecting the level occupation. Under the rotating wave approximation, the open system Hamiltonian of the spin-boson model reads

$$H/\hbar = \omega_0\sigma_{22} + \Omega_0\left[\sigma_{21}e^{i(\omega_0-\omega_L)t} + \text{H.c.}\right] + \int \mathrm{d}^3q\,\left[\omega_q b_{\boldsymbol{q}}^\dagger b_{\boldsymbol{q}} + g_{\boldsymbol{q}}\sigma_{22}\left(b_{\boldsymbol{q}}^\dagger e^{i\omega_q t} + \text{H.c.}\right)\right], \quad (4.8)$$

with system operators $\sigma_{ij} = |i\rangle\langle j|$, bosonic annihilation (creation) operators $b_{\boldsymbol{q}}^{(\dagger)}$ of phonon modes at frequency $\omega_{\boldsymbol{q}} = c_s|\boldsymbol{q}|$, $c_s$ the speed of sound, and a structured system-reservoir coupling element $g_{\boldsymbol{q}}$. $\Omega_0$ denotes the Rabi frequency of the external driving field at a laser frequency $\omega_L$. We note that in difference to the *independent boson model* where no external driving field is applied, there exists no analytical solution to the spin-boson model for arbitrary coupling elements $q_{\boldsymbol{q}}$. In the following, we derive a numerically exact solution for the reduced system time evolution dynamics of the spin-boson model using the real-time path integral approach.

### 4.2.2 Time-discrete expansion of the density matrix

For a full description of the open quantum system, the density matrix formalism is applied. Hence, the time evolution dynamics is governed by the von Neumann equation (see Ch. 2). Assuming an initially separable state between system and reservoir, the formal solution to the von Neumann equation is given by

$$\rho_S(t) = \mathrm{tr}_B\left[U(t,0)\rho(0)U^\dagger(t,0)\right], \quad (4.9)$$

with the time evolution operator

$$U(t,0) = T\exp\left[-\frac{i}{\hbar}\int_0^t \mathrm{d}t' H(t')\right], \quad (4.10)$$

and $T$ the time ordering operator [1]. However, for the numerical evaluation of the density matrix a discretized representation is required. Using the Trotter decomposition [39], one obtains an approximate representation of the time-ordered time evolution operator,

$$U(t,0) \approx \prod_{n=1}^{N} \exp\left[-\frac{i}{\hbar}\Delta t H(n\Delta t)\right], \tag{4.11}$$

which becomes exact for $N \to \infty$ and $\Delta t \to 0$, where $N\Delta t = t$ and $\Delta t$ the time discretization [28, 31, 33]. In the following, we abbreviate $n\Delta t =: t_n$.

By insertion of multiple identity operators $\mathbb{1}_n$, the product over time steps is converted into a summation over a multidimensional configuration space, yielding

$$U(t,0) = U(t_N, t_{N-1})\mathbb{1}_{N-1}U(t_{N-1}, t_{N-2})\mathbb{1}_{N-2}\ldots\mathbb{1}_1 U(\Delta t, 0). \tag{4.12}$$

As a result, the density matrix takes the form

$$\rho(t) = e^{-iH(t_N)\Delta t/\hbar}\mathbb{1}_{N-1}\ldots\mathbb{1}_1 e^{-iH(0)\Delta t/\hbar}\rho(0)e^{iH(0)\Delta t/\hbar}\mathbb{1}_1\ldots\mathbb{1}_{N-1}e^{iH(t_N)\Delta t/\hbar}, \tag{4.13}$$

with the identity operators constructed as a direct product of the spin system states $|i_n\rangle$ and unnormalized coherent phonon states $|\alpha_{\boldsymbol{q}_n}\rangle$ at times $t_n$,

$$\mathbb{1}_n = \sum_{i_n=1}^{2} |i_n\rangle\langle i_n| \otimes \prod_{\boldsymbol{q}} \int \frac{\mathrm{d}^2\alpha_{\boldsymbol{q}_n}}{\pi} |\alpha_{\boldsymbol{q}_n}\rangle\langle\alpha_{\boldsymbol{q}_n}|, \tag{4.14}$$

where

$$|\alpha_{\boldsymbol{q}}\rangle = e^{-|\alpha_{\boldsymbol{q}}|^2/2} \sum_{n_{\boldsymbol{q}}=0}^{\infty} \frac{\alpha_{\boldsymbol{q}}^{n_{\boldsymbol{q}}}}{\sqrt{n_{\boldsymbol{q}}}} |n_{\boldsymbol{q}}\rangle, \tag{4.15}$$

and $|n_{\boldsymbol{q}}\rangle$ denoting thermal states with occupation numbers $n_{\boldsymbol{q}}$ of modes $\boldsymbol{q}$. With this, we have derived a time-discrete representation of the density matrix with time ordering. In the course of the following path integral derivation, the integrals arising from the identity operators are carried out explicitly.

As a first step, the reservoir degrees of freedom are formally traced out, i.e., $\rho_S(t) = \mathrm{tr}_B\{\rho(t)\}$, yielding (see Appendix A)

$$\mathrm{tr}_B\{\ldots\} = \prod_{\boldsymbol{q}} \sum_{n_{\boldsymbol{q}}=0}^{\infty} \langle n_{\boldsymbol{q}}|\ldots|n_{\boldsymbol{q}}\rangle \equiv \prod_{\boldsymbol{q}} \int \frac{\mathrm{d}^2\alpha_{\boldsymbol{q}}}{\pi} \langle\alpha_{\boldsymbol{q}}|\ldots|\alpha_{\boldsymbol{q}}\rangle. \tag{4.16}$$

Hence, the reduced system density matrix elements at time $t_N = N\Delta t$ are given by

$$\begin{aligned}\langle i_N|\,\rho_S(t_N)\,|i'_N\rangle = \prod_{\boldsymbol{q}} \int \frac{\mathrm{d}^2\alpha_{\boldsymbol{q}_N}}{\pi} \int \frac{\mathrm{d}^2\alpha_{\boldsymbol{q}_0}}{\pi} \int \frac{\mathrm{d}^2\beta_{\boldsymbol{q}_0}}{\pi} \\ \times \langle\alpha_{\boldsymbol{q}_N}, i_N|\,U(t_N,t_{N-1})\mathbb{1}_{N-1}\ldots\mathbb{1}_1 U(\Delta t,0)\,|\alpha_{\boldsymbol{q}_0}, i_0\rangle \\ \times \langle\alpha_{\boldsymbol{q}_0}, i_0|\,\rho(0)\,|\beta_{\boldsymbol{q}_0}, i'_0\rangle \\ \times \langle\beta_{\boldsymbol{q}_0}, i'_0|\,U^\dagger(0,\Delta t)\mathbb{1}_1\ldots\mathbb{1}_{N-1}U^\dagger(t_{N-1},t_N)\,|\alpha_{\boldsymbol{q}_N}, i'_N\rangle.\end{aligned} \tag{4.17}$$

### 4.2.3 Evaluation of discrete time steps

In order to evaluate Eq. (4.17) with respect to the spin-boson model Hamiltonian [Eq. (4.8)], we first calculate the time evolution operator [Eq. (4.11)] for a single time step, namely

$$\begin{aligned}\langle \alpha_{\boldsymbol{q}_n}, i_n | \, U(t_n, t_{n-1}) \, | \alpha_{\boldsymbol{q}_{n-1}}, i_{n-1} \rangle &= \prod_{\boldsymbol{q}} \langle \alpha_{\boldsymbol{q}_n}, i_n | \, e^{-i\Delta t H(t_n)/\hbar} \, | \alpha_{\boldsymbol{q}_{n-1}}, i_{n-1} \rangle \\ = \prod_{\boldsymbol{q}} \langle \alpha_{\boldsymbol{q}_n} | \alpha_{\boldsymbol{q}_{n-1}} \rangle \, e^{-i\Delta t \left[ \omega_{\boldsymbol{q}} \alpha^*_{\boldsymbol{q}_n} \alpha_{\boldsymbol{q}_{n-1}} + i_n g_{\boldsymbol{q}} \left( \alpha^*_{\boldsymbol{q}_n} + \alpha_{\boldsymbol{q}_{n-1}} \right) \right]} \, \langle i_n | \, e^{-i\Delta t H_\Omega(t_n)} \, | i_{n-1} \rangle \, . \end{aligned} \tag{4.18}$$

Here the Trotter splitting has been applied once more [28, 33], and $H_\Omega = \Omega_0[\sigma_{21} e^{i(\omega_0 - \omega_L)t} + \text{H.c.}]$ denotes the external driving term of the open system Hamiltonian. Using the definition from Eq. (4.15), the first resulting product is evaluated as

$$\langle \alpha_{\boldsymbol{q}_n} | \alpha_{\boldsymbol{q}_{n-1}} \rangle = \exp\left( -\frac{|\alpha_{\boldsymbol{q}_n}|^2}{2} - \frac{|\alpha_{\boldsymbol{q}_{n-1}}|^2}{2} + \alpha^*_{\boldsymbol{q}_n} \alpha_{\boldsymbol{q}_{n-1}} \right) . \tag{4.19}$$

For the examination of the driving term $\langle i_n | \, e^{-i\Delta t H_\Omega(t_n)} \, | i_{n-1} \rangle =: M_{i_n i_{n-1}}$, the exponential function is expanded as a series, yielding

$$M_{i_n i_{n-1}} = \langle i_n | \begin{pmatrix} \cos(\Omega_0 \Delta t) & -i e^{i(\omega_0 - \omega_L)\Delta t} \sin(\Omega_0 \Delta t)/\hbar \\ -i e^{-i(\omega_0 - \omega_L)\Delta t} \sin(\Omega_0 \Delta t)/\hbar & \cos(\Omega_0 \Delta t) \end{pmatrix} | i_{n-1} \rangle \, , \tag{4.20}$$

and resulting in $M_{i_n i_{n-1}} = \mathbb{1} \delta_{i_n, i_{n-1}}$ for the case $\Omega_0 = 0$, corresponding to the independent boson model. $M_{i_n i_{n-1}}$ is referred to as the field transformation matrix. In total, Eq. (4.18) takes the form

$$\begin{aligned}\langle \alpha_{\boldsymbol{q}_n}, i_n | \, U(t_n, t_{n-1}) \, | \alpha_{\boldsymbol{q}_{n-1}}, i_{n-1} \rangle = & M_{i_n i_{n-1}} \prod_{\boldsymbol{q}} \exp\Big\{ \alpha^*_{\boldsymbol{q}_n} \alpha_{\boldsymbol{q}_{n-1}} - \frac{|\alpha_{\boldsymbol{q}_n}|^2}{2} - \frac{|\alpha_{\boldsymbol{q}_{n-1}}|^2}{2} \\ & - i\Delta t \left[ \omega_{\boldsymbol{q}} \alpha^*_{\boldsymbol{q}_n} \alpha_{\boldsymbol{q}_{n-1}} + i_n g_{\boldsymbol{q}} \left( \alpha^*_{\boldsymbol{q}_n} + \alpha_{\boldsymbol{q}_{n-1}} \right) \right] \Big\} . \end{aligned} \tag{4.21}$$

As a next step, we evaluate $N$ time steps while taking the limit $\Delta t \to 0$, resulting in

$$\begin{aligned} & \langle \alpha_{\boldsymbol{q}_N}, i_N | \, U(t_N, t_{N-1}) \mathbb{1}_{N-1} \dots \mathbb{1}_1 U(\Delta t, 0) \, | \alpha_{\boldsymbol{q}_0}, i_0 \rangle \\ & = \prod_{\boldsymbol{q}} \int \frac{\mathrm{d}^2 \alpha_{\boldsymbol{q}_{N-1}}}{\pi} \dots \int \frac{\mathrm{d}^2 \alpha_{\boldsymbol{q}_1}}{\pi} \sum_{i_1, \dots, i_{N-1} = 1}^{2} M_{i_N i_{N-1}} \dots M_{i_1 i_0} \\ & \times \exp\left\{ \sum_{n=1}^{N} \left[ \alpha^*_{\boldsymbol{q}_n} \alpha_{\boldsymbol{q}_{n-1}} - \frac{|\alpha_{\boldsymbol{q}_n}|^2}{2} - \frac{|\alpha_{\boldsymbol{q}_{n-1}}|^2}{2} - i\Delta t \omega_{\boldsymbol{q}} \alpha^*_{\boldsymbol{q}_n} \alpha_{\boldsymbol{q}_{n-1}} - i\Delta t g_{\boldsymbol{q}} \left( \alpha^*_{\boldsymbol{q}_n} + \alpha_{\boldsymbol{q}_{n-1}} \right) i_n \right] \right\} \\ & \overset{\Delta t \to 0}{=} \prod_{\boldsymbol{q}} \int \frac{\mathrm{d}^2 \alpha_{\boldsymbol{q}_{N-1}}}{\pi} \dots \int \frac{\mathrm{d}^2 \alpha_{\boldsymbol{q}_1}}{\pi} \sum_{i_1, \dots, i_{N-1} = 1}^{2} M_{i_N i_{N-1}} \dots M_{i_1 i_0} \exp\left\{ -\frac{|\alpha_{\boldsymbol{q}}(t)|^2}{2} - \frac{|\alpha_{\boldsymbol{q}}(0)|^2}{2} \right. \\ & \left. + \alpha^*_{\boldsymbol{q}}(t) \alpha_{\boldsymbol{q}}(t) - \int_0^t \mathrm{d}\tau \left[ \alpha^*_{\boldsymbol{q}}(\tau) \dot{\alpha}_{\boldsymbol{q}}(\tau) + i\omega_{\boldsymbol{q}} \alpha^*_{\boldsymbol{q}}(\tau) \alpha_{\boldsymbol{q}}(\tau) + i g_{\boldsymbol{q}} \left( \alpha_{\boldsymbol{q}}(\tau) + \alpha^*_{\boldsymbol{q}}(\tau) \right) j(\tau) \right] \right\} \\ & = \sum_{i_1, \dots, i_{N-1} = 1}^{2} M_{i_N i_{N-1}} \dots M_{i_1 i_0} \prod_{\boldsymbol{q}} \exp\left\{ -\frac{|\alpha_{\boldsymbol{q}}(t)|^2}{2} - \frac{|\alpha_{\boldsymbol{q}}(0)|^2}{2} \right\} \int \mathcal{D}\alpha \, T \left[ e^{S(\alpha_{\boldsymbol{q}}, \alpha^*_{\boldsymbol{q}})} \right] , \end{aligned} \tag{4.22}$$

with

$$j^{(\prime)}(\tau) := \sum_{n=1}^{N} i_n^{(\prime)} \,\Theta[\tau - (n-1)\Delta t]\,\Theta[n\Delta t - \tau], \tag{4.23}$$

and $\Theta(t)$ the Heaviside function. In this limit, the time evolution operator matrix elements are transformed to a path integral over phonon variables, compactly written in the last line in Eq. (4.22) with the action $S(\alpha_{\boldsymbol{q}}, \alpha^*_{\boldsymbol{q}})$. Note that an exponential prefactor is excluded from $S$, since it belongs to the identity of the unnormalized coherent phonon states.

### 4.2.4 Extremal action

As outlined in Sec. 4.1, the path integral for the time evolution operator can be evaluated by calculating deviations from the classical trajectory via the extremal action $S_{cl}$. Therefore, as a next step we minimize the action $S(\alpha_{\boldsymbol{q}}, \alpha^*_{\boldsymbol{q}})$, leading to the Euler-Langrange Eq. (4.3). Assuming fixed start and end positions, the Lagrangian takes the form

$$L(\alpha_{\boldsymbol{q}}, \alpha^*_{\boldsymbol{q}}) = -\left\{\alpha^*_{\boldsymbol{q}}(\tau)\dot{\alpha}_{\boldsymbol{q}}(\tau) + i\omega_{\boldsymbol{q}}\alpha^*_{\boldsymbol{q}}(\tau)\alpha_{\boldsymbol{q}}(\tau) + ig_{\boldsymbol{q}}\left[\alpha_{\boldsymbol{q}}(\tau) + \alpha^*_{\boldsymbol{q}}(\tau)\right] j(\tau)\right\}, \tag{4.24}$$

and the resulting differential equations for $\alpha_{\boldsymbol{q}}$ and $\alpha^*_{\boldsymbol{q}}$ read

$$-i\left[\omega_{\boldsymbol{q}}\alpha^*_{\boldsymbol{q}}(\tau) + j(\tau)g_{\boldsymbol{q}}\right] + \dot{\alpha}^*_{\boldsymbol{q}}(\tau) = 0, \tag{4.25a}$$

$$-i\left[\omega_{\boldsymbol{q}}\alpha_{\boldsymbol{q}}(\tau) + j(\tau)g_{\boldsymbol{q}}\right] - \dot{\alpha}_{\boldsymbol{q}}(\tau) = 0, \tag{4.25b}$$

with boundary conditions $\alpha^*_{\boldsymbol{q}}(t) = \alpha^*_{\boldsymbol{q}_N}$, $\alpha_{\boldsymbol{q}}(0) = \alpha_{\boldsymbol{q}_0}$ resulting from the transition from the discrete to the continuous form in Eq. (4.22). Formally solving these differential equations and inserting the solutions for $\alpha_{\boldsymbol{q}}(\tau)$ and $\alpha^*_{\boldsymbol{q}}(\tau)$ into $S(\alpha_{\boldsymbol{q}}, \alpha^*_{\boldsymbol{q}})$ yields the extremal action,

$$\begin{aligned} S_{cl}(\alpha_{\boldsymbol{q}}, \alpha^*_{\boldsymbol{q}}) = \alpha_{\boldsymbol{q}_0}\alpha^*_{\boldsymbol{q}_N}e^{-i\omega_{\boldsymbol{q}}t} - ig_{\boldsymbol{q}}\int_0^t \mathrm{d}\tau' \left[\alpha_{\boldsymbol{q}_0}e^{-i\omega_{\boldsymbol{q}}\tau'} + \alpha^*_{\boldsymbol{q}_N}e^{-i\omega_{\boldsymbol{q}}(t-\tau')}\right] j(\tau') \\ - g_{\boldsymbol{q}}^2\int_0^t \mathrm{d}\tau \int_0^\tau \mathrm{d}\tau'\, e^{-i\omega_{\boldsymbol{q}}(\tau-\tau')} j(\tau) j(\tau'), \end{aligned} \tag{4.26}$$

and determines the path integral for the time evolution operator,

$$\int \mathcal{D}\alpha\, T\left[e^{S(\alpha_{\boldsymbol{q}}, \alpha^*_{\boldsymbol{q}})}\right] \equiv e^{S_{cl}(\alpha_{\boldsymbol{q}}, \alpha^*_{\boldsymbol{q}})}. \tag{4.27}$$

### 4.2.5 Initial state

Apart from the time evolution operator, the density matrix elements [Eq. (4.17)] depend on the initial open system state $\langle \alpha_{\boldsymbol{q}_0}, i_0 | \, \rho_S(0) \otimes \rho_B(0) \, | \beta_{\boldsymbol{q}_0}, i_0' \rangle$. Assuming a thermal reservoir state and using Wick's theorem, we can write $\rho_B$ as a super-Poissonian distribution [28, 33],

$$\rho_B = \frac{1}{Z} e^{-\beta \sum_{\boldsymbol{q}} \hbar\omega_{\boldsymbol{q}} b^\dagger_{\boldsymbol{q}} b_{\boldsymbol{q}}} = \prod_{\boldsymbol{q}} \left(1 - e^{-\beta\hbar\omega_{\boldsymbol{q}}}\right) e^{-\beta\hbar\omega_{\boldsymbol{q}} b^\dagger_{\boldsymbol{q}} b_{\boldsymbol{q}}} = \prod_{\boldsymbol{q}} \frac{\bar{n}_{\boldsymbol{q}}^{n_{\boldsymbol{q}}}}{(1+\bar{n}_{\boldsymbol{q}})^{n_{\boldsymbol{q}}+1}}, \tag{4.28}$$

with $\bar{n}_{\boldsymbol{q}} = \langle b_{\boldsymbol{q}}^\dagger b_{\boldsymbol{q}} \rangle$ and $Z$ the partition function. The initial state then takes the form

$$\begin{aligned}
&\langle \alpha_{\boldsymbol{q}_0}, i_0 | \, \rho_S(0) \otimes \rho_B(0) \, | \beta_{\boldsymbol{q}_0}, i_0' \rangle \\
&= \langle i_0 | \, \rho_S(0) \, | i_0' \rangle \, \langle \alpha_{\boldsymbol{q}_0} | \sum_{n_{\boldsymbol{q}'}=0}^{\infty} \prod_{\boldsymbol{q}'} \frac{\bar{n}_{\boldsymbol{q}'}^{n_{\boldsymbol{q}'}}}{(1+\bar{n}_{\boldsymbol{q}'})^{n_{\boldsymbol{q}'}+1}} \, | n_{\boldsymbol{q}'} \rangle \, \langle n_{\boldsymbol{q}'} | \beta_{\boldsymbol{q}_0} \rangle \\
&= \langle i_0 | \, \rho_S(0) \, | i_0' \rangle \sum_{n_{\boldsymbol{q}'}=0}^{\infty} \prod_{\boldsymbol{q}'} \frac{\bar{n}_{\boldsymbol{q}'}^{n_{\boldsymbol{q}'}}}{(1+\bar{n}_{\boldsymbol{q}'})^{n_{\boldsymbol{q}'}}} \frac{1}{(1+\bar{n}_{\boldsymbol{q}'})} \, \langle \alpha_{\boldsymbol{q}_0} | n_{\boldsymbol{q}'} \rangle \, \delta_{\boldsymbol{q}_0 \boldsymbol{q}'} \frac{\beta_{\boldsymbol{q}_0}^{n_{\boldsymbol{q}_0}}}{\sqrt{n_{\boldsymbol{q}_0}!}} e^{-|\beta_{\boldsymbol{q}_0}|^2/2} \\
&= \langle i_0 | \, \rho_S(0) \, | i_0' \rangle \sum_{n_{\boldsymbol{q}'}=0}^{\infty} \prod_{\boldsymbol{q}'} \frac{\bar{n}_{\boldsymbol{q}_0}^{n_{\boldsymbol{q}_0}}}{(1+\bar{n}_{\boldsymbol{q}_0})^{n_{\boldsymbol{q}_0}}} \frac{1}{(1+\bar{n}_{\boldsymbol{q}_0})} \frac{\alpha_{\boldsymbol{q}_0}^{*\, n_{\boldsymbol{q}_0}} \beta_{\boldsymbol{q}_0}^{n_{\boldsymbol{q}_0}}}{n_{\boldsymbol{q}_0}!} e^{-|\alpha_{\boldsymbol{q}_0}|^2/2 - |\beta_{\boldsymbol{q}_0}|^2/2} \\
&= \langle i_0 | \, \rho_S(0) \, | i_0' \rangle \, (1-\xi_{\boldsymbol{q}_0}) \exp\left( \xi_{\boldsymbol{q}_0} \alpha_{\boldsymbol{q}_0}^* \beta_{\boldsymbol{q}_0} - \frac{|\alpha_{\boldsymbol{q}_0}|^2}{2} - \frac{|\beta_{\boldsymbol{q}_0}|^2}{2} \right),
\end{aligned} \tag{4.29}$$

with $\xi_{\boldsymbol{q}} := \bar{n}_{\boldsymbol{q}}/(1+\bar{n}_{\boldsymbol{q}})$. Having determined the initial state, we can explicitly trace out the reservoir by carrying out the remaining three integrals in Eq. (4.17).

### 4.2.6 Tracing out the reservoir

Inserting the initial state representation of Eq. (4.29), the time evolution operator in the continuous limit [Eq. (4.22)] and the extremal action [Eq. (4.26)] into Eq. (4.17), the density matrix elements take the form

$$\begin{aligned}
&\langle i_N | \, \rho_S(t) \, | i_N' \rangle = \prod_{\boldsymbol{q}} \int \frac{\mathrm{d}^2 \alpha_{\boldsymbol{q}_N}}{\pi} \int \frac{\mathrm{d}^2 \alpha_{\boldsymbol{q}_0}}{\pi} \int \frac{\mathrm{d}^2 \beta_{\boldsymbol{q}_0}}{\pi} \sum_{i_1,\ldots,i_{N-1}=1}^{2} \sum_{i_1',\ldots,i_{N-1}'=1}^{2} \\
&\times M_{i_N i_{N-1}} \ldots M_{i_1 i_0} M^*_{i_0' i_1'} \ldots M^*_{i_{N-1}' i_N'} (1-\xi_{\boldsymbol{q}_0}) \, \langle i_0 | \, \rho_S(0) \, | i_0' \rangle \\
&\times \exp\Big\{ - |\alpha_{\boldsymbol{q}_N}|^2 - |\alpha_{\boldsymbol{q}_0}|^2 - |\beta_{\boldsymbol{q}_0}|^2 + \xi_{\boldsymbol{q}_0} \alpha_{\boldsymbol{q}_0}^* \beta_{\boldsymbol{q}_0} + \alpha_{\boldsymbol{q}_0} \alpha_{\boldsymbol{q}_N}^* e^{-i\omega_{\boldsymbol{q}} t} + \beta_{\boldsymbol{q}_0}^* \alpha_{\boldsymbol{q}_N} e^{i\omega_{\boldsymbol{q}} t} \\
&- i g_{\boldsymbol{q}} \int_0^t \mathrm{d}\tau' \left[ \alpha_{\boldsymbol{q}_0} e^{-i\omega_{\boldsymbol{q}}\tau'} + \alpha_{\boldsymbol{q}_N}^* e^{-i\omega_{\boldsymbol{q}}(t-\tau')} \right] j(\tau') - g_{\boldsymbol{q}}^2 \int_0^t \mathrm{d}\tau \int_0^\tau \mathrm{d}\tau' \, e^{-i\omega_{\boldsymbol{q}}(\tau-\tau')} j(\tau) j(\tau') \\
&+ i g_{\boldsymbol{q}} \int_0^t \mathrm{d}\tau' \left[ \beta_{\boldsymbol{q}_0}^* e^{i\omega_{\boldsymbol{q}}\tau'} + \alpha_{\boldsymbol{q}_N} e^{i\omega_{\boldsymbol{q}}(t-\tau')} \right] j'(\tau') - g_{\boldsymbol{q}}^2 \int_0^t \mathrm{d}\tau \int_0^\tau \mathrm{d}\tau' \, e^{i\omega_{\boldsymbol{q}}(\tau-\tau')} j'(\tau) j'(\tau') \Big\}.
\end{aligned} \tag{4.30}$$

The remaining three integrals have the form of Gaussian integrals and are solved explicitly in Appendix A. The resulting final expression for the density matrix elements in continuous representation reads

$$\begin{aligned}
\langle i_N | \, \rho_S(t) \, | i_N' \rangle = &\sum_{i_1,\ldots,i_{N-1}=1}^{2} \sum_{i_1',\ldots,i_{N-1}'=1}^{2} M_{i_N i_{N-1}} \ldots M_{i_1 i_0} M^*_{i_0' i_1'} \ldots M^*_{i_{N-1}' i_N'} \\
&\times \exp\left[ S_{inf}(t) \right] \langle i_0 | \, \rho_S(0) \, | i_0' \rangle ,
\end{aligned} \tag{4.31}$$

where we introduced the *influence functional*

$$S_{inf}(t) = -\int_0^t \mathrm{d}\tau \int_0^\tau \mathrm{d}\tau' \, \left[j(\tau) - j'(\tau)\right] \left[\eta(\tau-\tau')j(\tau') - \eta^*(\tau-\tau')j'(\tau')\right], \tag{4.32}$$

and the reservoir autocorrelation function [28, 31–33, 74]

$$\eta(\tau-\tau') := \sum_{\boldsymbol{q}} g_{\boldsymbol{q}}^2 \{(2\bar{n}_{\boldsymbol{q}_0}+1)\cos\left[\omega_{\boldsymbol{q}}(\tau-\tau')\right] - i\sin\left[\omega_{\boldsymbol{q}}(\tau-\tau')\right]\}. \tag{4.33}$$

### 4.2.7 Time-discrete influence functional

For the numerical evaluation of Eq. (4.31), we have to go back to a time-discrete representation by reinserting the definition $j^{(\prime)}(\tau) := \sum_{n=1}^N i_n^{(\prime)} \Theta[\tau-(n-1)\Delta t]\Theta[n\Delta t - \tau]$. The influence functional [Eq. (4.32)] then takes the form

$$\begin{aligned} S_{inf}(t_N) &= -\sum_{n=1}^N \sum_{m=1}^n \left(i_n - i_n'\right) \left[\eta_{n-m} i_m - \eta_{n-m}^* i_m'\right] \\ &=: \sum_{n=1}^N \sum_{m=1}^n S_{i_n' i_m'}^{i_n i_m}, \end{aligned} \tag{4.34}$$

with

$$\eta_{n-m} := \int_{(n-1)\Delta t}^{n\Delta t} \mathrm{d}\tau \int_{(m-1)\Delta t}^{m\Delta t} \mathrm{d}\tau' \, \eta(\tau-\tau'). \tag{4.35}$$

For the evaluation of the time integrals in Eq. (4.35), we have to distinguish between the cases $n > m$ and $n = m$. For the case $n > m$, the elements of the influence functional read [28, 31, 33]

$$\begin{aligned} S_{i_n' i_m'}^{i_n i_m} = &-\sum_{\boldsymbol{q}} \frac{2g_{\boldsymbol{q}}^2}{\omega_{\boldsymbol{q}}^2} \left[1-\cos(\omega_{\boldsymbol{q}}\Delta t)\right] \left(i_n - i_n'\right) \\ &\times \Big( \{(2\bar{n}_{\boldsymbol{q}_0}+1)\cos\left[\omega_{\boldsymbol{q}}(n-m)\Delta t\right] - i\sin\left[\omega_{\boldsymbol{q}}(n-m)\Delta t\right]\} i_m \\ &- \{(2\bar{n}_{\boldsymbol{q}_0}+1)\cos\left[\omega_{\boldsymbol{q}}(n-m)\Delta t\right] + i\sin\left[\omega_{\boldsymbol{q}}(n-m)\Delta t\right]\} i_m' \Big). \end{aligned} \tag{4.36}$$

At $n = m$, they are given by

$$\begin{aligned} S_{i_n' i_m'}^{i_n i_m} = &-\sum_{\boldsymbol{q}} \frac{g_{\boldsymbol{q}}^2}{\omega_{\boldsymbol{q}}^2} \left(i_n - i_n'\right) \\ &\times \Big( \{(2\bar{n}_{\boldsymbol{q}_0}+1)\left[1-\cos(\omega_{\boldsymbol{q}}\Delta t)\right] - i\omega_{\boldsymbol{q}}\Delta t + i\sin\left(\omega_{\boldsymbol{q}}\Delta t\right)\} i_m \\ &- \{(2\bar{n}_{\boldsymbol{q}_0}+1)\left[1-\cos(\omega_{\boldsymbol{q}}\Delta t)\right] + i\omega_{\boldsymbol{q}}\Delta t - i\sin\left(\omega_{\boldsymbol{q}}\Delta t\right)\} i_m' \Big). \end{aligned} \tag{4.37}$$

Finally, this yields the time-discrete path integral representation of the density matrix describing the reduced system time evolution dynamics of the spin-boson model,

$$\langle i_N|\,\rho_S(t_N)\,|i'_N\rangle = \prod_{n=1}^{N}\sum_{i_{n-1}=1}^{2}\sum_{i'_{n-1}=1}^{2} M_{i_n i_{n-1}} M^*_{i'_{n-1} i'_n} \times \prod_{m=1}^{n} \exp\left(S^{i_n i_m}_{i'_n i'_m}\right)\langle i_0|\,\rho_S(0)\,|i'_0\rangle\,, \tag{4.38}$$

with the field transformation matrix

$$M_{i_n i_{n-1}} = \langle i_n| \begin{pmatrix} \cos(\Omega_0\Delta t) & -ie^{i(\omega_0-\omega_L)\Delta t}\sin(\Omega_0\Delta t)/\hbar \\ -ie^{-i(\omega_0-\omega_L)\Delta t}\sin(\Omega_0\Delta t)/\hbar & \cos(\Omega_0\Delta t) \end{pmatrix} |i_{n-1}\rangle\,. \tag{4.39}$$

Again, it is noted that for $\Omega_0 = 0$ and therefore $M_{i_n i_{n-1}} = \mathbb{1}\delta_{i_n,i_{n-1}}$, Eq. (4.38) directly yields the time-discrete path integral representation of the independent boson model.

### 4.2.8 Finite memory approximation

The evaluation of Eq. (4.38) becomes increasingly expensive for increasing numbers of time steps, since the history of all preceding paths at times $0,\ldots,t_{n-1}$ must be taken into account for the calculation of time step $t_n$. In order to make the time-discrete path integral representation numerically accessible, the *augmented density tensor* scheme is introduced [37, 38]. Here, the essential approximation is based on the fact that often times the reservoir has a sharp finite memory, corresponding to finite system-reservoir correlations in time.

Exploiting the finite memory length of environment-induced correlations for an efficient approximation of the full path integral, only the last $n_c$ time steps are taken into account for the calculation of the current path, while disregarding all prior paths with zero or close to zero contributions. This treatment is known as the *finite memory approximation* and results in the augmented density tensor representation, reading at time $t_N = N\Delta t$

$$\langle i_N|\,\rho_S(t_N)\,|i'_N\rangle = \prod_{n=1}^{N}\sum_{i_{n-1}=1}^{2}\sum_{i'_{n-1}=1}^{2} M_{i_n i_{n-1}} M^*_{i'_{n-1} i'_n} \times \prod_{m=n-n_c}^{n} \exp\left(S^{i_n i_m}_{i'_n i'_m}\right)\langle i_0|\,\rho_S(0)\,|i'_0\rangle\,. \tag{4.40}$$

In an *improved* version of the truncation scheme, rather than cutting off the memory after $n_c$ steps, in the case of $n-m \equiv n_c$ all former paths up to $t_{n_c} = n_c\Delta t$ are additionally incorporated in the time integration in Eq. (4.35) [102],

$$\eta_{n_c} := \eta_{n-m} + \sum_{k=1}^{n-n_c-1} \eta_{n-k}. \tag{4.41}$$

## 4.3 Efficient tensor network implementation

### 4.3.1 Matrix product states and matrix product operators

Matrix product states (MPS) are representations of arbitrary quantum states in the form of one-dimensional arrays of contracted tensors (see Fig. 4.3). The tensors may, e.g., represent the physical sites of a quantum many-body state, or the full system state during one step of its time evolution dynamics. Information stored in the tensors can be accessed and manipulated via their respective *site indices*, illustrated by unconnected vertical links in Fig. 4.3. The network is conjoined via contracted *link indices* (horizontal lines) allowing for information exchange between the individual tensors. This representation features a high degree of compression of the corresponding Hilbert space dimension, combining a reduction from exponential to polynomial scaling of the respective degrees of freedom with the ability to perform operations directly on the compressed states [39–45]. For the construction of an MPS the *singular value decomposition* is employed, where an arbitrary matrix $M$ of dimension $N_A \times N_B$ is decomposed into a product of matrices according to [39]

$$M = USV^\dagger. \tag{4.42}$$

Here, $U$ denotes a matrix of dimension $N_A \times \min(N_A, N_B)$ featuring orthonormal columns, $V^\dagger$ has orthonormal rows and is of dimension $\min(N_A, N_B) \times N_B$, and $S$ represents a diagonal matrix of dimension $\min(N_A, N_B) \times \min(N_A, N_B)$ with non-negative entries $S_{ii} = s_i \geq 0$, which are referred to as the *singular values* of matrix $M$. When $M$ represents a quantum state, the latter can be interpreted as entanglement weights [39, 40]. In this case, the singular value decomposition corresponds to a *Schmidt decomposition*, i.e., the decomposition of a general quantum state living in a bipartite product space into a product of orthonormal basis vectors of the respective product spaces [103]. The number of nonzero singular values determines the *Schmidt rank* of matrix $M$ and is at the core of the employed compression scheme [39, 40, 42]:

An arbitrary matrix $M$ with Schmidt rank $d$ can be efficiently and accurately approximated by a matrix $M'$ with rank $d' < d$ via $M' = US'V^\dagger$ and

$$S' = \mathrm{diag}(s'_1, s'_2, \ldots, s'_{d'}, 0, \ldots, 0), \tag{4.43}$$

where the $d - d'$ smallest occurring singular values in $S$ have been set to zero, effectively truncating the column and row dimension of $U$ and $V^\dagger$, respectively. As a result, the complexity of matrix $M$ is decreased without loss of crucial entanglement information. In order to perform operations on the decomposed quantum state, quantum operators are restated in the same fashion as *matrix product operators* (MPOs). Here, the resulting tensors feature two physical site indices accounting for the input and corresponding output state as a result of the operator action. To apply an MPO to an MPS, each tensor of the MPO is contracted with a corresponding tensor of the MPS with matching input site indices. In consequence of the contraction, a new MPS with updated site indices is constituted.

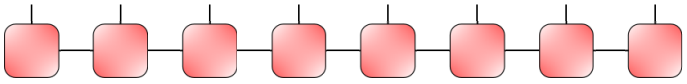

*Figure 4.3:* Diagrammatic representation of a matrix product state, constituting a decomposed and compressed description of an arbitrary quantum state. Vertical lines emerging from each tensor (red shapes) represent the physical *site indices* of the compressed quantum state. Horizontal lines are *link indices* conjoining the network and allowing for information transfer between the tensors.

### 4.3.2 Tensor network realization of path integrals

Under the improved finite memory approximation, the time evolution of the augmented density tensor can be reformulated as a tensor network [75, 76]. Using standard tensor compression techniques [39], this architecture enables efficient and numerically exact calculations of the reduced open system dynamics. For the explicit tensor network implementation, the augmented density tensor [Eq. (4.40)] is first mapped to a vector $\rho_{j_n}$ in Liouville space,

$$\rho_{j_N}(t_N) = \prod_{n=1}^{N} \prod_{m=n-n_c}^{n} I(j_n, j_m)\rho_{j_0}(0), \tag{4.44}$$

with

$$I(j_n, j_m) := \sum_{j_{n-1}=1}^{4} \tilde{M}_{j_n j_{n-1}} \exp\left(\tilde{S}^{j_n j_m}\right). \tag{4.45}$$

Here, left and right system indices $i_k$, $i'_k$ have been combined to a single index $j_k$ for each time step, resulting in Liouville space representations $\tilde{M}_{j_n j_{n-1}}$ and $\tilde{S}^{j_n j_m}$ of the field transformation matrix and the influence functional, respectively. Afterwards, the augmented density tensor is rewritten as an MPS, storing both present and past system states in individual tensors,

$$\rho_{j_n}(t_n) = \sum_{j_0,\ldots,j_{n-1}} A^{j_0, j_1, \ldots, j_{n-1}, j_n}, \tag{4.46}$$

here shown for the case $n \leq n_c$. In this representation, stored information is compressed efficiently using standard tensor network techniques, i.e., by consecutive applications of the singular value decomposition [39–42]. In consequence, memory requirements for the augmented density tensor are reduced from exponential to polynomial scaling with respect to the number of preceding paths $n_c$ taken into account for the calculation of the current system state [75], enabling simulations of memory depths inaccessible in traditional path integral implementations.

The time evolution is carried out by a network of MPOs, shown schematically in Fig. 4.4(a) (green shapes). The augmented density tensor is stored as an MPS, containing the present system state and up to $n_c - 1$ past states stored in individual tensors, with the oldest state located at the left end of the MPS. During the first time step, the initial system state $\rho_{j_0}(0)$ (red shape) is contracted with the first MPO in the network [dashed frame in Fig. 4.4(a)].

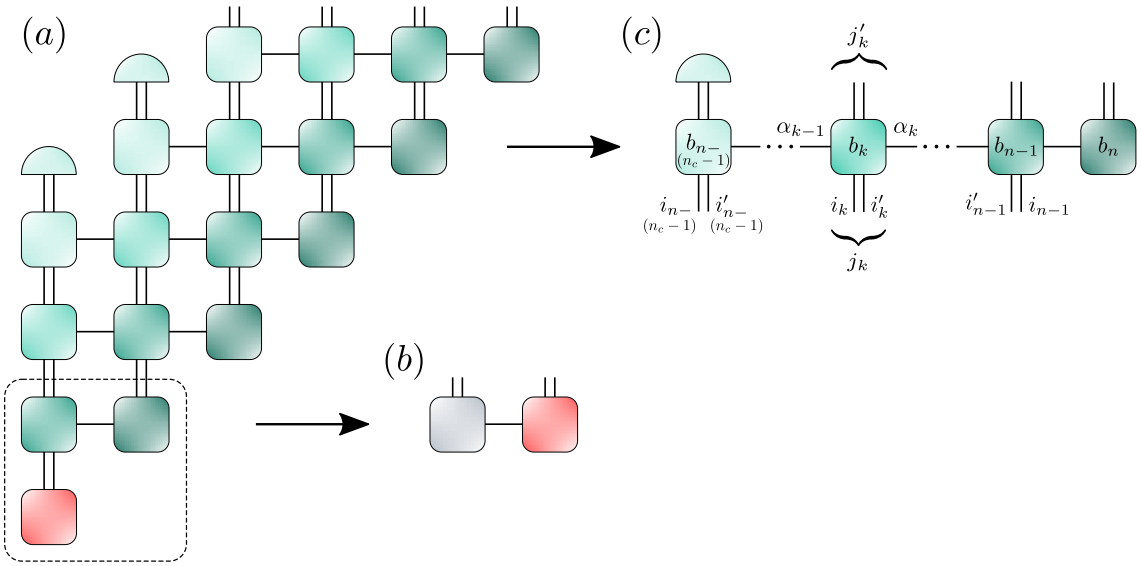


*Figure 4.4:* (a) Efficient tensor network implementation of real-time path integrals. (b) System MPS containing the current (red) and past system state (grey) after the first network contraction. (c) MPO structure for the calculation of the $n$-th time step.

As a result, the system state is updated and the preceding path is stored to its left, increasing the length of the MPS by one [see Fig. 4.4(b)]. Once step $n = n_c$ is reached, the oldest path in the MPS is summed over by application of a delta tensor [semicircular shape in Fig. 4.4(a)], corresponding to the improved finite memory approximation [75, 102]. At this stage, the MPS length remains fixed for the rest of the time evolution. Moreover, for time-independent problems such as the spin-boson model the structure of the MPO remains unchanged for all time steps $n \geq n_c$ apart from the index nomenclature. In consequence, the MPO constructed for the calculation of time step $n = n_c$ can be reused for the execution of all following steps, resulting in an additional performance gain. Fig. 4.4(c) shows the structure of the MPO during the $n$-th time step with $n \geq n_c$, given by [75]

$$B^{j'_{n-(n_c-1)},\ldots,j'_{n-1},j'_n}_{j'_{n-(n_c-1)},\ldots,j'_{n-2},j'_{n-1}} = \left[b_{n-(n_c-1)}\right]^{\alpha_{n-(n_c-1)},j'_{n-(n_c-1)}}_{j_{n-(n_c-1)}} \left(\prod_{m=n-(n_c-2)}^{n-1} [b_m]^{\alpha_m,j'_m}_{\alpha_{m-1},j_m}\right) [b_n]^{j'_n}_{\alpha_{n-1}}, \tag{4.47}$$

with $\alpha_k$ and $j'_k$ denoting MPO link indices and updated system states, respectively, and new tensors

$$[b_m]^{\alpha',j'}_{\alpha,j} = \delta^{\alpha'}_{\alpha}\,\delta^{j'}_{j}\,I(\alpha',j'), \tag{4.48a}$$

$$\left[b_{n-(n_c-1)}\right]^{\alpha',j'}_{j} = \sum_{\alpha}\left[b_{n-(n_c-1)}\right]^{\alpha',j'}_{\alpha,j} = \delta^{j'}_{j}\,I(\alpha',j'), \tag{4.48b}$$

$$[b_n]^{j'}_{\alpha} = \delta^{j}_{\alpha'}\,[b_n]^{\alpha',j'}_{\alpha,j} = \delta^{j'}_{\alpha}\,I(j',j'). \tag{4.48c}$$

Lastly, the network contraction for the calculation of the $n$-th time step reads

$$A^{j'_{n-(n_c-1)},\ldots,j'_{n-1},j'_n} = B^{j'_{n-(n_c-1)},\ldots,j'_{n-1},j'_n}_{j_{n-(n_c-1)},\ldots,j_{n-2},j_{n-1}} A^{j_{n-(n_c-1)},\ldots,j_{n-2},j_{n-1}}. \tag{4.49}$$

In summary, we have introduced the concept of real-time path integrals and used it to derive a highly efficient and numerically exact representation of the spin-boson model. Using state-of-the-art tensor network architectures, numerically exact calculations of the reduced system time evolution dynamics with deep system memory become feasible, enabling high-performing simulations of open quantum systems interacting with harmonic structured reservoirs and diagonal system-reservoir couplings.

# 5 Artificial neural networks

During the past decade, data-based computation, broadly referred to as machine learning, has become one of the most important and rapidly growing fields in technological research. With implications for all major industries, similar to the rise of personal computers during the past century, it is considered the paramount disruptive technology of our time. The fundamental idea of machine learning is to recognize recurrent patterns in large amounts of data via iterative training. Based on the structure of the input data, the algorithm makes predictions on problems that are as of yet unresolved. Already, applications range from image and facial recognition to resource management optimization, autonomous driving, estimations on future stock market development and countless others [46, 78]. In one of the most successful realizations of machine learning, a network of interconnected nodes is optimized to extrapolate new data from an existing training data set. These so-called artificial neural networks are reminiscent of the way biological neurons process information by interacting with each other over synapse formation.

Aside from the aforementioned industrial applications, interest in machine learning techniques has recently grown in physical research fields. In the context of open quantum systems and their notoriously inaccessible Hilbert space dimensions, the concept of efficiently sampling core information from large amounts of data appears as a promising new approach for an approximate description. In recent breakthroughs, artificial neural networks have been successfully employed for the description of quantum states [47–55] and open spin-1/2 quantum systems with Markovian dynamics [56–59]. Exploiting an almost limitless potential for parallelization and accurate information compression of Hilbert space by Metropolis sampling of possible system configurations in a Markov chain Monte Carlo approach, simulations of very large systems have been realized [46, 104–106]. Specifically, the *restricted Boltzmann machine* neural network architecture has emerged as a natural and highly efficient representation of the density matrix for small molecular and spin-1/2 quantum systems [47, 51, 107–112], since it features a one-to-one mapping of spins to artificial neurons and facilitates direct access to the stationary state via iterative application of a variational principle [113, 114]. High numerical performance and fast convergence times have been achieved for the simulation of symmetric and periodic spin systems, outperforming established numerical techniques such as quantum Monte Carlo or tensor network approaches for certain scenarios and including calculations for both stationary states [56, 57] and real-time evolution dynamics [58, 59].

In this Chapter, we introduce the core concepts of machine learning and artificial neural networks for open quantum systems. In Sec. 5.1, some of the basic ideas and principles of machine learning are introduced. Afterwards, in Sec. 5.2 the restricted Boltzmann machine architecture is established as a specific class of artificial neural networks. These

networks allow for an straightforward representation of the density matrix for spin-1/2 quantum systems, which is demonstrated in detail in Sec. 5.3. Due to the structure of this representation, symmetries inherent to the considered system can be exploited to drastically decrease the required number of connections in the network. As a result, even large symmetric systems can be described efficiently, constituting a key advantage of the neural network approach. The implementation of symmetries is discussed in Sec. 5.4. Having derived an efficient neural network representation of the density matrix, we introduce the core algorithms required for the training of the probabilistic network. For the sampling of input data, the Metropolis algorithm is presented in Sec. 5.5. In Sec. 5.6, the stochastic reconfiguration approach is established to approximate system observables and occurrence probabilities as statistical expectation values over the sampled training data. Afterwards, we derive optimization schemes for calcualting both the stationary states and the full time evolution dynamics of open quantum systems. Lastly, we provide details on the numerical implementation and the training procedure in Sec. 5.7.

## 5.1 Basic principles and definitions

### 5.1.1 Supervised and unsupervised learning

In any machine learning application, an algorithm is fed with input data to produce an answer to a given problem. We note that in the following, the terms *training* and *learning* are used synonymously and refer to the same process. In the case of supervised learning, the algorithm is fed with a training data set $\mathcal{D} = \{(x_1, y_1), \dots, (x_{N_s}, y_{N_s})\}$ consisting of $N_s$ samples of inputs $x_n \in \mathcal{X}$ and corresponding target outputs $y_n \in \mathcal{Y}$, where $\mathcal{X}$ and $\mathcal{Y}$ denote the input and output domains, respectively. To extrapolate from the existing data, the algorithm searches for underlying patterns in the training data set. The goal is to find a rule connecting inputs and outputs, for instance in the form of a deterministic model function $f(x, \boldsymbol{\vartheta}) = y$. Here, a set of latent parameters $\boldsymbol{\vartheta}$ is varied and optimized until the differences between the training data and values obtained from the model function are minimized [46]. Once training is finished, the algorithm is fed with new and unclassified input $\tilde{x}$ and produces corresponding output $\tilde{y}$ using the optimized model function. It is apparent that increasing the sample size $N_s$ of the training data likely improves the accuracy of the answers obtained from the machine. Perhaps the most prominent example of supervised machine learning is modern image recognition: The algorithm is fed with a large number of images as input samples $x_n$ together with labels naming the depicted objects, acting as the corresponding target outputs $y_n$. The goal of the learning procedure is to find a relationship between the pixel matrices of the images and their respective contents. Once the learning process is finished, the algorithm is fed with new images of varying objects. If training was successful, the algorithm will be able to correctly identify images of training objects [46].

Unsupervised learning, on the other hand, describes training procedures where only input data is provided, with no explicit target outputs available. Again, the goal is to find underlying structures and patterns in the input data. A prime example of unsupervised

learning and the main focus in this work is the search for a model probability distribution reproducing the statistics of a given input data set, often referred to as generative modeling [78]. As in the supervised learning case, the model probability distribution depends on a set of latent parameters $\boldsymbol{\vartheta}$. To obtain a probability function which fits the distribution of the input data, these parameters are adjusted until the likelihood of reproducing the training data is maximized. In particular, here we estimate the density matrix $\rho$ of a considered system by an iteratively optimized model distribution $\rho_{\boldsymbol{\vartheta}}$.

### 5.1.2 Models

In the context of machine learning, a model defines the relationship between input and output data and is obtained by training [46]. We differentiate between deterministic and probabilistic models. As mentioned in the previous Section, a deterministic model denotes a function

$$f(x, \boldsymbol{\vartheta}) = y, \tag{5.1}$$

with inputs $x \in \mathcal{X}$, outputs $y \in \mathcal{Y}$ and a set of training parameters $\boldsymbol{\vartheta}$. To obtain a deterministic model function, the variational parameters are optimized by an existing training data set of inputs and corresponding outputs. Alternatively, unsupervised machine learning can be employed to produce a probabilistic model. Here, the input training data is produced, e.g., by drawing samples from the configuration space of an existing probability distribution $P(x, y)$, which is referred to as the target distribution. These sample configurations are used to approximate the target function by a probabilistic model distribution

$$p(x, y, \boldsymbol{\vartheta}), \tag{5.2}$$

again depending on a set of latent parameters $\boldsymbol{\vartheta}$ to be optimized. In the context of open quantum systems, the full density matrix $\rho$ takes the role of the target distribution to be approximated, since it is often times inaccessible due to exponential scaling of the Hilbert space dimension. Using the unsupervised learning approach, we solve this problem by introducing a model distribution $\rho_{\boldsymbol{\vartheta}}$ with vastly reduced degrees of freedom $\boldsymbol{\vartheta}$. By drawing sample configurations from the systems' Hilbert space as input data, the variational parameters $\boldsymbol{\vartheta}$ are optimized to obtain a compressed representation of the full density matrix.

### 5.1.3 Cost functions

Having established the core ideas of machine learning, we still require a strategy to obtain a model function and quantify its ability to generalize from the input data. The model function is determined by the learning parameters $\boldsymbol{\vartheta}$, which are optimized by the training data set. To this end, we define a *cost function*

$$C(\boldsymbol{\vartheta}) = L(x, y, \boldsymbol{\vartheta}) + R(\boldsymbol{\vartheta}). \tag{5.3}$$

Most importantly, it consists of a loss function $L(x, y, \boldsymbol{\vartheta})$ measuring the differences between predictions from the model function and samples from the training data. Secondly, a

regularizer function $R(\boldsymbol{\vartheta})$ can be included to prevent the model from overfitting, e.g., by putting restraints on the length of the parameter vector $\boldsymbol{\vartheta}$ [46]. Once a cost function which fits the objective has been constructed, the training procedure is carried out as follows: Samples from the training data set are fed into the cost function, with the goal of finding the optimal set of parameters $\boldsymbol{\vartheta}$ which minimize $C(\boldsymbol{\vartheta})$. To find the model parameters resulting in the most efficient cost function, they are iteratively updated and reinserted into the cost function until a minimum is reached.

### 5.1.4 Stochastic gradient descent

The optimization of the cost function lies at the core of any machine learning application. Stochastic gradient descent describes the standard optimization algorithm for probabilistic models. It represents an iterative and stepwise search for the cost function minimum, based on samples drawn from the training data. Especially in the field of artificial neural networks, gradient-based minimization methods such as stochastic gradient descent are standard practice [46]. The basic idea of gradient descent is to update the learning coefficients $\boldsymbol{\vartheta}$ successively towards the direction of steepest descent of the cost function. The update rule for iteration $t \to t+1$ is given by

$$\boldsymbol{\vartheta}^{(t+1)} = \boldsymbol{\vartheta}^{(t)} - \nu \nabla_{\boldsymbol{\vartheta}} C(\boldsymbol{\vartheta}^{(t)}), \tag{5.4}$$

with an external parameter $\nu$ referred to as the *learning rate* in the context of machine learning. Stochastic gradient descent refers to a special case of gradient descent where only a subset of the training data set is used for the calculation of each update. The resulting stochastic nature of the gradient direction helps to find the global minimum faster, while reducing the risk of getting stuck in local minima [46].

## 5.2 Restricted Boltzmann machines

The model function is determined by the set of training parameters $\boldsymbol{\vartheta}$. In linear regression models, the desired model function is designed to be linearly dependent on the parameters $\boldsymbol{\vartheta}$, but may have nonlinear dependencies on the input data. Nonlinear regression models, on the other hand, are nonlinear in both the input data and the parameters [46]. In this Section, we introduce the concept of artificial neural networks, which are the most successful realization of nonlinear regression models. Artificial neural networks are inspired by biological neurons interacting with each other via synapses. They consist of a set of interconnected artificial neurons which model the state space of spins up or down, i.e., each taking one of two possible configurations $+1$ or $-1$ [46]. The set of training parameters $\boldsymbol{\vartheta}$ determines the shape of the neural network and is split up into *weights* and *biases*. Weights denote the connection strengths between interconnected pairs of neurons, whereas each neuron is assigned an individual bias or local field strength. The neural network is trained by optimization of the parameters $\boldsymbol{\vartheta}$, until an optimal representation of the underlying target function is achieved.

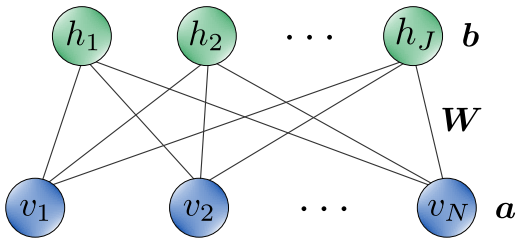


*Figure 5.1:* Graphical representation of a restricted Boltzmann machine featuring $N$ visible and $J$ hidden units with biases $\boldsymbol{a}$, $\boldsymbol{b}$, and connected by weights $\boldsymbol{W}$.

Here we focus on a specific class of artificial neural networks, which allows for a direct mapping of the density matrix for spin-1/2 systems: The *restricted Boltzmann machine*. This architecture defines a probabilistic model distribution over the states of a set of binary neurons or units $\boldsymbol{s} = (s_1, \ldots, s_G)$, where each of the neurons carries a probability of being in either state $+1$ or $-1$. $\boldsymbol{s}$ is further divided into a set of visible neurons $\boldsymbol{v} = (v_1, \ldots, v_N)$ and a set of hidden neurons $\boldsymbol{h} = (h_1, \ldots, h_J)$. While the visible neurons carry the information of the model distribution and act as input and output gates, the hidden units are auxiliary degrees of freedom to improve the networks' ability to approximate the target function. Boltzmann machines belong to the class of recurrent neural networks, i.e., representations where all neurons are connected to each other by weights. In a restricted Boltzmann machine, visible neurons are only connected to hidden neurons and vice versa. A graphical representation is shown in Fig. 5.1. Since it has been found that this network architecture can be trained much more efficiently than regular Boltzmann machines [46], current research on machine learning for open quantum systems focuses on restricted Boltzmann machines [47, 51, 56–59, 79].

The model distribution of a restricted Boltzmann machine is given by a Boltzmann probability distribution [46],

$$p(\boldsymbol{v}, \boldsymbol{\vartheta}) = \frac{1}{Z_{\boldsymbol{\vartheta}}} \sum_{\boldsymbol{h}} e^{-E(\boldsymbol{v},\boldsymbol{h},\boldsymbol{\vartheta})}, \tag{5.5}$$

with a partition function

$$Z_{\boldsymbol{\vartheta}} = \sum_{\boldsymbol{v},\boldsymbol{h}} e^{-E(\boldsymbol{v},\boldsymbol{h},\boldsymbol{\vartheta})}, \tag{5.6}$$

and an Ising-type energy contribution $E$ depending on the optimization parameters,

$$E(\boldsymbol{v}, \boldsymbol{h}, \boldsymbol{\vartheta}) = -\sum_{i=1}^{N}\sum_{j=1}^{J} W_{ji} h_j v_i - \sum_{i=1}^{N} a_i v_i - \sum_{j=1}^{J} b_j h_j. \tag{5.7}$$

The parameter vector $\boldsymbol{\vartheta}$ consists of biases $a_i$ and $b_j$ of visible and hidden neurons, respectively, and of weights $W_{ij}$ connecting the visible and hidden units to each other. Since only the visible units are of interest, all hidden neurons are traced out from the model distribution in Eq. (5.5). Lastly, the cost function of a restricted Boltzmann machine is defined by a maximum log-likelihood estimation,

$$C(\boldsymbol{\vartheta}) = \sum_{n=1}^{N_\mathrm{s}} \log p(\boldsymbol{v}^n, \boldsymbol{\vartheta}), \tag{5.8}$$

with $\boldsymbol{v}^n$ denoting the $n$-th sample of a visible unit configuration drawn from the training data.

## 5.3 Neural density operator

As a next step, a neural network representation of arbitrary spin-1/2 quantum states is derived. We start with the simpler case of pure wave functions. As motivated in the last Section, a Boltzmann probability distribution can be constituted by a neural network in the form of a restricted Boltzmann machine. The restricted Boltzmann machine representation of a pure wave function featuring $N$ visible spins (or neurons) $\boldsymbol{\sigma}$ and $J$ auxiliary hidden spins $\boldsymbol{h}$ is provided by [47]

$$\psi_{\boldsymbol{\vartheta}}(\boldsymbol{\sigma}) = \sum_{\boldsymbol{h}} \exp\left(\sum_{i=1}^{N}\sum_{j=1}^{J} W_{ji} h_j \sigma_i + \sum_{i=1}^{N} a_i \sigma_i + \sum_{j=1}^{J} b_j h_j\right). \tag{5.9}$$

Note that this representation cannot constitute the wave function exactly. Rather, it is designed as an approximative architecture with the achievable accuracy limited by the number of neurons. For an analytically exact neural network depiction of pure wave functions, so-called deep networks featuring multiple layers of hidden neurons are required [115]. Since the network does not feature any intralayer connections, the hidden layer can be traced out explicitly:

$$\begin{aligned}
\psi_{\boldsymbol{\vartheta}}(\boldsymbol{\sigma}) &= \sum_{h_1=\pm 1} \dots \sum_{h_J=\pm 1} \exp\left(\sum_{i=1}^{N}\sum_{j=1}^{J} W_{ji} h_j \sigma_i + \sum_{i=1}^{N} a_i \sigma_i + \sum_{j=1}^{J} b_j h_j\right) \\
&= \exp\left(\sum_{i=1}^{N} a_i \sigma_i\right) \sum_{h_1=\pm 1} \exp\left(\sum_{i=1}^{N} W_{1i} h_1 \sigma_i + b_1 h_1\right) \dots \sum_{h_J=\pm 1} \exp\left(\sum_{i=1}^{N} W_{Ji} h_J \sigma_i + b_J h_J\right) \\
&= \exp\left(\sum_{i=1}^{N} a_i \sigma_i\right) \prod_{j=1}^{J} \left[\exp\left(\sum_{i=1}^{N} W_{ji} \sigma_i + b_j\right) + \exp\left(-\sum_{i=1}^{N} W_{ji} \sigma_i - b_j\right)\right] \\
&= 2 \exp\left(\sum_{i=1}^{N} a_i \sigma_i\right) \prod_{j=1}^{J} \cosh\left(\sum_{i=1}^{N} W_{ji} \sigma_i + b_j\right).
\end{aligned} \tag{5.10}$$

However, an arbitrary mixed state cannot be represented analogously due to its nondiagonal elements. To resolve this problem, an additional set of hidden units, often referred to as an ancillary layer, is incorporated in the network to create a diagonalized representation of the mixed state [51]. In other words, to depict an arbitrary mixed state in terms of a restricted Boltzmann machine, it must first be purified by introducing ancillary degrees of freedom. As a result, the density matrix representation of a mixed state is estimated by a mapping $\rho_{\boldsymbol{\vartheta}}$, called *neural density operator*. Given two input states $\boldsymbol{\sigma}$ and $\boldsymbol{\eta}$, it returns the corresponding matrix element $\rho_{\boldsymbol{\vartheta}}(\boldsymbol{\sigma}, \boldsymbol{\eta}) = \langle \boldsymbol{\sigma} | \, \rho_{\boldsymbol{\vartheta}} \, | \boldsymbol{\eta} \rangle$. Moreover, the neural density operator must fulfil the same properties as the regular density matrix (see Ch. 2),

$$\mathrm{tr}\{\rho_{\boldsymbol{\vartheta}}\} = 1, \tag{5.11a}$$

$$\rho_{\boldsymbol{\vartheta}}^{\dagger} = \rho_{\boldsymbol{\vartheta}}, \tag{5.11b}$$

$$\langle \boldsymbol{\sigma} | \, \rho_{\boldsymbol{\vartheta}} \, | \boldsymbol{\sigma} \rangle \geq 0 \; \forall \boldsymbol{\sigma}. \tag{5.11c}$$

In general, the neural density operator can be written in terms of the pure state restricted Boltzmann machine representation,

$$\rho_{\boldsymbol{\vartheta}}(\boldsymbol{\sigma}, \boldsymbol{\eta}) = \sum_{\boldsymbol{h}^{\mu}} \psi_{\boldsymbol{\vartheta}}(\boldsymbol{\sigma}, \boldsymbol{h}^{\mu}) \psi_{\boldsymbol{\vartheta}}^{*}(\boldsymbol{\eta}, \boldsymbol{h}^{\mu}), \tag{5.12}$$

where we introduced the ancillary hidden layer $\boldsymbol{h}^{\mu}$ to index the different wave functions forming the mixed state [51]. In total, this results in three hidden layers: $\boldsymbol{h}^{\sigma} = (h_1^{\sigma}, \ldots, h_M^{\sigma})$ and $\boldsymbol{h}^{\eta} = (h_1^{\eta}, \ldots, h_M^{\eta})$ with $M$ units each for the wave functions $\psi_{\boldsymbol{\vartheta}}(\boldsymbol{\sigma}, \boldsymbol{h}^{\mu})$ and $\psi_{\boldsymbol{\vartheta}}^{*}(\boldsymbol{\eta}, \boldsymbol{h}^{\mu})$, respectively, and $\boldsymbol{h}^{\mu} = (h_1^{\mu}, \ldots, h_K^{\mu})$ featuring $K$ units for the mixing of the states.

Inserting the restricted Boltzmann machine representation for pure states [Eq. (5.10)], the neural density operator takes the form

$$\begin{aligned}
\rho_{\boldsymbol{\vartheta}}(\boldsymbol{\sigma}, \boldsymbol{\eta}) = \sum_{\boldsymbol{h}^{\sigma}} \sum_{\boldsymbol{h}^{\eta}} \sum_{\boldsymbol{h}^{\mu}} & \exp\left[ \sum_{k=1}^{K} \left( c_k + c_k^{*} \right) h_k^{\mu} \right] \\
& \times \exp\left( \sum_{i=1}^{N} a_i \sigma_i + \sum_{m=1}^{M} b_m h_m^{\sigma} + \sum_{i=1}^{N} \sum_{m=1}^{M} W_{mi} h_m^{\sigma} \sigma_i + \sum_{i=1}^{N} \sum_{k=1}^{K} U_{ki} h_k^{\mu} \sigma_i \right) \\
& \times \exp\left( \sum_{i=1}^{N} a_i^{*} \eta_i + \sum_{m=1}^{M} b_m^{*} h_m^{\eta} + \sum_{i=1}^{N} \sum_{m=1}^{M} W_{mi}^{*} h_m^{\eta} \eta_i + \sum_{i=1}^{N} \sum_{k=1}^{K} U_{ki}^{*} h_k^{\mu} \eta_i \right).
\end{aligned} \tag{5.13}$$

The training parameters $\boldsymbol{\vartheta} = (\boldsymbol{a}, \boldsymbol{b}, \boldsymbol{c}, \boldsymbol{W}, \boldsymbol{U})$ are complex-valued and contain biases $\boldsymbol{a}$ for visible units $\boldsymbol{\sigma}$ and $\boldsymbol{\eta}$, $\boldsymbol{b}$ for auxiliary hidden units $\boldsymbol{h}^{\sigma}$ and $\boldsymbol{h}^{\eta}$, and $\boldsymbol{c}$ for the ancillary hidden layer $\boldsymbol{h}^{\mu}$, respectively. The complex weights $\boldsymbol{W}$ connect the visible layers $\boldsymbol{\sigma}$ and $\boldsymbol{\eta}$ to their auxiliary hidden counterparts $\boldsymbol{h}^{\sigma}$ and $\boldsymbol{h}^{\eta}$. In addition, weights $\boldsymbol{U}$ denote the coupling elements between the visible layers and the ancillary mixing layer $\boldsymbol{h}^{\mu}$. Fig. 5.2 shows a graphical representation of the restricted Boltzmann machine as stated in Eq. (5.13), constituting the neural density operator. Once again, all hidden layers can be traced out explicitly, yielding [51, 58, 59]

$$\begin{aligned}
\rho_{\boldsymbol{\vartheta}}(\boldsymbol{\sigma}, \boldsymbol{\eta}) = 8 \exp & \left( \sum_{i=1}^{N} a_i \sigma_i \right) \exp\left( \sum_{i=1}^{N} a_i^{*} \eta_i \right) \\
& \times \prod_{m=1}^{M} \cosh\left( b_m + \sum_{i=1}^{N} W_{mi} \sigma_i \right) \cosh\left( b_m^{*} + \sum_{i=1}^{N} W_{mi}^{*} \eta_i \right) \\
& \times \prod_{k=1}^{K} \cosh\left( c_k + c_k^{*} + \sum_{i=1}^{N} U_{ki} \sigma_i + \sum_{i=1}^{N} U_{ki}^{*} \eta_i \right).
\end{aligned} \tag{5.14}$$

This parametrization fulfills all properties of the density matrix [Eq. (5.11)]. Note that a normalizing partition function $Z$ as introduced in Eq. (5.5) is so far missing from the representation: In its current form, the neural density operator remains unnormalized

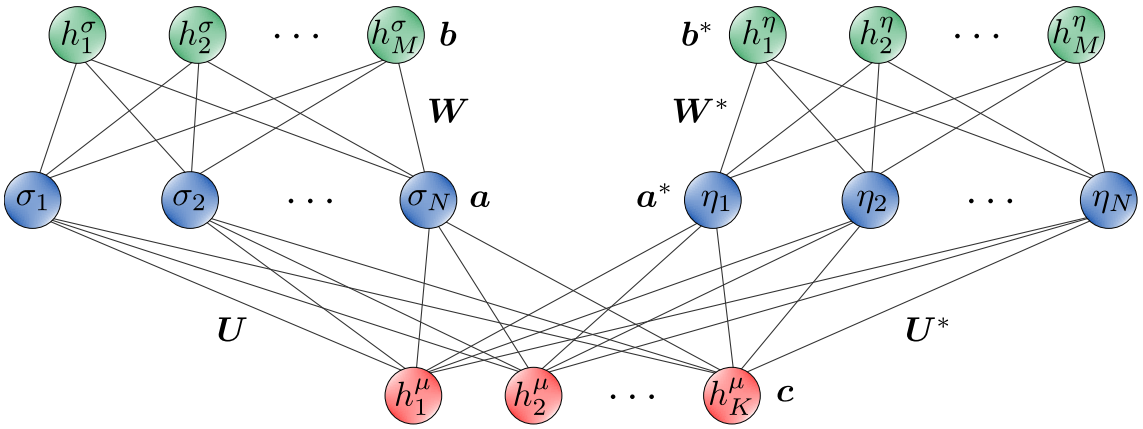


*Figure 5.2:* Restricted Boltzmann machine representation of the neural density operator $\rho_{\boldsymbol{\vartheta}}$.

since the partition function is often times inaccessible in large quantum systems. We will resolve this problem by approximating $Z$ using the system sample configurations drawn for training, which is explained in detail in the upcoming Sections. Moreover, the networks' ability to accurately represent an arbitrary density matrix is given by the number of hidden units $M$ and $K$. Specifically, we define the hidden node densities

$$\alpha = \frac{M}{N}, \quad \beta = \frac{K}{N}, \tag{5.15}$$

which determine the representational power of the network [46, 78]. In the numerical implementation, the real and imaginary part of all training parameters are stored and calculated separately. Due to the structure of Eq. (5.14), only the real part of the ancillary bias $\boldsymbol{c}$ is required. The total number $n_p$ of variational parameters stored in $\boldsymbol{\vartheta}$ is thus given by

$$n_p = 2N + 2M + K + 2MN + 2KN, \tag{5.16}$$

representing the number of degrees of freedom of the neural density operator. In comparison to the $N(N+1)/2$ independent density matrix elements required for the calculation of a system of $N$ spin-1/2 particles, this mapping yields a high grade of compression of the relevant system information and lies at the core of the imposed truncation scheme.

## 5.4 Implementation of symmetries

Often times, physical systems and their corresponding Hamiltonians feature intrinsic symmetries, for instance in the form of site-translation invariance in a spin chain system. These symmetries are also inherent to the states of the respective system and maintained during its time evolution dynamics. Using the artificial neural network implementation, this property can be exploited to further decrease the computational cost for the calculation of symmetric open spin-1/2 quantum systems. Specifically, the number of variational parameters can be reduced by taking symmetries inherent to the Hamiltonian into account.

To this end, we consider a set of linear transformations $T_s$, $s = \{1, \dots, S\}$, defining a symmetry group [47]. The visible units of the restricted Boltzmann machine are then transformed via

$$T_s \sigma_i = \tilde{\sigma}_i(s), \tag{5.17a}$$

$$T_s \eta_i = \tilde{\eta}_i(s). \tag{5.17b}$$

As a result, the neural density operator can be rewritten to be invariant against transformations imposed by $T_s$:

$$\begin{aligned}
\rho_{\boldsymbol{\vartheta}}^{\alpha,\beta}(\boldsymbol{\sigma},\boldsymbol{\eta}) = \sum_{\boldsymbol{h}_s^\sigma} \sum_{\boldsymbol{h}_s^\eta} \sum_{\boldsymbol{h}_{s'}^\mu} & \exp\left[\sum_{f'=1}^{\beta} \left(c^{(f')} + c^{(f')*}\right) \sum_{s'=1}^{S'} h_{f',s'}^{\mu}\right] \\
& \times \exp\left[\sum_{f=1}^{\alpha} a^{(f)} \sum_{s=1}^{S} \sum_{i=1}^{N} \tilde{\sigma}_i(s) + \sum_{f=1}^{\alpha} b^{(f)} \sum_{s=1}^{S} h_{f,s}^{\sigma}\right. \\
& \left. + \sum_{f=1}^{\alpha} \sum_{s=1}^{S} h_{f,s}^{\sigma} \sum_{i=1}^{N} W_i^{(f)} \tilde{\sigma}_i(s) + \sum_{f'=1}^{\beta} \sum_{s'=1}^{S'} h_{f',s'}^{\mu} \sum_{i=1}^{N} U_i^{(f')} \tilde{\sigma}_i(s')\right] \\
& \times \exp\left[\sum_{f=1}^{\alpha} a^{(f)*} \sum_{s=1}^{S} \sum_{i=1}^{N} \tilde{\eta}_i(s) + \sum_{f=1}^{\alpha} b^{(f)*} \sum_{s=1}^{S} h_{f,s}^{\eta}\right. \\
& \left. + \sum_{f=1}^{\alpha} \sum_{s=1}^{S} h_{f,s}^{\eta} \sum_{i=1}^{N} W_i^{(f)*} \tilde{\eta}_i(s) + \sum_{f'=1}^{\beta} \sum_{s'=1}^{S'} h_{f',s'}^{\mu} \sum_{i=1}^{N} U_i^{(f')*} \tilde{\eta}_i(s')\right].
\end{aligned} \tag{5.18}$$

The dimensions of the variational parameters $\boldsymbol{\vartheta}^{(f)}$ have been modified in the process. Biases $a^{(f)}$, $b^{(f)}$ and $c^{(f')}$ are vectors in feature space with $f = 1, \dots, \alpha$, $f' = 1, \dots, \beta$, and $\alpha$ and $\beta$ denote the auxiliary and ancillary hidden unit densities, respectively [Eq. (5.15)]. The restated weights $W_i^{(f)}$ and $U_i^{(f')}$ have $\alpha \times N$ and $\beta \times N$ elements, respectively. This representation corresponds to a neural density operator featuring $M = S \times \alpha$ auxiliary units and $K = S' \times \beta$ ancillary units. As before, all hidden spins can be traced out explicitly, yielding

$$\begin{aligned}
\rho_{\boldsymbol{\vartheta}}^{\alpha,\beta}(\boldsymbol{\sigma},\boldsymbol{\eta}) = 8 \exp & \left[\sum_{f=1}^{\alpha} \sum_{s=1}^{S} \sum_{i=1}^{N} a^{(f)} \tilde{\sigma}_i(s)\right] \exp\left[\sum_{f=1}^{\alpha} \sum_{s=1}^{S} \sum_{i=1}^{N} a^{(f)*} \tilde{\eta}_i(s)\right] \\
& \times \prod_{f=1}^{\alpha} \prod_{s=1}^{S} \cosh\left[b^{(f)} + \sum_{i=1}^{N} W_i^{(f)} \tilde{\sigma}_i(s)\right] \cosh\left[b^{(f)*} + \sum_{i=1}^{N} W_i^{(f)*} \tilde{\eta}_i(s)\right] \\
& \times \prod_{f'=1}^{\beta} \prod_{s'=1}^{S'} \cosh\left[c^{(f')} + c^{(f')*} + \sum_{i=1}^{N} U_i^{(f')} \tilde{\sigma}_i(s') + \sum_{i=1}^{N} U_i^{(f')*} \tilde{\eta}_i(s')\right].
\end{aligned} \tag{5.19}$$

For the specific case of site-translation invariance, the symmetry group defined by $T_s$ has an orbit of $S = N$ elements [47]. This means that using the symmetry propoerties of the system, a given spin configuration is translated into $N$ copies. The translation-invariant parameters $\boldsymbol{\vartheta}^{(f)}$ simultaneously act on all copies of the configuration for a given feature $f$. As a result, far fewer parameters are required for the same total number of units as before.

## 5.5 Metropolis sampling

In this Section, we take first steps towards the numerical realization of the neural network. The training of the network is carried out by optimization of the variational coefficients $\boldsymbol{\vartheta}$, until an optimal mapping of the full density matrix is obtained. In the limit case of small systems where the full Hilbert space is accessible, all possible configurations of the density matrix can be taken into account for the optimization of the training parameters. Yet, it is noted that the resulting neural density operator is still an approximative representation due to the underlying restricted Boltzmann machine architecture [115]. However, in general the Hilbert space of open quantum systems quickly becomes inaccessibly large, making the full density matrix inaccessible as well. To find an accessible approximation, $N_s$ sample configurations of the system, i.e., visible spin configurations $(\boldsymbol{\sigma}, \boldsymbol{\eta})$, are drawn from the configuration space of the target distribution. The samples are drawn using the Metropolis algorithm [104], a Markov chain Monte Carlo method to obtain a sequence of samples from the phase space of a probability distribution, corresponding to a random walk in configuration space [46, 105, 106]. The Metropolis algorithm is applicable to symmetric probability distributions while its generalization, the Metropolis-Hastings algorithm, can be used to sample arbitrary distributions [116].

In the following, we briefly outline the steps of the Metropolis algorithm for symmetric distributions. Its goal is to approximate an inaccessible target distribution $P(x)$ by a model distribution $p(x)$, which is proportional to the target distribution. This is performed by drawing samples $x$ from the configuration space of the target distribution. For the initialization of the Metropolis algorithm, a random sample $x_t$ is drawn from the configuration space of the target distribution $P(x)$, acting as the *current* sample. As a first step, a new or *proposed* sample $x'$ is drawn on the basis of $x_t$, based on a proposal distribution $g(x'|x_t)$ denoting the probability of drawing sample $x'$ given sample $x_t$. Next, the proposed samples' target probability $P(x')$ is compared to the target probability of the current sample $P(x_t)$ via the acceptance probability function

$$A(x', x_t) = \min\left[1, \frac{P(x')}{P(x_t)} \frac{g(x_t|x')}{g(x'|x_t)}\right] = \min\left[1, \frac{p(x')}{p(x_t)} \frac{g(x_t|x')}{g(x'|x_t)}\right], \tag{5.20}$$

measuring the occurrence probability of the proposed sample $x'$ in comparison to $x_t$. Taking the ratio of target probabilities in Eq. (5.20) bypasses the issue of their factual inaccessibility, since the model distribution $p(x)$ is proportional to $P(x)$. Hence, $p(x)$ can be used in its place for the calculation of the acceptance ratio. Lastly, the algorithm has to choose whether it accepts or rejects the proposed sample $x'$ as the next sample $x_{t+1}$ in the Markov chain. To this end, a uniform random number $r \in [0, 1]$ is generated and its value is compared to the acceptance probability [105]:

$$\begin{aligned} &\texttt{if } r \leq A(x', x_t): \quad x_{t+1} = x', \\ &\texttt{if } r > A(x', x_t): \quad x_{t+1} = x_t. \end{aligned} \tag{5.21}$$

In summary, the Metropolis algorithm performs a random walk in configuration space, sometimes accepting and sometimes rejecting proposed steps. Due to the selection rule

of Eq. (5.21), drawn samples with a higher occurrence probability according to the target distribution $P(x)$ are more likely to be accepted, whereas samples with a low probability are more often rejected. In consequence, the algorithm chooses a selection of samples which are used to efficiently approximate the target distribution by the model distribution.

## 5.6 Stochastic reconfiguration for Liouvillians

At the core of all machine learning algorithms lies the optimization of a predefined cost function towards a global minimum. In this Section, we introduce the stochastic reconfiguration algorithm [117–119], which allows for the application of this approach to the Liouvillian of open spin-1/2 quantum systems by approximating system observables and occurrence probabilities as statistical expectation values over the sample configurations drawn for the training of the network. While it is in principle possible to simulate real-time dynamics of open systems using artifical neural networks [58, 59], the approach excels in finding stationary states, such as nonequilibrium steady states or ground state energies of the system. Here we derive strategies to calculate both stationary states and Markovian time evolution dynamics of open spin-1/2 quantum systems, imposed by a Lindblad master equation as introduced in Ch. 3. We start from the neural density operator representation [Eq. (5.14)]. Given this parametrization of the density matrix, our goal is to find an approximate solution of the Lindblad master equation describing the Markovian time evolution dynamics of a considered system. To enable the application to established machine learning strategies, the master equation is first stated as a variational optimization problem. In the following it is solved using the stochastic reconfiguration method and time-dependent variational Monte Carlo techniques, which are extended to the dissipative case [56–59].

We start by rewriting the density matrix as a vector, such that the Lindblad master equation of the general form (see Ch. 3)

$$\partial_t \rho = -\frac{i}{\hbar}\left[H,\rho\right] + \frac{\gamma}{2}\sum_{i=1}^{N}\left(2J_i\rho J_i^\dagger - J_i^\dagger J_i\rho - \rho J_i^\dagger J_i\right) \tag{5.22}$$

can be stated by means of a non-Hermitian Liouvillian superoperator,

$$\partial_t \boldsymbol{\rho} = \boldsymbol{\mathcal{L}}\boldsymbol{\rho}. \tag{5.23}$$

As mentioned in Sec. 5.3, all training parameters are split up into their real and imaginary parts and written in a single vector,

$$\boldsymbol{\vartheta} = \left(\mathrm{Re}\{\boldsymbol{a}\},\mathrm{Im}\{\boldsymbol{a}\},\mathrm{Re}\{\boldsymbol{b}\},\mathrm{Im}\{\boldsymbol{b}\},\mathrm{Re}\{\boldsymbol{c}\},\mathrm{Re}\{\boldsymbol{W}\},\mathrm{Im}\{\boldsymbol{W}\},\mathrm{Re}\{\boldsymbol{U}\},\mathrm{Im}\{\boldsymbol{U}\}\right), \tag{5.24}$$

containing $n_p$ real-valued elements [Eq. (5.16)].

### 5.6.1 Stationary states

When the training objective is to find the stationary state of an open quantum system, the variational parameters must be trained to fulfill the condition

$$\partial_t \boldsymbol{\rho} = \boldsymbol{\mathcal{L}}\boldsymbol{\rho} = 0. \tag{5.25}$$

To this end, we define a corresponding cost function [57, 59],

$$C(\boldsymbol{\vartheta}) = \|\boldsymbol{\mathcal{L}}\boldsymbol{\rho}_{\boldsymbol{\vartheta}}\|_2^2\,, \tag{5.26}$$

and rewrite it by inserting multiple identities, yielding

$$\begin{aligned} C(\boldsymbol{\vartheta}) &= \sum_{\boldsymbol{\sigma}_1,\boldsymbol{\eta}_1} \langle\boldsymbol{\eta}_1|\left\{\mathcal{L}\boldsymbol{\rho}_{\boldsymbol{\vartheta}}\right\}^\dagger|\boldsymbol{\sigma}_1\rangle\langle\boldsymbol{\sigma}_1|\left\{\mathcal{L}\boldsymbol{\rho}_{\boldsymbol{\vartheta}}\right\}|\boldsymbol{\eta}_1\rangle \\ &= \sum_{\boldsymbol{\sigma}_1,\boldsymbol{\eta}_1}\sum_{\boldsymbol{\sigma}_2,\boldsymbol{\eta}_2}\sum_{\boldsymbol{\sigma}_3,\boldsymbol{\eta}_3} \boldsymbol{\rho}_{\boldsymbol{\vartheta}}^\dagger(\boldsymbol{\sigma}_3,\boldsymbol{\eta}_3)\mathcal{L}^\dagger(\boldsymbol{\sigma}_1,\boldsymbol{\eta}_1,\boldsymbol{\sigma}_3,\boldsymbol{\eta}_3)\mathcal{L}(\boldsymbol{\sigma}_1,\boldsymbol{\eta}_1,\boldsymbol{\sigma}_2,\boldsymbol{\eta}_2)\boldsymbol{\rho}_{\boldsymbol{\vartheta}}(\boldsymbol{\sigma}_2,\boldsymbol{\eta}_2), \end{aligned} \tag{5.27}$$

with

$$\begin{aligned} &\langle\boldsymbol{\sigma}_1|\left\{\mathcal{L}\boldsymbol{\rho}_{\boldsymbol{\vartheta}}\right\}|\boldsymbol{\eta}_1\rangle \\ &= \langle\boldsymbol{\sigma}_1|\left\{-\frac{i}{\hbar}[H,\boldsymbol{\rho}_{\boldsymbol{\vartheta}}] + 2J\boldsymbol{\rho}_{\boldsymbol{\vartheta}}J^\dagger - J^\dagger J\boldsymbol{\rho}_{\boldsymbol{\vartheta}} - \boldsymbol{\rho}_{\boldsymbol{\vartheta}}J^\dagger J\right\}|\boldsymbol{\eta}_1\rangle \\ &= \sum_{\boldsymbol{\sigma}_2,\boldsymbol{\eta}_2}\langle\boldsymbol{\sigma}_1|\Big\{-\frac{i}{\hbar}[H,|\boldsymbol{\sigma}_2\rangle\langle\boldsymbol{\sigma}_2|\boldsymbol{\rho}_{\boldsymbol{\vartheta}}|\boldsymbol{\eta}_2\rangle\langle\boldsymbol{\eta}_2|] + 2J|\boldsymbol{\sigma}_2\rangle\langle\boldsymbol{\sigma}_2|\boldsymbol{\rho}_{\boldsymbol{\vartheta}}|\boldsymbol{\eta}_2\rangle\langle\boldsymbol{\eta}_2|J^\dagger \\ &- J^\dagger J|\boldsymbol{\sigma}_2\rangle\langle\boldsymbol{\sigma}_2|\boldsymbol{\rho}_{\boldsymbol{\vartheta}}|\boldsymbol{\eta}_2\rangle\langle\boldsymbol{\eta}_2| - |\boldsymbol{\sigma}_2\rangle\langle\boldsymbol{\sigma}_2|\boldsymbol{\rho}_{\boldsymbol{\vartheta}}|\boldsymbol{\eta}_2\rangle\langle\boldsymbol{\eta}_2|J^\dagger J\Big\}|\boldsymbol{\eta}_1\rangle \\ &= \sum_{\boldsymbol{\sigma}_2,\boldsymbol{\eta}_2}\langle\boldsymbol{\sigma}_1|\Big\{-\frac{i}{\hbar}[H,|\boldsymbol{\sigma}_2\rangle\langle\boldsymbol{\eta}_2|] + 2J|\boldsymbol{\sigma}_2\rangle\langle\boldsymbol{\eta}_2|J^\dagger \\ &- J^\dagger J|\boldsymbol{\sigma}_2\rangle\langle\boldsymbol{\eta}_2| - |\boldsymbol{\sigma}_2\rangle\langle\boldsymbol{\eta}_2|J^\dagger J\Big\}|\boldsymbol{\eta}_1\rangle\langle\boldsymbol{\sigma}_2|\boldsymbol{\rho}_{\boldsymbol{\vartheta}}|\boldsymbol{\eta}_2\rangle \\ &= \sum_{\boldsymbol{\sigma}_2,\boldsymbol{\eta}_2}\mathcal{L}(\boldsymbol{\sigma}_1,\boldsymbol{\eta}_1,\boldsymbol{\sigma}_2,\boldsymbol{\eta}_2)\boldsymbol{\rho}_{\boldsymbol{\vartheta}}(\boldsymbol{\sigma}_2,\boldsymbol{\eta}_2). \end{aligned} \tag{5.28}$$

Again we are faced with the issue of inaccessiblity, since $C(\boldsymbol{\vartheta})$ cannot be computed without the knowledge of $\boldsymbol{\rho}_{\boldsymbol{\vartheta}}$. However, it can be approximated as a statistical expectation value over the probability distribution

$$p_{\boldsymbol{\vartheta}}(\boldsymbol{\sigma},\boldsymbol{\eta}) = |\rho_{\boldsymbol{\vartheta}}(\boldsymbol{\sigma},\boldsymbol{\eta})|^2. \tag{5.29}$$

This approach is analogous to the concept of variational Monte Carlo techniques and constitutes the stochastic reconfiguration method [119]. We introduce the estimator of the Liouvillian superoperator,

$$\tilde{\mathcal{L}}(\boldsymbol{\sigma}_1,\boldsymbol{\eta}_1) := \sum_{\boldsymbol{\sigma}_2,\boldsymbol{\eta}_2}\frac{\mathcal{L}(\boldsymbol{\sigma}_1,\boldsymbol{\eta}_1,\boldsymbol{\sigma}_2,\boldsymbol{\eta}_2)\rho_{\boldsymbol{\vartheta}}(\boldsymbol{\sigma}_2,\boldsymbol{\eta}_2)}{\rho_{\boldsymbol{\vartheta}}(\boldsymbol{\sigma}_1,\boldsymbol{\eta}_1)}, \tag{5.30}$$

and rewrite the cost function accordingly,

$$C(\boldsymbol{\vartheta}) = \sum_{\boldsymbol{\sigma},\boldsymbol{\eta}} p_{\boldsymbol{\vartheta}}(\boldsymbol{\sigma},\boldsymbol{\eta})\tilde{\mathcal{L}}^{\dagger}(\boldsymbol{\sigma},\boldsymbol{\eta})\tilde{\mathcal{L}}(\boldsymbol{\sigma},\boldsymbol{\eta}). \tag{5.31}$$

The statistical expectation values are obtained by Monte Carlo sampling of the Hilbert space, using the Metropolis algorithm where $N_s$ samples of visible unit configurations $(\boldsymbol{\sigma}_n,\boldsymbol{\eta}_n)$ are drawn (see Sec. 5.5). To construct statistical expectation values, the occurrence probability $p_{\boldsymbol{\vartheta}}(\boldsymbol{\sigma}_n,\boldsymbol{\eta}_n)$ of each drawn sample is calculated [see Eq. (5.29)]. However, at this stage the neural density operator is still unnormalized due to the inaccessibility of the full partition function (see Sec. 5.3). To represent a probability, $p_{\boldsymbol{\vartheta}}(\boldsymbol{\sigma},\boldsymbol{\eta})$ must still be normalized. To this end, an approximate partition function is constructed from all drawn samples,

$$Z_{p_{\boldsymbol{\vartheta}}} = \sum_{n=1}^{N_s} p_{\boldsymbol{\vartheta}}(\boldsymbol{\sigma}_n,\boldsymbol{\eta}_n), \tag{5.32}$$

and the occurrence probability of sample $(\boldsymbol{\sigma}_n,\boldsymbol{\eta}_n)$ is given by

$$\tilde{p}_{\boldsymbol{\vartheta}}(\boldsymbol{\sigma}_n,\boldsymbol{\eta}_n) = \frac{1}{Z_{p_{\boldsymbol{\vartheta}}}} p_{\boldsymbol{\vartheta}}(\boldsymbol{\sigma}_n,\boldsymbol{\eta}_n). \tag{5.33}$$

As a result, the cost function is approximated as

$$C(\boldsymbol{\vartheta}) \approx \sum_{n=1}^{N_s} \tilde{p}_{\boldsymbol{\vartheta}}(\boldsymbol{\sigma}_n,\boldsymbol{\eta}_n)\tilde{\mathcal{L}}^{\dagger}(\boldsymbol{\sigma}_n,\boldsymbol{\eta}_n)\tilde{\mathcal{L}}(\boldsymbol{\sigma}_n,\boldsymbol{\eta}_n). \tag{5.34}$$

Inserting the identity for the normalized probability distribution $\tilde{p}_{\boldsymbol{\vartheta}}(\boldsymbol{\sigma}_n,\boldsymbol{\eta}_n)$, the cost function takes the form

$$\begin{aligned} C(\boldsymbol{\vartheta}) &= \sum_{n=1}^{N_s} \frac{|\rho_{\boldsymbol{\vartheta}}(\boldsymbol{\sigma}_n,\boldsymbol{\eta}_n)|^2}{\sum_{m=1}^{N_s}|\rho_{\boldsymbol{\vartheta}}(\boldsymbol{\sigma}_m,\boldsymbol{\eta}_m)|^2} \\ &\times \sum_{k=1}^{N_s} \frac{\rho^{\dagger}_{\boldsymbol{\vartheta}}(\boldsymbol{\sigma}_k,\boldsymbol{\eta}_k)}{\rho^{\dagger}_{\boldsymbol{\vartheta}}(\boldsymbol{\sigma}_n,\boldsymbol{\eta}_n)} \mathcal{L}^{\dagger}(\boldsymbol{\sigma}_n,\boldsymbol{\eta}_n,\boldsymbol{\sigma}_k,\boldsymbol{\eta}_k) \sum_{p=1}^{N_s} \mathcal{L}(\boldsymbol{\sigma}_n,\boldsymbol{\eta}_n,\boldsymbol{\sigma}_p,\boldsymbol{\eta}_p) \frac{\rho_{\boldsymbol{\vartheta}}(\boldsymbol{\sigma}_p,\boldsymbol{\eta}_p)}{\rho_{\boldsymbol{\vartheta}}(\boldsymbol{\sigma}_n,\boldsymbol{\eta}_n)} \\ &= \frac{1}{\sum_{m=1}^{N_s}|\rho_{\boldsymbol{\vartheta}}(\boldsymbol{\sigma}_m,\boldsymbol{\eta}_m)|^2} \\ &\times \sum_{n,k,p=1}^{N_s} \rho^{\dagger}_{\boldsymbol{\vartheta}}(\boldsymbol{\sigma}_k,\boldsymbol{\eta}_k)\mathcal{L}^{\dagger}(\boldsymbol{\sigma}_n,\boldsymbol{\eta}_n,\boldsymbol{\sigma}_k,\boldsymbol{\eta}_k)\mathcal{L}(\boldsymbol{\sigma}_n,\boldsymbol{\eta}_n,\boldsymbol{\sigma}_p,\boldsymbol{\eta}_p)\rho_{\boldsymbol{\vartheta}}(\boldsymbol{\sigma}_p,\boldsymbol{\eta}_p). \end{aligned} \tag{5.35}$$

In order to apply the standard stochastic gradient descent procedure for the optimization of the artificial neural network, we require the gradient of the cost function $\nabla_{\boldsymbol{\vartheta}} C(\boldsymbol{\vartheta})$ with respect to all parameters $\boldsymbol{\vartheta}$ (see Sec. 5.1). The cost function gradient is formally calculated

using the product rule, yielding [57]

$$\begin{aligned}
&\nabla_{\vartheta_l} C(\boldsymbol{\vartheta}) \\
&= 2\mathrm{Re}\Bigg\{ \sum_{n=1}^{N_s} \tilde{p}_{\boldsymbol{\vartheta}}(\boldsymbol{\sigma}_n,\boldsymbol{\eta}_n)\tilde{\mathcal{L}}^{\dagger}(\boldsymbol{\sigma}_n,\boldsymbol{\eta}_n) \sum_{m=1}^{N_s} \mathcal{L}(\boldsymbol{\sigma}_n,\boldsymbol{\eta}_n,\boldsymbol{\sigma}_m,\boldsymbol{\eta}_m) \frac{\boldsymbol{\rho}_{\boldsymbol{\vartheta}}(\boldsymbol{\sigma}_m,\boldsymbol{\eta}_m)}{\boldsymbol{\rho}_{\boldsymbol{\vartheta}}(\boldsymbol{\sigma}_n,\boldsymbol{\eta}_n)} O_{\vartheta_l}(\boldsymbol{\sigma}_m,\boldsymbol{\eta}_m) \\
&- \left[\sum_{n=1}^{N_s} \tilde{p}_{\boldsymbol{\vartheta}}(\boldsymbol{\sigma}_n,\boldsymbol{\eta}_n) O_{\vartheta_l}(\boldsymbol{\sigma}_n,\boldsymbol{\eta}_n)\right]\left[\sum_{n=1}^{N_s} \tilde{p}_{\boldsymbol{\vartheta}}(\boldsymbol{\sigma}_n,\boldsymbol{\eta}_n)\tilde{\mathcal{L}}^{\dagger}(\boldsymbol{\sigma}_n,\boldsymbol{\eta}_n)\tilde{\mathcal{L}}(\boldsymbol{\sigma}_n,\boldsymbol{\eta}_n)\right]\Bigg\},
\end{aligned} \tag{5.36}$$

where we introduced logarithmic derivatives in the form of diagonal matrices $\boldsymbol{O}_{\vartheta_l}$ with elements

$$[\boldsymbol{O}_{\vartheta_l}]_{\boldsymbol{\sigma\eta},\boldsymbol{\sigma\eta}} = O_{\vartheta_l}(\boldsymbol{\sigma},\boldsymbol{\eta}) = \frac{\partial \ln \rho_{\boldsymbol{\vartheta}}(\boldsymbol{\sigma},\boldsymbol{\eta})}{\partial \vartheta_l}, \tag{5.37}$$

corresponding to the gradients of the neural density operator with respect to all variational parameters $\vartheta_l$ and for a specific sample configuration $(\boldsymbol{\sigma},\boldsymbol{\eta})$. The network is trained via the standard stochastic gradient descent formula, updating the variational parameters during each iteration $t \to t+1$ via

$$\vartheta_l^{(t+1)} = \vartheta_l^{(t)} - \nu \nabla_{\vartheta_l} C(\boldsymbol{\vartheta}^{(t)}), \tag{5.38}$$

at learning rate $\nu$.

### 5.6.2 Time evolution dynamics

As a second application, we demonstrate the ability of artificial neural networks to model Markovian dynamics of open spin-1/2 systems. For the full time evolution dynamics prescribed by Eq. (5.23), we first calculate the formal time derivative of the neural density operator,

$$\partial_t \boldsymbol{\rho}_{\boldsymbol{\vartheta}} = \sum_{l=1}^{n_p} \frac{\partial \boldsymbol{\rho}_{\boldsymbol{\vartheta}}}{\partial \vartheta_l} \dot{\vartheta}_l = \sum_{l=1}^{n_p} \dot{\vartheta}_l \boldsymbol{O}_{\vartheta_l} \boldsymbol{\rho}_{\boldsymbol{\vartheta}}. \tag{5.39}$$

Note that both the density matrix $\boldsymbol{\rho}$ and the neural density operator $\boldsymbol{\rho}_{\boldsymbol{\vartheta}}$ are unknown, representing the target and model distribution, respectively. Again, the only information available are the neural density operator elements $\boldsymbol{\rho}_{\boldsymbol{\vartheta}}(\boldsymbol{\sigma}_n,\boldsymbol{\eta}_n)$ for individual sample configurations $(\boldsymbol{\sigma}_n,\boldsymbol{\eta}_n)$ and the current parameter set $\boldsymbol{\vartheta}$. To find an approximation of the Lindblad dynamics, we require a closed set of equations of motion for the time-dependent variational parameters $\vartheta_l(t)$. They are optimized by minimizing the difference between the approximate variational evolution of the neural density operator [Eq. (5.39)] and the equation of motion for the density matrix as prescribed by Eq. (5.23). Taking the square norm difference between these two expressions defines the cost function [58, 59],

$$\begin{aligned}
C(\boldsymbol{\vartheta}) &= \left\| \sum_l \dot{\vartheta}_l \boldsymbol{O}_{\vartheta_l} \boldsymbol{\rho}_{\boldsymbol{\vartheta}} - \boldsymbol{\mathcal{L}}\boldsymbol{\rho} \right\|_2^2 \\
&= \left( \sum_l \dot{\vartheta}_l \boldsymbol{\rho}_{\boldsymbol{\vartheta}}^{\dagger} \boldsymbol{O}_{\vartheta_l}^{\dagger} - \boldsymbol{\rho}^{\dagger}\boldsymbol{\mathcal{L}}^{\dagger} \right) \left( \sum_l \dot{\vartheta}_l \boldsymbol{O}_{\vartheta_l} \boldsymbol{\rho}_{\boldsymbol{\vartheta}} - \boldsymbol{\mathcal{L}}\boldsymbol{\rho} \right).
\end{aligned} \tag{5.40}$$

Here we minimize Eq. (5.40) with respect to the time derivative of a specific coefficient $\dot{\vartheta}_{l'}$ by solving $\partial C(\boldsymbol{\vartheta})/\partial\dot{\vartheta}_{l'} = 0$, yielding

$$\left(\sum_l \dot{\vartheta}_l \boldsymbol{\rho}_{\boldsymbol{\vartheta}}^\dagger \boldsymbol{O}_{\vartheta_l}^\dagger - \boldsymbol{\rho}^\dagger \boldsymbol{\mathcal{L}}^\dagger\right) \boldsymbol{O}_{\vartheta_{l'}} \boldsymbol{\rho}_{\boldsymbol{\vartheta}} + \boldsymbol{\rho}_{\boldsymbol{\vartheta}}^\dagger \boldsymbol{O}_{\vartheta_{l'}}^\dagger \left(\sum_l \dot{\vartheta}_l \boldsymbol{O}_{\vartheta_l} \boldsymbol{\rho}_{\boldsymbol{\vartheta}} - \boldsymbol{\mathcal{L}}\boldsymbol{\rho}\right) = 0. \tag{5.41}$$

Eq. (5.41) is rearranged as a system of linear equations [117–119]

$$\sum_l S_{l'l} \dot{\vartheta}_l = f_{l'}, \tag{5.42}$$

where we introduced the covariance matrix $\boldsymbol{S}$ with elements

$$S_{l'l} = \boldsymbol{\rho}_{\boldsymbol{\vartheta}}^\dagger \boldsymbol{O}_{\vartheta_{l'}}^\dagger \boldsymbol{O}_{\vartheta_l} \boldsymbol{\rho}_{\boldsymbol{\vartheta}} + \boldsymbol{\rho}_{\boldsymbol{\vartheta}}^\dagger \boldsymbol{O}_{\vartheta_l}^\dagger \boldsymbol{O}_{\vartheta_{l'}} \boldsymbol{\rho}_{\boldsymbol{\vartheta}}, \tag{5.43}$$

and the vector of forces $\boldsymbol{f}$ with entries

$$f_l = \boldsymbol{\rho}_{\boldsymbol{\vartheta}}^\dagger \boldsymbol{O}_{\vartheta_l}^\dagger \boldsymbol{\mathcal{L}}\boldsymbol{\rho} + \boldsymbol{\rho}^\dagger \boldsymbol{\mathcal{L}}^\dagger \boldsymbol{O}_{\vartheta_l} \boldsymbol{\rho}_{\boldsymbol{\vartheta}}. \tag{5.44}$$

In correspondence to the stationary case, we evaluate these quantities using the stochastic reconfiguration approach, yielding statistical expectation values as approximate expressions for the covariance matrix and vector of forces [57, 119],

$$\begin{aligned} S_{l'l} \approx 2\mathrm{Re}\Bigg\{ &\sum_{n=1}^{N_s} \tilde{p}_{\boldsymbol{\vartheta}}(\boldsymbol{\sigma}_n, \boldsymbol{\eta}_n) O_{\vartheta_{l'}}^\dagger(\boldsymbol{\sigma}_n, \boldsymbol{\eta}_n) O_{\vartheta_l}(\boldsymbol{\sigma}_n, \boldsymbol{\eta}_n) \\ &- \left[\sum_{n=1}^{N_s} \tilde{p}_{\boldsymbol{\vartheta}}(\boldsymbol{\sigma}_n, \boldsymbol{\eta}_n) O_{\vartheta_l}^\dagger(\boldsymbol{\sigma}_n, \boldsymbol{\eta}_n)\right] \left[\sum_{n=1}^{N_s} \tilde{p}_{\boldsymbol{\vartheta}}(\boldsymbol{\sigma}_n, \boldsymbol{\eta}_n) O_{\vartheta_l}(\boldsymbol{\sigma}_n, \boldsymbol{\eta}_n)\right] \Bigg\}, \end{aligned} \tag{5.45}$$

and

$$\begin{aligned} f_l \approx 2\mathrm{Re}\Bigg\{ &\sum_{n=1}^{N_s} \tilde{p}_{\boldsymbol{\vartheta}}(\boldsymbol{\sigma}_n, \boldsymbol{\eta}_n) O_{\vartheta_l}^\dagger(\boldsymbol{\sigma}_n, \boldsymbol{\eta}_n) \tilde{\mathcal{L}}(\boldsymbol{\sigma}_n, \boldsymbol{\eta}_n) \\ &- \left[\sum_{n=1}^{N_s} \tilde{p}_{\boldsymbol{\vartheta}}(\boldsymbol{\sigma}_n, \boldsymbol{\eta}_n) O_{\vartheta_l}^\dagger(\boldsymbol{\sigma}_n, \boldsymbol{\eta}_n)\right] \left[\sum_{n=1}^{N_s} \tilde{p}_{\boldsymbol{\vartheta}}(\boldsymbol{\sigma}_n, \boldsymbol{\eta}_n) \tilde{\mathcal{L}}(\boldsymbol{\sigma}_n, \boldsymbol{\eta}_n)\right] \Bigg\}. \end{aligned} \tag{5.46}$$

Inverting the covariance matrix in Eq. (5.42) finally results in the equation of motion for the variational parameters,

$$\partial_t \vartheta_{l'} = \sum_l S_{l'l}^{-1} f_l. \tag{5.47}$$

Finally, when assuming discrete time steps, $\partial_t \vartheta_{l'} \approx \Delta\vartheta_{l'}/\Delta t$, the learning parameters are updated during each time step via

$$\vartheta_{l'}^{(t+1)} = \vartheta_{l'}^{(t)} + \Delta t \sum_l S_{l'l}^{-1} f_l, \tag{5.48}$$

with a step size or learning rate $\Delta t = \nu$ and in resemblance to the update procedure prescribed by the stochastic gradient descent method [see Eq. (5.4)]. Fig. 5.3 schematically

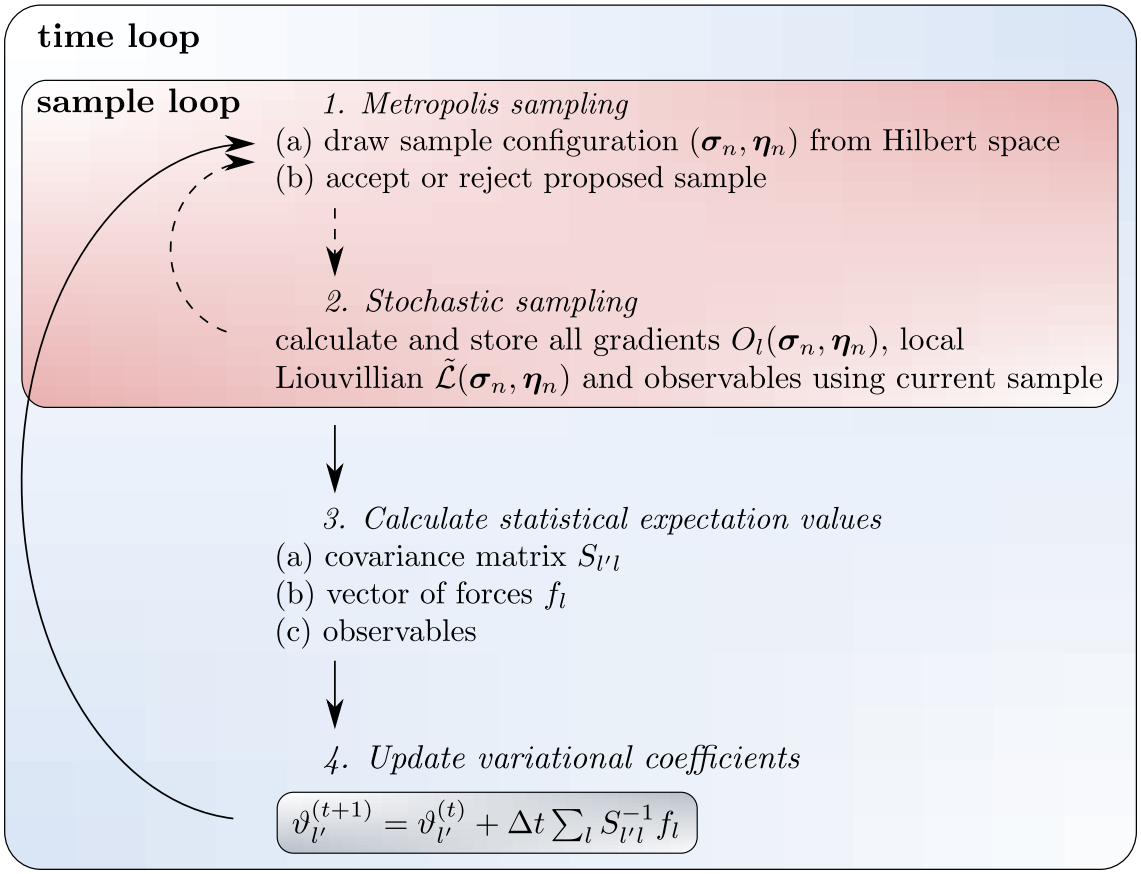


*Figure 5.3:* Flow diagram schematically depicting the network training algorithm for the calculation of time evolution dynamics.

shows a flow diagram of all steps taken during the time evolution of the artificial neural network. Lastly, we note that it is in principle possible to find the stationary state of a system using Eq. (5.47) and setting $S_{l'l} \equiv \mathbb{1}$, such that $\partial_t \vartheta_{l'} = f_{l'}$. However, in this description information is lost during the initial steps of the derivation, namely the adjunct Liouvillian operator, resulting in decreased stability of the optimization procedure for the steady state [57, 59].

## 5.7 Numerical execution

We conclude this Chapter by providing details on the numerical implementation. The interplay of all introduced algorithms and their specific execution is explained. Moreover, we provide some additional techniques to increase numerical stability and performance.

### 5.7.1 Observables

As a last step for the calculation of open quantum systems, we require a strategy for the evaluation of observables. In the density matrix formalism, the expectation value of arbitrary observables $\boldsymbol{X}$ is provided by

$$\langle \boldsymbol{X} \rangle = \mathrm{tr}\{\boldsymbol{X}\boldsymbol{\rho}\}. \tag{5.49}$$

Again following the stochastic reconfiguration approach, $\langle \boldsymbol{X} \rangle$ is interpreted as a statistical expectation value over a probability distribution (see Sec. 5.6). For diagonal observables we can additionally define the probability distribution

$$q_{\boldsymbol{\vartheta}}(\boldsymbol{\sigma}) = \rho_{\boldsymbol{\vartheta}}(\boldsymbol{\sigma}, \boldsymbol{\sigma}), \tag{5.50}$$

which again must be normalized by approximating the partition function over all drawn samples. The occurrence probability of sample $(\boldsymbol{\sigma}_n)$ is thus given by

$$\tilde{q}_{\boldsymbol{\vartheta}}(\boldsymbol{\sigma}_n) = \frac{1}{Z_{q_{\boldsymbol{\vartheta}}}} q_{\boldsymbol{\vartheta}}(\boldsymbol{\sigma}_n), \tag{5.51}$$

with

$$Z_{q_{\boldsymbol{\vartheta}}} = \sum_{n=1}^{N_s} q_{\boldsymbol{\vartheta}}(\boldsymbol{\sigma}_n). \tag{5.52}$$

Now the expectation value obtained from the density matrix can be approximated as a statistical expectation value over all sample configurations, $\langle \boldsymbol{X} \rangle \approx \langle \boldsymbol{X} \rangle_q$, with

$$\langle \boldsymbol{X} \rangle_q = \sum_{n=1}^{N_s} \tilde{q}_{\boldsymbol{\vartheta}}(\boldsymbol{\sigma}_n) \sum_{\boldsymbol{\xi}} \frac{X(\boldsymbol{\sigma}_n, \boldsymbol{\xi}) \rho_{\boldsymbol{\vartheta}}(\boldsymbol{\xi}, \boldsymbol{\sigma}_n)}{\rho_{\boldsymbol{\vartheta}}(\boldsymbol{\sigma}_n, \boldsymbol{\sigma}_n)}. \tag{5.53}$$

### 5.7.2 Sampling

As a first step of the implementation, the Metropolis algorithm is used to draw sample configurations $(\boldsymbol{\sigma}_n, \boldsymbol{\eta}_n)$ from configuration space of the target distribution. Specifically, neural density operator elements $\rho_{\boldsymbol{\vartheta}}(\boldsymbol{\sigma}_n, \boldsymbol{\eta}_n)$ are generated to estimate the target distribution $\rho$ by the model distribution $\rho_{\boldsymbol{\vartheta}}$ via occurrence probabilites $p_{\boldsymbol{\vartheta}}(\boldsymbol{\sigma}, \boldsymbol{\eta})$. For the calculation of diagonal system observables, diagonal sample configurations $(\boldsymbol{\sigma}_n, \boldsymbol{\sigma}_n)$ are simultaneously drawn to generate occurrence probabilities $q_{\boldsymbol{\vartheta}}(\boldsymbol{\sigma})$. During each step of the sampling procedure, the new proposed sample is compared to the last sample configuration. Depending on their probability ratio, the proposed sample is either accepted or rejected following a Markov chain Monte Carlo approach (see Sec. 5.5). The acceptance function can, e.g., take the form of an exponential function [57],

$$A_{exp}[(\boldsymbol{\sigma}_{n+1}, \boldsymbol{\eta}_{n+1}); (\boldsymbol{\sigma}_n, \boldsymbol{\eta}_n)] = \exp\left[ -\frac{p_{\boldsymbol{\vartheta}}(\boldsymbol{\sigma}_n, \boldsymbol{\eta}_n)}{p_{\boldsymbol{\vartheta}}(\boldsymbol{\sigma}_{n+1}, \boldsymbol{\eta}_{n+1})} \right], \tag{5.54}$$

or is modeled by a linear ratio [58],

$$A_{lin}[(\boldsymbol{\sigma}_{n+1}, \boldsymbol{\eta}_{n+1}); (\boldsymbol{\sigma}_n, \boldsymbol{\eta}_n)] = \min\left[1, \frac{p_{\boldsymbol{\vartheta}}(\boldsymbol{\sigma}_{n+1}, \boldsymbol{\eta}_{n+1})}{p_{\boldsymbol{\vartheta}}(\boldsymbol{\sigma}_n, \boldsymbol{\eta}_n)}\right]. \tag{5.55}$$

For the easiest realization, the proposed samples $p_{\boldsymbol{\vartheta}}(\boldsymbol{\sigma}_{n+1}, \boldsymbol{\eta}_{n+1})$ are chosen randomly from full configuration space. For an improved mapping, it is also possible to employ a set of selection rules taking the role of to the proposal distribution function $g(x'|x_t)$ in Eq. (5.20) [58]. Here we provide an example of such a selection rule set for a spin-1/2 quantum system of $N$ sites. When sampling from Hilbert space to approximate the distribution $p_{\boldsymbol{\vartheta}}(\boldsymbol{\sigma}, \boldsymbol{\eta})$, four types of moves are allowed to form a new proposed sample based on the current sample $(\boldsymbol{\sigma}_n, \boldsymbol{\eta}_n) = (\sigma_{1,n}, \ldots, \sigma_{i,n}, \ldots, \sigma_{N,n}; \eta_{1,n}, \ldots, \eta_{i,n}, \ldots, \eta_{N,n})$ with $\sigma_{i,n} = \pm 1$, $\eta_{i,n} = \pm 1$:

1. a single index of a random site $i$ is flipped, either $\sigma_{i,n}$ or $\eta_{i,n}$.

2. both indices $\sigma_{i,n}$ and $\eta_{i,n}$ of a random site $i$ are flipped.

3. two neighboring indices of a random site $i$ are flipped, either $\sigma_{i,n}$ and $\sigma_{i+1,n}$ or $\eta_{i,n}$ and $\eta_{i+1,n}$.

4. a random new configuration $(\boldsymbol{\sigma}_{\tilde{n}}, \boldsymbol{\eta}_{\tilde{n}})$ is drawn from a uniform distribution.

While the last move only occurs at a probability of 1%, the remaining moves are set equally probable. For the diagonal sampling procedure to generate the distribution $q_{\vartheta}(\boldsymbol{\sigma})$, three possible moves are allowed given a current sample $(\boldsymbol{\sigma}_n)$:

1. the index $\sigma_{i,n}$ of a random site $i$ is flipped.

2. two neighboring indices $\sigma_{i,n}$ and $\sigma_{i+1,n}$ of a random site $i$ are flipped.

3. a random new configuration $(\boldsymbol{\sigma}_{\tilde{n}})$ is drawn from a uniform distribution.

Again, while the first two moves have the same probability of occurring, a completely new configuration is only drawn at a probability of 1%.

### 5.7.3 Logarithmic derivatives

Once a drawn sample is either accepted or rejected as new current sample $(\boldsymbol{\sigma}_n, \boldsymbol{\eta}_n)$, we have to calculate all corresponding neural density operator gradients $\boldsymbol{O}_{\vartheta_l}(\boldsymbol{\sigma}_n, \boldsymbol{\eta}_n)$ [Eq. (5.37)]. The logarithmic derivatives of the neural density operator with respect to all variational

parameters $\boldsymbol{\vartheta} = (\boldsymbol{a}, \boldsymbol{b}, \boldsymbol{c}, \boldsymbol{W}, \boldsymbol{U})$ are given by

$$\frac{\partial \ln[\rho_{\boldsymbol{\vartheta}}(\boldsymbol{\sigma}_n, \boldsymbol{\eta}_n)]}{\partial \mathrm{Re}\{a_i\}} = \sigma_{i,n} + \eta_{i,n}, \tag{5.56a}$$

$$\frac{\partial \ln[\rho_{\boldsymbol{\vartheta}}(\boldsymbol{\sigma}_n, \boldsymbol{\eta}_n)]}{\partial \mathrm{Im}\{a_i\}} = i\,(\sigma_{i,n} - \eta_{i,n})\,, \tag{5.56b}$$

$$\frac{\partial \ln[\rho_{\boldsymbol{\vartheta}}(\boldsymbol{\sigma}_n, \boldsymbol{\eta}_n)]}{\partial \mathrm{Re}\{b_m\}} = \xi_1(m, \boldsymbol{\sigma}_n) + \xi_1^*(m, \boldsymbol{\eta}_n), \tag{5.56c}$$

$$\frac{\partial \ln[\rho_{\boldsymbol{\vartheta}}(\boldsymbol{\sigma}_n, \boldsymbol{\eta}_n)]}{\partial \mathrm{Im}\{b_m\}} = i\,[\xi_1(m, \boldsymbol{\sigma}_n) - \xi_1^*(m, \boldsymbol{\eta}_n)]\,, \tag{5.56d}$$

$$\frac{\partial \ln[\rho_{\boldsymbol{\vartheta}}(\boldsymbol{\sigma}_n, \boldsymbol{\eta}_n)]}{\partial \mathrm{Re}\{W_{mi}\}} = \sigma_{i,n}\xi_1(m, \boldsymbol{\sigma}_n) + \eta_{i,n}\xi_1^*(m, \boldsymbol{\eta}_n), \tag{5.56e}$$

$$\frac{\partial \ln[\rho_{\boldsymbol{\vartheta}}(\boldsymbol{\sigma}_n, \boldsymbol{\eta}_n)]}{\partial \mathrm{Im}\{W_{mi}\}} = i\,[\sigma_{i,n}\xi_1(m, \boldsymbol{\sigma}_n) - \eta_{i,n}\xi_1^*(m, \boldsymbol{\eta}_n)]\,, \tag{5.56f}$$

$$\frac{\partial \ln[\rho_{\boldsymbol{\vartheta}}(\boldsymbol{\sigma}_n, \boldsymbol{\eta}_n)]}{\partial \mathrm{Re}\{c_k\}} = 2\xi_2(k, \boldsymbol{\sigma}_n, \boldsymbol{\eta}_n), \tag{5.56g}$$

$$\frac{\partial \ln[\rho_{\boldsymbol{\vartheta}}(\boldsymbol{\sigma}_n, \boldsymbol{\eta}_n)]}{\partial \mathrm{Re}\{U_{ki}\}} = (\sigma_{i,n} + \eta_{i,n})\,\xi_2(k, \boldsymbol{\sigma}_n, \boldsymbol{\eta}_n), \tag{5.56h}$$

$$\frac{\partial \ln[\rho_{\boldsymbol{\vartheta}}(\boldsymbol{\sigma}_n, \boldsymbol{\eta}_n)]}{\partial \mathrm{Im}\{U_{ki}\}} = i\,(\sigma_{i,n} - \eta_{i,n})\,\xi_2(k, \boldsymbol{\sigma}_n, \boldsymbol{\eta}_n), \tag{5.56i}$$

with

$$\xi_1(m, \boldsymbol{\pi}_n) = \tanh\left[b_m + \sum_{i=1}^{N} W_{mi}\pi_{i,n}\right], \tag{5.57a}$$

$$\xi_2(k, \boldsymbol{\sigma}_n, \boldsymbol{\eta}_n) = \tanh\left[c_k + c_k^* + \sum_{i=1}^{N} (U_{ki}\sigma_{i,n} + U_{ki}^*\eta_{i,n})\right]. \tag{5.57b}$$

This procedure is repeated for $N_s$ individual samples $(\boldsymbol{\sigma}_n, \boldsymbol{\eta}_n)$. Once all gradients are calculated and stored, the covariance matrix [Eq. (5.45)] can be calculated for the time evolution dynamics case. It is noted that the variational coefficients must be initialized at small nonzero values, e.g., $\vartheta_l \in [-0.01, 0.01]\backslash\{0\}$. When initialized at zero, the evaluation of Eq. (5.56) becomes trivial and the respective parameters remain zero throughout the entire training procedure. In addition, choosing large values for the initial variational coefficients may result in numerical divergence.

### 5.7.4 Local Liouvillian

Aside from the logarithmic derivatives, the local estimator of the Liouvillian $\tilde{\mathcal{L}}(\boldsymbol{\sigma}_n, \boldsymbol{\eta}_n)$ [Eq. (5.30)] must be calculated individually for each sample. For a given Hamiltonian $H$, the first term of the local Liouvillian reads [58]

$$-\frac{i}{\hbar}\frac{\langle \boldsymbol{\sigma}_n | \,[H, \rho]\, | \boldsymbol{\eta}_n \rangle}{\rho_{\boldsymbol{\vartheta}}(\boldsymbol{\sigma}_n, \boldsymbol{\eta}_n)} = -\frac{i}{\hbar}\sum_{\boldsymbol{\xi}}\left[H(\boldsymbol{\sigma}_n, \boldsymbol{\xi})\frac{\rho_{\boldsymbol{\vartheta}}(\boldsymbol{\xi}, \boldsymbol{\eta}_n)}{\rho_{\boldsymbol{\vartheta}}(\boldsymbol{\sigma}_n, \boldsymbol{\eta}_n)} - \frac{\rho_{\boldsymbol{\vartheta}}(\boldsymbol{\sigma}_n, \boldsymbol{\xi})}{\rho_{\boldsymbol{\vartheta}}(\boldsymbol{\sigma}_n, \boldsymbol{\eta}_n)}H(\boldsymbol{\xi}, \boldsymbol{\eta}_n)\right], \tag{5.58}$$

with

$$H(\boldsymbol{\sigma}, \boldsymbol{\eta}) = \langle \boldsymbol{\sigma} | \, H \, | \boldsymbol{\eta} \rangle \, . \tag{5.59}$$

The second term of $\tilde{\mathcal{L}}(\boldsymbol{\sigma}_n, \boldsymbol{\eta}_n)$ arises from the dissipator

$$\mathcal{D}[\sqrt{\gamma/2}J]\rho = \frac{\gamma}{2} \sum_{i=1}^{N} \left( 2J_i \rho J_i^\dagger - J_i^\dagger J_i \rho - \rho J_i^\dagger J_i \right), \tag{5.60}$$

resulting in

$$\begin{aligned} \frac{\langle \boldsymbol{\sigma}_n | \, \mathcal{D}[\sqrt{\gamma/2}J]\rho \, | \boldsymbol{\eta}_n \rangle}{\rho_{\boldsymbol{\vartheta}}(\boldsymbol{\sigma}_n, \boldsymbol{\eta}_n)} = \frac{\gamma}{2} \sum_{i=1}^{N} \Bigg[ & 2 \sum_{\boldsymbol{\sigma}', \boldsymbol{\eta}'} \langle \boldsymbol{\sigma}_n | \, J_i \, | \boldsymbol{\sigma}' \rangle \langle \boldsymbol{\eta}' | \, J_i^\dagger \, | \boldsymbol{\eta}_n \rangle \frac{\rho_{\boldsymbol{\vartheta}}(\boldsymbol{\sigma}', \boldsymbol{\eta}')}{\rho_{\boldsymbol{\vartheta}}(\boldsymbol{\sigma}_n, \boldsymbol{\eta}_n)} \\ & - \sum_{\boldsymbol{\xi}} \langle \boldsymbol{\sigma}_n | \, J_i^\dagger J_i \, | \boldsymbol{\xi} \rangle \frac{\rho_{\boldsymbol{\vartheta}}(\boldsymbol{\xi}, \boldsymbol{\eta}_n)}{\rho_{\boldsymbol{\vartheta}}(\boldsymbol{\sigma}_n, \boldsymbol{\eta}_n)} - \sum_{\boldsymbol{\xi}} \frac{\rho_{\boldsymbol{\vartheta}}(\boldsymbol{\sigma}_n, \boldsymbol{\xi})}{\rho_{\boldsymbol{\vartheta}}(\boldsymbol{\sigma}_n, \boldsymbol{\eta}_n)} \langle \boldsymbol{\xi} | \, J_i^\dagger J_i \, | \boldsymbol{\eta}_n \rangle \Bigg]. \end{aligned} \tag{5.61}$$

### 5.7.5 Pre-conditioning

The current training iteration is completed by updating the variational parameters $\boldsymbol{\vartheta}$. In the time evolution dynamics case, their time derivatives are evaluated as prescribed by Eq. (5.47), requiring the inversion of the positive semi-definite covariance matrix $\boldsymbol{S}^{-1}$. This poses a numerical challenge since $\boldsymbol{S}$ may be ill conditioned, e.g., featuring very small eigenvalues, with the inversion resulting in dramatically increased statistical noise [118]. Hence to ensure invertibility and improve the accuracy of the calculation, the covariance matrix is modified first.

To avoid the issue of large statistical noise, the diagonal elements of $\boldsymbol{S}$ are regularized according to [47, 118, 119]

$$\tilde{S}_{l'l} = S_{l'l} + \lambda(t) \delta_{ll'} S_{l'l}, \tag{5.62}$$

with a regularizer function

$$\lambda(t) = \max \left( \lambda_0 b^t, \lambda_{min} \right), \tag{5.63}$$

which decays at increasing time steps $t$ and features parameters $b$, $\lambda_0$ and $\lambda_{min}$. Moreover, the covariance matrix may feature eigenvalues that differ in several orders of magnitude. To stabilize the inversion, it is helpful to pre-condition $\boldsymbol{S}$ by means of a rescaling [119],

$$S_{l'l}^{pc} = \frac{1}{\sqrt{S_{l'l'} S_{ll}}} S_{l'l}. \tag{5.64}$$

The vector of forces and the time derivatives of the learning parameters are rescaled accordingly,

$$f_l^{pc} = \frac{1}{\sqrt{S_{ll}}} f_l, \tag{5.65a}$$

$$\dot{\vartheta}_{l'}^{pc} = \sqrt{S_{l'l'}} \dot{\vartheta}_{l'}. \tag{5.65b}$$

$\boldsymbol{S}$, $\boldsymbol{f}$ and $\dot{\boldsymbol{\vartheta}}$ are pre-conditioned first. Afterwards, the covariance matrix is regularized. After solving the set of linear equations of motion, the resulting variational parameter derivatives are rescaled back again via

$$\dot{\vartheta}_{l'} = \frac{1}{\sqrt{S_{l'l'}}} \dot{\vartheta}^{pc}_{l'}. \tag{5.66}$$

Finally, the parameters are updated for the next step of the time evolution using Eq. (5.48), concluding the current training iteration of the artificial neural network.

# Part II

# Non-Markovian phenomena in open quantum systems

# 6 Memory-critical dynamical buildup of phonon-dressed Majorana fermions

In this Chapter, we explore the dynamical impact of non-Markovian dissipative interactions on topological state of matter, giving rise to a quantum memory. Specifically, the open system dynamics of a one-dimensional polaronic topological superconductor with phonon-dressed $p$-wave pairing is investigated, where the dynamics is induced by a fast temperature increase. For rising memory depths, the topological properties are shown to transit from monotonic relaxation to a plateau of substantial value into a collapse-and-buildup behavior, even when the system is close to the topological phase boundary. Above a critical memory depth, the system can approach a dressed state in dynamical equilibrium with phonons with close to perfect buildup of topological correlation. The Chapter is closely based on the publication "Memory-critical dynamical buildup of phonon-dressed Majorana fermions" by O. Kästle et al. [69]

## 6.1 Introduction

Exploring topological properties of nonequilibrium open quantum systems represents a major objective for the realization, probing and utilization of topological states of matter [120–134]. Recent investigations of topological systems interacting with an environment have focused on Markovian reservoir couplings described by a Lindblad master equation for the reduced system density matrix, resulting in open-dissipative time evolution dynamics [135–148]. However, experimental solid-state realizations of topological systems are often based on semiconductor nanostructures, which inevitably interact with a structured phonon environment, resulting from the deformation of host materials and lattice vibrations. The most prominent examples of topological solid-state setups are based on topological superconductors [149–159]. Due to the arising dynamical interplay with the structured phonon reservoir, the Markovian approach based on the Lindblad formalism often fails to correctly describe these scenarios: Dissipation-induced decoherence to the structured environment enables quantum memory effects via time-delayed information backflow to the system [2, 3], resulting in a time scaling of the system dynamics which is absent in a Markovian context. In consequence, a unique dynamical interplay between topological properties and non-Markovian dissipation may arise.

In this Chapter, we demonstrate that quantum memory effects resulting from a non-Markovian parity-preserving interaction of a topological $p$-wave supercondutor surrounded by a phonon environment can result in a recovery and long-term stabilization of topological properties not exhibited in a corresponding Markovian setup [69]. We employ the

polaron master equation (see Ch. 3) for the description of open-dissipative dynamics of a *polaronic* topological superconductor with phonon-renormalized Hamiltonian parameters. Specifically, we investigate a Kitaev superconducting wire - the paradigmatic example of a setup supporting Majorana fermions - weakly coupled to a 3D bulk phonon reservoir [160]. A perfect realization of the Kitaev wire features a gapped energy spectrum, causing the emergence of Majorana zero modes. They are robust against external perturbations and exhibit permanent and topologically protected edge-edge correlations. In the presence of a phonon reservoir with energies surpassing the spectral gap, dephasing processes arise. In this scenario, the otherwise topologically protected Majorana edge correlations typically decay if the phonon reservoir is treated in a Markovian description, even if parity is preserved [144]. Here, we show that this is not the case if the microscopic properties of the electron-phonon interactions are taken fully into account, as they give rise to a non-Markovian and partially time-reversible dynamics [69]. In contrast to Markovian decoherence destroying topological properties in the long term limit, we show that a finite quantum memory enables substantial preservation of topological properties far from equilibrium, even when the polaron Hamiltonian approaches the topological phase boundary. Depending on the memory depth, i.e., the characteristic time scale of the quantum memory, the dynamical Majorana edge correlation can perform a collapse-and-buildup relaxation. Strikingly, above a critical value of the memory depth, the edge correlation can be recovered almost completely, corresponding to a *polaronic state* of the topological superconductor in a phonon-mediated dynamical equilibrium [69].

The polaronic Kitaev chain and its theoretical background are introduced in Sec. 6.2. First, the bare Kitaev chain and the considered fermion-phonon interaction are discussed, before the open system Hamiltonian is transformed into the polaronic frame. Afterwards, we introduce the non-Markovian polaron master equation for the dissipative Kitaev wire and discuss the impact of time-resolved phonon correlations on the open system dynamics. In Sec. 6.3, the unfolding non-Markovian Majorana edge correlation dynamics are presented and compared to calculations using a Markovian Lindblad-type master equation with a time-independent dephasing rate. We discuss the emergence of a critical memory depth in the non-Markovian framework in Sec. 6.4, enabling a recovery and stabilization of topological properties via time-delayed system-reservoir correlations. Sec. 6.5 includes further discussions on the impact of additional $p$-wave interparticle interaction on the Majorana edge correlation, the inclusion of the polaron energy shift in the open system Hamiltonian, the nature of the observed correlation and additional calculations for an initially nonideal Kitaev chain. Lastly, we summarize our findings and discuss resulting implications and perspectives for the field in Sec. 6.6.

## 6.2 Polaronic Kitaev chain

Symmetry-protected topological states exist in a wide variety of quantum systems, such as spin chains and fermionic systems [161–168]. These non-Abelian anyonic particles are robust against microscopic imperfections, making them promising candidates for topological quantum computing [169–173]. The most prominent example of such topological states are

Majorana zero modes [174–178] emerging at the edges of the 1D Kitaev superconducting wire [160]. Several setups for the physical realization of Majorana edge states based on the Kitaev model have been proposed both in solid-state structures [179–182] and setups of ultracold atoms and molecules [136, 183–185]. Recent experiments based on these proposals strongly imply the emergence of Majorana states [151–154, 156, 186–188], with ongoing discussions regarding the role of dissipative processes [93, 94, 137, 140, 141, 143, 144, 189–196]. Current studies of dissipative Kitaev superconductors have demonstrated, e.g., that the absorption of thermal phonons at finite temperatures allows for the excitation of the electronic ground state to a delocalized state whose energy surpasses the topological energy gap, resulting in an energy level broadening [93]. Moreover, it has been shown that a finite tunneling rate of superconducting quasiparticles from the $p$-wave superconductor to the wire results in the decay of Majorana bound states [137]. Coupling the chain to an ungapped fermionic bath has the same effect, since these sorts of environmental interactions explicitly break the parity of the fermionic ground state [197]. Using classical noise as a model of dissipation, it has been demonstrated that due to motional narrowing in fast noise, dephasing processes are suppressed in the limit of fast fluctuations, enabling quantum operations on the Majorana modes [143]. Furthermore, in a Markovian phonon environment, the edge-edge correlation decays exponentially even if parity is preserved, while an incorporation of disorder can be used to increase the Majorana lifetime [144]. With respect to non-Markovian system-reservoir interactions, it has been shown that an impurity or a qubit can be employed as a non-Markovian quantum probe of a topological reservoir [198–200] and that topological phenomena induced by Markovian dissipation processes can sustain in non-Markovian regimes [201].

In contrast, in the following we demonstrate that tailoring the coupling to a super-Ohmic reservoir may suppress the decay of and even fully restore topological properties of a phonon-dressed Kitaev wire, opening up new prospects for the control of memory-dependent topological phenomena. Specifically, we investigate the fate of Majorana edge modes in the presence of a parity-preserving, structured phonon reservoir. For its description we choose the polaron master equation [1, 14, 80, 87–92] to include as much information about the electron-phonon interaction as possible, while still remaining in a reduced density matrix description in second order [14, 80, 89].

### 6.2.1 $p$-wave superconducting chain coupled to phonons

We consider the paradigmatic Kitaev $p$-wave superconductor [160], with a super-Ohmic coupling to a structured 3D phonon reservoir (see Fig. 6.1). The bare Kitaev Hamiltonian reads

$$H_k/\hbar = \sum_{l=1}^{N-1} \left[ \left( -J c_l^\dagger c_{l+1} + \Delta c_l c_{l+1} \right) + \text{H.c.} \right] - \mu \sum_{l=1}^{N} c_l^\dagger c_l, \tag{6.1}$$

describing spinless fermions $c_l$, $c_l^\dagger$ on a chain of $N$ sites $l$, with a nearest-neighbor tunneling amplitude $J \in \mathbb{R}$, superconductive pairing amplitude $\Delta \in \mathbb{R}$, and chemical potential $\mu$. For the case $|\mu| < 2J$ and $\Delta \neq 0$, the system exhibits a topological phase featuring unpaired

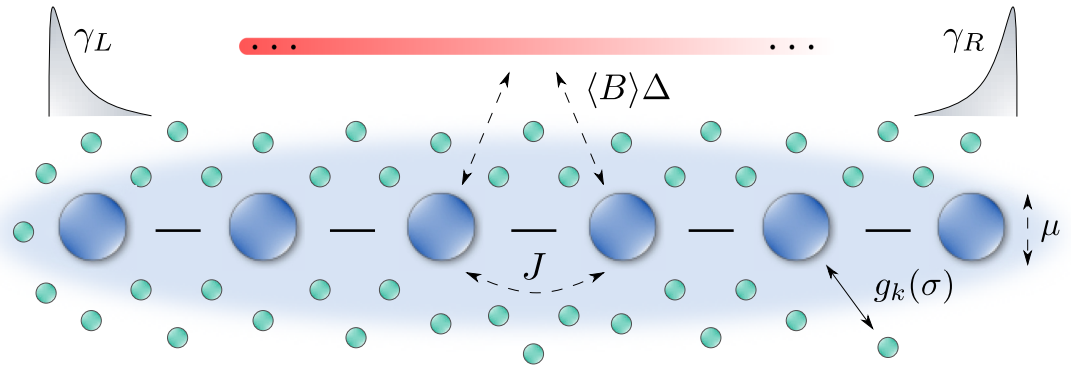


*Figure 6.1:* Sketch of a polaronic Kitaev chain featuring phonon-dressed spinless fermions (blue circles) with nearest-neighbor tunneling $J$ and coupled to a structured reservoir of bulk phonons (green circles). They are arranged in close proximity to a superconducting wire (red shape), exhibiting a renormalized $p$-wave pairing $\langle B\rangle\Delta$ at temperature $T$ [see Eq. (6.4)]. In the topological ground state of the ideal chain, two unpaired Majorana edge modes $\gamma_L$, $\gamma_R$ emerge at the boundary sites (grey shapes). The system-reservoir coupling $g_k$ features a mode-dependence with respect to the spectral width $\sigma$. In an initially nonideal scenario, a chemical potential $\mu$ acts as a perturbation on the chain.

Majorana edge modes $\gamma_{L/R} = \sum_j f_{L/R,j} b_j$ located at the boundary sites of the chain, with Majorana operators $b_{2j-1} = c_j + c_j^\dagger$, $b_{2j} = -i(c_j - c_j^\dagger)$ and $f_{L/R,j}$ denoting Majorana wave functions exponentially localized near the left ($L$) and right ($R$) edges. As an observable, we consider the nonlocal correlation $\theta = -i\langle\gamma_L\gamma_R\rangle = \pm 1$ exhibited by the Majorana modes which corresponds to the fermionic parity of the ground states.

The entire chain is coupled to a structured 3D phonon reservoir with parity-preserving interaction, described by [96–98, 202–207]

$$H_b/\hbar = \int \mathrm{d}^3k \left[\omega_{\boldsymbol{k}} r_{\boldsymbol{k}}^\dagger r_{\boldsymbol{k}} + \sum_{l=1}^{N} g_{\boldsymbol{k}} c_l^\dagger c_l (r_{\boldsymbol{k}}^\dagger + r_{\boldsymbol{k}})\right]. \tag{6.2}$$

Here, operators $r_{\boldsymbol{k}}^\dagger$, $r_{\boldsymbol{k}}$ denote bosonic creation and annihilation operators of phonons with momentum $\boldsymbol{k}$ and frequencies $\omega_k = c_s|\boldsymbol{k}|$, where $c_s$ is the sound velocity of the considered environment. This form of coupling is commonly applied to describe the formation of polarons (see Sec. 3.3) [14, 87–89, 92, 100]. Specifically, in solid-state setups it can be used to represent the coupling of semiconductor nanostructures to longitudinal acoustic phonons which typically feature a long wavelength. Without loss of generality, here we choose a generic super-Ohmic fermion-phonon coupling $g_{\boldsymbol{k}}$ with the frequency-dependence modeled by a Gaussian function,

$$g_k = f_{ph}\sqrt{\frac{|\boldsymbol{k}|}{\sigma^2}}\exp\left(-\frac{k^2}{\sigma^2}\right), \tag{6.3}$$

where $\sigma$ and $f_{ph}$ denote a spectral width and a dimensionless amplitude, respectively. In the considered scenario, the topological superconductor and reservoir are initially in

equilibrium at low temperatures, before a fast and sudden temperature increase induces the open system dynamics.

The total Hamiltonian of the dissipative Kitaev chain is denoted by $H_0 = H_k + H_b$ and can arise in condensed matter systems ranging from from atom-molecule and solid-state setups, where the reservoir is realized via a superconducting wire and the coupling amplitude $\Delta$ is induced by the proximity effect, to setups with ultracold fermionic atoms in an optical lattice, where the interaction arises via coupling to an $s$-wave superfluid with Raman lasers [190].

### 6.2.2 Dressed-state representation

Due to the exponential scaling of the Hilbert space dimension, the inclusion of a structured phonon reservoir $H_b$ renders calculations of open system dynamics very expensive, e.g., in a Heisenberg picture approach, and thus requires an approximative treatment. Here we choose a polaron representation of the coupled system (see Fig. 6.1), which can be effectively described by a second-order perturbative polaron master equation for the polaronic *dressed-state* system-reservoir Hamiltonian [1, 14, 15, 80, 87–92, 208, 209]. The phonon-renormalized Hamiltonian in dressed-state representation retains the coherent process constituted by higher-order contributions from the fermion-phonon interaction. By combining the polaronic picture with second-order perturbation theory, dynamical non-Markovian features arising in the long term limit are accounted for. In contrast, merely applying the typical second-order Born approximation of the bare reservoir Hamiltonian $H_b$ is not sufficient [96, 202–204].

As a first step, the dissipative Kitaev Hamiltonian $H_0 = H_k + H_b$ is transformed into the dressed-state representation. To this end, we define collective bosonic operators $R^\dagger = \int \mathrm{d}^3k\ (g_{\boldsymbol{k}}/\omega_{\boldsymbol{k}}) r^\dagger_{\boldsymbol{k}}$ and apply the unitary polaron transformation $H_\mathrm{p} = U_\mathrm{p} H_0 U_\mathrm{p}^{-1}$ via transformation matrices $U_\mathrm{p} = \exp[\sum_{l=1}^{N} c_l^\dagger c_l (R^\dagger - R)]$. Detailed calculations are provided in Appendix B, resulting in a phonon-dressing of fermionic operators $c_l^\dagger \to e^{-(R-R^\dagger)} c_l^\dagger$. The polaron-transformed total Hamiltonian is derived as

$$H_\mathrm{p}/\hbar = \sum_{l=1}^{N-1} \Big[ -J c_l^\dagger c_{l+1} + \Delta e^{-2(R-R^\dagger)} c_{l+1}^\dagger c_l^\dagger + \mathrm{H.c.} \Big] - \mu \sum_{l=1}^{N} c_l^\dagger c_l + \int \mathrm{d}^3k\ \omega_k r^\dagger_{\boldsymbol{k}} r_{\boldsymbol{k}}. \quad (6.4)$$

In the dressed-state representation, the considered fermion-phonon interaction constitutes a polaronic Kitaev chain featuring phonon-dressed $p$-wave pairing with phonon-induced quantum fluctuations, decreasing the tunneling capability. This representation intuitively shows that arising Majorana modes are damped as a consequence of the environmental coupling, since $p$-wave pairing is essential for the formation of the topological edge states. When considering a scenario with individual reservoirs for each chain site, the nearest-neighbor tunneling is also subject to the phonon-dressing, weakening its coupling amplitude and further decreasing the potential of Majorana emergence in the system. For the moment, we have neglected an energy renormalization term arising in the derivation

of Eq. (6.4), given by

$$H_{\text{shift}}/\hbar = \int \mathrm{d}^3k \, \frac{g_k^2}{\omega_k} \left( \sum_{l=1}^{N} c_l^\dagger c_l \right)^2 , \tag{6.5}$$

known as the polaron shift. It is regarded as standard practice to disregard this contribution if the initial state of the respective system is an equilibrium [1, 32]. Since we consider the Kitaev chain to be ideal and initially in ground state configuration, neglecting the term is justified. However, as a comparison and to ensure validity of the results in the presence of this energy renormalization, in Sec. 6.5 we reproduce all of our key findings in the presence of the polaron energy shift in a numerically exact fashion, demonstrating that its inclusion does not affect the qualitative physics.

Before continuing with the derivation of the polaron master equation, we rewrite Eq. (6.4) as $H_{\text{p}} = H_{\text{p,s}} + H_{\text{p,I}} + H_{\text{p,b}}$ with $H_{\text{p,b}}/\hbar = \int \mathrm{d}^3k \, \omega_k r_{\boldsymbol{k}}^\dagger r_{\boldsymbol{k}}$ for the free reservoir contribution. In the limiting case without coupling, $g_k \to 0$, the bare Kitaev Hamiltonian dynamics can be recovered by introducing a Franck-Condon renormalization to the dressed-state interaction Hamiltonian $H_{\text{p,I}}$, such that $\mathrm{tr}_B\{[H_{\text{p,I}}, \rho(t)]\} = 0$, with $\rho(t)$ denoting the total density operator (see Sec. 3.4). Tracing out the reservoir, the renormalized system Hamiltonian is given by

$$H_{\text{p,s}}/\hbar = \sum_{l=1}^{N-1} \left[ -J c_l^\dagger c_{l+1} + \langle B \rangle \, \Delta c_{l+1}^\dagger c_l^\dagger + \text{H.c.} \right] - \mu \sum_{l=1}^{N} c_l^\dagger c_l , \tag{6.6}$$

with a pairing renormalization factor $\langle B \rangle = \mathrm{tr}_B\{\exp[-2(R - R^\dagger)]\}$ determined explicitly below. Lastly, the renormalized system-reservoir interaction in the polaron picture reads

$$H_{\text{p,I}}/\hbar = \Delta \sum_{l=1}^{N-1} \left[ \left( e^{-2(R-R^\dagger)} - \langle B \rangle \right) c_{l+1}^\dagger c_l^\dagger + \text{H.c.} \right] . \tag{6.7}$$

The Franck-Condon renormalization is carried out in detail in Appendix B.

### 6.2.3 Polaron master equation

In the present study, we focus on the limit $\langle B \rangle \ll 1$, which allows to treat $H_{\text{p,I}}$ perturbatively in second-order Born theory, as dynamical decoupling effects cannot occur [1, 89]. In Appendix B, we present a detailed derivation of the polaron master equation for the reduced system density matrix $\rho_S(t)$ of the polaronic Kitaev chain, yielding

$$\begin{aligned} \dot{\rho}_S(t) = -i \left[ H_{\text{p,s}}/\hbar, \rho_S(t) \right] - \frac{\langle B \rangle^2}{\hbar^2} \int_0^t \mathrm{d}\tau \Big\{ & \left( \cosh\left[\phi(\tau)\right] - 1 \right) \left[ X_a, X_a(-\tau)\rho_S(t) \right] \\ & - \sinh\left[\phi(\tau)\right] \left[ X_b, X_b(-\tau)\rho_S(t) \right] + \text{H.c.} \Big\} . \end{aligned} \tag{6.8}$$

Here,

$$X_a = -J \sum_{l=1}^{N-1} \left( c_l^\dagger c_{l+1}^\dagger + c_{l+1} c_l \right) , \tag{6.9a}$$

$$X_b = J \sum_{l=1}^{N-1} \left( c_l^\dagger c_{l+1}^\dagger - c_{l+1} c_l \right) , \tag{6.9b}$$

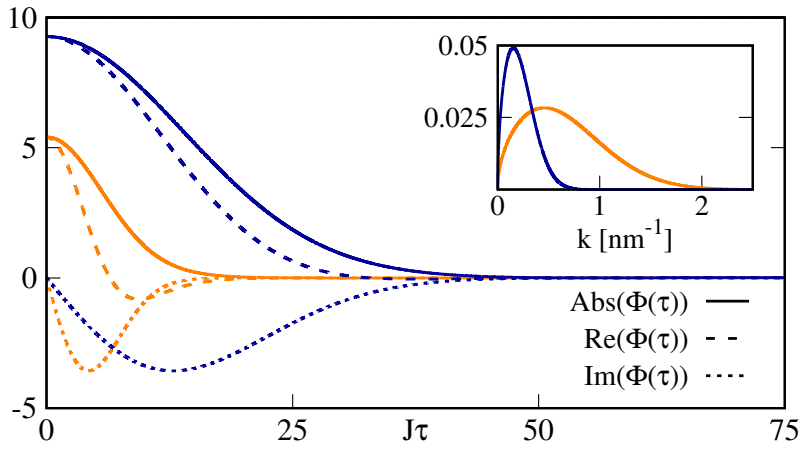


*Figure 6.2:* Phonon correlation function $\phi(\tau)$ at spectral widths $\sigma = 0.2$ (blue lines) and $\sigma = 0.6$ (orange lines) of the Gaussian coupling element $g_k$ shown in the inset.

denote collective system operators, whose dynamics obeys a *time-reversed* unitary evolution governed by the renormalized system Hamiltonian $H_{\mathrm{p,s}}$, $X_{a,b}(-\tau) \equiv e^{-iH_{\mathrm{p,s}}\tau} X_{a,b} e^{iH_{\mathrm{p,s}}\tau}$. Moreover, $\phi(\tau)$ represents the phonon correlation function

$$\phi(\tau) = \int \mathrm{d}^3k \left|\frac{2g_k}{\omega_k}\right|^2 \left[\coth\left(\frac{\hbar\omega_k}{2k_BT}\right)\cos\left(\omega_k\tau\right) - i\sin(\omega_k\tau)\right], \tag{6.10}$$

with $k_B$ denoting the Boltzmann constant. The renormalization factor $\langle B\rangle$ is determined by the initial phonon correlation, $\langle B\rangle = \exp[-\phi(0)/2]$, and features temperature dependence.

Eq. (6.8) provides the time evolution dynamics for the polaronic Kitaev chain. It features a phonon-renormalized Hamiltonian $H_{\mathrm{p,s}}$ and a memory kernel that involves both reservoir and system correlators $\phi(\tau)$ and $X_{a,b}(-\tau)$. Crucially, the correlation of a super-Ohmic phonon reservoir only has a finite lifetime $\tau_M$ (see Fig. 6.2), such that $\phi(\tau) \approx 0$ for $\tau > \tau_M$. In consequence of the finite memory depth, once the time evolution surpasses $t > \tau_M$, only system correlators $X_{a,b}(-\tau)$ within the past times $\tau \leq \tau_M$ contribute to the memory kernel in Eq. (6.8) and the integral becomes effectively time-independent for times $t > \tau_M$. Hence, the contribution of the memory effect depends on the time scale on which the system correlators $X_{a,b}(-\tau)$ evolve, yielding a substantial impact when it is comparable to $\tau_M$. It is typically determined by the inverse $E_\Delta^{-1}$ of the bulk energy gap of $H_{\mathrm{p,s}}$. For a given temperature and sound velocity $c_s$, the phonon correlation function $\phi(\tau)$ and $\tau_M$ critically depend on the spectral bandwidth $\sigma$ of the fermion-phonon coupling element $g_k$, as exemplified in Fig. 6.2. The bandwidth and mode localization of the coupling element (inset in Fig. 6.2) critically determine the depth of the memory kernel: Choosing a large spectral width $\sigma$ results in short lifetimes $\tau_M$ (orange lines in Fig. 6.2) and the integral in Eq. (6.8) quickly converges to a constant value. At the same time, the initial phonon correlation $\phi(0)$ is decreased, yielding a larger renormalization parameter $\langle B\rangle$. Vice versa, a smaller Gaussian width $\sigma$ (blue lines) leads to increasing correlation lifetimes and a decreased renormalized coupling.

As a measure of topological properties we choose the Majorana mode correlation [143]

$$\theta(t) = -i\mathrm{tr}\{\rho_S(t)\gamma_L\gamma_R\} = -\sum_{i,l=1}^{2N} f_{L,i}f_{R,l}\Gamma_{il}(t), \tag{6.11}$$

where $\Gamma_{il}(t) = i\mathrm{tr}\{\rho(t)[b_i, b_l]\}/2$ and $f_{L/R,i}$ denote the Majorana wave functions of the *initial* Kitaev Hamiltonian in the Majorana basis. Specifically, we consider an ideal Kitaev chain initially prepared in its even-parity ground state with $\Delta = J$ and $\mu = 0$, where $f_{L,i} = \delta_{i,1}$ and $f_{R,l} = \delta_{l,2N}$, such that the Majorana correlation $\theta(t)$ reduces to $\theta(t) = -\Gamma_{1,2N}(t)$ and $\theta(0) = 1$. To induce the time evolution dynamics of the polaronic Kitaev chain for times $t > 0$, we assume a fast temperature increase to $T = 4\,\mathrm{K}$, resulting in the parameter dressing $\Delta \to \Delta\langle B\rangle$ of the Hamiltonian. Here, the coupling of the chain to the environment acts as a time-reversible perturbation to the closed system. In response, system and reservoir synchronize and a new polaronic equilibrium state emerges. We solve the integro-differential equation numerically via two nested fourth order Runge-Kutta algorithms: The first time integration is required to evaluate the integral over all past times $\tau$. In a second time integration, the reduced system dynamics are calculated using the previously determined integral up to the current time step. Due to the numerically very expensive size of the density matrix and its full memory kernel, all calculations are performed for $N = 4$ sites. For the electron-phonon coupling element, we consider phonon modes in the range of $k \in [0.0, 4.0]\,\mathrm{nm}^{-1}$ and $f_{ph} = 0.1$.

## 6.3 Memory-induced loss and rephasing of topological properties

As a first step, we identify the non-Markovian character of the unfolding time evolution dynamics by comparing results obtained from the polaron master Eq. (6.8) with a Markovian Lindblad master equation for phenomenological decoherence at a constant dephasing rate $\gamma$, given by (see Sec. 3.2)

$$\dot{\rho}_S = -i\,[H_k/\hbar, \rho_S] + \frac{\gamma}{2}\sum_{l=1}^{N}\left(2c_l^\dagger c_l \rho_S c_l^\dagger c_l - \{c_l^\dagger c_l, \rho_S\}\right). \tag{6.12}$$

In this description, a structured reservoir with super-Ohmic coup ling $g_k \sim k^{-1}$ must be presumed when considering 3D bulk phonons, resulting in a constant coupling $g_k = g_0$ incorporated in the damping constant $\gamma$. The green line in Fig. 6.3 depicts the non-Markovian polaronic time evolution dynamics of the Majorana correlation $\theta(t)$ at a spectral coupling width $\sigma = 0.6$, corresponding to a superconducting gap renormalization parameter $\langle B\rangle = 0.07$. Taking full account of the system-reservoir memory allows a substantial Majorana edge correlation to be retained at long times. After an initial decay, the Majorana edge correlation stabilizes well above zero. The long lived and substantial occurrence of Majorana modes seen in the non-Markovian dynamics is quite remarkable. This is particularly true since $H_{\mathrm{p,s}}$ is near the topological phase boundary due to the strongly

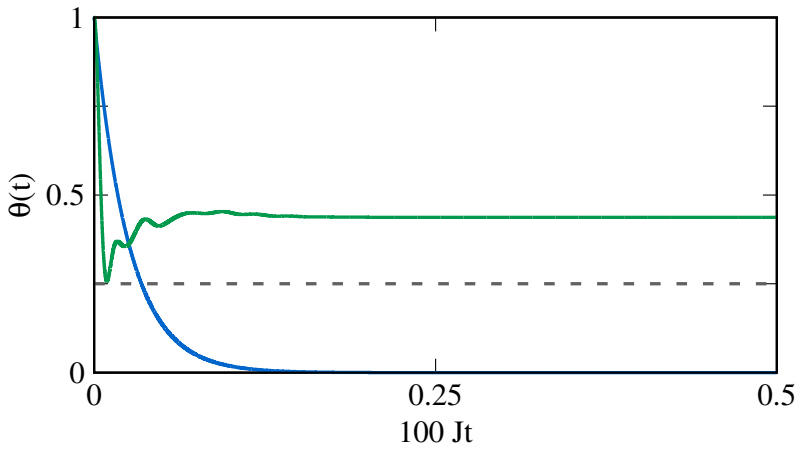


*Figure 6.3:* Time evolution dynamics of the polaronic topological Kitaev chain, showing a comparison of the Majorana correlation $\theta(t)$ calculated using a time-independent Lindblad-type master equation for dephasing (blue line) and non-Markovian dynamics obtained from the polaron master Eq. (6.8) with full account of memory (green line). The dashed grey line shows the asymptotic Majorana correlation in a coherent quench scenario to the phonon-dressed state $\Delta \to \Delta\langle B\rangle$.

suppressed renormalized pairing $\Delta\langle B\rangle \ll \Delta$. In comparison, in the Markovian description of decoherence the Majorana correlation inevitably collapses to zero in an exponential decay (blue line in Fig. 6.3) [144].

When the dissipative contribution in Eq. (6.8) is disregarded, the dynamics formally reduces to that of a coherent quench of the pairing, leading to a renormalized superconducting gap from $\Delta$ to $\Delta\langle B\rangle$. In this case, the Majorana correlation approaches an asymptotic value determined by the overlap of the Majorana wave functions for the pre- and post-quench topological Hamiltonians [143], which is small if the post-quench Hamiltonian is near the phase boundary (dashed grey line). The resulting stationary correlation differs significantly from the non-Markovian behavior in Fig. 6.3 and underlines the crucial role of the memory effect. Due to the dependence of the memory on both the phonon correlation $\phi(\tau)$ and the reversed dynamics of system correlations $X_{a,b}(-\tau)$, it simultaneously introduces decoherence and backflow of coherence to the system. The interplay of these two competing processes defines the non-Markovian character of the dynamics: The polaronic Kitaev chain is initially prepared in its ground state and then perturbed by a temperature increase to $T$, yielding a renormalization of the chain towards the topological phase boundary via the initial phonon correlation $\phi(0) = \int \mathrm{d}^3k\ |2g_k(\sigma)/\omega_k|^2 \coth\left[\hbar\omega_k/(2k_BT)\right]$. This quench generates a significant amount of bulk excitations and populates the Majorana edge mode, effectively changing the parity of Majorana states. In addition, phonon-induced dephasing processes set in, resulting in strong decoherence in the dressed Kitaev wire. In contrast, the time-reversed dynamics of system correlations $X_{a,b}(-\tau)$ reinstate coherence of the superconducting $p$-wave pairing via the system memory, which is the key ingredient for the emergence of a topological phase. During the initial memory times $\tau < \tau_M$, this rephasing process is in the buildup stage and only has a marginal impact on the evolution of the system. In consequence, an irreversible loss of parity information occurs during

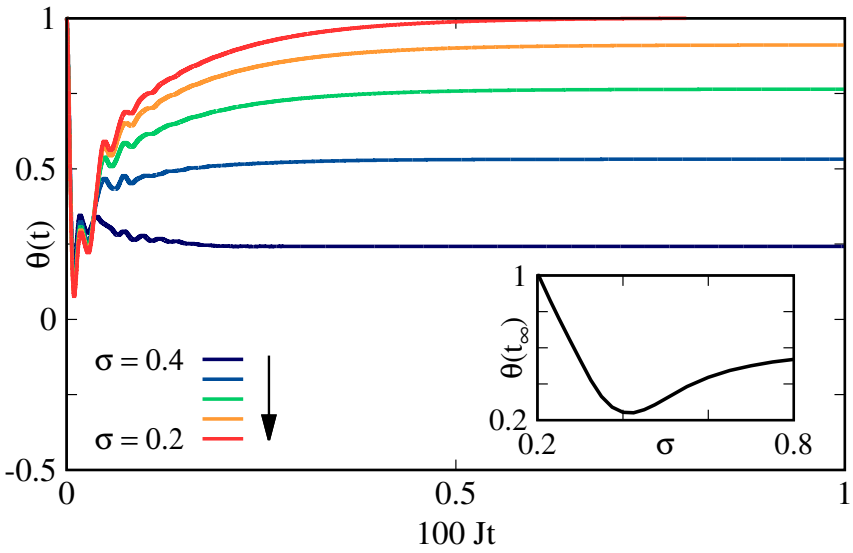


*Figure 6.4:* Non-Markovian time evolution dynamics of the Majorana correlation $\theta(t)$ for several bandwidths $\sigma$ of the fermion-phonon coupling $g_k$. The inset shows the corresponding steady-state value $\theta(t_\infty)$ as a function of $\sigma$.

the short-time dynamics. However, once the phonon correlation has decayed to zero at times $\tau > \tau_M$, the full potential of the memory kernel unfolds, leading to strong rephasing and a growth of topological properties due to $X_{a,b}(-\tau)$. In return, considerable Majorana correlation is sustained in the long term in Fig. 6.3. It is noted that in spite of the small size of the considered system, the asymptotic nonlocal Majorana edge correlation is indeed of topological origin rather than resembling a phonon-mediated long-range correlation. As verification of the topological nature of the observed correlation, in Sec. 6.5 we calculate the Majorana correlations between all chain sites, showing increasing decay with relative spacing, whereas the edge-edge correlation is significant.

## 6.4 Critical memory depth

The distinct non-Markovian relaxation behavior of the Majorana edge correlation depends crucially on the memory depth, which can be tuned through the spectral fermion-phonon coupling bandwidth $\sigma$. Fig. 6.4 shows the non-Markovian time evolution dynamics of $\theta(t)$ for various spectral widths $\sigma$. In comparison to the case $\sigma = 0.6$ (green line in Fig. 6.3), an initial decrease of $\sigma$ leads to a steeper monotonic decay of $\theta(t)$, resulting in a decreased asymptotic stationary state (dark blue line in Fig. 6.4). However, when further decreasing the coupling bandwidth, the previously monotonic relaxation becomes non-monotonic. While the initial short-time decoherence caused by phonon correlations is accelerated, the Majorana edge correlation recovers substantially in the long term limit (light blue line). This buildup behavior becomes even more distinct for further decreasing values of $\sigma$, leading to stationary state correlations larger than the $\sigma = 0.6$ case (green and orange lines in Fig. 6.4). Strikingly, once the coupling width $\sigma$ surpasses a critical

value, the asymptotic edge correlation approaches unity, $\theta(t_\infty) \to 1$ (red line). The inset of Fig. 6.4 shows the non-monotonic progression of $\theta(t_\infty)$ as a function of $\sigma$. Starting at a large value of the coupling width, the asymptotic edge correlation first decreases towards a minimum, before striving towards a perfect topological correlation in the limit of low $\sigma$.

This intriguing phenomenon can be explained by the dependence of $\phi(\tau)$ on the spectral coupling bandwidth: As described above, reducing $\sigma$ increases the lifetime of the phonon correlation $\phi(\tau)$ and therefore the memory depth. However, this also comes at the cost of a decreased renormalization parameter $\langle B\rangle = \exp[-\phi(0)/2]$ (see Fig. 6.2). While the former enhances the rephasing of superconductive pairing via an increasing time scale of the time-reversed evolution of $X_{a,b}(-\tau)$, the latter further suppresses the bulk gap $E_\Delta$ of $H_{\mathrm{p,s}}$ and decreases the impact of the memory. When $\sigma$ is initially decreased from 0.6, the suppressive effect dominates and aggravates the decay. However, by further reducing $\sigma$ the influence of the memory-enabled rephasing effect increases, allowing phonons and fermions to synchronize and thereby inducing a backflow of parity information. As a result, a new dressed polaronic state emerges, where the buildup of Majorana correlation starts to dominate over decoherence, resulting in a recovery of correlation. In general, this recovery sets in at times $t > \tau_M$ given that $E_\Delta \tau_M \gtrsim 1$ is satisfied. Importantly, the existence of a critical $\sigma$ corresponds to a critical memory depth, which allows for the formation of a new polaronic steady state in dynamical equilibrium with the phonon reservoir at $T = 4\,\mathrm{K}$. Remarkably, above this critical bandwidth $\sigma$ the Majorana edge mode correlation exhibits $\theta \approx 1$. In the considered scenario, the critical value of $\sigma$ is between 0.21 and 0.20, corresponding to a superconducting pairing renormalization $\langle B\rangle = 0.01$, but it is dependent on the specific model and the remaining system parameters. These findings open up new perspectives for the design and control of topological superconductors, since the fermion-phonon coupling bandwidth can be controlled in solid-state setups by nanotechnological design, e.g., using alloys, impurities and confinement potentials [210–213].

## 6.5 Discussion

We have demonstrated the emergence of memory-critical Majorana edge correlation dynamics in a topological Kitaev superconductor, resulting from non-Markovian interaction with phonons and leading to a revival of topological properties. We consolidate these findings by considering the impact of an additional $p$-wave interparticle interaction to the chain. To demonstrate the negligible impact of the polaron energy renormalization on the system dynamics [see Eq. (6.5)], we provide additional calculations of the edge dynamics including the polaron shift. Moreover, the arising correlations between all pairs of sites in the chain are calculated, implicating their topological origin rather than merely representing phonon-mediated long-range correlations. Lastly, we calculate the Majorana edge correlation dynamics for an initially nonideal Kitaev chain setup with a nonzero chemical potential, recreating the memory-critical behavior.

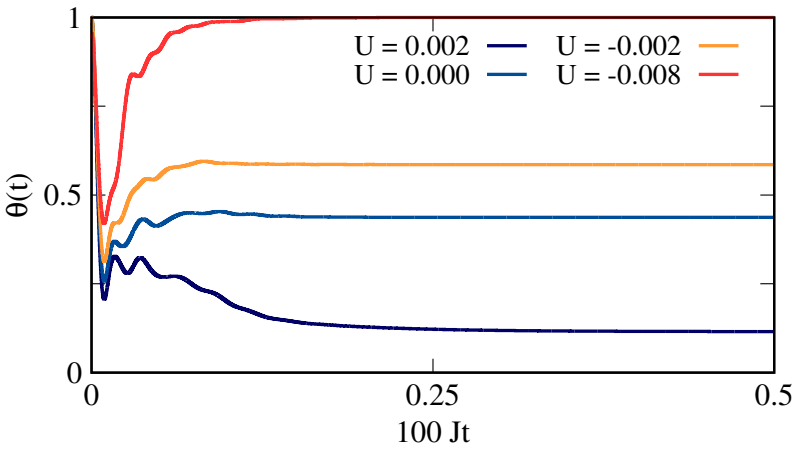


*Figure 6.5:* Non-Markovian time evolution dynamics of the Majorana edge correlation for the renormalized system Hamiltonian $H_{\mathrm{p,s}}$, calculated in the presence of a weak attractive $p$-wave interparticle interaction $U$. Calculations are performed at parameters $N = 4$, $J = \Delta = 0.01$, $\mu = 0$ and $\sigma = 0.6$ and for various amplitudes $U$.

### 6.5.1 Impact of interparticle interactions

As demonstrated in the polaron picture, the environmental coupling weakens fermionic $p$-wave pairing to the superconducting wire [Eq. (6.4)], thus corrupting the stability of the Majorana edge correlation. We have shown that non-Markovian phonon interactions can counteract this effect, providing a substantial stabilization mechanism for topological properties. To further investigate the role of attractive coupling for the longevity of Majorana correlations, here we consider an additional perturbation caused by weak attractive $p$-wave interparticle interactions. Therefore, Eq. (6.4) is expanded by a fermionic $p$-wave interaction term, given by

$$H_{\mathrm{int}}/\hbar = U \sum_{l=1}^{N-1} \left( c_l^\dagger c_l - \frac{1}{2} \right) \left( c_{l+1}^\dagger c_{l+1} - \frac{1}{2} \right), \tag{6.13}$$

with a weak interaction strength $|U| \ll 1$. We note that the interaction must be treated numerically exact, since resorting to approximate descriptions such as a mean field approach would inevitably lead to a decay of entanglement over time. The exact treatment is feasible for the chosen system size $N = 4$.

Fig. 6.5 shows the resulting non-Markovian time evolution dynamics of the Majorana edge correlation $\theta(t)$ at a fermion-phonon coupling width $\sigma = 0.6$ and for varying interaction amplitudes $U$. The light blue line shows the case without additional $p$-wave interaction $U = 0$. In comparison, introducing a *repulsive* interparticle interaction $U > 0$ results in a significant decline of the stationary topological correlation (dark blue line), since repulsive interactions energetically suppress fermionic pairing. On the contrary, adding a weak *attractive* interaction $U < 0$ can further enhance the asymptotic Majorana correlation for a sub-critical memory depth (orange and red lines), which is given for the considered bandwidth $\sigma = 0.6$. Depending on the amplitude $|U|$, attractive pairing not only shortens

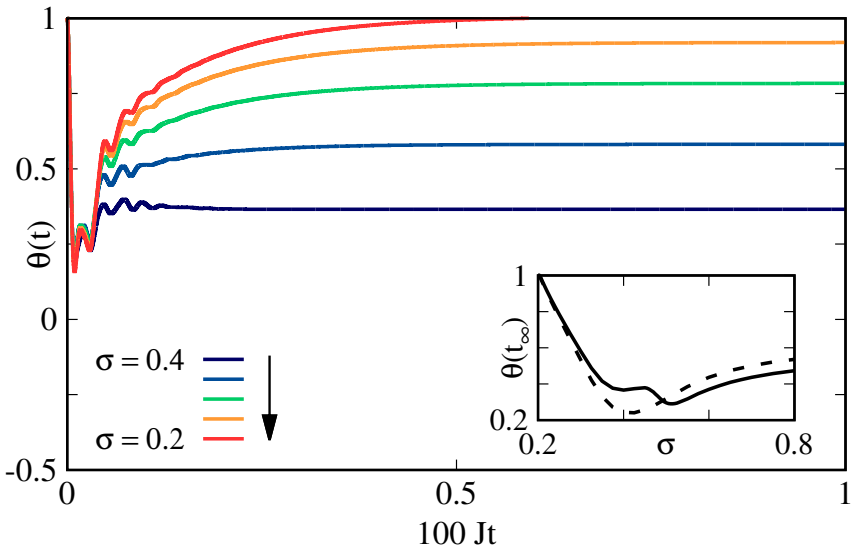


*Figure 6.6:* Non-Markovian dynamics of the polaronic Majorana edge correlation $\theta(t)$ for various phonon coupling bandwidths $\sigma$, now including the polaron energy renormalization term $H_{\text{shift}}$. The resulting steady state values $\theta(t_\infty)$ are shown as a function of $\sigma$ in the inset, where a comparison of the cases including the polaron shift (solid line) and disregarding it (dashed line) is provided. As before, the results are obtained using the parameters $N = 4$, $J = \Delta = 0.01$, $\mu = 0$, $f_{\text{ph}} = 0.1$ and phonon modes within $k \in [0.0, 4.0]$ nm$^{-1}$.

the required time for a revivial of topological correlation (see Fig. 6.4), but can even result in a complete recovery in the sub-critical memory regime (red line). This behavior can be intuitively understood, since the attractive interparticle interaction is energetically favorable for the coherent formation of superconductive pairing. As demonstrated before, the latter provides a counteracting mechanism against phonon-induced dephasing processes and thereby stabilizes the systems' topological phase.

### 6.5.2 Polaron energy shift

During the polaron transformation of the dissipative Kitaev Hamiltonian, an additional energy renormalization term arises [see Eq. (6.5)] which has been neglected so far. It is justified to disregard this so-called polaron shift under certain conditions, which are fulfilled in the investigated scenario: With respect to non-Markovian dynamical phenomena, neglecting the polaron shift is standard practice if the initial condition is an equilibrium, as established by Leggett [1, 32]. As an initial condition, we have assumed the even parity ground state of the Kitaev chain which constitutes an equilibrium state. Therefore, we have disregarded Eq. (6.5) in the full polaron Hamiltonian according to the convention.

However, to this day the question whether it is necessary to take generic account of the polaron shift remains an open question in non-Markovian physics. In order to demonstrate that the presented results are invariant against this energy renormalization regardless of

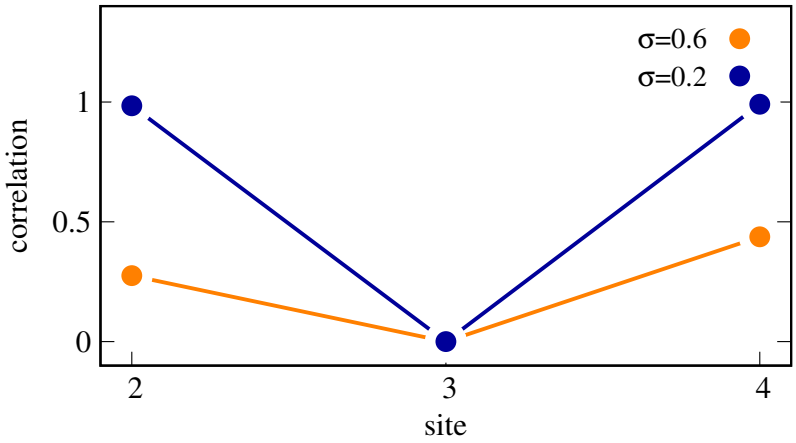


*Figure 6.7:* Asymptotic site-site correlations $-i\langle b_1 b_{2j}\rangle(t_\infty) = \lim_{t\to+\infty}(-i\mathrm{tr}\{\rho_S(t) b_1 b_{2j}\})$ between the Majorana operators $b_1$ and $b_{2j}$ for lattice sites $j = 2, 3, 4$ for the considered Kitaev wire at parameters $N = 4$, $J = \Delta = 0.01$, $\mu = 0$ and $f_{\mathrm{ph}} = 0.1$. Calculations are shown for two fermion-phonon coupling bandwidths $\sigma = \{0.6, 0.2\}$.

the initial condition and the aforementioned convention, we here provide additional calculations of the non-Markovian Majorana edge correlation in the presence of the polaron energy shift. The considered system size of $N = 4$ allows for a numerically exact treatment of Eq. (6.5). Fig. 6.6 shows the corresponding non-Markovian dynamics for $\theta(t)$, now including Eq. (6.5) in the full polaron Hamiltonian. The inset again provides the asymptotic Majorana edge correlation as a function of the spectral reservoir coupling bandwidth $\sigma$, showing a comparison between the cases of including the polaron shift (solid line) and disregarding it (dashed line). When comparing Fig. 6.6 to Fig. 6.4, it becomes apparent that the inclusion of the polaron shift does not alter the qualitative dynamics and the memory-critical recovery mechanism for the topological correlation. The polaron renormalization term is proportional to the coupling bandwidth $\sigma$, albeit this only impacts the number of nonzero phonon modes taken into account for the energy shift. This dependence is of a much lower scale than the influence of $\sigma$ on the lifetime $\tau_M$ of the phonon correlation function $\phi(\tau)$, which has been shown to critically determine the stationary topological properties of the superconducting Kitaev wire. In consequence, the main difference when taking the polaron shift into account is the formation of a plateau of the stationary Majorana edge correlation at intermediate $\sigma$ and slightly decreased values in the limit of large bandwidths (solid line in inset of Fig. 6.6).

### 6.5.3 Topological correlation

In the present investigation, the numerically accessible size of the Kitaev chain is severely limited by the expensive calculation of the density matrix and the finite memory kernel of the integro-differential polaron master equation. Therefore, the considered chain size is chosen at $N = 4$ sites. In order to demonstrate that the reported stationary Majorana edge correlation is genuinely of topological origin, we calculate the stationary state site-site correlations $\lim_{t\to+\infty}(-i\mathrm{tr}[\rho_S(t) b_1 b_{2j}])$ between the Majorana operators $b_1$ and $b_{2j}$

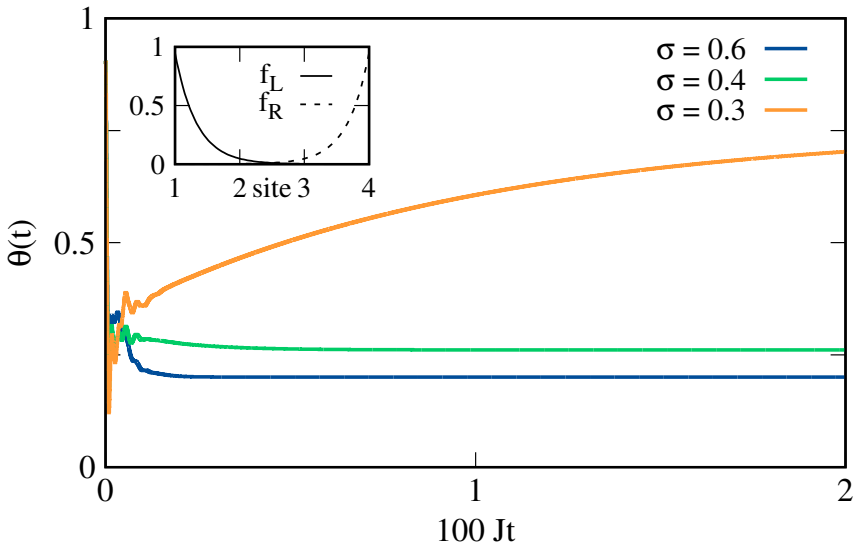


*Figure 6.8:* Majorana edge correlation dynamics $-i\langle\gamma_L\gamma_R\rangle(t)$ for a nonideal Kitaev chain at parameters $J = \Delta = 0.01$, $\mu = 0.1J$, $N = 4$ and various spectral coupling widths $\sigma$. The inset shows the exponential model functions employed for the Majorana wave functions $f_L$ and $f_R$.

for all chain sites $j = 2, 3, 4$. Fig. 6.7 shows the resulting asymptotic correlations for two reservoir coupling bandwidths $\sigma = \{0.6, 0.2\}$. In the figure, the site-site correlation decays with increasing separation lengths $d = j - 1$ and vanishes almost entirely at $d = 2$, underlining that phonon-mediated long-range correlations do not play a significant role for the formation of the correlation. However, the site-site correlation increases to a substantial value at the right boundary $d = 3$, representing a topological signature of the nonlocal Majorana edge modes: If the observed correlation beyond nearest-neighbor sites at separation lengths $d > 1$ were to originate from phonon-mediated effects, one would expect a monotonous decay with increasing distances $d$.

### 6.5.4 Nonideal Kitaev chain

The presented results are based on an initially ideal Kitaev wire, i.e., featuring strictly zero overlap between the Majorana wave functions $f_{L/R,j}$ located at the left and right boundaries of the chain, even in the case of a system of $N = 4$ sites [143]. In the presence of a small perturbation caused, e.g., by a nonzero chemical potential $|\mu| > 0$, the initial Kitaev chain is no longer ideal, corresponding to an extension of the Majorana wave functions into the bulk [144, 150, 214]. In this scenario, the Majorana edge correlation is given by $-i\langle\gamma_L\gamma_R\rangle$, with $\gamma_{L/R} = \sum_j f_{L/R,j} b_j$ and Majorana operators $b_{2j-1} = c_j + c_j^\dagger$, $b_{2j} = -i(c_j - c_j^\dagger)$. Fig. 6.8 shows the resulting Majorana edge correlation dynamics for an initially nonideal polaronic Kitaev Hamiltonian with parameters $N = 4$, $J = \Delta = 0.01$, $\mu = 0.1J$ and various spectral coupling widths $\sigma$. Since only qualitative differences with respect to the ideal chain dynamics are of interest, the Majorana wave functions $f_{L/R}$ with

finite localization lengths are modeled via normed exponential decay functions, depicted in the inset in Fig. 6.8 and featuring a small nonzero overlap between them.

The nonideal setup poses an additional perturbation to the polaronic state. As a result, for a given parameter configuration the stationary edge correlation is decreased with respect to the ideal case (blue and green lines). However, the memory-enabled recovery of topological properties can still be observed when $\sigma$ is tuned below a threshold value (orange line). Hence, for sufficiently small deviations from the ideal setup the dynamical recovery of Majorana correlation is preserved under nonideal initial conditions, demonstrating the robustness of the effect and the generality of the presented results.

## 6.6 Conclusion

In summary, we have demonstrated the emergence of memory-critical Majorana edge correlation dynamics in a topological superconductor, enabled by non-Markovian fermion-phonon interactions and resulting in a revival of topological properties. This mechanism uniquely arises from the phonon-renormalized topological Hamiltonian, where the phonon environment leads to a suppression of superconductive tunneling, and from its interplay with a quantum memory effect. As a result, dephasing and information backflow processes are simultaneously induced. While the presented analysis is based on the ideal Kitaev chain, we expect the essential physics to emerge in a wide class of topological materials interacting with a super-Ohmic reservoir. In this context, we have reproduced our key findings in an initially nonideal Kitaev chain setup with Majorana wave function overlap. Moreover, we have shown that the reservoir-induced suppression of superconductive pairing can be further counteracted via attractive $p$-wave interparticle interactions, providing an additional mechanism for the recovery and stabilization of topological properties.

The experimental realization of Majorana fermions in condensed matter setups, e.g., based on hybrid superconductor and semiconductor nanowires, is currently subject to significant research efforts. The fermion-phonon reservoir coupling considered in the present investigations can for instance occur in InAs nanowires [149–154], where the acoustic phonon wavelengths are in the 100 nm length range of typical nanowire realizations and feature super-Ohmic coupling. Aside from solid-state setups, the fundamental non-Markovian mechanism of a reservoir-induced recovery of topological properties is expected to also be observable in realizations of ultracold quantum gases coupled to a superfluid reservoir, where excitations result in the emergence of phonon interactions [183, 190, 215]. In a broader context, one can also consider experimental scenarios where interactions with a structured bosonic reservoir are intentionally induced, as long as the coupling leads to non-Markovian system-reservoir correlations. Recent related studies have shown that an impurity or a qubit can be employed as a non-Markovian quantum probe for a topological reservoir [198–200], and that topological system properties stemming from Markovian dissipation can be sustained in non-Markovian regimes [201]. In difference to these investigations on topological systems with non-Markovian system-reservoir dynamics, we have demonstrated that tailoring the coupling to a super-Ohmic reservoir can improve the longevity and grade of topological properties, and even fully restore them. Our findings

open up new intriguing prospects for the investigation and control of memory-dependent topological phenomena, for instance with respect to current efforts to realize topological quantum computing [123, 216].

# 7 Unidirectional quantum transport in optically driven V-type quantum dot chains

In this Chapter, we present a mechanism to achieve complete population inversion in an optically driven InAs/GaAs semiconductor quantum dot featuring a $V$-type energy structure. The unfolding nonequilibrium stationary state is induced by the interaction of a non-Markovian decoherence mechanism introduced by acoustic phonons with the systems' $V$-type interband transitions. In a second step, we apply the population inversion mechanism to create unidirectional excitation transport in a chain of coupled quantum dots without application of an external bias and independent of the unitary interdot coupling mechanism. The Chapter is closely based on the publication "Unidirectional quantum transport in optically driven $V$-type quantum dot chains" by O. Kästle et al. [70]

## 7.1 Introduction

The control and utilization of non-Markovian phenomena has become a main focus of attention for the development of quantum optical devices and quantum information technology [4–10]. Specifically, investigations of the interplay of phonon-assisted coherence and dissipative processes in semiconductor nanostructures such as quantum dots have emerged as a growing field of research [11–24]. For instance, non-Markovian system-reservoir couplings have been tailored to create population inversion in such emitters to a certain degree [29, 34, 35, 217, 218], making them potential candidates for chip-integrated single-exciton light sources. Approaches to achieve population inversion encompass adiabatic rapid passage in quantum emitters [219] and hybrid setups of quantum dots interacting with metal nanoparticles [220] and cavities [221–223]. Most recently, population inversion has been achieved in a single InAs/GaAs quantum dot using pulsed excitations tuned within the exciton phonon sideband, enabled by a phonon-mediated thermalization of the optically dressed states [224, 225]. Already, these examples demonstrate the potential of tailored electron-phonon interactions for controlled optical excitations.

In this Chapter, we describe non-Markovian undirectional quantum transport enabled by electron-phonon interactions in quantum dots featuring $V$-type transitions and continuously driven by a single laser field [226–228]. We demonstrate the occurrence of a non-reciprocal phonon-assisted energy transfer in single quantum dots and quantum dot chains as a result of resonant excitation of an electronic state and its interaction with a lower-energy state [70]. Specifically, the non-Markovian description of the environment

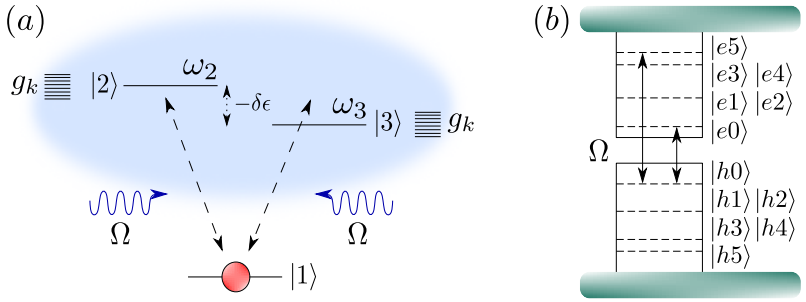


*Figure 7.1:* (a) Schematic of the considered $V$-type emitter model with two excited states featuring an energy detuning $\delta\epsilon = \hbar(\omega_3 - \omega_2)$. The two transitions are driven by a continuous laser field at a Rabi frequency $\Omega$ and in resonance with the transition between states $|1\rangle$ and $|2\rangle$. The excited states are interacting with a structured 3D acoustic phonon reservoir via coupling elements $g_{\boldsymbol{k}}$. Initially, a single electron is located in state $|1\rangle$. (b) Schematic quantum dot energy level structure of InAs embedded in GaAs, enabling $V$-type transitions between electron and hole states.

enables information backflow, such that excitation transfer within the system is supported by the structured reservoir [1, 3, 80]. The observed effects are non-Markovian in nature, since a Lindblad form for pure dephasing derived from the considered full Hamiltonian fails to capture the presented mechanism, even in the case of a time-dependent pure dephasing rate. Moreover, the reported inversion mechanism also cannot be reproduced by a Redfield master equation subjected to the first and second Markovian approximation. The implications of this effect on the considered $V$-type systems are demonstrated in two subsequent steps:

(i) For a single quantum dot, it results in the preparation of a highly nonequilibrium stationary state. For certain parameter choices, complete population inversion is achieved in the detuned excited state and can be maintained for a wide range of coupling and driving amplitudes. In difference to previously reported mechanisms [12, 29, 34, 217–219, 222], the reported inversion is induced in a $V$-type emitter via continuous optical excitation and without a cavity mode.

(ii) The observed population inversion is applied to create excitation transport in a chain-like spatial distribution of several quantum dots. Exploiting the population trapping in the red-detuned excited state of each emitter, we predict the emergence of unidirectional excitation transport from one end of the quantum dot chain to the other. Unidirectional energy transport via electronic excitation transfer has been widely investigated in semiconductor nanostructures [229–236], biological systems [237] and molecules [238, 239]. Moreover, it has been shown that non-Markovian system-reservoir interactions can affect non-reciprocal quantum transport [240] and increase its efficiency [241] on the basis of well-established transfer protocols, e.g., enabled by an external bias [242]. In difference to these investigations, here we provide an example in which unidirectional quantum transport results without the application of an external potential, but from the interplay between incoherence and coherence in the system alone. Due to the robustness of the underlying mechanism, the transport endures the perturbative effects such as radia-

tive decay phenomena or intraband phonon couplings, and emerges independently of the specific interdot coupling mechanism.

Two independent theoretical approaches are employed for the description of the system. In a first step, the system dynamics is calculated using a polaron master equation in second-order perturbation theory with respect to the polaron Hamiltonian [1, 14, 80, 87–92, 99, 100]. Afterwards, we reproduce the dynamics in a Heisenberg picture correlation expansion to gain insight into the key interaction processes enabling the population inversion mechanism and the specific channels of information backflow between system and reservoir.

In Sec. 7.2, we introduce the investigated $V$-type system in detail and derive both the polaron master equation and the Heisenberg equations of motion for its description. Afterwards, we analyze the emergence of complete population inversion in the Heisenberg picture description in Sec. 7.3. In Sec. 7.4, multiple $V$-type emitters are combined to a quantum dot chain exhibiting unidirectional quantum transport. We discuss our findings in Sec. 7.5, where we compare the solutions obtained from the Heisenberg picture and polaron master equation approach, incorporate extensions to our model and discuss the linear absorption spectrum of the $V$-type emitter and its eigenstate dynamics. In addition, we provide calculations for alternative interdot coupling mechanisms for the quantum dot chain, demonstrating the emergence of unidirectional transport regardless of the specific coupling type. Lastly, we conclude our investigation in Sec. 7.6.

## 7.2 V-type emitter model

The investigated $V$-type emitter model system shown in Fig. 7.1(a) consists of a single ground state $|1\rangle$ and two excited states $|2\rangle$ and $|3\rangle$, with an energy detuning $\delta\epsilon = \hbar(\omega_3 - \omega_2)$ between them. The two allowed transitions are driven by a single continuous laser field at a Rabi frequency $\Omega$, which is tuned in resonance to the transition between states $|1\rangle$ and $|2\rangle$. Such a scenario is constituted, e.g., by conical InAs quantum dots surrounded by a bulk of GaAs [243]. The energy level structure for this case is shown schematically in Fig. 7.1(b). Here, the electronic structure comprises six confined electron and hole states denoted by $|e0\rangle, \ldots, |e5\rangle$ and $|h0\rangle, \ldots, |h5\rangle$ within the envelope wave function and effective mass approximation [226, 227, 244, 245]. Due to the rotational symmetry of the conical quantum dot structure, the first and second as well as the third and fourth states in both bands are degenerate [226, 227]. As a result, the dipole selection rules permit two possible interband transitions from the heavy hole state $|h0\rangle$ to the electronic states $|e0\rangle$ and $|e5\rangle$ [see Fig. 7.1(b)], manifesting the $V$-type transition pattern in the here considered three-level system [226]. We note that interband transitions to the states $|e1\rangle$-$|e4\rangle$ are not explicitly dipole-forbidden, however, they are impeded by many-body Coulomb effects giving rise to an energy renormalization with strong impact on the oscillator strengths [226]. In the following, the transitions between $|h0\rangle$ and $|e0\rangle$ and between $|h0\rangle$ and $|e5\rangle$ are assumed to be dominant, which is for instance achieved via tuning of the excitation strength to control Coulomb renormalization effects or doping of the semiconductor material. We choose the laser frequency as the rotating frame and apply the rotating wave approximation. As a

result, the Hamiltonians describing the quantum dot $H_{el}$ and the electron-light coupling $H_l$ read

$$H_{el} = \hbar\left(\Delta_2\sigma_{22} + \Delta_3\sigma_{33}\right), \tag{7.1}$$
$$H_l = \hbar\Omega(\sigma_{12} + \sigma_{13} + \text{H.c.}), \tag{7.2}$$

with operators $\sigma_{ij} = |i\rangle\langle j|$. $\Delta_i = \omega_i - \omega_L$ is the frequency detuning between the $i$-th excited state and the incoming laser field, cooresponding to an energy detuning $\delta\epsilon = \hbar(\Delta_3 - \Delta_2)$ between the excited states, and $\Omega$ denotes the real-valued and slowly varying envelope of the Rabi frequency of transitions between the ground and excited states.

In addition, decoherence effects caused by the surrounding GaAs material are accounted for by coupling a structured phonon reservoir to the electron states $|2\rangle$ and $|3\rangle$ of the quantum emitter [see Fig. 7.1(b)]. In our investigation, we consider a generic model of diagonal electron-phonon interactions $H_{el,ph}$ for 3D bulk phonons of the form [95, 96]

$$H_{el,ph} = \hbar\int \mathrm{d}^3k \ \left[g_{\boldsymbol{k}}^{(2)}\sigma_{22} + g_{\boldsymbol{k}}^{(3)}\sigma_{33}\right]\left(r_{\boldsymbol{k}}^\dagger + r_{\boldsymbol{k}}\right), \tag{7.3}$$

with bosonic creation and annihilation operators $r_{\boldsymbol{k}}^\dagger$, $r_{\boldsymbol{k}}$. The mode-dependent fermion-phonon coupling elements at states $|2\rangle$ and $|3\rangle$ are given by the overlap integrals with state $|1\rangle$ [80, 97, 98, 246],

$$g_{\boldsymbol{k}}^{(2)} := \sqrt{\frac{\hbar k}{2\rho c_s}}\left[D_2\exp\left(-\frac{\hbar k^2}{4m_2\omega_2}\right) - D_1\exp\left(-\frac{\hbar k^2}{4m_1\omega_1}\right)\right], \tag{7.4a}$$

$$g_{\boldsymbol{k}}^{(3)} := \sqrt{\frac{\hbar k}{2\rho c_s}}\left[D_3\exp\left(-\frac{\hbar k^2}{4m_3\omega_3}\right) - D_1\exp\left(-\frac{\hbar k^2}{4m_1\omega_1}\right)\right], \tag{7.4b}$$

where $c_s$, $D_i$, $m_i$, $\hbar\omega_i$ and $\rho$ denote the sound velocity, deformation potentials, effective masses, confinement energies and the mass density of GaAs, respectively. Moreover, we assume identical overlaps between level $|1\rangle$ and both excited states, yielding a single fermion-phonon coupling element $g_{\boldsymbol{k}} := g_{\boldsymbol{k}}^{(2)} = g_{\boldsymbol{k}}^{(3)}$. The spectral density is therefore given by $J(\omega) = \int \mathrm{d}^3k \ |g_{\boldsymbol{k}}|^2\delta(\omega - \omega_{\boldsymbol{k}})$, with $\omega_k = c_s|\boldsymbol{k}|$ denoting the acoustic phonon frequencies [80]. We emphasize that the following investigations describe a generic effect which is robust against the employed coupling element, as long as Stokes processes can emerge via phonon-assisted resonances. In addition to the here applied coupling, Gaussian and Lorentzian shaped couplings $g_k$ have been confirmed to result in qualitative and quantitative comparable results. For now, phonon-induced intraband couplings $\sim g_{\boldsymbol{k}}^{23}\sigma_{23}$ and radiative decay are neglected, since all key results can be shown to be robust against their presence (see Sec. 7.5). Together with the free phonon evolution

$$H_{ph} = \hbar\int \mathrm{d}^3k \ \omega_k r_{\boldsymbol{k}}^\dagger r_{\boldsymbol{k}}, \tag{7.5}$$

we arrive at the full open system Hamiltonian $H = H_{el} + H_l + H_{ph} + H_{el,ph}$. In Appendix C, we provide a table containing all parameters employed for calculations.

For the numerical evaluation, we employ the standard second-order perturbative polaron master equation (see Ch. 3) [1, 14, 80, 87–92, 99, 100],

$$\dot{\rho}_S(t) = -\frac{i}{\hbar}\left[H_{p,0}, \rho_S(t)\right] - \frac{1}{\hbar^2}\int_0^t d\tau\ \mathrm{tr}_B\{[H_{p,I}, [H_{p,I}(-\tau), \rho_S(t)\otimes\rho_B]]\}, \tag{7.6}$$

where $H_{p,0}$ and $H_{p,I}$ refer to the polaron-transformed free evolution and system-reservoir interaction Hamiltonians, respectively,

$$H_{p,0} = \hbar\sum_{i=2,3}\left[\bar{\Delta}_i\sigma_{ii} + \bar{\Omega}(\sigma_{1i}+\sigma_{i1})\right], \tag{7.7a}$$

$$H_{p,I} = \hbar\sum_{i=2,3}\left\{(\sigma_{1i}+\sigma_{i1})\left[\Omega\cosh\left(R^\dagger - R\right) - \bar{\Omega}\right] + \Omega(\sigma_{i1}-\sigma_{1i})\sinh\left(R^\dagger - R\right)\right\}. \tag{7.7b}$$

Here we have defined collective bosonic operators $R^{(\dagger)} = \int \mathrm{d}^3k\ (g_{\boldsymbol{k}}/\omega_k) r_{\boldsymbol{k}}^{(\dagger)}$, $\bar{\Delta}_i$ denotes a polaron-shifted detuning and a Franck-Condon renormalization is applied by introducing

$$\bar{\Omega} = \Omega\exp\left[-\int \mathrm{d}^3k\ \frac{g_{\boldsymbol{k}}}{2\omega_k}\coth\left(\frac{\hbar\omega_k}{2k_BT}\right)\right], \tag{7.8}$$

such that $\mathrm{tr}_B\{[H_{p,I}, \rho(t)]\} = 0$. Moreover, $H_{p,0}$ governs the time-reversed unitary evolution of the interaction $H_{p,I}(-\tau) = U^\dagger(-\tau,0)H_{p,I}U(-\tau,0)$ via $U(t,0) = \exp(-i/\hbar H_{p,0}t)$ (see Ch. 3). As a result, the equations of motion for the density matrix elements $\rho_{mn}$ are given by

$$\begin{aligned}\dot{\rho}_{mn} = &\sum_{i=2,3}\left[i\bar{\Delta}_i\left(\rho_{mi}\delta_{ni} - \rho_{in}\delta_{mi}\right) + i\bar{\Omega}(\rho_{m1}\delta_{ni} + \rho_{mi}\delta_{n1} - \rho_{in}\delta_{m1} - \rho_{1n}\delta_{mi})\right] \\ &- \frac{\bar{\Omega}^2}{\hbar^2}\sum_{i,j=2,3}\int_0^t d\tau\,\langle m|\,\chi^{ij}(\tau)\,|n\rangle\,,\end{aligned} \tag{7.9}$$

with

$$\begin{aligned}\langle m|\,\chi^{ij}(\tau)\,|n\rangle = \sum_{q=1}^{3}\Big\{&\rho_{qn}\Big[\left(G_+(\tau)X^{iq}_{+,j}(-\tau) - iG_-(\tau)X^{iq}_{-,j}(-\tau)\right)\delta_{m1} \\ &+ \left(G_+(\tau)X^{1q}_{+,j}(-\tau) + iG_-(\tau)X^{1q}_{-,j}(-\tau)\right)\delta_{mi}\Big] \\ &+ \rho_{mq}\Big[\left(G^*_+(\tau)X^{q1}_{+,j}(-\tau) - iG^*_-(\tau)X^{q1}_{-,j}(-\tau)\right)\delta_{ni} \\ &+ \left(G^*_+(\tau)X^{qi}_{+,j}(-\tau) + iG^*_-(\tau)X^{qi}_{-,j}(-\tau)\right)\delta_{n1}\Big] \\ &+ \rho_{q1}\Big[-G_+(\tau)X^{mq}_{+,j}(-\tau) + iG_-(\tau)X^{mq}_{-,j}(-\tau)\Big]\delta_{ni} \\ &+ \rho_{qi}\Big[-G_+(\tau)X^{mq}_{+,j}(-\tau) - iG_-(\tau)X^{mq}_{-,j}(-\tau)\Big]\delta_{n1} \\ &+ \rho_{1q}\Big[-G^*_+(\tau)X^{qn}_{+,j}(-\tau) - iG^*_-(\tau)X^{qn}_{-,j}(-\tau)\Big]\delta_{mi} \\ &+ \rho_{iq}\Big[-G^*_+(\tau)X^{qn}_{+,j}(-\tau) + iG^*_-(\tau)X^{qn}_{-,j}(-\tau)\Big]\delta_{m1}\Big\}.\end{aligned} \tag{7.10}$$

Here, we have abbreviated $\langle m|\, X_{\pm,i}(-\tau)\,|n\rangle = X^{mn}_{\pm,i}(-\tau)$ and defined system correlations $X_{+,i}(\tau) := [\sigma_{1i}(\tau) + \sigma_{i1}(\tau)]$, $X_{-,i}(\tau) := i\,[\sigma_{i1}(\tau) - \sigma_{1i}(\tau)]$ and the phonon correlation function

$$\phi(\tau) = \int \mathrm{d}^3k\, \frac{g_{\boldsymbol{k}}^2}{\omega_k^2} \left[ \coth\left(\frac{\hbar\omega_k}{2k_BT}\right) \cos(\omega_k\tau) - i\sin(\omega_k\tau) \right], \tag{7.11}$$

with $G_+(\tau) := \cosh[\phi(\tau)] - 1$, $G_-(\tau) := \sinh[\phi(\tau)]$ and $\bar{\Omega} = \Omega \exp[-\phi(0)/2]$. The polaron master equation approach offers the advantage of high numerical performance and stability, allowing for long simulation times and accurate results in the weak and moderate electron-phonon coupling regime [29, 207, 247, 248]. A detailed derivation of the polaron master equation for the $V$-type emitter model is presented in Appendix C.

In addition, we calculate the system dynamics using a Heisenberg picture correlation expansion up to second order in the phonon contributions, which is better suited to unravel the underlying physical interactions [19, 97, 205, 207, 249–251]. The equivalence of the two descriptions in the here considered parameter regime is demonstrated in Sec. 7.5. The Heisenberg equations of motion for the electronic contributions are prescribed by $-i\hbar\dot{\sigma}_{mn}(t) = [H, \sigma_{mn}(t)]$, resulting in

$$\begin{aligned}
\frac{\mathrm{d}}{\mathrm{d}t}\langle\sigma_{mn}\rangle = i\Big[&\Delta_2\left(\langle\sigma_{2n}\rangle\,\delta_{m2} - \langle\sigma_{m2}\rangle\,\delta_{n2}\right) + \Delta_3\left(\langle\sigma_{3n}\rangle\,\delta_{m3} - \langle\sigma_{m3}\rangle\,\delta_{n3}\right) \\
&+ \Omega\Big(\langle\sigma_{1n}\rangle\,\delta_{m2} + \langle\sigma_{2n}\rangle\,\delta_{m1} - \langle\sigma_{m2}\rangle\,\delta_{n1} - \langle\sigma_{m1}\rangle\,\delta_{n2} \\
&+ \langle\sigma_{1n}\rangle\,\delta_{m3} + \langle\sigma_{3n}\rangle\,\delta_{m1} - \langle\sigma_{m3}\rangle\,\delta_{n1} - \langle\sigma_{m1}\rangle\,\delta_{n3}\Big) \\
&+ \int \mathrm{d}^3k\; g_{\boldsymbol{k}}\Big(\langle\sigma_{2n}r^\dagger_{\boldsymbol{k}}\rangle\,\delta_{m2} + \langle\sigma_{3n}r^\dagger_{\boldsymbol{k}}\rangle\,\delta_{m3} - \langle\sigma_{m2}r^\dagger_{\boldsymbol{k}}\rangle\,\delta_{n2} - \langle\sigma_{m3}r^\dagger_{\boldsymbol{k}}\rangle\,\delta_{n3} \\
&+ \langle\sigma_{2n}r_{\boldsymbol{k}}\rangle\,\delta_{m2} + \langle\sigma_{3n}r_{\boldsymbol{k}}\rangle\,\delta_{m3} - \langle\sigma_{m2}r_{\boldsymbol{k}}\rangle\,\delta_{n2} - \langle\sigma_{m3}r_{\boldsymbol{k}}\rangle\,\delta_{n3}\Big)\Big],
\end{aligned} \tag{7.12}$$

where we have disregarded the time argument of the operators for brevity and assigned indices $m, n = \{1, 2, 3\}$ to the emitter levels. The remaining higher-order equations of motion for the phonon-assisted transitions ($m \neq n$) and occupations ($m = n$) $\langle\sigma_{mn}r^{(\dagger)}_{\boldsymbol{k}}\rangle$ are provided in Appendix C. To close the system of equations, we employ a second-order Born factorization in the limit where the correlation expansion manages to reproduce the full *independent boson model*. Here, the phonon number expectation value is assumed as a thermal Bose distribution [1], i.e.,

$$\langle r^\dagger_{\boldsymbol{k}} r_{\boldsymbol{k}}\rangle \approx \left[\exp\left(\frac{\hbar\omega_k}{k_BT}\right) - 1\right]^{-1}, \tag{7.13}$$

with $k_B$ denoting the Boltzmann constant. For an explicit illustration of the involved oscillator strengths, we additionally discuss the resulting linear absorption spectrum of the considered $V$-type emitter model in Sec. 7.5.

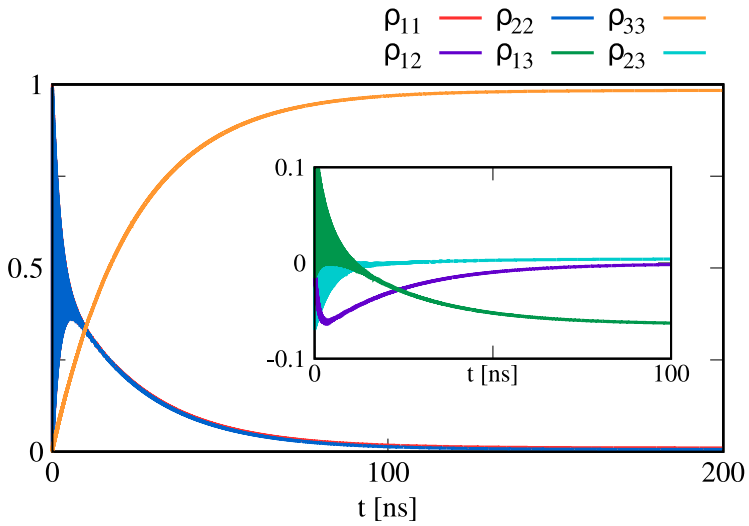


*Figure 7.2:* $V$-type emitter population dynamics obtained from the polaron master equation, exhibiting complete population inversion in the red-shifted excited state $|3\rangle$. The corresponding coherence dynamics is shown in the inset.

## 7.3 Complete population inversion by non-Markovian reservoir interaction

We start with the single emitter case, where an electron is initially located in the ground state $|1\rangle$ and the laser frequency is chosen in resonance with the transition between the ground state $|1\rangle$ and the excited state $|2\rangle$, such that $\Delta_2 = 0$ and therefore $\delta\epsilon = \hbar\Delta_3 \neq 0$, corresponding to a negative energy detuning ($\omega_3 < \omega_L$) within range of the acoustic phonon spectral density maximum. Fig. 7.2 shows the polaron master equation dynamics for the level populations $\sigma_{11}$, $\sigma_{22}$ and $\sigma_{33}$ after switching on the driving field at a Rabi frequency $\Omega$. In the stationary state, the system exhibits complete population inversion: The laser-detuned excited state $|3\rangle$ becomes almost fully occupied, $\langle\sigma_{33}\rangle \to 1$, while the populations of the resonantly pumped levels $|1\rangle$ and $|2\rangle$ decline to zero. Due to the more intuitive nature of the Heisenberg picture description, the following analysis of this behavior is based on the Heisenberg equations of motion [Eq. (7.12)].

Fig. 7.3 shows a diagrammatic representation of the interactions between coherences, occupations and their phonon-assisted amplitudes in correspondence to their occurrence in the Heisenberg equations of motion. As illustrated in the diagram, a direct optical transition from the resonantly driven excited state $|2\rangle$ to the detuned excited state $|3\rangle$ is not allowed. Therefore, the population transfer to level $|3\rangle$ must be carried out by the structured reservoir. Red shapes and arrows in Fig. 7.3 highlight the crucial interactions of populations and coherences facilitating the excitation transfer to the laser-detuned level $|3\rangle$. As a result of the continuous resonant driving of transitions between levels $|1\rangle$ and $|2\rangle$, energy is dissipated to the phonon environment via the coherence $\sigma_{12}$: The non-Markovian nature of the reservoir enables backflow of excitation to the system via phonon-assisted transitions $\sigma_{ij} r_{\boldsymbol{k}}^{(\dagger)}$, which form a gateway from the optically driven amplitude $\sigma_{12}$ to the

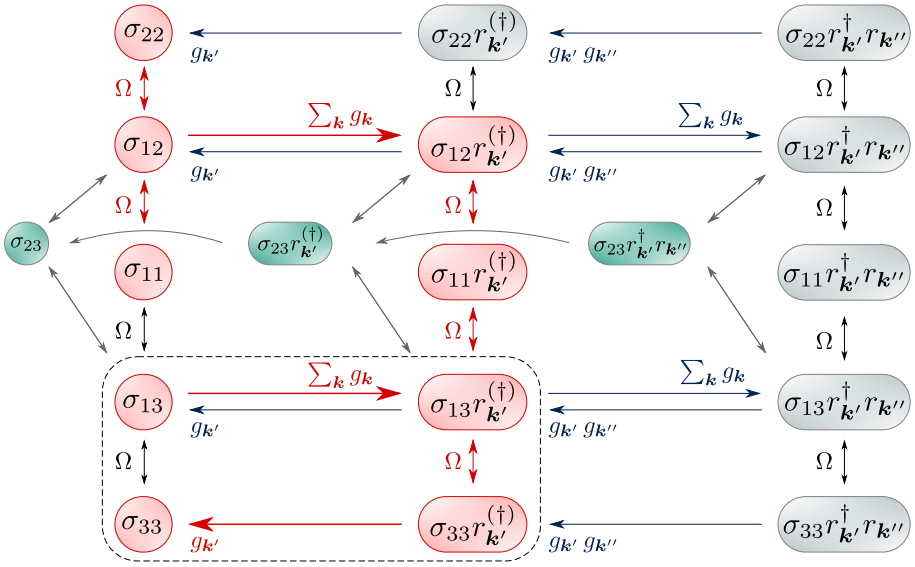


*Figure 7.3:* Diagrammatic representation of the Heisenberg equations of motion up to second order in phonon contributions for the $V$-type emitter. Red shapes and arrows highlight the key interactions enabling the observed population inversion. Green shapes represent the coherence $\sigma_{23}$ and its phonon-assisted amplitudes.

detuned state $\sigma_{33}$ (see Fig. 7.3). More explicitly, the energy is transported from $\sigma_{12} r_{\boldsymbol{k}}^{(\dagger)}$ via $\sigma_{11} r_{\boldsymbol{k}}^{(\dagger)}$, $\sigma_{13} r_{\boldsymbol{k}}^{(\dagger)}$ and $\sigma_{33} r_{\boldsymbol{k}}^{(\dagger)}$ to the detuned excited state $\sigma_{33}$. Once the excitation is transferred to $\sigma_{33}$, laser-driven transitions back to the ground state can in principle take place via the coherence $\sigma_{13}$. However, dissipative losses to the phonon mode continuum occur on a much faster time scale: Enabled by non-Markovian system-reservoir interactions via phonon-assisted amplitudes $\sigma_{13} r_{\boldsymbol{k}}^{(\dagger)}$ and $\sigma_{33} r_{\boldsymbol{k}}^{(\dagger)}$, the excitation becomes dynamically trapped in the laser-detuned state $\sigma_{33}$ (dashed frame in Fig. 7.3). Since energy localized in the two resonantly driven states $|1\rangle$ and $|2\rangle$ is permanently dissipated to level $|3\rangle$ through the reservoir, their population uniformly decays towards zero.

The relevant time scale enabling the population inversion is highly dependent on the relation between the driving strength $\Omega$ and the fermion-phonon coupling amplitude $g_k$. In Fig. 7.2, we employ a set of parameters with an energy detuning $\delta\epsilon = -1\,\mathrm{meV}$ (see Appendix C), resulting in the observed complete population inversion. However, the unfolding grade of inversion is highly susceptible to the choice of parameters and can be tuned, e.g., via the laser field amplitude and reservoir temperature. Moreover, the fermion-phonon coupling $g_{\boldsymbol{k}}$ can be tailored by nanotechnological engineering, e.g., using alloys, impurities and confinement potentials [210–213]. The coherence $\sigma_{23}$ and its phonon-assisted amplitudes (green shapes in Fig. 7.3) can be suspected to additionally facilitate the transfer, since they constitute a direct connection between the two excited states via the transition amplitudes $\sigma_{12}$ and $\sigma_{13}$. However, manually turning off all contributions from $\sigma_{23}$ and $\sigma_{23} r_{\boldsymbol{k}'}^{(\dagger)}$ does not prohibit the complete inversion exhibited in Fig. 7.2. The coherence dynamics $\sigma_{12}$, $\sigma_{13}$ and $\sigma_{23}$ of the $V$-type emitter is depicted in the inset: While $\sigma_{12}$ and $\sigma_{23}$ decay to zero in the course of time, $\sigma_{13}$ remains finite in the steady state

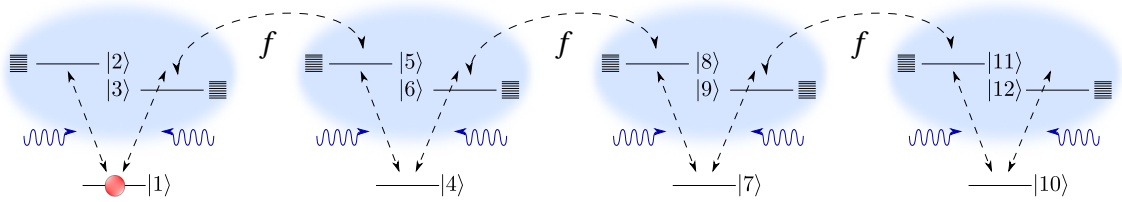


*Figure 7.4:* Multiple $V$-type emitters arranged in a chain and coupled by Dexter-type electron transfer at a coupling amplitude $f$, enabling a single interdot carrier transition via electronic wave function overlap.

since excitation in the laser-detuned level is constantly dissipated to the reservoir, dynamically trapping the energy and allowing for the formation of the observed nonequilibrium stationary state, which is not observed in a Lindblad-based evaluation of the here considered Hamiltonians. Furthermore, the grade of stationary population inversion is highly temperature-dependent: Increasing the temperature improves the potential for phonon-assisted transitions of energy back to the ground state and therefore perturbs the dynamical trapping of excitation, resulting in decreasing inversion. In the high-temperature regime, the level populations start to equilibrate until the inversion completely vanishes. We further elaborate on the temperature dependence in Sec. 7.5, where we also discuss the emergence of the effect from a different perspective via the bare eigenstate dynamics of the $V$-type model system.

## 7.4 Unidirectional quantum transport in a quantum dot chain

As an example application of the reported population inversion mechanism for quantum dot-based coherent transport devices, we arrange multiple $V$-type emitters in a closely spaced chain-like distribution schematically shown in Fig. 7.4. Here, we consider a generic Dexter-type bidirectional *electron transfer* as the enabling resonance energy transfer mechanism between the quantum dots [252]. This process describes a Coulomb-induced direct and spin-preserving electron exchange between semiconductor nanostructures and thus requires electronic wave function overlap between the respective donor and acceptor levels [252, 253]. Dexter transfer has been shown to take place, e.g., in self-assembled InAs quantum dot chains [254–260].

For a straightforward realization, we first consider the case where only two levels of neighboring quantum dots in the chain have an electronic wave function overlap, namely between the detuned excited state of the first and the resonantly driven excited state of the second emitter (see Fig. 7.4). In an experimental scenario, such a coupling can be achieved, e.g., by engineering the wave function overlap via the potential barriers between neighboring quantum emitters [261], or by tailoring of the relevant confinement potentials via electrical gating [262]. Furthermore, it is possible to utilize multiple type-2 quantum dots where the electrons and holes are not co-localized in the exciton states [263]. This simple coupling

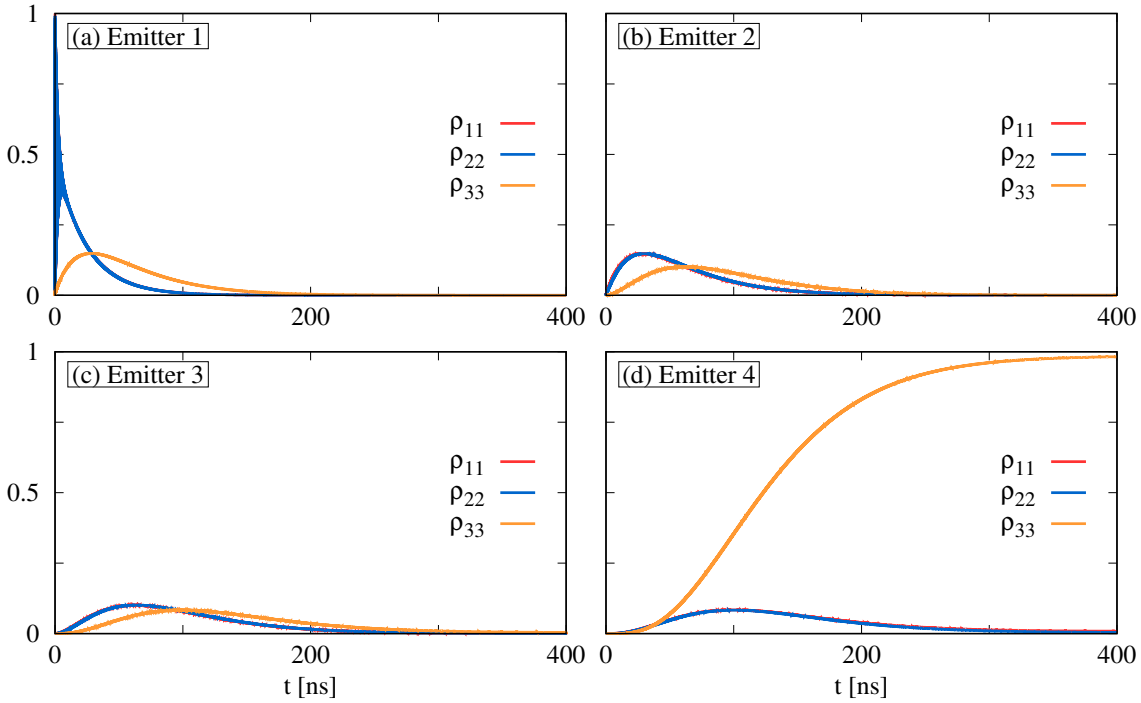


*Figure 7.5:* Population dynamics for a chain of $N = 4$ $V$-type emitters coupled via Dexter-type carrier transfer enabling a single interdot transition. All parameters are unchanged with respect to the single emitter calculations shown in Fig. 7.2.

scheme results in the most distinct unidirectional transport effect, however, in Sec. 7.5 we show that the mechanism still arises if all excited states of adjacent quantum dots are Dexter-coupled, albeit at a considerably lower degree. Moreover, we discuss Förster-type excitation transfer as an additional interdot coupling mechanism, yielding comparable results. Here we assume the single carrier case with a single electron initially localized in the ground state of the first emitter in the chain (see Fig. 7.4). Physical realizations of such a scenario can be achieved, e.g., by a doping of the first quantum dot and utilizing empty intersubband transitions in the conduction bands to facilitate $V$-type transitions. The resulting Dexter interdot coupling Hamiltonian is given by

$$H_D = \hbar f \sum_{l=0}^{N-2} \left[ \sigma_{(3+3l)(5+3l)} + \text{H.c.} \right], \tag{7.14}$$

with $f$ denoting the coupling amplitude between the emitters. Moreover, each emitter is assigned a separate phonon reservoir with independent coupling elements $g_{k_l}$. For a chain of $N$ quantum emitters, the resulting polaron master equation reads

$$\begin{aligned} \dot{\rho}_S(t) = &- \frac{i}{\hbar} \left[ H_{p,0}, \rho_S(t) \right] \\ &- \frac{\bar{\Omega}^2}{\hbar^2} \sum_{l,l'=0}^{N-1} \sum_{i,j=2,3} \int_0^t d\tau \sum_{s=\pm} \left\{ G_s(\tau) \left[ X_{s,j}^{[l]}, X_{s,i}^{[l']\prime} \rho_S \right] + \text{H.c.} \right\}, \end{aligned} \tag{7.15}$$

with

$$X^{[l]}_{+,i}(\tau) = \left[\sigma_{(1+3l)(i+3l)}(\tau) + \sigma_{(i+3l)(1+3l)}(\tau)\right], \tag{7.16a}$$

$$X^{[l]}_{-,i}(\tau) = i\left[\sigma_{(i+3l)(1+3l)}(\tau) - \sigma_{(1+3l)(i+3l)}(\tau)\right], \tag{7.16b}$$

and $H_{p,0}$ now comprising the Dexter interdot coupling Hamiltonian [Eq. (7.14)]. A detailed derivation of the polaron master equation for a chain of $N$ $V$-type emitters is provided in Appendix C.

The unfolding population dynamics for a chain of $N = 4$ emitters is shown in Fig. 7.5. Analogous to the single emitter case, a non-reciprocal, phonon-assisted excitation transfer to the detuned excited state takes place in each quantum dot, resulting in excitation transfer to the detuned state of the last emitter in the chain and corresponding to *perfect unidirectional electron transport*. This mechanism is facilitated by the population inversion effect rather than the here employed interdot coupling scheme: Initially, the population in level $|3\rangle$ of the first emitter rises at the same rate as in the single emitter case (see Fig. 7.2). Once a threshold occupation is attained, the Dexter coupling to the neighboring system begins to dominate, resulting in carrier transfer and an asymptotic decline of $|3\rangle$ towards zero, while the resonantly driven levels $|4\rangle$ and $|5\rangle$ of the second emitter start to become uniformly occupied. Once the excitation transfer sets in, the population inversion commences in the second emitter and in turn leads to a fast population decline in levels $|4\rangle$ and $|5\rangle$ and rising occupation in the laser-detuned level $|6\rangle$. This pattern repeats within each chain link until all excitation is transferred to the detuned excited state of the last emitter. Due to the temperature-dependent grade of population trapping, increasing temperatures result in a decreased stationary state inversion in the last emitter and overall slowed down transport, however, the unidirectional transport mechanism endures as long as population inversion is achieved.

The transport mechanism also withstands perturbations such as radiative decay processes, demonstrating the robustness of the underlying inversion mechanism. To account for incoherent radiative dissipation from the excited states to the ground state, we introduce a Lindblad dissipator of the form

$$\mathcal{L}_{rad}\rho = \gamma_r \sum_{l=1}^{N-1} \sum_{i=2,3} \left[2\sigma_{(1+3l)(i+3l)}\rho\sigma_{(i+3l)(1+3l)} - \{\sigma_{(i+3l)(i+3l)}, \rho\}\right], \tag{7.17}$$

where $\gamma_r$ denotes the radiative decay rate. In correspondence to Fig. 7.5, Fig. 7.6 shows the quantum dot chain population dynamics for $N = 4$ emitters including radiative decay at rate $\gamma_r = 0.1\,\mathrm{ns}^{-1}$. As a result of incoherent dissipation, the grade of inversion in the last emitter is decreased, however, the transfer mechanism itself is not suppressed by the radiative decay. Driven by the continuous laser field, the excitation is still transmitted to the last site of the quantum dot array.

In realistic scenarios, non-diagonal fermion-phonon interactions between the excited states of the emitters may impose an additional perturbation on the system. In Sec. 7.5, we demonstrate that the inclusion of intraband coupling processes slows down the population inversion process, but does not change the qualitative outcome. Moreover, we

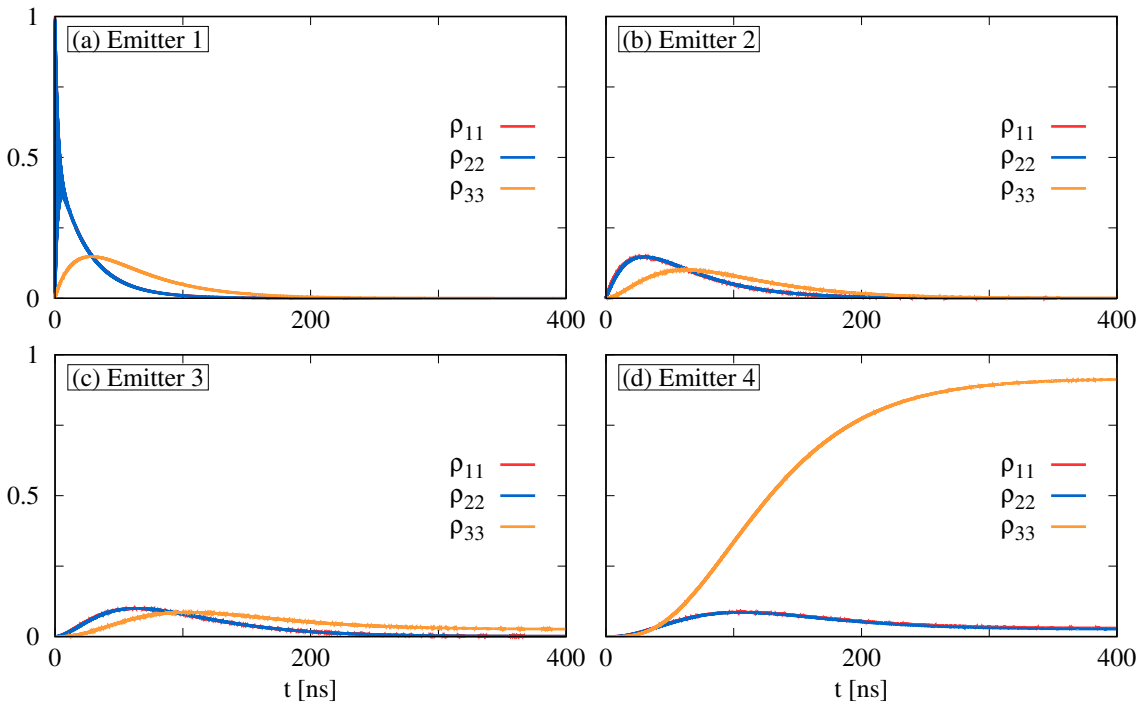


*Figure 7.6:* Population dynamics for a chain of $N = 4$ $V$-type emitters including radiative decay. All system parameters are set equal to the calculations presented in Fig. 7.5.

demonstrate the emergence of unidirectional quantum transport *regardless* of the employed interdot coupling by additionally considering (i) Dexter coupling with electronic wave function overlap between all excited states of adjacent emitters and (ii) Förster-type coupling between neighboring quantum dots [264], both exhibiting comparable unidirectional transport dynamics. In the latter scenario, *excitation energy transfer* is induced via dipole-dipole interactions and has been shown to arise in quantum dot arrays [230, 265–267]. Based on the predicted population inversion towards the red-detuned excited states in $V$-type quantum emitters, we have established a mechanism for unidirectional spatio-temporal transport of both excitation and carriers in quantum dot chains, constituting an example in which unidirectional, non-reciprocal quantum transport is achieved without application of an external bias and enabled solely by the interplay between coherence and incoherence in the system itself.

## 7.5 Discussion

### 7.5.1 Comparison between Heisenberg and polaron description

Aside from the second-order perturbative polaron master equation, we have employed a correlation expansion up to second order in phonon contributions in the Heisenberg

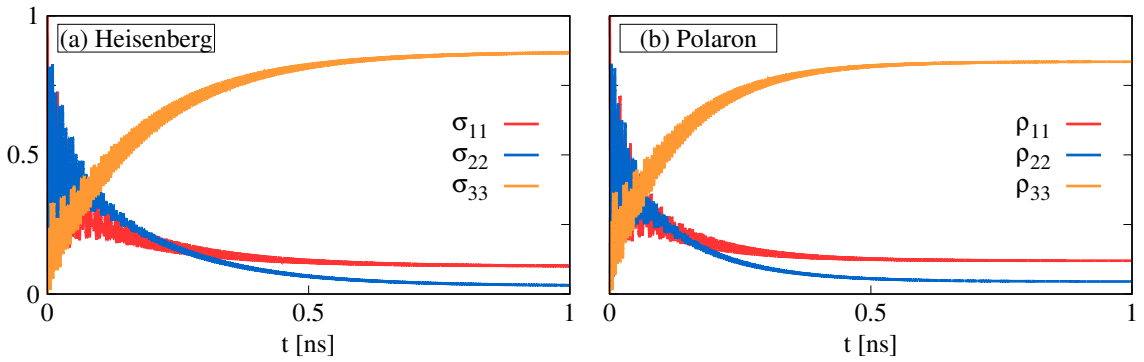


*Figure 7.7:* $V$-type emitter population dynamics calculated (a) using the Heisenberg picture approach and (b) using the polaron master equation.

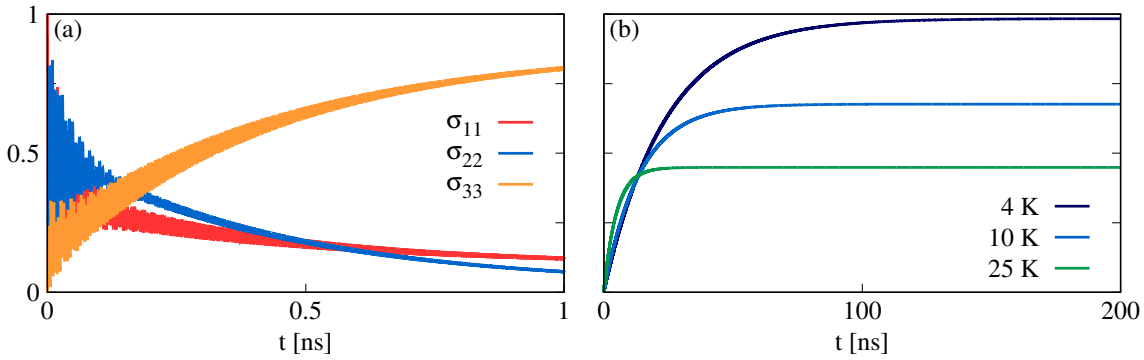


*Figure 7.8:* (a) $V$-type emitter population dynamics calculated in the Heisenberg picture including intraband couplings at amplitude $g_{\boldsymbol{k}}^{intra} = 0.1 g_{\boldsymbol{k}}$ and otherwise unchanged parameters with respect to Fig. 7.7. (b) Population dynamics of the laser-detuned excited state for increasing temperatures obtained from the polaron master equation.

picture to backtrace the key interactions responsible for the observed population inversion. The polaron master equation has been used for numerical calculations, since it allows for long simulation times and offers high performance and stability. The Heisenberg approach, on the other hand, requires a very fine time discretization and breaks down after a few million time steps, therefore limiting the accessible time evolution dynamics. Here we demonstrate the equivalence of the two approaches in a parameter regime where both implementations are stable and the systems' stationary state is obtained within accessible time frames. Fig. 7.7 shows the unfolding population dynamics at $T = 4\,\mathrm{K}$, $\delta\epsilon = -1.0\,\mathrm{meV}$, $\hbar\Omega = 0.3291\,\mathrm{meV}$ and a rescaled coupling element $\tilde{g}_k = 2.5 g_k$, obtained from (a) the Heisenberg correlation expansion and (b) the polaron master equation. During the polaron transformation of the system Hamiltonian, a polaron energy shift arises in the energy detuning between the excited states, i.e., $\Delta \to \bar{\Delta}$ [see Eq. (7.7)]. This energy shift does not affect the qualitative physical behavior with respect to the Heisenberg description, however, it leads to a small phase shift with minor impact on the population dynamics which becomes visible when comparing Figs. 7.7(a) and (b). Otherwise, the results obtained from the two descriptions are in excellent agreement with each other.

### 7.5.2 Dependence on intraband phonon coupling and temperature

As of yet, we have neglected possibly arising intraband phonon couplings between the two excited states of the $V$-type emitter [see Eq. (7.3)]. Since couplings of this form may occur in experimental scenarios featuring excited states with a low energy detuning, we have to validate their absence in our model. To this end, we calculate the Heisenberg picture population dynamics for a single emitter using an extended interaction Hamiltonian of the form

$$H_{el,ph} = \hbar \int \mathrm{d}^3k \, \left[ g_{\boldsymbol{k}} \left( \sigma_{22} + \sigma_{33} \right) + g_{\boldsymbol{k}}^{intra} \left( \sigma_{23} + \sigma_{32} \right) \right] \left( r_{\boldsymbol{k}}^{\dagger} + r_{\boldsymbol{k}} \right), \tag{7.18}$$

which explicitly includes real-valued intraband couplings $g_{\boldsymbol{k}}^{intra}$ between the two excited states. Fig. 7.8(a) shows the resulting occupation dynamics including intraband phonon couplings and otherwise unchanged parameters with respect to Fig. 7.7. Moreover, we have set the intraband coupling strength to a tenth of the interband coupling amplitude, i.e., $g_{\boldsymbol{k}}^{intra} = 0.1 g_{\boldsymbol{k}}$. As can be seen in Fig. 7.8, the population inversion slightly slows down while the overall qualitative behavior is maintained. Hence, disregarding the impact of possible intraband couplings is justified in the present investigation.

Fig. 7.8(b) illustrates the temperature-dependence of the stationary state population inversion, showing the $V$-type emitter population dynamics of the detuned excited state for increasing temperatures. Due to an increased potential for phonon-assisted transitions back to the ground state, the grade of inversion decreases for increasing temperatures. In the high-temperature regime, the system starts to equilibrate until the population inversion has vanished.

### 7.5.3 Linear absorption spectrum

As an illustration of the involved oscillator strengths, in Fig. 7.9 we show the linear absorption spectrum $\alpha(\omega) \sim \mathrm{Im}[\sigma_{12}(\omega)] + \mathrm{Im}[\sigma_{13}(\omega)]$ [80, 246, 268] (green line) calculated in the limit $\Omega \to 0$ at an incoherent decay rate $\gamma = 500\,\mathrm{ps}^{-1}$, $T = 4\,\mathrm{K}$, $\hbar\omega_{12} = 1\,\mathrm{eV}$ and $\hbar\omega_{13} = 0.999\,\mathrm{eV}$, corresponding to an energy detuning $\delta\epsilon = -1\,\mathrm{meV}$. Here, $\sigma_{mn}(\omega)$ represents the Fourier transform of the time-dependent coherence $\sigma_{mn}(t)$ $(m \neq n)$, prescribed by $\sigma_{mn}(\omega) = \int_{-\infty}^{\infty} \mathrm{d}t \; \sigma_{mn}(t) \exp(i\omega t)$. The blue line shows a comparison calculation without reservoir coupling, $g_{\boldsymbol{k}} = 0$, to highlight the impact of phonon interactions. The inset in Fig. 7.9 shows the absorption spectra on a logarithmic scale.

In the weak coupling and low temperature limit where the second-order Heisenberg correlation expansion is valid, the shape of the resulting absorption spectrum is determined by the employed oscillator strengths and the energy detuning $\delta\epsilon$ between the excited states of the $V$-type emitter. Fig. 7.9 features two peaks at $\hbar\omega_{12} = 1\,\mathrm{eV}$ and $\hbar\omega_{13} = 0.999\,\mathrm{eV}$, corresponding to the two allowed transitions between the ground state and excited states (green line). Compared to the case without phonon interactions (blue line), phonon-induced fluctuations in the form of absorption and emission processes give rise to phonon resonances with the system coherences and a modulation of the eigenenergies. As a result, the sidebands of the peaks feature an asymmetric broadening visible on a logarithmic scale (green

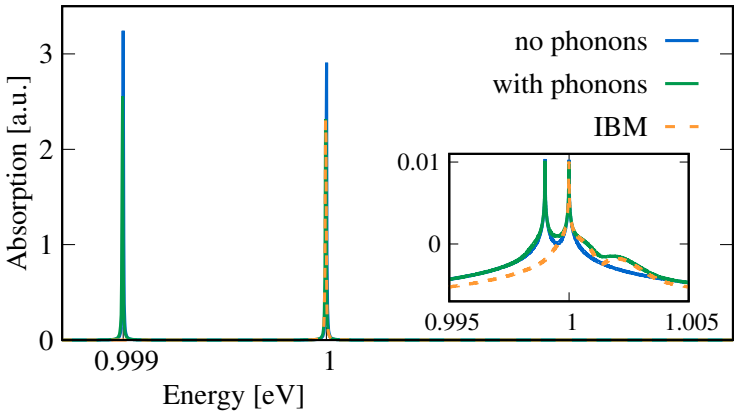


*Figure 7.9:* Linear absorption spectrum of the considered $V$-type emitter, calculated in the Heisenberg picture up to second order (blue line). For comparison, the spectrum resulting without the presence of a phonon reservoir is additionally shown (green line). The corresponding absorption spectrum of the analytically solvable *independent boson model* for a two-level system is depicted in orange. The inset shows the same spectra on a logarithmic scale, where a phonon-induced asymmetric broadening of the absorption peaks becomes visible.

line in inset). As an additional comparison, the dashed orange line in Fig. 7.9 shows the linear absorption spectrum of the exactly solvable *independent boson model* [96, 205, 269], describing a two-level system coupled to a structured phonon reservoir in the linear regime. The spectrum is obtained with the same set of parameters used for the $V$-type emitter case. Here, only a single optical transition is present, resulting in a single absorption peak. We note that the shape of the phonon sidebands visible on a logarithmic scale is dependent on the specific confinement potentials and the electronic wave function overlap (see inset). Overall, the spectrum is in very good agreement with the $V$-type model case, verifying the validity of the second-order Heisenberg correlation expansion in the employed parameter regime, with only minor variations on the logarithmic scale caused by superpositions with the second absorption peak.

### 7.5.4 Bare eigenstate dynamics

In addition to the interaction processes visible in the Heisenberg correlation expansion approach (see Sec. 7.3), the emergence of population inversion in the considered $V$-type emitter can be examined from a different perspective, i.e., via the dynamics of the bare density matrix eigenstates which are shown to be highly dependent on the energy detuning $\delta\epsilon$. In the absence of a phonon reservoir, the system Hamiltonian in matrix form is given by

$$H = \Omega \begin{pmatrix} 0 & 1 & 1 \\ 1 & 0 & 0 \\ 1 & 0 & \dfrac{\delta\epsilon}{\Omega} \end{pmatrix}. \tag{7.19}$$

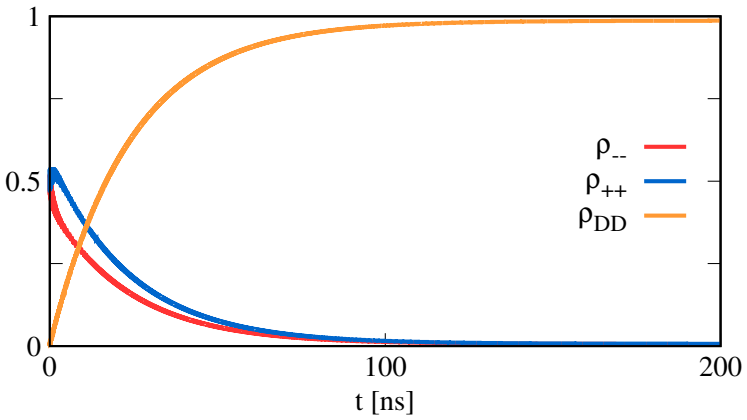


*Figure 7.10:* Population of density matrix eigenstates $|-\rangle$, $|+\rangle$ and $|D\rangle$ at $\delta\epsilon < 0$, corresponding to the single $V$-type emitter setup calculated in Fig. 7.2.

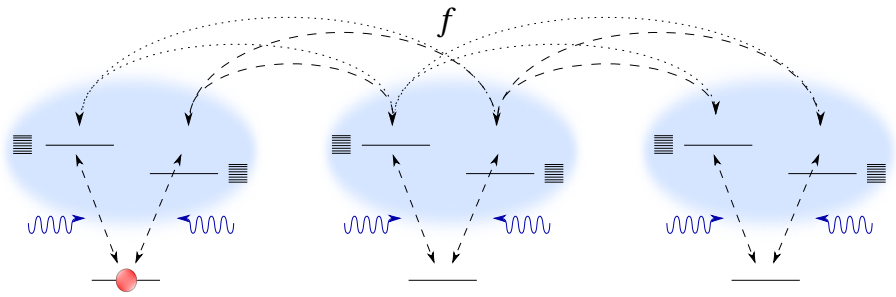


*Figure 7.11:* Dexter-coupled chain of $V$-type emitters with carrier transfer between *all* excited states of adjacent emitters at amplitude $f$.

When considering $\delta\epsilon = 0.0\,\mathrm{meV}$, the resulting eigenvalues can be calculated analytically, yielding

$$\lambda_- = -\sqrt{2}\Omega, \quad \lambda_+ = \sqrt{2}\Omega, \quad \lambda_D = 0. \tag{7.20}$$

Therefore, at zero energy detuning and without phonon interactions, the bare eigenstates of the system feature a vanishing eigenvalue $\lambda_D = 0$, corresponding to a dark state. In terms of the original basis states, the respective eigenstates read

$$|-\rangle = (-\sqrt{2}\,|1\rangle + |2\rangle + |3\rangle)/2, \tag{7.21a}$$

$$|+\rangle = (\sqrt{2}\,|1\rangle + |2\rangle + |3\rangle)/2, \tag{7.21b}$$

$$|D\rangle = (|2\rangle - |3\rangle)/\sqrt{2}. \tag{7.21c}$$

In correspondence to its vanishing eigenvalue, the asymmetric state $|D\rangle$ is completely unoccupied for the case $\delta\epsilon = 0$. The occupation dynamics of the system density matrix eigenstates $\rho_{--}$, $\rho_{++}$ and $\rho_{DD}$ for the here considered negative detuning $\delta\epsilon < 0$ are shown in Fig. 7.10, corresponding to the $V$-type emitter dynamics shown in Fig. 7.2. In this case, the asymmetric eigenstate $|D\rangle$ begins to weakly interact with the phonon reservoir and the laser field and becomes fully occupied via a non-reciprocal Stokes process (orange line in Fig. 7.10). Such effects have been shown to also emerge, e.g., in laser-pulsed exciton and biexciton systems [29, 34, 35, 217, 218].

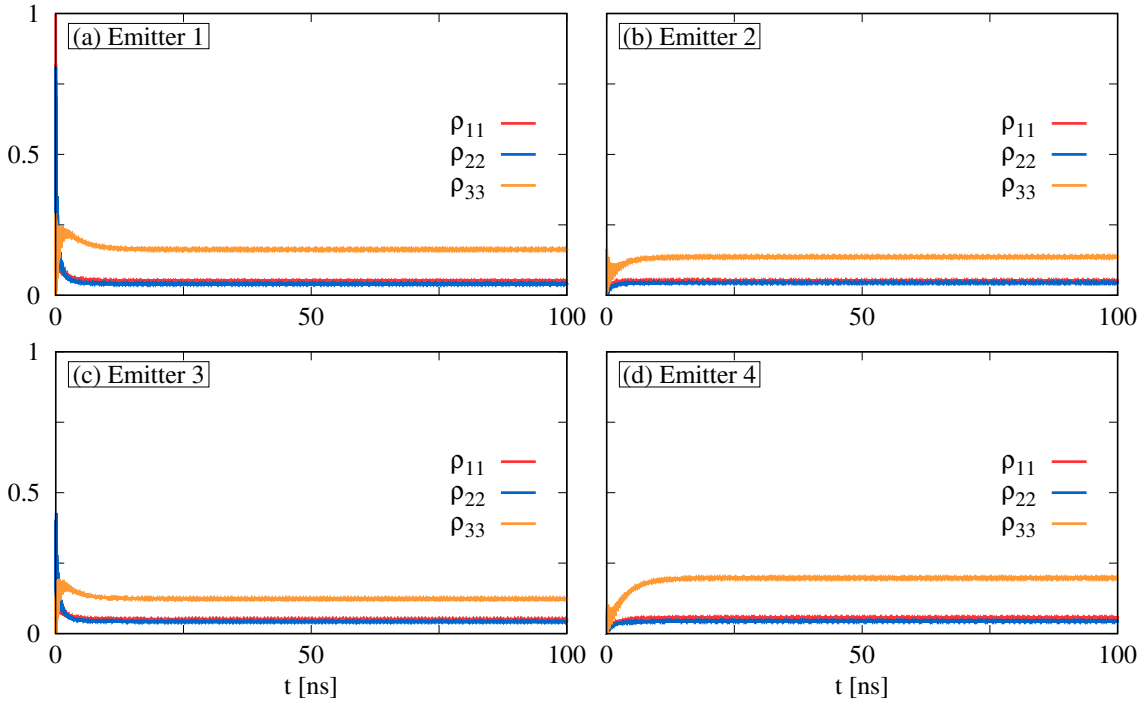


*Figure 7.12:* $V$-type emitter population dynamics for a Dexter-coupled chain of length $N = 4$ with carrier transfer between *all* excited states of neighboring emitters.

### 7.5.5 Alternative interdot coupling mechanisms: Dexter coupling

As an alternative interdot coupling mechanism enabling resonance energy transfer in the chain, we additionally consider Dexter-type electron transfer where *all* excited states of neighboring emitters feature wave function overlap (see Fig. 7.11) [252, 253]. Again, the single excitation case with a single electron initially localized in the ground state of the first emitter in the chain is considered. The resulting Dexter-type interdot coupling Hamiltonian is given by

$$H_D = \hbar f \sum_{l=0}^{N-2} \left[\sigma_{(2+3l)(5+3l)} + \sigma_{(2+3l)(6+3l)} + \sigma_{(3+3l)(5+3l)} + \sigma_{(3+3l)(6+3l)} + \text{H.c.}\right], \quad (7.22)$$

where $f$ again denotes the Dexter coupling amplitude. Increasing the wave function overlap has a considerable effect on the chain dynamics: Fig. 7.12 shows the resulting population dynamics for $N = 4$ emitters, corresponding to the parameters employed in Fig. 7.5. Since the excited states of all emitters support interdot coupling, energy is also transported from the end of the chain back to the first site, resulting in a periodic stationary state current in the quantum dot chain. Crucially, the population inversion still imposes unidirectionality, such that the total current is still directed from the first to the last site in the emitter array. The laser-detuned levels feature the majority of population, with the largest amount located in the last site of the chain. To conclude, unidirectional electron transfer can still be observed in the form of a directed stationary state current.

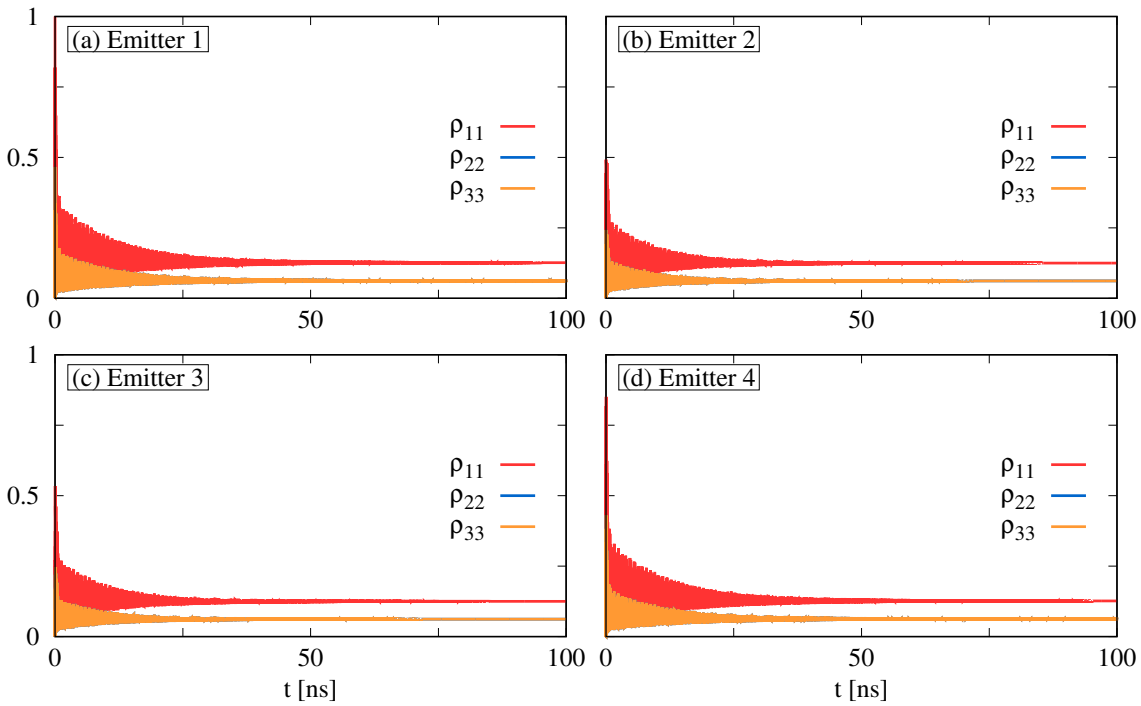


*Figure 7.13:* $V$-type emitter population dynamics at zero energy detuning $\delta\epsilon = 0$ and otherwise corresponding to the setup shown in Fig. 7.12.

To demonstrate the key role of the population trapping for the unidirectional transport mechanism, we additionally calculate the Dexter coupling setup shown in Fig. 7.12 once more at *zero energy detuning* $\delta\epsilon = 0.0\,\text{meV}$, where no population inversion is observed. The resulting chain dynamics is depicted in Fig. 7.13. In this case, carrier transport still takes place, however, without the emergence of a stationary state current: All quantum dots exhibit the same stationary state occupations, with the majority of excitation localized in the ground states (red lines). Hence, the here employed interdot coupling is not the crucial ingredient for the emergence of unidirectional transport, but rather the population trapping mechanism enabled by non-Markovian reservoir interactions.

### 7.5.6 Alternative interdot coupling mechanisms: Förster coupling

As a second alternative realization of interdot coupling, we employ a bidirectional dipole-dipole induced Förster excitation transfer mechanism [264]. Here, dipole-forbidden excitation transfer between closely located quantum dots can be enabled, e.g., via optical near-field interactions caused by exciton-polariton coupling [232, 270–274]. Here we consider such dipole-forbidden Förster-type couplings to enable excitation transport in the quantum dot chain via a wetting layer modeled by an additional level $|0\rangle$ in each emitter (see Fig. 7.14). The system is initialized with a single electron located in the ground state of the first emitter. In the remaining sites, a single excitation is initially localized in state

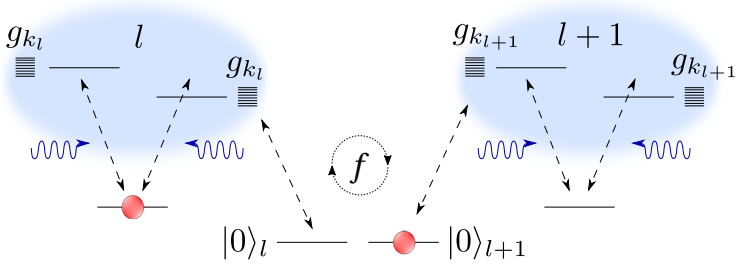


*Figure 7.14:* Realization of Förster-type dipole-dipole excitation transfer in a quantum dot chain at amplitude $f$ via an additional electron reservoir state $|0\rangle$.

$|0\rangle$. The resulting Förster-type interdot coupling Hamiltonian is given by

$$H_F = \hbar f \sum_{l=1}^{N-1} \left( \sigma_{03}^{l} \sigma_{20}^{l+1} + \text{H.c.} \right), \tag{7.23}$$

where the index $l$ denotes the emitters and $f$ refers to the Förster coupling amplitude.

Fig. 7.15 shows the population dynamics for a Förster-coupled $V$-type emitter chain of length $N = 2$, consistent with the chain dynamics observed for the case of a single Dexter-type transition between neighboring quantum emitters (see Fig. 7.5): Once more, the excitation is transferred through the reservoir to the detuned excited state on the first site and transported to the second emitter via dipole-dipole induced Förster interactions, where it becomes dynamically trapped in the laser-detuned level. Initially, the occupation of the first detuned level $|3\rangle_1$ rises in accordance with the single emitter setup (see Fig. 7.2), before dipole-dipole interactions with the neighboring site facilitate Förster resonance energy transfer and lead to an asymptotic decline of $|3\rangle_1$ towards zero. In consequence, the resonantly pumped levels $|1\rangle_2$ and $|2\rangle_2$ on the second site become uniformly occupied. Afterwards, the population inversion mechanism engages in the second quantum dot, yielding a quick rise of population in the laser-detuned level $|3\rangle_2$ accompanied by a decline in the resonantly driven levels $|1\rangle_2$ and $|2\rangle_2$. In the stationary state, all excitation is transported to the detuned excited level of the second emitter. In conclusion, we have demonstrated that the observed unidirectional quantum transport is robust against the specific interdot coupling mechanism in the quantum dot array and uniquely dependent on the underlying population inversion effect.

## 7.6 Conclusion

We have predicted the preparation of a nonequilibrium stationary state in a continuously driven $V$-type emitter featuring complete population inversion and enabled by non-Markovian system-reservoir interactions with the detuned excited states. Strikingly, the observed energy transfer mechanism has been shown to be robust against perturbations and external conditions such as incoherent radiative decay processes or phonon-induced intraband couplings, which may arise in $V$-type systems featuring a small energy detuning

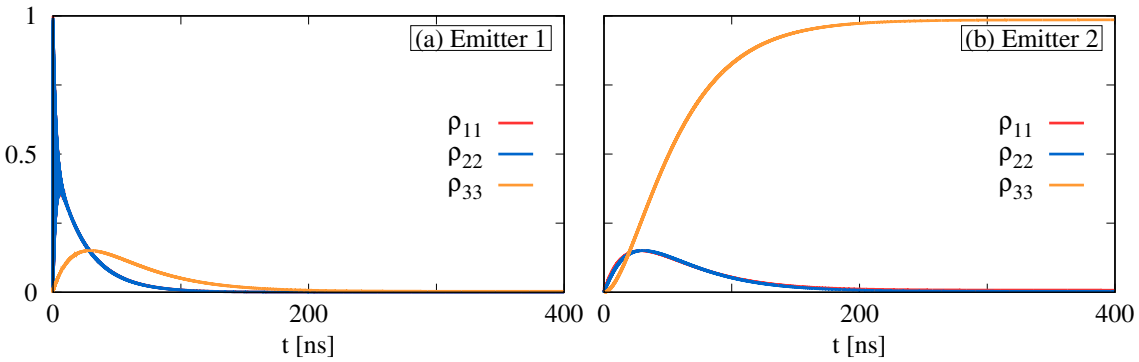


*Figure 7.15:* $V$-type emitter dynamics for a chain of length $N = 2$ coupled by Förster-type resonance energy transfer using the same set of parameters as for the single $V$-type emitter dynamics shown in Fig. 7.2.

between the excited states, allowing for complete inversion in a wide regime of tunable coupling and driving parameters.

As an example application of the reported inversion mechanism, we have predicted the emergence of unidirectional quantum transport of both carriers and excitation in an array of InAs/GaAs quantum dots, depending on the employed bidirectional interdot coupling mechanism. In summary, the presented non-Markovian population inversion can be accomplished in a wide array of realistic experimental conditions, giving rise to a range of potential applications utilizing carrier or excitation transport in quantum optical devices analogous to propositions of photonic unidirectional quantum transport in comparable scenarios [275–281]. The reported effect is also relevant for biological systems in the context of excitation transport processes for light harvesting mechanisms [237].

# 8 Dissipative coherent quantum feedback in Liouville space

In this Chapter, we consider a quantum optical system simultaneously coupled to both a continuous and a time-discrete structured reservoir. For the description of the continuous environment, a tensor network implementation of real-time path integrals is employed, improving the memory scaling from exponential to polynomial efficiency. Combined with a tensor network implementation of a time-discrete quantum memory, we construct a quasi-2D tensor network accounting for both diagonal and off-diagonal system-reservoir interactions with a twofold memory for continuous and discrete retardation effects. As an example application, we investigate the non-Markovian dynamical interplay between a structured acoustic phonon environment and time-discrete coherent photon feedback acting on an initially excited two-level system. As a result of emerging inter-reservoir correlations, long-living population trapping in the emitter is observed. The Chapter is closely based on the publication "Continuous and time-discrete non-Markovian system-reservoir interactions: Dissipative coherent quantum feedback in Liouville space" by O. Kästle et al. [71]

## 8.1 Introduction

Given the exponential scaling of the Hilbert space dimension for increasing system sizes, the accurate description of open quantum systems poses an immense challenge [25–27, 44]. Various theoretical approaches have been proposed to reduce their complexity, ranging from correlation expansions [28, 29] and second-order perturbative master equations [2, 3] to numerically exact path integral formulations for pure decoherence effects [30–38]. In general, all of these approaches have focused on system-reservoir interactions with a single structured environment, for instance in the form of a continuous reservoir or a time-discrete quantum memory, leading to time-delayed information backflow to the system and emerging non-Markovian phenomena [60–68].

In this Chapter, we develop a numerically exact tensor network implementation to describe two non-Markovian processes in the form of continuous and time-discrete retardation effects simultaneously, where both off-diagonal and diagonal system-reservoir couplings are accounted for, i.e., interactions with or without energy exchange between system and environment. Established tensor network techniques for the description of a time-discrete quantum memory focus on systems where decoherence effects are not crucially important, and thus rely on a wave function ansatz to solve the quantum stochastic Schrödinger equation [282–284]. Here, we first extend this architecture to a time bin-based density matrix


*Figure 8.1:* Sketch of an open quantum system coupled to both a time-discrete and a continuous structured reservoir.

formalism in Liouville space, allowing for the inclusion of Markovian and non-Markovian decoherence effects. Secondly, we combine this generalized MPS algorithm with a tensor network implementation of real-time path integrals (see Ch. 4) to incorporate the interplay with a continuous harmonic reservoir of independent oscillators [75–77, 102, 285], resulting in a novel quasi-2D tensor network architecture [286–289]. In this formalism, simulations of quantum systems coupled to two structured reservoirs become feasible (see Fig. 8.1), equally accounting for diagonal and off-diagonal interactions and maintaining crucial entanglement information in between system and reservoirs. Potential applications encompass, e.g., waveguide quantum electrodynamical setups with dephasing [67, 290–292] realized via additional decay channels, or multiple spatially separated solid-state quantum emitters coupled to an environment and initially prepared in a dark state [293]. To demonstrate the potential of the presented method, we specifically consider a two-level quantum emitter interacting with a structured reservoir of independent oscillators and additionally featuring a time-discrete quantum memory in the form coherent quantum feedback, extending the paradigm of the spin-boson model to feedback-related phenomena [74]. The unfolding non-Markovian interplay between decoherence and relaxation effects is shown to result in a dynamical protection of coherence against destructive interference processes, facilitating dynamical population trapping in the system. This observation expands upon the localized phase stabilization effect in the spin-boson model [74, 75] from an incoherent feedback-induced perspective, where the coherent external driving is replaced by another structured reservoir.

In Sec. 8.2, we briefly recall the numerically exact tensor network implementation of real-time path integrals to account for continuous reservoirs (see Ch. 4) and provide benchmark calculations for the independent boson model and the spin-boson model. Afterwards, the MPS realization of a time-discrete quantum memory in Liouville space is introduced in Sec. 8.3. In Sec. 8.4, we combine the two MPS algorithms to construct a quasi-2D tensor network architecture, enabling numerically exact calculations of a quantum system simultaneously exposed to two non-Markovian system-reservoir interactions. As an example application, in Sec. 8.5 we demonstrate the dynamical protection of feedback-induced coherence, resulting in population trapping in a two-level system. In Sec. 8.6, a convergence analysis of the reported results with respect to all relevant physical and numerical parameters is performed. Lastly, we summarize our findings in Sec. 8.7.

## 8.2 Path integral formulation for continuous reservoirs

As a first step, we calculate the time evolution dynamics of both the independent boson model and the spin-boson model using a numerically exact implementation of real-time path integrals [30–38] in a tensor network approach (see Ch. 4). In this framework, first introduced by *Strathearn et al.* [75, 76, 102, 285], the time-discrete path integral formulation of the reduced system density matrix is efficiently encoded in high-dimensional tensors.

The first objective is to derive a path integral solution of the von Neumann equation given a Hamiltonian $H(t)$ describing a time-dependent system-reservoir interaction [1, 268],

$$\dot{\rho}(t) = \mathcal{L}(t)\rho(t) = -\frac{i}{\hbar}[H(t), \rho(t)], \tag{8.1}$$

where $\rho(t)$ denotes the density matrix and $\mathcal{L}(t)$ the considered Liouvillian superoperator. Since the history of all preceding paths at times $0, \dots, t_{n-1}$ has to be taken into account for the evaluation of the current time step $t_n$, the numerical calculation of the path integral solution becomes very demanding after only a few time steps. To enhance numerical accessibility, in the case of finite system-reservoir correlations the *augmented density tensor* scheme can be applied [37, 38]. Here, a finite reservoir memory depth allows to only consider the last $n_c$ time steps for the calculation of the current path. This approach is referred to as the *finite memory approximation* and leads to the augmented density tensor representation, constituting a discrete path integral formulation as a solution to the system part of Eq. (8.1) with traced out reservoir contributions. At time $t_N = N\Delta t$ it is given by

$$\rho_{i_N i'_N}(t_N) = \prod_{n=1}^{N} \sum_{i_{n-1}} \sum_{i'_{n-1}} M_{i_n i_{n-1}} M^*_{i'_{n-1} i'_n} \prod_{m=n-n_c}^{n} \exp\left(S^{i_n i_m}_{i'_n i'_m}\right) \rho_{i_0 i'_0}(0), \tag{8.2}$$

with indices $i_n$, $i'_n$ storing the left and right configuration of the system at time $t_n = n\Delta t$ and $M_{i_n i_{n-1}}$ denoting the field transformation matrix which, e.g., accounts for an external driving field $\Omega_0$ present in the spin-boson model case. In the absence of external driving, $\Omega_0 = 0$, it is simply given by $M_{i_n i_{n-1}} = \mathbb{1}\delta_{i_n, i_{n-1}}$. The influence functional reads

$$S^{i_n i_m}_{i'_n i'_m} = -\left(i_n - i'_n\right)\left(\eta_{n-m} i_m - \eta^*_{n-m} i'_m\right), \tag{8.3}$$

with

$$\eta_{n-m} = \int_{(n-1)\Delta t}^{n\Delta t} \mathrm{d}\tau \int_{(m-1)\Delta t}^{m\Delta t} \mathrm{d}\tau'\, \phi(\tau - \tau'), \tag{8.4}$$

and $\phi(\tau - \tau')$ denoting the reservoir autocorrelation function [31, 32, 74]. Under the *improved* finite memory approximation, for $n-m \equiv n_c$ all preceding paths up to $t_{n_c} = n_c\Delta t$ are additionally included in the integration, yielding $\eta_{n_c} := \eta_{n-m} + \sum_{k=1}^{n-n_c-1} \eta_{n-k}$ (see Ch. 4) [102]. With this truncation, the augmented density tensor and its time evolution dynamics can be stated efficiently in the form of a tensor network [75]: As a first step, Eq. (8.2) is mapped to a vector $\rho_{j_n}$ in Liouville space,

$$\rho_{j_N}(t_N) = \prod_{n=1}^{N} \prod_{m=n-n_c}^{n} I(j_n, j_m)\rho_{j_0}(0), \tag{8.5}$$

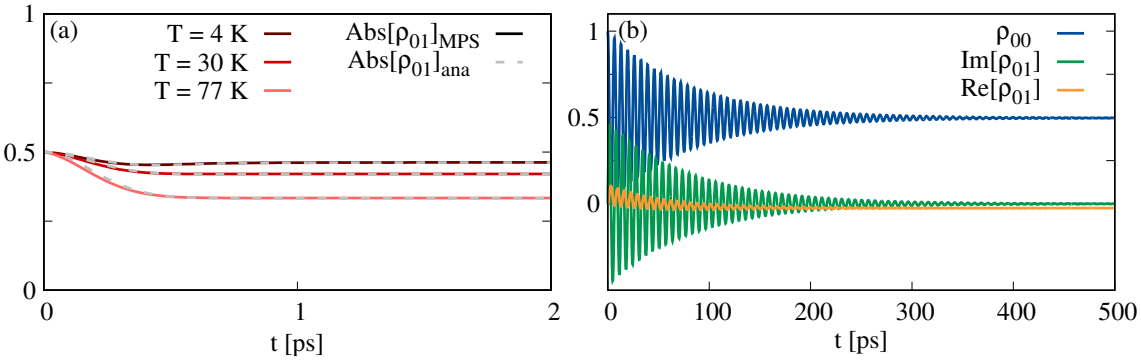


*Figure 8.2:* (a) Path integral solution of the independent boson model calculated at varying temperatures (solid lines) and compared to corresponding analytical solutions (dashed lines). (b) Path integral solution of the spin-boson model time evolution dynamics at a reservoir memory depth $n_c = 100$, driving field strength $\Omega_0 = 0.5\,\mathrm{ps}^{-1}$ and temperature $T = 77\,\mathrm{K}$.

with $I(j_n, j_m) := \sum_{j_{n-1}} \tilde{M}_{j_n j_{n-1}} \exp(\tilde{S}^{j_n j_m})$. The left and right system indices $i_k$, $i'_k$ are rewritten as a single index $j_k$ for each time step, yielding Liouville space representations $\tilde{M}_{j_n j_{n-1}}$ and $\tilde{S}^{j_n j_m}$ of the field transformation matrix and the influence functional. In addition, the augmented density tensor is decomposed into MPS format, with the present and up to $n_c - 1$ past states stored in individual tensors and the oldest state located at the left MPS boundary site. As a result of tensor compression via consecutive applications of the singular value decomposition at a finite Schmidt value cutoff precision [39], the required memory is reduced from exponential to polynomial scaling with respect to the number of incorporated paths $n_c$ [75].

The system time evolution dynamics is imposed by application of a network of MPOs (see Ch. 4). During each time step $n$, the current system state $\rho_{j_n}(t_n)$ is contracted with an MPO in the network, resulting in an updated system state MPS with the preceding path stored to the left of the system tensor, increasing the MPS length by one. After reaching step $n = n_c$, the oldest path in the MPS is summed over by application of a delta tensor in correspondence to the improved finite memory approximation [75, 102]. From this point on, the length of the MPS remains constant for the rest of the time evolution. In addition, for time-independent problems, aside from the index nomenclature the structure of the MPO remains unchanged for all time steps $n \geq n_c$, further improving performance. For the description of a continuous reservoir of noninteracting harmonic oscillators, we consider the Hamiltonian [96]

$$H_C/\hbar = \int \mathrm{d}^3 q \, \left[\omega_q b_{\boldsymbol{q}}^\dagger b_{\boldsymbol{q}} + g_{\boldsymbol{q}} \sigma_{11} \left(b_{\boldsymbol{q}}^\dagger e^{i\omega_q t} + \mathrm{H.c.}\right)\right], \tag{8.6}$$

imposing a diagonal system-reservoir coupling without energy transfer. Here, $\sigma_{ij} = |i\rangle\langle j|$ denotes system operators, $b_{\boldsymbol{q}}^{(\dagger)}$ are bosonic annihilation (creation) operators of reservoir modes at frequency $\omega_q = c_s|\boldsymbol{q}|$ and $c_s$ the sound velocity, and $g_{\boldsymbol{q}}$ denotes the mode $\boldsymbol{q}$-dependent system-reservoir coupling amplitude. The corresponding correlation function

is given by

$$\phi(\tau-\tau') = \int \mathrm{d}^3q\; g_{\boldsymbol{q}}^2 \Bigg\{ \coth\left(\frac{\hbar\omega_{\boldsymbol{q}}}{2k_BT}\right)\cos[\omega_q(\tau-\tau')] - i\sin[\omega_q(\tau-\tau')]\Bigg\}, \tag{8.7}$$

with $T$ the reservoir temperature and $k_B$ the Boltzmann constant. For our investigation, we employ a generic coupling element describing, e.g., acoustic bulk phonons interacting with a quantum emitter. Specifically, we choose the acoustic bulk phonon coupling element of GaAs, given by $g_{\boldsymbol{q}}^{ii} = \sqrt{\hbar q/(2\rho c_s)}D_i \exp[-\hbar q^2/(4m_i\omega_i)]$, resulting in a transition coupling element $g_{\boldsymbol{q}} := g_{\boldsymbol{q}}^{22} - g_{\boldsymbol{q}}^{11}$ [80, 97, 98, 251], with deformation potentials $D_i$, effective masses $m_i$, confinement energies $\hbar\omega_i$ and the mass density of GaAs $\rho$.

To verify the accuracy of the employed MPS path integral implementation, we first calculate the independent boson model where an analytical solution is available. It consists of a single two-level emitter embedded in a structured harmonic reservoir and subjected to pure dephasing, as described by Eq. (8.6). Fig. 8.2(a) shows the unfolding time evolution dynamics of the polarization $\rho_{01}(t)$ at varying temperatures $T$, initially prepared at $\rho_{01}(0) = 0.5i$ (solid lines). The corresponding analytical solution (dashed grey lines) is prescribed by [80]

$$\rho_{01}(t) = \exp\Bigg\{-\int \mathrm{d}^3q\; \frac{g_{\boldsymbol{q}}^2}{\omega_q^2}\left[i\omega_q t - i\sin(\omega_q t) + \coth\left(\frac{\hbar\omega_q}{2k_BT}\right)[1-\cos(\omega_q t)]\right]\Bigg\}\rho_{01}(0), \tag{8.8}$$

and exhibits excellent agreement with the numerical results for all featured temperature regimes. Moreover, due to the high numerical performance of the employed tensor network implementation, reservoir memory depths of $n_c = 100$ and beyond become accessible. As a second benchmark and to underline the performance capabilities of the MPS approach, we additionally calculate the time evolution dynamics of the spin-boson model by adding an additional continuous driving term at amplitude $\Omega_0$ to Eq. (8.6), i.e., $H_{SBM} = H_C + \Omega_0(\sigma_{01} + \sigma_{10})$. The resulting time evolution dynamics of the emitter ground state population and the system coherence are shown in Fig. 8.2(b), calculated at parameters $n_c = 100$, $\Omega_0 = 0.5\,\mathrm{ps}^{-1}$ and $T = 77\,\mathrm{K}$ for the memory, driving field and temperature, respectively.

## 8.3 Time-discrete memory in Liouville space

In addition to the continuous structured reservoir, we consider a discrete non-Markovian time-bin based quantum memory. Established realizations of such a time-discrete reservoir rely on an MPS-encoded wave function ansatz to solve to quantum stochastic Schrödinger equation [282–284]. However, we require a compatible formulation to the previously introduced path integral formalism defined in terms of the density matrix in Liouville space. Therefore, here we present an MPS implementation of a time-discrete quantum memory *in Liouville space*. The dynamics of the system density matrix is once more prescribed by a Liouvillian superoperator [see Eq. (8.1)], where a Hamiltonian $H_D$ accounts for the time-delayed system-reservoir coupling, such that interactions taking place at a given time $t$ couple back into the system and influence its state at a later time $t+\tau$, where $\tau$ denotes

the retardation time. Such a time-discrete coupling can arise, e.g., in a two-level system with states $|0\rangle$, $|1\rangle$ and an energy difference $\hbar\omega_0$ between them, located in front of a mirror with a round trip time $\tau$. The corresponding Hamiltonian is given by

$$H_D/\hbar = \omega_0\sigma_{11} + \sqrt{\frac{2\Gamma}{\pi}} \int \mathrm{d}k \ \sin\left(\frac{\omega_k\tau}{2}\right) \left[\sigma_{10} c_k e^{i(\omega_0-\omega_k)t} + \mathrm{H.c.}\right], \tag{8.9}$$

featuring off-diagonal coupling and energy exchange between system and environment, with system operators $\sigma_{ij} = |i\rangle\langle j|$, bosonic annihilation (creation) operators $c_k^{(\dagger)}$ of photon modes at frequency $\omega_k = ck$ with $c$ the speed of light, and a constant electron-photon coupling amplitude $\Gamma$.

The time evolution dynamics prescribed by the Liouvillian $\mathcal{L}(t)$ is translated into a time bin-based MPS realization [282–284, 288], maintaining crucial system-reservoir correlations and scaling with the feedback time $\tau$. When considering additional phenomenological dissipative channels, the Liouvillian is extended by the standard Lindblad operator [1, 268]. We start from the formal solution of the system part of Eq. (8.1) for the density matrix,

$$\rho(t) = T \exp\left[\int_0^t \mathrm{d}t' \ \mathcal{L}(t')\right] \rho(0), \tag{8.10}$$

with $T$ denoting the time-ordering operator. As a first step to restate Eq. (8.10) in terms of a tensor network algorithm it is rewritten in a time-discrete basis, yielding at time $t_N = N\Delta t$

$$\rho(t_N) = L(N, N-1)L(N-1, N-2)\ldots L(1,0), \tag{8.11}$$

at a time discretization $\Delta t$ and using time-bin normalized operators

$$L(n, n-1) = \exp\left[\sqrt{\Delta t}\int_{(n-1)\Delta t}^{n\Delta t} \mathrm{d}t' \ \mathcal{L}(t')\right]. \tag{8.12}$$

The Liouvillian time step operator $L(n, n-1)$ prescribes the time evolution dynamics during the $n$-th time step $t_{n-1} \to t_n$. As a next step, it is approximated by a *tenth order* series expansion,

$$L(n, n-1) \approx \sum_{m=0}^{10} \frac{\sqrt{\Delta t}^m}{m!} \left[\int_{(n-1)\Delta t}^{n\Delta t} \mathrm{d}t' \ \mathcal{L}(t')\right]^m. \tag{8.13}$$

In this format, Eq. (8.13) can be incorporated in a tensor network-based implementation of the time-discrete quantum memory, schematically shown in Fig. 8.3: Fig. 8.3(a) shows the time-bin based MPS at the start of the time evolution ($t = 0$), with the square red tensor storing the initial system density matrix. To account for a time-discrete memory, here $n_d = 4$ circular tensors located to the left of the system state contain the state of the reservoir in Liouville space at preceding times, with the oldest state located at the left boundary of the MPS (blue). In the here considered scenario, these memory bins are initially empty. The circular tensors located to the right of the system bin store the reservoir states for all future time steps, which have not been carried out yet and contain

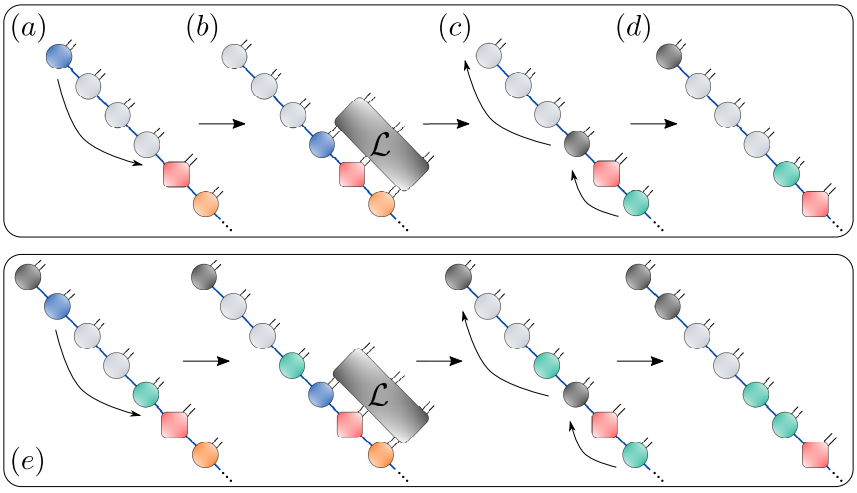


*Figure 8.3:* Tensor network realization of a time-discrete memory in Liouville space. (a)-(d) depict the operations performed during the initial time step, where the system state (red square) interacts with both present and past reservoir bins (orange and blue circles) by application of the Liouvillian $\mathcal{L}(t)$. (e) shows the second time step with analogous operations.

the full reservoir entanglement information, e.g., at a finite temperature. Since we assume an initial vacuum state, a new empty reservoir bin (orange) is added to the right of the system bin and represents the *current* state of the reservoir [see Fig. 8.3(a)].

The implementation of the time-discrete memory is explained next. Here, we introduce the memory retardation time $\tau = n_d \Delta t$ given by the number of initial memory bins $n_d$. For the first step of the time evolution [see Fig. 8.3(a)], the first memory bin (blue) is pushed to the left of the system bin (red) by consecutive applications of the singular value decomposition, maintaining crucial entanglement information (see Ch. 4) [39]. Afterwards, the time-discrete Liouvillian operator $L(1,0)$ prescribing the evolution during the first time step is applied to the system bin (red), the current memory bin (blue) and the current reservoir bin (orange), as depicted in Fig. 8.3(b). After contraction with the Liouvillian operator, the three bins are updated and the processed memory bin [dark grey bin in Fig. 8.3(c)] is swapped back to its original position on the left end of the MPS, where it remains for the rest of the time evolution [see Fig. 8.3(d)]. Crucially, the updated reservoir bin (green) is pushed to the left of the system bin and takes the role of a memory bin for a subsequent time step of the evolution [see Figs. 8.3(c),(d)]. In Fig. 8.3(d), the execution of the first time step is complete. All following time steps are carried out in the same fashion, as shown schematically for the second time step in Fig. 8.3(e). After the calculation of $n_d$ time steps, all memory bins initialized at the left of the system bin have been processed and pushed to the end of the MPS. At step $n_d + 1$, the reservoir bin employed during the first time step and pushed to the left of the MPS [green bin in Fig. 8.3(d)] becomes the current memory bin, storing information of a previous system state. By application of the corresponding Liouvillian time step operator, reservoir-induced memory effects unfold in the system according to the time-ordered problem.

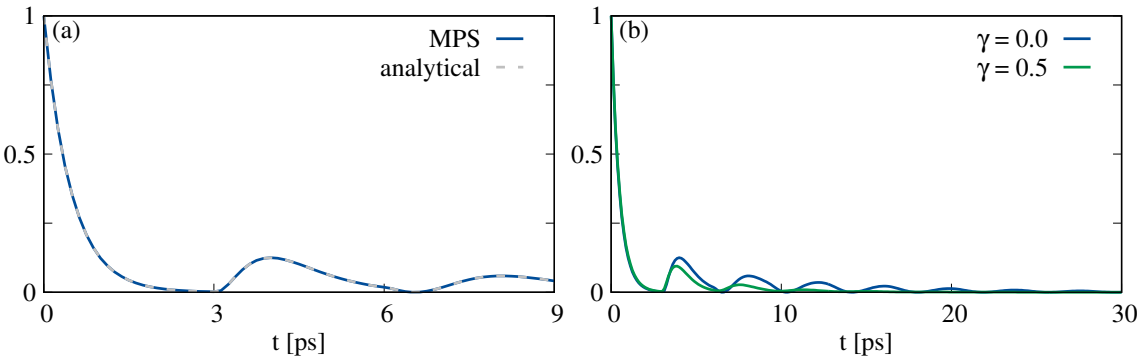


*Figure 8.4:* (a) Population dynamics of a two-level system subjected to time-discrete coherent quantum feedback [Eq. (8.9)] at parameters $\tau = 3\,\mathrm{ps}$ and $\Gamma = 31.6\,\mathrm{ps}^{-1}$. Numerical calculations carried out via the MPS algorithm (solid blue line) are in excellent agreement with the analytical result for the single excitation case (dashed grey line). (b) MPS population dynamics under time-discrete feedback calculated with an additional, analytically not accessible phenomenological dephasing rate $\gamma = 0.5\,\mathrm{ps}^{-1}$ (green line) and compared to the case without dephasing (blue line).

To verify the accuracy of the presented time-discrete memory algorithm in Liouville space, we first calculate the time evolution dynamics resulting from Eq. (8.9). Fig. 8.4(a) depicts the resulting emitter population dynamics at a retardation time $\tau = 3.0\,\mathrm{ps}$ and $\Gamma = 31.6\,\mathrm{ps}^{-1}$ obtained from the numerical MPS implementation (solid blue line) and compared to the analytical solution up to $t = 3\tau$ which is only available in the single excitation regime (dashed grey line). The latter is prescribed by $\langle\sigma_{11}(t)\rangle = |\langle\sigma_{01}(t)\rangle|^2$ with [294–296]

$$\langle\sigma_{01}(t)\rangle = \sum_{n=0}^{\infty} \frac{e^{-\Gamma t}}{n!} \left[\Gamma e^{(\Gamma - i\omega_0)\tau}(t - n\tau)\right]^n \Theta(t - n\tau), \tag{8.14}$$

exhibiting excellent agreement with the numerical result. In the here considered regime $\Gamma\tau \gg 1$, the delay in the amplitude dominates the time evolution dynamics and leads to emitter re-excitations at integer multiples of the feedback time $\tau$. However, the phase of the amplitude $\varphi = \omega_0\tau$ becomes irrelevant after the initial $\tau$-intervals due to increased decay of the mixing terms in the absolute square of Eq. (8.14). In previous realizations of a time-discrete quantum memory, investigations of the impact of phase-destroying processes have been limited to a special case, i.e., the emergence of an Ornstein-Uhlenbeck process during the initial feedback intervals [296]. Moreover, only an analytical approach had been available, limiting calculations to a small number of $\tau$-intervals and prohibiting access to the stationary state. The here presented numerical approach overcomes these limitations: The proposed Liouville space architecture allows to incorporate Markovian decoherence in the form of Lindblad dissipators without increased numerical costs.

Fig. 8.4(b) shows the time evolution dynamics of an initially excited two-level emitter subjected to coherent quantum feedback and additional phenomenological dephasing at rate $\gamma$, realized by embedding a Lindblad dissipator into the Liouvillian [Eq. (8.1)] and setting $H = H_D$, [1, 268]

$$\mathcal{D}\left[\sqrt{\gamma/2}\tilde{\sigma}_{11}\right]\rho(t) = \frac{\gamma}{2}[2\tilde{\sigma}_{11}\rho(t)\tilde{\sigma}_{11} - \{\rho(t), \tilde{\sigma}_{11}\}], \tag{8.15}$$

with the system operator rewritten in full configuration space, $\tilde{\sigma}_{11} = \mathbb{1}_D \sigma_{11} \mathbb{1}_D$, via the time-discrete reservoir basis $\mathbb{1}_D = \int \mathrm{d}k \sum_{n=0}^{\infty} |\{n_k\}\rangle \langle\{n_k\}|$. For comparison, we show the cases $\gamma = 0$ (blue line) and $\gamma = 0.5\,\mathrm{ps}^{-1}$ (green line). Crucially, the impact of pure dephasing begins to govern the dynamics only after the time-discrete memory signal re-excites the system and the stabilization of the incoming and outgoing phase becomes a factor. When considering an additional pure dephasing $\gamma \neq 0$, the initial decay of population remains unchanged, but the re-excitation becomes less distinct after the first feedback interval. After a few $\tau$-intervals only incoherent re-excitation occurs, resulting in a faster decay to zero without population trapping and regardless of the feedback phase $\varphi$.

These findings highlight the robustness of quantum feedback processes when accounting for additional Markovian dissipative channels. Due to the inevitable loss of quantum feedback-induced coherence, the presence of additional Markovian decoherence results in a degrading of the feedback signal. However, this is not necessarily the case when considering *non-Markovian* dissipation channels, which are incorporated next.

## 8.4 Quasi-2D tensor network

For a joint description of non-Markovian decoherence and time-discrete system-reservoir interactions, we combine the MPS implementation of the time-discrete quantum memory in Liouville space with the tensor network realization of real-time path integrals for continuous harmonic reservoirs, resulting in a *quasi-2D tensor network* architecture. The two networks are connected by link indices containing the arising entanglement information to enable a numerically exact description of correlation buildup *in between the reservoirs*. In scenarios involving multiple non-Markovian reservoirs connected to each other, such inter-reservoir correlations may have a crucial influence on the time evolution dynamics. Therefore, the arising inter-reservoir entanglement must be taken into account without strict truncation, for instance in the form of a high Schmidt value cutoff precision $d_{cut}$. The overall grade of entanglement in the system rises *intensively* with respect to the single reservoir setup. However, setups featuring two non-Markovian environments without crucial interactions between them, e.g., due to dynamical decoupling, allow for a much more restrictive truncation without loss of accuracy. In the here considered scenario, we have chosen a high Schmidt value cutoff precision $d_{cut} = 10^{-12}$, resulting in the conservation of relevant entanglement information during the time evolution.

Accurately depicting the dynamical interplay of the two reservoirs with each other and the system is an immense numerical challenge and poses strict limitations on the accessible memory depths for the here considered setup: While both of the presented MPS algorithms individually enable simulations of a single reservoir with deep memories, their combination results in restrictions caused by arising inter-reservoir entanglement. In consequence, the total number of memory bins in the quasi-2D network is constricted to $n_c + n_d < 20$ for the here considered model, as is the case in established path integral implementations for a single reservoir [32–36, 74]. It is noted once more that these limitations are a natural result of the high correlation degree in between system and reservoirs. The here presented

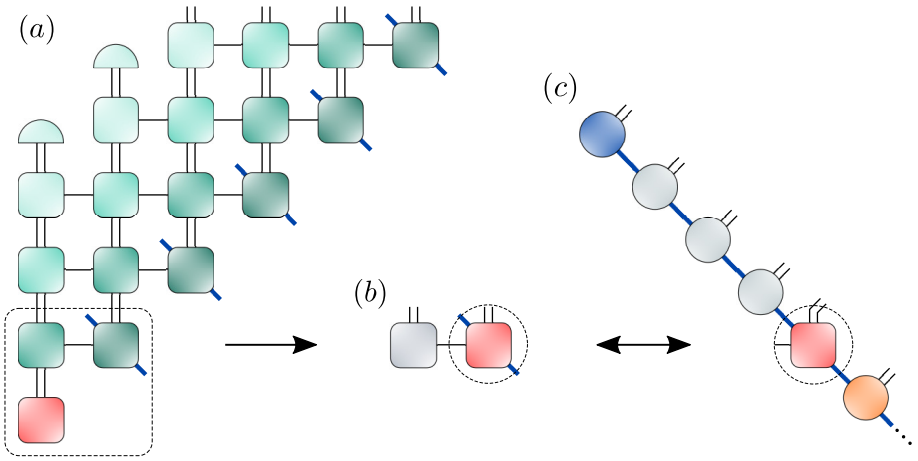


*Figure 8.5:* Implementation of the quasi-2D tensor network. (a) MPS-based path integral implementation for the simulation of continuous structured reservoirs. (b) MPS containing the current (red) and preceding system states (grey) after completion of the first network contraction [dashed square in (a)]. For the realization of the quasi-2D tensor network, an additional link index connects the current state tensor to the discrete memory MPS (blue diagonal line). (c) Time-discrete memory MPS during the initial time step, with the shared current system state tensor (red) acting as a junction between the reservoirs and the two networks (dashed circles).

quasi-2D tensor network is a first step towards investigations of the mostly unexplored field of multiple non-Markovian reservoir interactions, explicitly enabling information backflow in between the twofold reservoir memories.

Fig. 8.5 illustrates the construction of the quasi-2D tensor network via combination of the two previously introduced MPS algorithms for the continuous [Figs. 8.5(a),(b)] and time-discrete structured reservoirs [Fig. 8.5(c)]. They are connected to each other via a *shared* current system state tensor (red shape), acting as a junction link between the two reservoirs [dashed circles and blue lines in Figs. 8.5(b),(c)] and allowing for the storage of arising inter-reservoir correlations. During each step of the time evolution, the system bin is first subjected to the action of the continuous reservoir by a single contraction in the network shown in Fig. 8.5(a) (dashed frame). Afterwards, the updated current system bin [red shape in Fig. 8.5(b)] is inserted into the second MPS algorithm responsible for the action of the time-discrete reservoir [Fig. 8.5(c)]. The resulting quasi-2D tensor network effectively stores the history of both system-reservoir interactions, maintaining the relevant entanglement information in the open system and allowing for the calculation of two dynamically interacting time-delayed processes. As a first application and to demonstrate the capabilities of the presented quasi-2D network, we investigate the interplay of a continuous reservoir of independent oscillators with a time-discrete quantum memory realized by coherent quantum feedback. For specific memory depths and initial states, this scenario is shown to result in a dynamical protection of coherent quantum feedback properties in the open system and population trapping in the presence of non-Markovian decoherence processes.

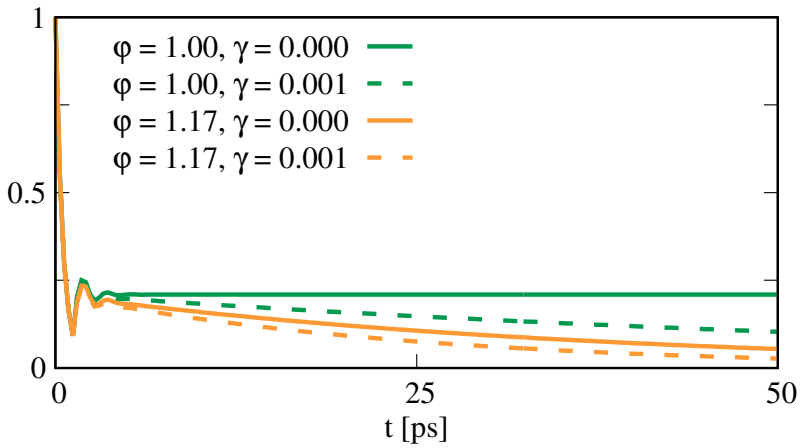


*Figure 8.6:* Excited state occupation dynamics of the two-level system subjected to time-discrete photon feedback at varying feedback phases $\varphi = \omega_0\tau/(2\pi)$ and constant phenomenological dephasing rates $\gamma$.

## 8.5 Memory-induced dynamical population trapping

Coherent quantum feedback mechanisms have been shown to feature a wide variety of non-Markovian phenomena [295, 297–302], e.g., leading to Ornstein-Uhlenbeck-type events in the presence of white noise [296], coherent population trapping [206, 283, 293, 303–305], or the formation of large entangled photon states [306]. However, until now these effects have not been investigated in the presence of additional non-Markovian dissipative channels or decoherence mechanisms. To explore the influence of dephasing on feedback-induced decoherence effects, we consider a two-level system placed in front of a mirror with a round trip time $\tau$, representing the time-discrete reservoir schematically shown in Fig. 8.1 and explicitly given by Eq. (8.9). The system is imprinted with a time-delayed coherence by the photon-induced feedback, taking the form of a feedback phase $\varphi = \omega_0\tau/(2\pi)$. This phase has a crucial impact on the system dynamics and is given by the feedback time $\tau$ and the transition frequency $\omega_0$ of the electronic coherence operator $\sigma_{12}$. We specifically consider a scenario which exhibits a pronounced quantum optical effect, i.e., coherent population trapping in an initially excited two-level emitter resulting from a continuum bound state at feedback phases $\varphi \in \mathbb{Z}$ [206, 283, 293, 296, 303–305]. The relevant system parameters are chosen at $\Gamma = 0.9\,\mathrm{ps}^{-1}$, $\tau = 1.2\,\mathrm{ps}$ and $n_d = 4$, yielding a time discretization $\Delta t = 0.3\,\mathrm{ps}$, for instance common for semiconductor quantum dot devices [206, 302, 305], and $\Gamma\tau \approx 1.1$, corresponding to the strong non-Markovian regime [282, 290, 296]. The coarse time discretization is justified by the tenth order series expansion of the time-discrete Liouvillian operator [see Eq. (8.13)], such that the employed $n_d = 4$ time bins are sufficient to achieve convergent results (see Sec. 8.6).

To demonstrate the potential of the presented quasi-2D tensor network approach, we first calculate the system dynamics prescribed by Eq. (8.9) for the case of Markovian dephasing introduced by the Lindblad dissipator in Eq. (8.15) at a phenomenological dephasing rate $\gamma$. Afterwards, it is compared to the case of non-Markovian decoherence imposed

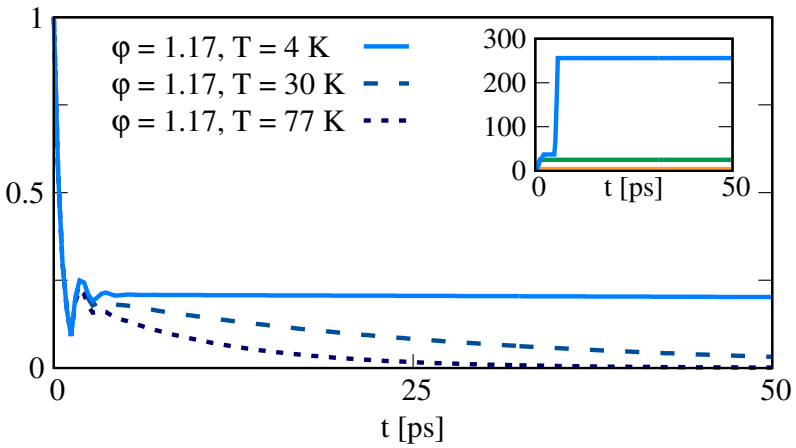


*Figure 8.7:* Excited state emitter occupation dynamics resulting from time-discrete photon and continuous phonon system-reservoir interactions at $\varphi \notin \mathbb{Z}$ and varying temperatures $T$. The inset shows the dimension of the link index connecting the system bin to the time-discrete memory MPS in the presence of a structured phonon reservoir (blue), without phonon coupling (green) and for phenomenological dephasing (orange).

by the continuous reservoir schematically shown in Fig. 8.1, resulting in an additional diagonal system-reservoir coupling. Fig. 8.6 shows the unfolding excited state emitter occupation dynamics for the case of Markovian dephasing at varying $\gamma$ and feedback phases $\varphi$. Without dissipation, $\gamma = 0$, the feedback phase can be periodically tuned to an ideal value $\varphi \in \mathbb{Z}$, such that constructive interference leads to a decoupling of the system from the environment, resulting in coherent population trapping (solid green line in Fig. 8.6). Introducing a nonzero dephasing $\gamma = 0.001\,\mathrm{ps}^{-1}$ to the system does not affect the population dynamics until the time-discrete feedback sets in, since the radiative decay is frequency-independent until the first feedback interval at $t = \tau$ (dashed green line). At this point, phenomenological dephasing destroys the coherent phase interference, resulting in an asymptotic decline of population to zero without population trapping. When choosing a nonideal feedback phase, here $\varphi = 1.17$, and zero dephasing, destructive phase interference also results in an asymptotic decline towards zero (solid orange line). Setting $\gamma > 0$ further accelerates the population decay (dashed orange line) due to the phenomenological decoherence perturbing the phase relation $\varphi$. To conclude, without the presence of a structured continuous reservoir and at feedback phases $\varphi \notin \mathbb{Z}$, asymptotic population decay via thermalization inevitably occurs, and a Lindblad-based incorporation of Markovian decoherence cannot preserve quantum correlations between the reservoir and system states under any conditions.

As a next step, we consider the case of a non-Markovian system-reservoir interaction inducing decoherence to the system. Employing the quasi-2D tensor network architecture, we calculate two-level emitter population dynamics prescribed by $H_D + H_C$ [Eqs. (8.6), (8.9)] at a continuous reservoir memory depth $n_c = 4$ and leaving all remaining parameters unchanged with respect to the results shown in Fig. 8.6. Fig. 8.7 shows the unfolding time evolution dynamics at varying temperatures $T$. For the here employed parameters, population trapping can be achieved at $T = 4\,\mathrm{K}$ and a nonideal feedback phase $\varphi = 1.17$,

i.e., $\varphi \notin \mathbb{Z}$ (solid blue line). Here, time-delayed backflow of excitation from the continuous structured environment to the emitter leads to a decoupling from destructive phase interference with the time-discrete photon reservoir, thereby facilitating information exchange and correlation buildup in between the reservoirs. As a result, feedback-induced coherence in the system is dynamically protected for long times. After a typical excitation backflow time, dynamical population trapping at a finite temperature can always be found by tuning of the feedback phase $\varphi$, if the relevant diffusion processes occur on a comparable time scale as the coherence-inducing feedback dynamics. For increasing temperatures, the dynamics becomes mainly governed by the thermal properties of the continuous phonon reservoir: Dashed and dotted blue lines in Fig. 8.7 depict resulting thermalization dynamics with population decay at $T = 30\,\mathrm{K}$ and $T = 77\,\mathrm{K}$, respectively. The observed temperature dependence evidences the importance of the correlation lengths within the full system-reservoir dynamics. Moreover, these otherwise inaccessible microscopic environmental properties can be effectively probed via the observed population trapping effect.

In close analogy to the observed formation of a self-stabilizing dissipative structure, a localized phase stabilization can be observed in the spin-boson model with coherent driving $\Omega_0 \neq 0$ at Ohmic spectral densities and without feedback effects [74, 75], where the open system transitions into a localized phase with a nonzero stationary emitter occupation above a critical system-reservoir coupling amplitude. In the here considered scenario, time-discrete photonic feedback replaces the coherent external driving field, resulting in a localized phase stabilization via dissipative non-Markovian interactions. As an estimation of the correlation buildup in between the two reservoirs, the inset in Fig. 8.7 shows the dynamical evolution of the link index dimension connecting the current system bin to the time-discrete memory MPS (see Fig. 8.5). In the case of a structured continuous reservoir (blue line in inset), after a slow buildup phase during times $t < \tau$ the index dimension swiftly increases to a maximum determined by the employed memory depths. The unfolding high grade of inter-reservoir entanglement at comparably low finite memory sizes $n_d = 4$, $n_c = 4$ highlights the essential role of the interplay between the two non-Markovian reservoirs for the observed protection of coherence. Switching off the continuous reservoir coupling, $g_{\boldsymbol{q}} = 0$, leads to a vastly decreased maximum link dimension (green line in inset), since no entanglement buildup occurs between the reservoirs. In the case of a phenomenological dephasing (orange line in inset), the link index dimension between system and reservoir bin in the resulting 1D network is even further reduced due to its highly decreased complexity.

## 8.6 Convergence analysis

In this Section, we provide a thorough convergence analysis of the presented results with respect to the relevant system parameters. Due to the memory limitations arising from the intensive scaling of entanglement when describing two non-Markovian reservoirs simultaneously, we first verify numerical convergence with respect to the memory depth of the continuous harmonic reservoir $n_c$, corresponding to the validity of the finite memory

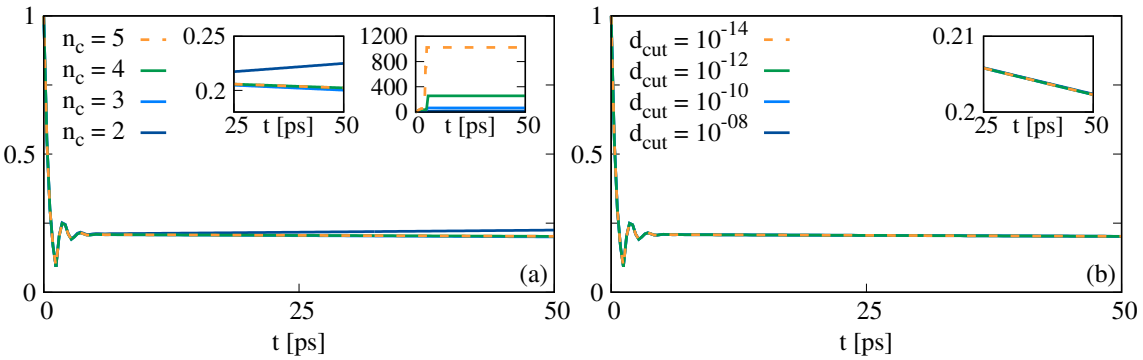


*Figure 8.8:* Convergence analysis of the calculations shown in Fig. 8.7 regarding (a) the continuous reservoir memory depth $n_c$ and (b) the Schmidt value cutoff precision $d_{cut}$ employed during the singular value decomposition. In (a), the left and right inset show a zoom-in on the dynamics and the resulting dimension of the link index connecting the two tensor networks, respectively. The inset in (b) depicts a zoom-in on the long term dynamics.

approximation for the considered setup. Fig. 8.8(a) shows the population dynamics corresponding to Fig. 8.7 at $\varphi = 1.17$, $T = 4\,\mathrm{K}$ and increasing memory depths $n_c$ of the continuous reservoir. The left and right inset show a zoom-in on the population dynamics and the resulting dimension of the link index connecting the two tensor networks, respectively. The latter again highlights the occurring exponential growth of inter-reservoir entanglement for increasing memory depths. At $n_c = 2$ [dark blue line in Fig. 8.8(a)], the results clearly do not converge, however, slightly increasing the memory depth to $n_c = 3$ and $n_c = 4$ (light blue and green lines) already leads to results in very good agreement with each other. Further increasing the memory depth to $n_c = 5$ (dashed orange line) leads to no visible deviation from the case $n_c = 4$ even at a close range (see left inset), verifying the numerical convergence at $n_c = 4$. In Fig. 8.8(b), we calculate the multiple reservoir case for varying Schmidt value cutoffs $d_{cut}$ applied during the tensor truncation procedure of the singular value decomposition [39]. Choosing cutoffs between $d_{cut} = 10^{-8}$ (dark blue line) and $d_{cut} = 10^{-14}$ (dashed orange line) leads to identical results even at a close range (see inset), demonstrating the numerical convergence with respect to the cutoff precision $d_{cut} = 10^{-12}$ employed for all calculations (green line). Therefore, no relevant entanglement information has been disregarded during the time propagation.

As a next step, we confirm numerical convergence of all presented results with respect to the employed time evolution step size $\Delta t$ to ensure the validity of the Trotter decomposition. In Fig. 8.9(a), we calculate the two-level emitter occupation dynamics when exposed to the time-discrete reservoir at $\varphi = 1.17$ (see Fig. 8.6) and decreasing step sizes $\Delta t$. Aside from small deviations during the initial steps of the time evolution, the results are in excellent agreement for all employed values of $\Delta t$, verifying the numerical convergence of the time-discrete MPS feedback algorithm at the chosen time discretization $\Delta t = 0.3\,\mathrm{ps}$ (light blue line). Fig. 8.9(b) shows the polarization dynamics of a two-level emitter coupled to a continuous reservoir, corresponding to the results shown in Fig. 8.2(b) and calculated at $T = 4\,\mathrm{K}$ and varying step sizes $\Delta t$. Once more, the unfolding time evolution dynamics

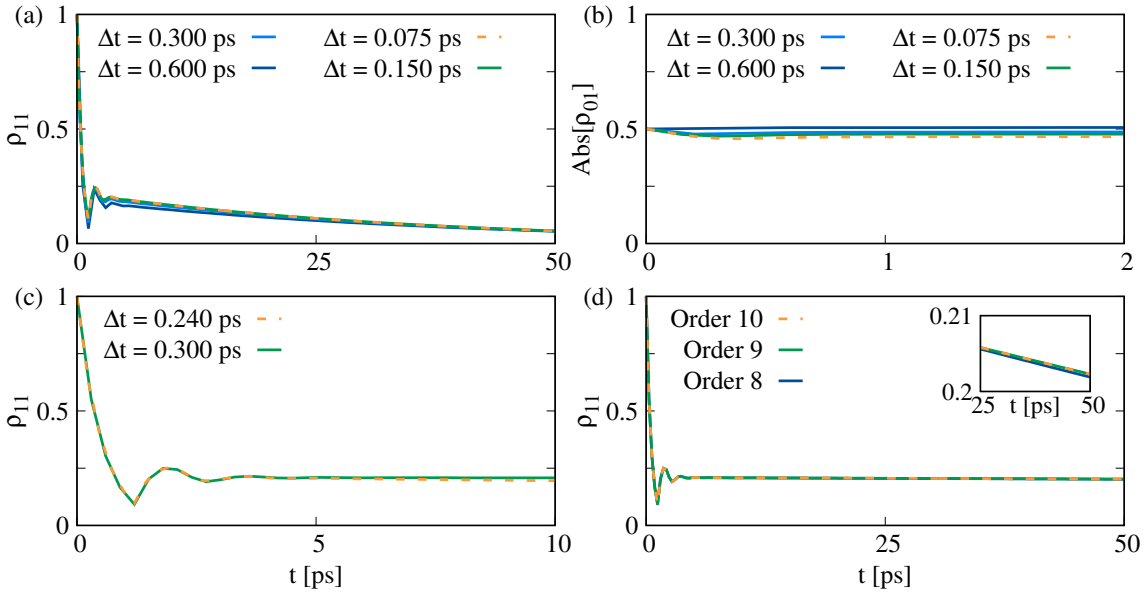


*Figure 8.9:* Convergence analysis of all calculations with respect to the time evolution step size $\Delta t$ applied in (a) the time-discrete reservoir algorithm (see Fig. 8.6), (b) the coherence time evolution dynamics for the continuous reservoir (see Fig. 8.2) and (c) the combined scenario (see Fig. 8.7). (d) shows a convergence analysis of the multiple reservoir case regarding the order of the series expansion applied to the time-discrete Liouvillian operator, with the inset showing a zoom-in on the long term dynamics.

at time discretizations $\Delta t = \{0.3\,\mathrm{ps}, 0.15\,\mathrm{ps}, 0.075\,\mathrm{ps}\}$ are in good agreement. Since the two individual algorithms for the time-discrete and continuous structured reservoir coupling both converge with respect to the time evolution step size, the combined setup in the quasi-2D tensor network can be expected to converge as well, since the involved time scales remain unchanged. In Fig. 8.9(c), we calculate the emitter occupation dynamics for the twofold reservoir case and varying time discretizations $\Delta t = \{0.3\,\mathrm{ps}, 0.24\,\mathrm{ps}\}$, corresponding to $n_d = \{4, 5\}$ time-discrete memory bins. Restricted by the accessible memory depths of both reservoirs and therefore the size of the time discretization at a given feedback time $\tau$, the convergence analysis with respect to the step size is limited to $t = 10\,\mathrm{ps}$, where good qualitative agreement can be observed. Finally, Fig. 8.9(d) shows a convergence analysis with respect to the series expansion order of the time-discrete Liouvillian operator [see Eq. (8.13)]. A small deviation between the series expansion orders eight and nine can be observed on a small scale (blue and green lines, see inset). However, comparing the dynamics corresponding to ninth and tenth order expansions of the Liouvillian exhibits excellent agreement, thus confirming the numerical convergence of the employed tenth order series expansion.

## 8.7 Conclusion

We have derived an MPS-based tensor network algorithm for the simulation of a time-discrete quantum memory based in Liouville space. Combining this method with a tensor network implementation of real-time path integrals for continuous structured reservoirs, we have established a novel quasi-2D tensor network architecture to enable simulations of quantum systems coupled to two non-Markovian environments with both diagonal and off-diagonal system-reservoir interactions and maintaining relevant system-reservoir and inter-reservoir entanglement. Arising correlations in between the structured reservoirs result in an intensive scaling of correlations with respect to the single reservoir setups. As a result, accessible memory depths are restricted to $n_c + n_d < 20$ in the here considered scenario. However, we stress that numerical convergence can be achieved in a wide range of conceivable setups, e.g., by tuning of the respective system and reservoir time scales. To further improve numerical efficiency with respect to memory scaling, it may be practical to trace out the time-discrete memory bins after their interaction with the system state via the Liouvillian operator. This treatment would allow for increased feedback times $\tau$ accompanied by smaller accessible time discretizations $\Delta t$ without altering the qualitative physics. The here established quasi-2D tensor network algorithm provides a numerically exact tool to gain access to the as of yet mostly unexplored field of multiple interacting non-Markovian environments.

As a first application, we have shown that the dynamical interaction and correlation buildup in between a structured phonon reservoir and time-discrete coherent photon feedback can result in a dynamical protection against destructive interference effects via time-delayed backflow of coherence, enabling the formation of dynamical population trapping. The formation of inter-reservoir correlations can be tuned via the relevant time scales of the non-Markovian system-reservoir interactions. The presented methods and results have potential applications in the fields of nonequilibrium physics, quantum thermodynamics and dynamical quantum phase transitions with ergodic, entropic or negentropic information exchange, where considering dynamical dissipative structures may unravel new phenomena. In future investigations, the presented quasi-2D network architecture may be further advanced to a true 2D implementation using projected entangled pair states with combined reservoir memory bins to enable simulations of multi-level systems and improving numerical performance.

# Part III

# Information compression in open quantum systems via artificial neural networks

# 9 Sampling asymmetric open quantum systems for artificial neural networks

In this Chapter, we extend the capabilities of the *restricted Boltzmann machine* neural network architecture using novel Hilbert space sampling techniques. Established artificial neural network methods based on the restricted Boltzmann machine and Metropolis sampling of configuration space have been shown to enable precise estimations of symmetric open spin-1/2 quantum systems. However, for systems without symmetries of translational invariance these techniques lead to systematic errors and poor scalability, independent of network parameters such as the sample size. To resolve this representational limit, we first propose a adjustment to the standard Metropolis algorithm, leading to enhanced convergence of the neural network. Secondly, we introduce a novel *hybrid sampling* strategy where asymmetric system properties are taken explicitly into account, resulting in high scalability and fast convergence times for asymmetric open spin-1/2 systems. The Chapter is closely based on the publication "Sampling asymmetric open quantum systems for artificial neural networks" by O. Kästle and A. Carmele [72].

## 9.1 Introduction

In recent breakthroughs, artificial neural networks have been successfully employed for the description of Markovian symmetric open spin-1/2 quantum systems [47–50, 52–54]. These network architectures offer a nearly limitless potential for numerical parallelization and can be iteratively optimized by application of a variational principle, giving direct access to the stationary state (see Ch. 5) [113, 114]. Combined with efficient compression of Hilbert space by application of the Metropolis algorithm where possible system configurations are sampled in a Markov chain Monte Carlo method, high-performing simulations of large symmetric systems have been fathomed [46, 104–106]. In particular, the restricted Boltzmann machine neural network architecture has emerged as a natural and highly efficient mapping of the density matrix of spin-1/2 quantum systems, since it allows for a one-to-one mapping of individual spins to artificial neurons while drastically reducing the required degrees of freedom [47, 51]. On its basis, simulations of large symmetric and periodic open spin-1/2 systems have been realized, including calculations for both stationary states [56, 57] and real-time evolution dynamics (see Ch. 5) [58, 59].

In this Chapter, we demonstrate that established configuration space sampling procedures are uneligible for the training of restricted Boltzmann machines constituting *asymmetric* open spin-1/2 quantum systems, i.e., setups without symmetries of translational invariance. As an example application, we investigate the stationary state of a boundary-driven

isotropic Heisenberg spin chain with open boundary conditions, featuring asymmetric properties [288, 289, 307–321]. As a first step, we provide converging neural network results for a symmetric Heisenberg chain and propose an adjustment to the standard Metropolis algorithm for the sampling of system configurations, further improving convergence and computational efficiency. Afterwards, we demonstrate that common Metropolis techniques for Hilbert space sampling result in a systematic overestimation of asymmetric system properties, independent of neural network parameters such as sample size or learning rate. To overcome this representational limitation, we introduce a *hybrid sampling* strategy to explicitly account for asymmetric system properties during Hilbert space compression. To this end, we combine the accuracy of exact Hilbert space mapping for sites with asymmetric properties with the performance advantage of regular sampling for the remaining subsystem. The presented sampling methods establish a powerful new ansatz for the optimization and training of artificial neural networks while maintaining a high scalability potential and fast convergence times at decreased noise.

The incoherently driven isotropic Heisenberg chain is introduced in Sec. 9.2. In Sec. 9.3, we discuss the implementation and training procedure of the employed neural network. Afterwards, we present an adjustment to the regular Metropolis algorithm in Sec. 9.4 and demonstrate resulting improvements in convergence using the example of a symmetric Heisenberg chain setup. In Sec. 9.5, we demonstrate that regular sampling strategies are unsuitable for the description of systems with asymmetric properties. As a solution, a *hybrid sampling* method is presented in Sec. 9.6, enabling accurate neural network simulations of large asymmetric systems. Lastly, we summarize our findings in Sec. 9.7.

## 9.2 Incoherently driven isotropic Heisenberg chain

To investigate the representational power of the restricted Boltzmann machine for systems without symmetries of translational invariance, we consider the incoherently driven isotropic Heisenberg chain shown schematically in Fig. 9.1, featuring $N$ spin-1/2 systems with next-neighbor coupling at amplitude $J$ and open boundary conditions. All sites $i$ of the chain are subjected to incoherent driving at rates $\gamma_{in}^{i}$ and dissipation at rates $\gamma_{out}^{i}$. The corresponding Hamiltonian reads [288, 289, 307–321]

$$H/\hbar = \frac{J}{4}\sum_{i=1}^{N-1}\left(\sigma_i^x\sigma_{i+1}^x + \sigma_i^y\sigma_{i+1}^y + \sigma_i^z\sigma_{i+1}^z\right), \tag{9.1}$$

where $\sigma_i$ denote Pauli spin matrices acting on individual sites $i$. To account for incoherent excitation and decay, we introduce the Lindblad dissipators [1, 268]

$$\mathcal{D}\left[\sqrt{\gamma_{out}^{i}/2}\sigma_i^-\right]\rho(t) = \frac{\gamma_{out}^{i}}{2}\left[2\sigma_i^-\rho(t)\sigma_i^+ - \{\sigma_i^+\sigma_i^-,\rho(t)\}\right], \tag{9.2a}$$

$$\mathcal{D}\left[\sqrt{\gamma_{in}^{i}/2}\sigma_i^+\right]\rho(t) = \frac{\gamma_{in}^{i}}{2}\left[2\sigma_i^+\rho(t)\sigma_i^- - \{\sigma_i^-\sigma_i^+,\rho(t)\}\right]. \tag{9.2b}$$

To incorporate asymmetric properties, a boundary-driven scenario with increased driving on the first chain site, $\gamma_{in}^{1} > \gamma_{out}^{1}$ (red shape in Fig. 9.1), increased decay on the right

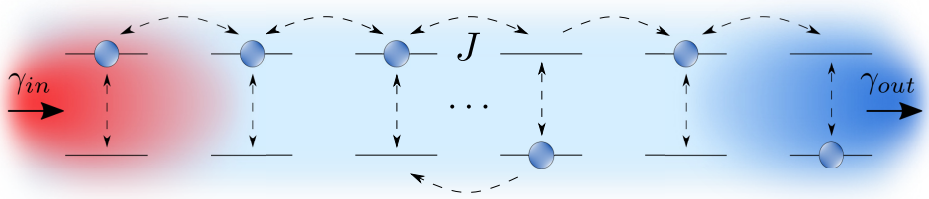


*Figure 9.1:* Schematic of a boundary-driven isotropic Heisenberg chain with increased driving on the left boundary, $\gamma_{in}^1 > \gamma_{out}^1$ (red shape), increased decay on the right boundary, $\gamma_{out}^N > \gamma_{in}^N$ (dark blue shape), and equal driving and dissipation $\gamma_{in}^i = \gamma_{out}^i$ in the bulk (light blue shape).

boundary, $\gamma_{out}^N > \gamma_{in}^N$ (dark blue shape), and equal driving and dissipation $\gamma_{in}^i = \gamma_{out}^i$ in the bulk (light blue shape) is assumed. In total, the resulting time evolution dynamics in Liouville space is prescribed by

$$\dot{\rho}(t) = \mathcal{L}\rho(t) = -i[H/\hbar, \rho(t)] + \sum_{i=1}^{N} \left\{ \mathcal{D}\left[\sqrt{\gamma_{out}^i/2}\sigma_i^-\right] + \mathcal{D}\left[\sqrt{\gamma_{in}^i/2}\sigma_i^+\right] \right\} \rho(t), \tag{9.3}$$

and can be solved, e.g., in a common fourth order Runge Kutta approach where system sizes of typically $N \lesssim 14$ can be accessed without requiring high-performing computational resources. In the following investigations, we employ such brute force density matrix calculations as a benchmark for the results obtained from the restricted Boltzmann machine neural network.

## 9.3 Neural network implementation

For a neural network realization of open spin-1/2 quantum systems, the density matrix is estimated by a probabilistic architecture, replacing $2^{2N}$ density matrix elements $\langle \boldsymbol{\sigma} | \rho | \boldsymbol{\eta} \rangle = \langle \sigma_1, \ldots, \sigma_N | \rho | \eta_1, \ldots, \eta_N \rangle$ of a setup consisting of $N$ spin-1/2 systems by a set of variational training parameters as degrees of freedom. The restricted Boltzmann machine architecture has recently emerged as a natural mapping of the density matrix for symmetric open spin-1/2 quantum systems, since it enables a straightforward mapping of spins to artificial neurons [47, 51, 56–59, 78, 79, 115, 322]. It generates a model distribution called *neural density operator* shown schematically in Fig. 9.2, featuring a visible layer of $2N$ sites $\boldsymbol{\sigma}$ and $\boldsymbol{\eta}$ for the representation of the left and right side of the density matrix, two auxiliary hidden layers each consisting of $M$ sites $\boldsymbol{h}^\sigma$ and $\boldsymbol{h}^\eta$, respectively, and an ancillary mixing layer of $K$ sites $\boldsymbol{h}^\mu$. Tracing out the hidden and ancillary degrees of freedom, the neural density operator elements are given by (see Ch. 5)

$$\begin{aligned} \rho_{\vartheta}(\boldsymbol{\sigma}, \boldsymbol{\eta}) = \prod_{m=1}^{M} \prod_{k=1}^{K} 8 \exp\left(\sum_{i=1}^{N} a_i \sigma_i\right) \exp\left(\sum_{i=1}^{N} a_i^* \eta_i\right) \cosh\left(b_m + \sum_{i=1}^{N} W_{mi} \sigma_i\right) \\ \times \cosh\left(b_m^* + \sum_{i=1}^{N} W_{mi}^* \eta_i\right) \cosh\left(c_k + c_k^* + \sum_{i=1}^{N} U_{ki} \sigma_i + \sum_{i=1}^{N} U_{ki}^* \eta_i\right), \end{aligned} \tag{9.4}$$

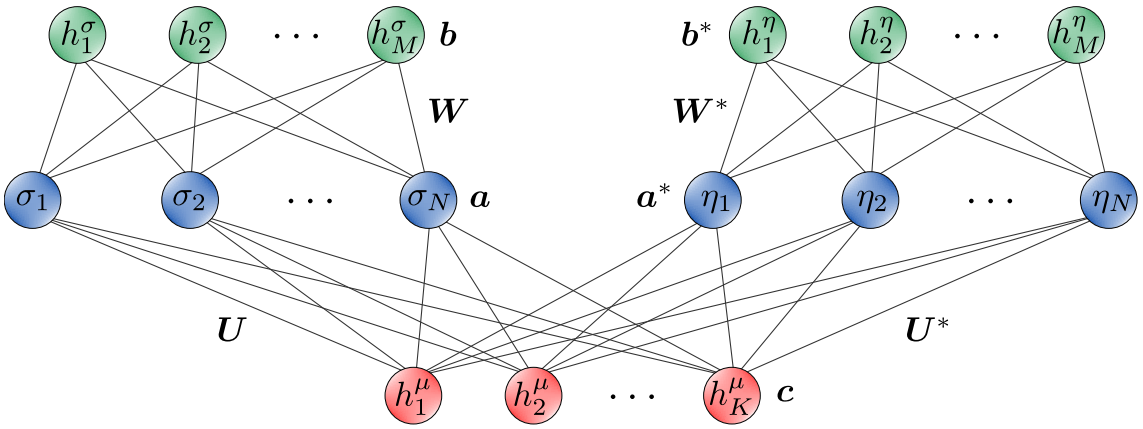


*Figure 9.2:* Schematic of a restricted Boltzmann machine constituting the *neural density operator* with variational parameters $\boldsymbol{\vartheta} = (\boldsymbol{a}, \boldsymbol{b}, \boldsymbol{c}, \boldsymbol{W}, \boldsymbol{U})$ as degrees of freedom, consisting of a visible layer (blue), two auxiliary hidden layers (green) and an ancillary mixing layer (red) connecting the left and right side.

depending on a set of complex training parameters $\boldsymbol{\vartheta} = (\boldsymbol{a}, \boldsymbol{b}, \boldsymbol{c}, \boldsymbol{W}, \boldsymbol{U})$ divided into real and imaginary parts, yielding a total of $n_p = 2N + 2M + K + 2MN + 2KN$ elements representing the neural network degrees of freedom. The training parameters consist of biases $\boldsymbol{a}$ for visible neurons, $\boldsymbol{b}$ for auxiliary hidden sites and $\boldsymbol{c}$ for the ancillary mixing layer, respectively. The complex weights $\boldsymbol{W}$ connect visible neurons $\boldsymbol{\sigma}$ and $\boldsymbol{\eta}$ to their auxiliary hidden counterparts $\boldsymbol{h}^\sigma$ and $\boldsymbol{h}^\eta$, whereas weights $\boldsymbol{U}$ couple visible units to the ancillary mixing layer $\boldsymbol{h}^\mu$ (see Fig. 9.2).

The training objective is to estimate the unknown density matrix $\rho$ by the neural density operator $\rho_{\boldsymbol{\vartheta}}$ via iterative variation of the parameter set $\boldsymbol{\vartheta}$. During each training iteration, input data is generated by drawing $N_s$ samples of possible system configurations from Hilbert space. Using the stochastic reconfiguration approach [117–119], occurrence probabilities and system observables are approximated as statistical expectation values over all drawn sample configurations. The normalized occurrence probability of the $n$-th drawn sample $(\boldsymbol{\sigma}_n, \boldsymbol{\eta}_n)$ is obtained via the estimated neural density operator partition function by summing over all $N_s$ samples drawn during one iteration, resulting in the probability

$$\tilde{p}_{\boldsymbol{\vartheta}}(\boldsymbol{\sigma}_n, \boldsymbol{\eta}_n) = \frac{|\rho_{\boldsymbol{\vartheta}}(\boldsymbol{\sigma}_n, \boldsymbol{\eta}_n)|^2}{\sum_{n=1}^{N_s} |\rho_{\boldsymbol{\vartheta}}(\boldsymbol{\sigma}_n, \boldsymbol{\eta}_n)|^2}. \tag{9.5}$$

In the same fashion, expectation values of diagonal observables are approximated as statistical averages [57–59, 117–119]

$$\langle X(\boldsymbol{\sigma}, \boldsymbol{\sigma}) \rangle \approx \langle\langle X(\boldsymbol{\sigma}, \boldsymbol{\sigma}) \rangle\rangle_q = \sum_{n=1}^{N_s} \tilde{q}_{\boldsymbol{\vartheta}}(\boldsymbol{\sigma}_n) \sum_{\boldsymbol{\xi}} \frac{X(\boldsymbol{\sigma}_n, \boldsymbol{\xi}) \rho_{\boldsymbol{\vartheta}}(\boldsymbol{\xi}, \boldsymbol{\sigma}_n)}{\rho_{\boldsymbol{\vartheta}}(\boldsymbol{\sigma}_n, \boldsymbol{\sigma}_n)}, \tag{9.6}$$

where we have introduced a probability distribution for diagonal samples

$$\tilde{q}_{\boldsymbol{\vartheta}}(\boldsymbol{\sigma}_n) = \frac{\rho_{\boldsymbol{\vartheta}}(\boldsymbol{\sigma}_n, \boldsymbol{\sigma}_n)}{\sum_{n=1}^{N_s} \rho_{\boldsymbol{\vartheta}}(\boldsymbol{\sigma}_n, \boldsymbol{\sigma}_n)}. \tag{9.7}$$

Since only diagonal observables are figures of merit in the here considered setup, $\tilde{q}_{\boldsymbol{\vartheta}}(\boldsymbol{\sigma})$ is employed to calculate diagonal expectation values for further improved numerical efficiency, while $\tilde{p}_{\boldsymbol{\vartheta}}(\boldsymbol{\sigma},\boldsymbol{\eta})$ is used for the training of the network.

The training goal is to estimate the stationary state of the considered model system, prescribed by the condition $\dot{\rho}(t) = \mathcal{L}\rho(t) = 0$. For the variational optimization of the network, we define a corresponding cost function $C(\boldsymbol{\vartheta}) = \|\mathcal{L}\rho_{\boldsymbol{\vartheta}}\|_2^2$ [57, 59]. During each training iteration $t \to t+1$, the variational parameters $\boldsymbol{\vartheta}$ constituting the degrees of freedom of the neural density operator are optimized and updated via the standard stochastic gradient descent procedure, obeying the rule

$$\vartheta_l^{(t+1)} = \vartheta_l^{(t)} - \nu \nabla_{\vartheta_l} C(\boldsymbol{\vartheta}^{(t)}), \tag{9.8}$$

with $\nu$ the learning rate [46]. During the initialization of the network, the variational parameters are first set to small nonzero random values, $\vartheta_l^{(0)} \in [-0.01, 0.01]\backslash\{0\}$. The corresponding cost function gradient is given by (see Ch. 5) [57]

$$\begin{aligned}
&\nabla_{\vartheta_l} C(\boldsymbol{\vartheta}) \\
&= 2\mathrm{Re}\Bigg\{ \sum_{n=1}^{N_s} \tilde{p}_{\boldsymbol{\vartheta}}(\boldsymbol{\sigma}_n,\boldsymbol{\eta}_n)\tilde{\mathcal{L}}^{\dagger}(\boldsymbol{\sigma}_n,\boldsymbol{\eta}_n) \sum_{m=1}^{N_s} \mathcal{L}(\boldsymbol{\sigma}_n,\boldsymbol{\eta}_n,\boldsymbol{\sigma}_m,\boldsymbol{\eta}_m) \frac{\boldsymbol{\rho}_{\boldsymbol{\vartheta}}(\boldsymbol{\sigma}_m,\boldsymbol{\eta}_m)}{\boldsymbol{\rho}_{\boldsymbol{\vartheta}}(\boldsymbol{\sigma}_n,\boldsymbol{\eta}_n)} O_{\vartheta_l}(\boldsymbol{\sigma}_m,\boldsymbol{\eta}_m) \\
&- \left[\sum_{n=1}^{N_s} \tilde{p}_{\boldsymbol{\vartheta}}(\boldsymbol{\sigma}_n,\boldsymbol{\eta}_n) O_{\vartheta_l}(\boldsymbol{\sigma}_n,\boldsymbol{\eta}_n)\right] \left[\sum_{n=1}^{N_s} \tilde{p}_{\boldsymbol{\vartheta}}(\boldsymbol{\sigma}_n,\boldsymbol{\eta}_n)\tilde{\mathcal{L}}^{\dagger}(\boldsymbol{\sigma}_n,\boldsymbol{\eta}_n)\tilde{\mathcal{L}}(\boldsymbol{\sigma}_n,\boldsymbol{\eta}_n)\right] \Bigg\},
\end{aligned} \tag{9.9}$$

where we have defined logarithmic derivatives as diagonal matrices with elements

$$[\boldsymbol{O}_{\vartheta_l}]_{\boldsymbol{\sigma}_n\boldsymbol{\eta}_n,\boldsymbol{\sigma}_n\boldsymbol{\eta}_n} = O_{\vartheta_l}(\boldsymbol{\sigma}_n,\boldsymbol{\eta}_n) = \frac{\partial[\ln \rho_{\boldsymbol{\vartheta}}(\boldsymbol{\sigma}_n,\boldsymbol{\eta}_n)]}{\partial\vartheta_l}, \tag{9.10}$$

corresponding to the gradients of the neural density operator with respect to all $l$ elements of the variational parameter vector $\boldsymbol{\vartheta}$ and for a given sample configuration $(\boldsymbol{\sigma}_n,\boldsymbol{\eta}_n)$. Furthermore, we have introduced the estimator of the Liouvillian, reading

$$\tilde{\mathcal{L}}(\boldsymbol{\sigma}_n,\boldsymbol{\eta}_n) := \sum_{\boldsymbol{\sigma}_m,\boldsymbol{\eta}_m} \frac{\mathcal{L}(\boldsymbol{\sigma}_n,\boldsymbol{\eta}_n,\boldsymbol{\sigma}_m,\boldsymbol{\eta}_m)\rho_{\boldsymbol{\vartheta}}(\boldsymbol{\sigma}_m,\boldsymbol{\eta}_m)}{\rho_{\boldsymbol{\vartheta}}(\boldsymbol{\sigma}_n,\boldsymbol{\eta}_n)}. \tag{9.11}$$

## 9.4 Symmetric systems: Improving sampling efficiency

To underline the representational capabilities of the neural network approach for systems with symmetries of translational invariance, we start with the symmetric isotropic Heisenberg chain with open boundary conditions, featuring identical incoherent driving and dissipation rates $\gamma_{in}^i = 1.05\gamma_{out}^i$ on *all* sites $i$. In recent studies, similar scenarios with periodic boundary conditions, coherent driving and symmetric dissipation have been successfully realized using the restricted Boltzmann machine architecture, rendering simulations of large systems with $N \geq 15$ feasible [57–59]. For these system sizes, an exact mapping of the density matrix becomes increasingly expensive due to the exponential

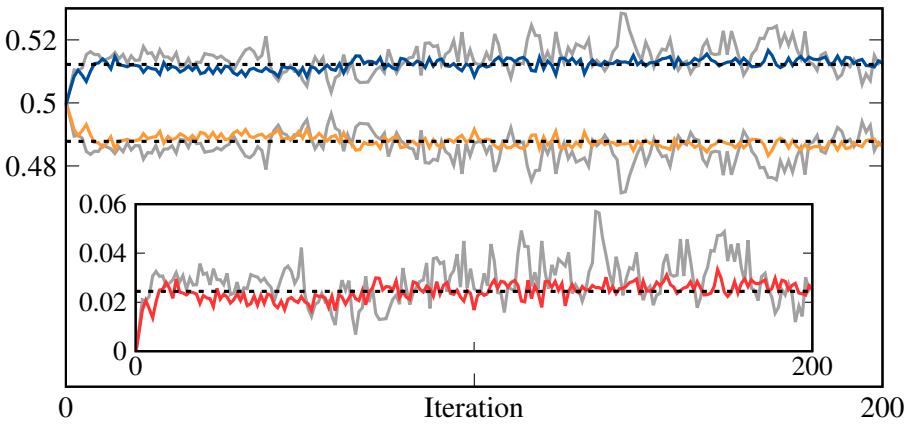


*Figure 9.3:* Neural network estimation for the stationary state of the *symmetric* Heisenberg chain of length $N = 10$, calculated via regular Metropolis sampling (grey lines) and the adjusted *accept-only* sampling method (colored lines). Orange and blue lines show the stationary ground and excited state populations, which are identical on all sites in the symmetric case. For improved visibility, ground and excited state populations are averaged over all sites. Benchmark results are indicated by dashed black lines. The inset shows the stationary state magnetization $m_z$.

growth of the Hilbert space dimension. In established approaches, the Metropolis algorithm is employed for an efficient compression of configuration space (see Ch. 5) [104]. It constitutes a Markov chain Monte Carlo method where $N_s$ system configurations are drawn as samples, corresponding to a random walk in Hilbert space [46, 105, 106]. A new sample configuration is drawn based on a set of selection rules imposed on the current sample and accepted or rejected at a certain acceptance probability. Here, we set the selection rule to flip the spin of each site at a probability of 50%. Moreover, we employ a linear acceptance probability (see Ch. 5)

$$A(n+1,n) = \min\left[1, \frac{\tilde{p}_{\vartheta}(\boldsymbol{\sigma}_{n+1}, \boldsymbol{\eta}_{n+1})}{\tilde{p}_{\vartheta}(\boldsymbol{\sigma}_n, \boldsymbol{\eta}_n)}\right], \tag{9.12}$$

with $(\boldsymbol{\sigma}_n, \boldsymbol{\eta}_n)$ and $(\boldsymbol{\sigma}_{n+1}, \boldsymbol{\eta}_{n+1})$ referring to the current and proposed sample, respectively. In case the proposed sample is rejected by the acceptance function, the standard Metropolis algorithm proceeds with the current sample. This strategy leads to convergent results for the case of symmetric systems and which be further improved for increasing sample sizes $N_s$, as demonstrated in the following.

As a first numerical test, the default Metropolis sampling method is employed. The resulting neural network estimations are compared to benchmarks obtained from a common Runge Kutta master equation implementation. Calculations are performed for system parameters $N = 10$, $\gamma_{in} = 0.21$, $\gamma_{out} = 0.20$ and $J = 2\gamma_{in}$. For the neural network, we choose to draw $N_s = 20000$ samples per iteration and employ hidden layer densities $M/N = K/N = 1$ at a learning rate $\nu = 0.1$. Using these parameters, the restricted Boltzmann machine compresses the system information onto $n_p = 450$ variational parameters compared to the $\approx 500000$ density matrix elements which must be calculated in a brute force approach. Grey lines in Fig. 9.3 depict neural network results for the mean

stationary ground and excited state populations using the regular Metropolis sampling algorithm. Since all sites of the chain take on the same steady state occupation in the symmetric scenario, the depicted results are averaged over all $N = 10$ sites for improved visibility. The inset shows the stationary state magnetization $m_z = (1/N) \sum_{i=1}^{N} \langle \sigma_i^z \rangle$ of the symmetric Heisenberg chain. Benchmark populations are indicated by dashed black lines and exhibit good agreement with the results obtained from regular Metropolis sampling. It is noted that the sample size $N_s$ can be further increased to improve convergence and reduce noise.

As a first improvement to the standard Metropolis approach, we propose an adjusted sampling method breaking the detailed balance condition in the Markov chain and resulting in a net stochastic flow and suppressed random walk behavior in Hilbert space [323]. In consequence, we achieve a considerable improvement of convergence and noise. Rather than proceeding with the current sample configuration in case of a rejection from the acceptance function [Eq. (9.12)], we propose an *accept-only* strategy: The procedure of drawing new sample configurations $(\boldsymbol{\sigma}_{n+1}, \boldsymbol{\eta}_{n+1})$ is repeated until one of them is accepted as the new current sample by the acceptance function. In consequence, no sample is used more than once in a row unless it is chosen by the selection rule at a probability of $1/2^N$, strongly reducing autocorrelations in the Markov chain. Colored lines in Fig. 9.3 depict corresponding neural network results for the symmetric Heisenberg chain obtained via the *accept-only* sampling strategy. Again, the stationary ground and excited states of all sites have been averaged over for improved visibility (orange and blue lines). The red line in the inset shows the corresponding magnetization $m_z$. Compared to the regular Metropolis sampling method (grey lines), the adjusted approach results in smoother lineshapes with fewer kinks and a considerably decreased standard deviation at the same sample size $N_s$, even more so when considering increasing chain lengths $N$. After 100 iterations, the maximum relative deviation of the results obtained from regular sampling from the benchmark is 3.35% compared to 0.99% for the *accept-only* strategy, corresponding to an improvement ratio of $3.35/0.99 \approx 3.38$.

## 9.5 Asymmetric systems: Systematic sampling errors

Next, we investigate the asymmetric Heisenberg chain at incoherent driving and decay parameters $\gamma_{in}^i = \gamma_{out}^i = 0.20$ on all bulk sites $i$, $\gamma_{in}^1 = 0.21$, $\gamma_{out}^1 = 0.20$ on the left boundary (red shape in Fig. 9.1) and $\gamma_{in}^N = 0.20$, $\gamma_{out}^N = 0.21$ on the right boundary (dark blue shape in Fig. 9.1), constituting a boundary-driven isotropic chain without symmetries of translational invariance. All other parameters remain unchanged with respect to the previously discussed symmetric setup. To investigate the representational power of the restricted Boltzmann machine for asymmetric systems, we start at a chain length $N = 6$ where an exact mapping of Hilbert space is straightforward: Instead of applying a selective sampling method, the neural network takes *all* possible system configurations into account to minimize the cost function. The resulting stationary state populations of the boundary and bulk sites of the asymmetric Heisenberg chain are shown in Fig. 9.4 (colored lines), perfectly matching their respective benchmark values (dashed grey lines). This proves that

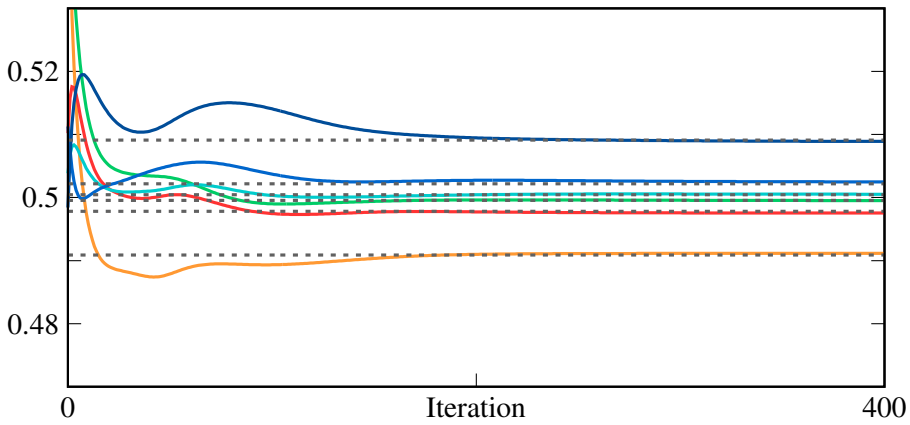


*Figure 9.4:* Stationary ground state populations for an *asymmetric* boundary-driven Heisenberg chain of length $N = 6$, calculated via an exact Hilbert space mapping. Dashed grey lines depict benchmark occupations. Orange and dark blue lines show the ground state populations of the left and right boundary sites.

the restricted Boltzmann machine architecture is not inherently limited to the description of symmetric setups and manages to accurately represent asymmetric systems in case of an exact Hilbert space mapping.

However, the numerical performance is drastically decreased when regular sampling is applied, as shown in Fig. 9.5: For improved visibility, the unfolding stationary ground state populations (grey lines) are averaged over 50 iterations (solid colored lines) and we have taken the mean values of all bulk site populations as well (solid red line). Dashed grey lines again depict the corresponding benchmark populations. While the populations of all sites in the symmetric bulk match their respective Runge Kutta benchmark results, the stationary state populations of the asymmetric boundary sites exhibit an overshooting behavior (solid orange and blue lines in Fig. 9.5), occurring independently of neural network parameters such as system and sample sizes $N$ and $N_s$, learning rate $\nu$ and hidden layer densities $M/N$ and $K/N$: Dashed colored lines in Fig. 9.5 show comparison results obtained at $N_s = 40000$, $\nu = 0.05$, $M/N = K/N = 2$ and averaged over 50 iterations, exhibiting the same overshooting behavior. Furthermore, this erroneous convergence emerges for both the standard Metropolis and the previously introduced *accept-only* sampling algorithm and occurs independently of the employed acceptance function and selection rules for sampling: The same behavior is still observed when choosing, e.g., an exponential acceptance function of the form $A(n+1, n) = \exp[-\tilde{p}_{\boldsymbol{\vartheta}}(\boldsymbol{\sigma}_n, \boldsymbol{\eta}_n)/\tilde{p}_{\boldsymbol{\vartheta}}(\boldsymbol{\sigma}_{n+1}, \boldsymbol{\eta}_{n+1})]$. Given the success of training for an exact Hilbert space mapping (see Fig. 9.4), this only leaves the sampling procedure as the cause of error: Due to the asymmetric properties of the system, Hilbert space elements with a low occurrence probability can still impose a large effect on the steady state under certain conditions. In this case, the application of standard sampling methods established for symmetric systems leads to a systematic error, since Hilbert space configurations with a higher probability of occurrence are favored per se, resulting in a selection bias [see Eq. (9.12)]. In conclusion, we have demonstrated that regular Metropolis sampling methods are unsuitable for the optimization of artificial neural

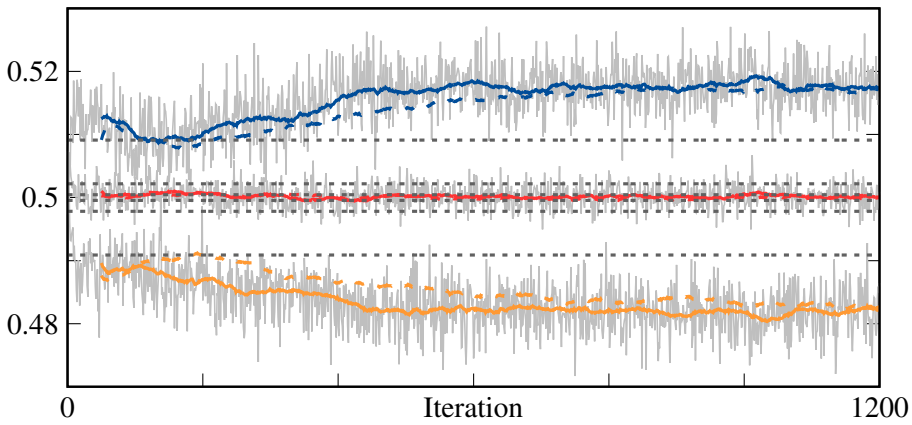


*Figure 9.5:* Results for an *asymmetric* chain of length $N = 6$, using the *accept-only* sampling strategy. Grey lines indicate raw results, with colored lines showing their averages over 50 iterations. Orange and blue lines depict the boundary site ground state populations. Occupations of all bulk sites are also averaged over for improved visibility (red line). Dashed colored lines depict averaged comparison results obtained at half the learning rate and doubled hidden layer densities and samples per iteration.

networks describing systems with asymmetric properties. To resolve this representational limitation, in the following we present a novel *hybrid sampling* approach to explicitly incorporate system asymmetries, allowing for an efficient and accurate compression of Hilbert space for asymmetric open spin-1/2 quantum systems.

## 9.6 Hybrid sampling for asymmetric systems

To resolve the systematic error occurring during the sampling of asymmetric systems, we introduce a *hybrid sampling* strategy, combining the precision of an exact configuration space mapping (see Fig. 9.4) with selective sampling to facilitate computational access to large systems. In the here considered boundary-driven isotropic Heisenberg chain, the asymmetric system properties are located at the boundary sites. The core concept of the proposed hybrid sampling method is to employ a regular Metropolis sampling approach to the symmetric bulk subsystem, while manually selecting the configurations of the asymmetric boundary sites during the sampling procedure: In analogy to the standard sampling algorithm, a new proposed sample $(\boldsymbol{\sigma}_{n+1}, \boldsymbol{\eta}_{n+1})$ is drawn first. To prevent the acceptance function from making arbitrary choices, the occurrence probability of the bulk site configuration, i.e., the symmetric subsystem of the chain, is calculated independently of the asymmetric boundary sites. To this end, we determine the mean probability of a given bulk configuration by averaging over all 16 possible boundary site configurations. Afterwards, the edge sites of the new proposed sample are manually set to one of the 16 possible settings. Once 16 different accepted bulk configurations have been applied, one cycle of all possible boundary configurations has been finished. It is noted that in the case of sampling diagonal configurations $(\boldsymbol{\sigma}_n, \boldsymbol{\sigma}_n)$, only four possible boundary settings are varied over. This procedure is repeated for all $N_s$ samples drawn during each iteration.

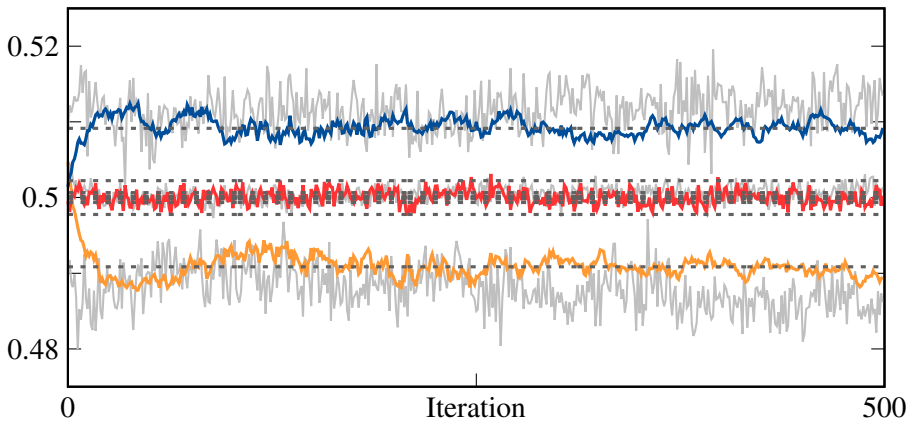


*Figure 9.6:* Stationary ground state populations of the boundary-driven *asymmetric* Heisenberg chain, calculated via the *hybrid sampling* approach for a chain of length $N = 10$. Orange and blue lines show the left and right boundary site populations. For improved visibility, ground state populations of all bulk sites are averaged over (red line, see Fig. 9.7). Dashed grey lines show corresponding benchmark values. Grey lines show comparison results obtained via regular Metropolis sampling.

This hybrid sampling approach combines the accuracy of exact Hilbert space mapping for asymmetric system parts with the high performance of selective Metropolis sampling for the remaining symmetric subsystem, counteracting the systematic overestimation of asymmetric properties during Hilbert space compression. It is noted that the mapping of the edge sites is still approximate, since we do not go through all 16 possible boundary setting for a *single* bulk configuration. Doing so would result in severely decreased bulk convergence, unless the sample size is drastically increased. The quality of convergence resulting from the hybrid sampling approach is limited only by the choice of neural network parameters. In Fig. 9.6, we show the stationary ground state populations of an asymmetric Heisenberg chain of length $N = 10$, calculated using $N_s = 40000$ samples per iteration and at learning rate $\nu = 0.05$. The remaining system and network parameters are unchanged with respect to Fig. 9.5. Strikingly, in difference to the calculations obtained via regular Metropolis sampling (solid grey lines), the stationary boundary site occupations (orange and blue lines) are in excellent agreement with their corresponding benchmark results (dashed grey lines). The applied hybrid sampling strategy prohibits the previously observed overshooting behavior by explicitly accounting for asymmetric system properties. At the same time fluctuations and noise are drastically reduced, yielding a maximum relative deviation of 0.45% between the boundary site occupations and their respective benchmark values after 300 iterations.

Again, all bulk site occupations in Fig. 9.6 have been averaged over for improved visibility (red line), since they are located very closely to each other. As a result, the varying neural network estimations of the bulk site populations overlap significantly, making a visual distinction difficult. However, they do converge to their respective benchmark occupations within the margin of error: As an example to demonstrate the convergence of the symmetric bulk subsystem, Fig. 9.7 shows all ground state occupations depicted in

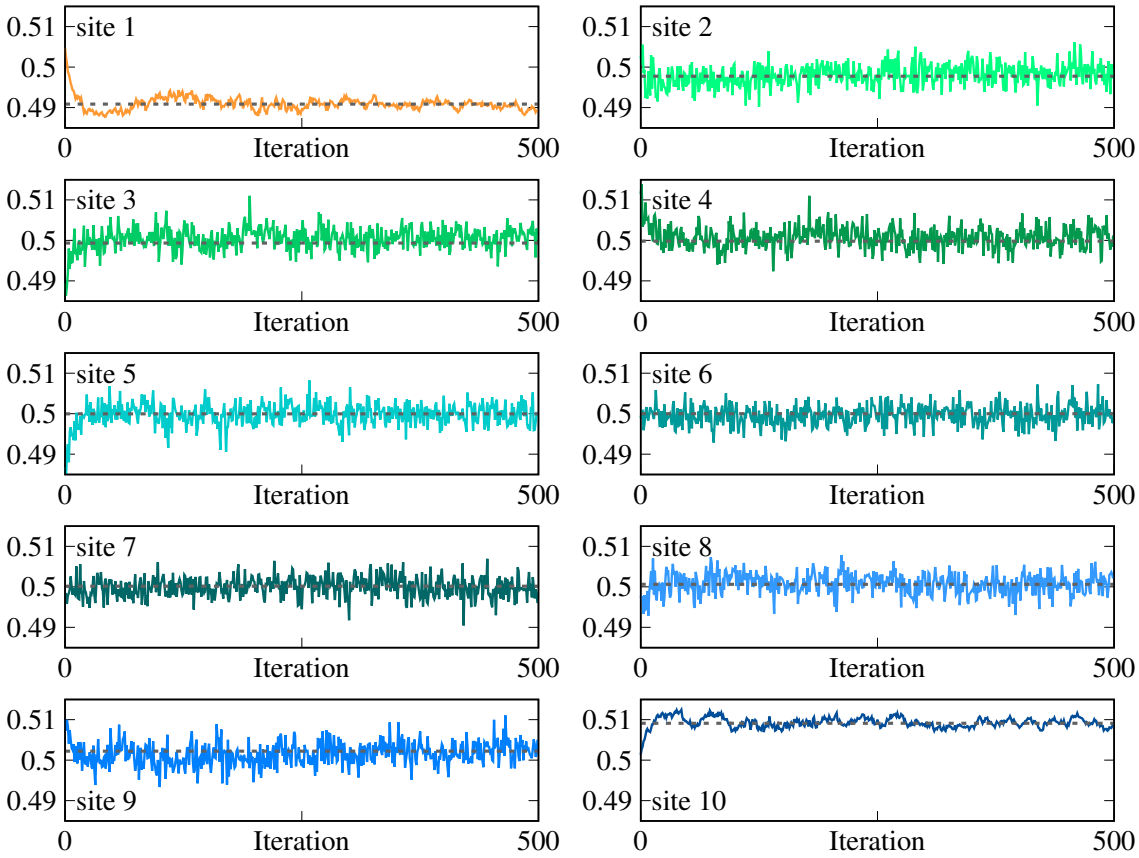


*Figure 9.7:* Unaveraged ground state occupations of all $N = 10$ sites in the *asymmetric* chain scenario and using *hybrid sampling* corresponding to Fig. 9.6, explicitly including the unaveraged stationary ground state occupations of all eight bulk sites.

Fig. 9.6 individually for each site (colored lines), including the unaveraged ground state populations of all eight bulk sites, exhibiting excellent agreement with their corresponding benchmarks (dashed grey lines). Again, the observed oscillations over iterations can be further reduced by increasing the sample size $N_s$. Lastly, we demonstrate the high performance and scalability potential of the presented hybrid sampling approach. Fig. 9.8 shows the stationary ground state populations of an asymmetric Heisenberg chain with $N = 16$ sites at neural network parameters $N_s = 40000$, $\nu = 0.05$ (grey lines) and $\nu = 0.025$ (colored lines). Bulk site occupations are again averaged over for improved visibility (red lines). As a guide for the eye, dashed grey lines indicate Runge Kutta benchmark results for the case $N = 10$. As expected, due to decreasing asymmetric system properties at unmodified incoherent driving and decay rates, for increasing chain lengths $N$ the boundary site occupations begin to strive towards the bulk occupation values. The boundary site populations (orange and blue lines) are once more in excellent agreement with their respective benchmark results after approximately 100 training iterations, underlining the capabilities of the presented hybrid sampling approach.

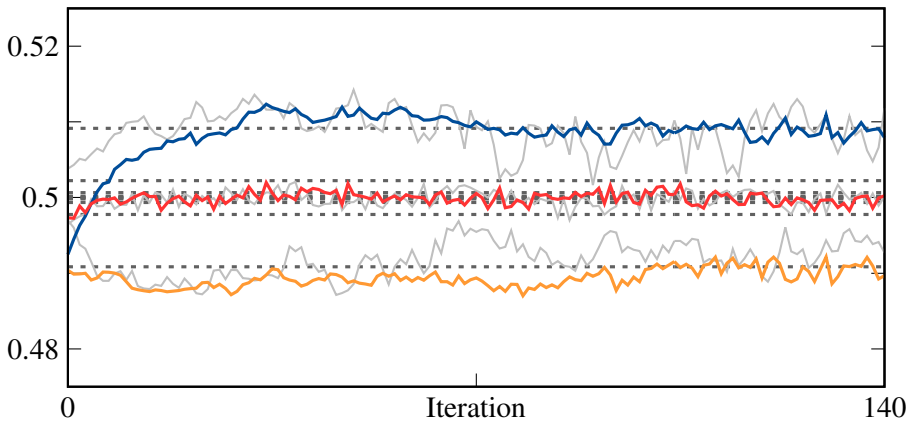


*Figure 9.8:* Stationary ground state populations of the boundary-driven *asymmetric* Heisenberg chain, calculated via the *hybrid sampling* approach for a chain of length $N = 16$ and network parameters $N_s = 40000$ and $\nu = 0.025$. Orange and blue lines show the left and right boundary site populations, with the ground state populations of all bulk sites averaged over for improved visibility (red line). Dashed grey lines depict benchmark occupations. Grey lines show comparison results at a doubled learning rate $\nu = 0.05$.

## 9.7 Conclusion

We have investigated the representational limits of established neural network sampling strategies. Based on the example of the boundary-driven isotropic Heisenberg chain without symmetries of translational invariance, we have shown that regular Metropolis-based compression approaches result in a systematic overestimation of asymmetric system properties during the selective Hilbert space sampling. To improve overall convergence and efficiency in the limit of low sample sizes, we have first introduced an *accept-only* strategy as an adjustment to the regular Metropolis algorithm, explicitly breaking the detailed balance condition in the Markov chain and suppressing the random walk behavior in configuration space during sampling. Afterwards, we have presented a hybrid sampling algorithm to combine the precision of exact Hilbert space mapping for asymmetric properties with high performing information compression via selective sampling of the remaining symmetric subsystem. As a result, we have achieved fast converging results with reduced noise even for large asymmetric open spin-1/2 systems. These adaptive sampling strategies represent a novel access point for the optimization and individual tailoring of artificial neural networks for a wide variety of open quantum systems, further improving upon their accuracy and performance. In conclusion, we have expanded the representational power of the restricted Boltzmann machine architecture beyond purely symmetric open quantum systems, further advancing its versatility and applicability in quantum simulations.

# 10 Efficient bit encoding of neural networks for Fock states

In this Chapter, we derive a bit encoding approach for a highly scalable and accurate representation of bosonic Fock number states in the restricted Boltzmann machine neural network architecture, for the first time expanding its representational power beyond the description of pure spin-1/2 open quantum systems. In regular master equation implementations of bosonic open systems, the number of degrees of freedom of the density matrix scales with the predetermined maximum boson number. In contrast, the complexity of the here presented neural network implementation rises only with the number of bit-encoded neurons, resulting in a vast degree of information compression. In the high boson number regime, the resulting compression efficiency is demonstrated to outperform even maximally optimized density matrix implementations based on a projector method to access the sparsest available representation of configuration space. The Chapter is closely based on the publication "Efficient bit encoding of neural networks for Fock states" by O. Kästle and A. Carmele [73].

## 10.1 Introduction

As discussed in previous Chapters, the restricted Boltzmann machine has emerged as a default neural network architecture for the description of quantum states [47–50, 52–55] and open spin-1/2 quantum systems with Markovian dynamics [56–59], since it facilitates a direct and highly efficient mapping of spin-1/2 systems to artificial neurons. In the last Chapter, we have extended the established representational limits of the restricted Boltzmann machine beyond symmetric and periodic spin systems to asymmetric setups by introducing adaptive strategies for the sampling of configuration space [72].

In this Chapter, the applicability of the restricted Boltzmann machine is further advanced to enable simulations of hybrid quantum systems featuring bosonic degrees of freedom. This is achieved by application of a bit encoding scheme to the visible neuron layer, allowing for a direct mapping of Fock number states to the neural network degrees of freedom in analogy to the established one-to-one assignment of spin-1/2 systems to artificial neurons and without modification of the underlying restricted Boltzmann machine architecture itself. In the high boson number regime, the resulting bit-encoded neural network is shown to accomplish vast degrees of information compression, surpassing even a maximally optimized density matrix implementation based on a fourth order Runge Kutta algorithm where a projector method is employed to attain the sparsest representation of Hilbert space available. We demonstrate both the accuracy and scalability potential of the proposed

neural encoding of Fock states. To this end, we first present neural network calculations of the stationary boson number statistics for a generic one-atom laser model [24, 324–327] in comparison to benchmark results obtained in a common density matrix approach. Afterwards, the method is benchmarked in the large boson number regime where the bit-encoded neural network achieves supremely efficient information compression, underlining the scalability potential of the approach. Applications of the presented technique include, e.g., neural network implementations of boson sampling algorithms [328, 329] or of recent efforts to measure quantum coherences via Fock state superposition [330].

The proposed bit encoding scheme for Fock states is introduced in Sec. 10.2, allowing for a direct mapping of boson occupation numbers to the visible neuron layer of the restricted Boltzmann machine. In Sec. 10.3, we briefly recapitulate the realization and training of the bit-encoded neural network. Afterwards, we discuss the attainable degrees of information compression compared to both a regular and a maximally optimized master equation implementation with respect to the required dimension of the Fock state basis in Sec. 10.4. As an example application, we specifically investigate the scaling of required degrees of freedom in a one-atom laser model featuring a sparse Hilbert space in stationary state. Using a Heisenberg projection method, the latter can be truncated for maximum efficiency. In Sec. 10.5, the accuracy of the bit-encoded neural network is demonstrated before confirming its scalability potential in Sec. 10.6. Lastly, we conclude our investigation and summarize our findings in Sec. 10.7.

## 10.2 Neural encoding of Fock states

Artificial neural networks consist of binary neurons, i.e., each neuron is configured in one of two possible settings $+1$ or $-1$. In case of the restricted Boltzmann machine architecture, this allows for a straightforward mapping of spin-1/2 systems, enabling a natural representation of the corresponding system density matrix [47, 51, 56–59, 72, 78, 79, 107, 115, 322]. When considering a system of $N$ spins $\sigma_n, \eta_n = \{-1, 1\}$, the $2^{2N}$ elements of the density matrix $\langle \sigma_1, \ldots, \sigma_N | \, \rho \, | \eta_1, \ldots, \eta_N \rangle$ are stated in terms of a model distribution called *neural density operator*, which is trained to estimate the stationary state by iterative variation of a set of neural network parameters (see Ch. 5). In order to unleash the full potential of the restricted Boltzmann machine architecture as a universal tool for the description of Markovian open quantum systems, in the following we develop a supremely efficient and highly scalable mapping of Fock number states via a bit encoding scheme [44, 45]:

Specifically, we derive a neural network representation of a quantum system comprising $N$ spin-1/2 systems and a single bosonic mode, corresponding to density matrix elements $\langle \sigma_1, \ldots, \sigma_N; n_\beta^\sigma | \, \rho \, | \eta_1, \ldots, \eta_N; n_\beta^\eta \rangle$ where $\sigma_n, \eta_n = \{-1, 1\}$ are the left and right spin configurations and $n_\beta^\sigma, n_\beta^\eta \in \mathbb{N}_0$ denote the left and right Fock state occupation. The boson number populations $n_\beta^\sigma$, $n_\beta^\eta$ are each encoded in $N_\beta$ bits $(\beta_1^\sigma, \ldots, \beta_{N_\beta}^\sigma)$ and $(\beta_1^\eta, \ldots, \beta_{N_\beta}^\eta)$

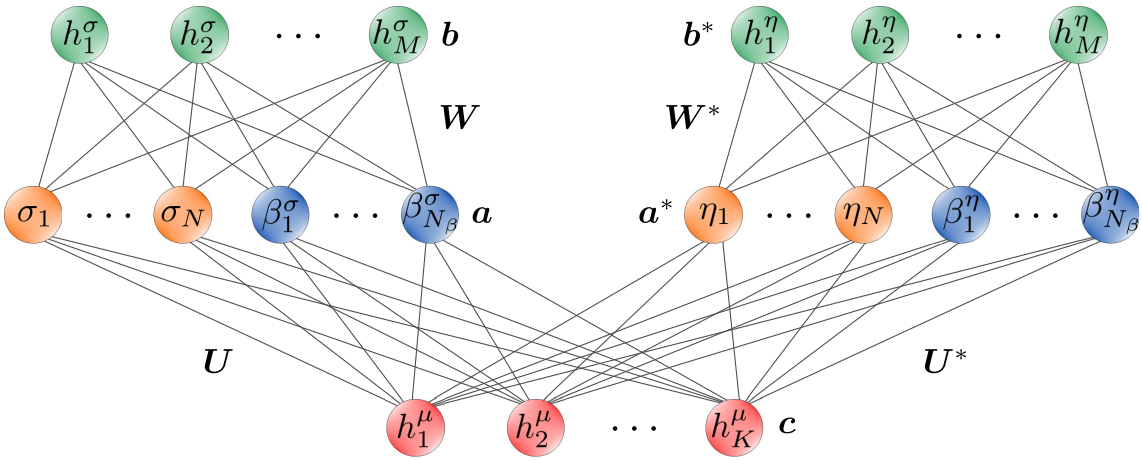


*Figure 10.1:* Restricted Boltzmann machine constituting the *neural density operator*, with a visible neuron layer comprising $N$ spin-1/2 systems (orange) and the bit-encoded boson number occupation via $N_\beta$ neurons (blue). In addition, it features two hidden layers (green) and an ancillary mixing layer (red). A set of variational training parameters $\boldsymbol{\vartheta} = (\boldsymbol{a}, \boldsymbol{b}, \boldsymbol{c}, \boldsymbol{W}, \boldsymbol{U})$ represents the neural network degrees of freedom.

via the decomposition rule

$$n_\beta = \sum_{i=1}^{N_\beta} 2^{i-1} \delta_{\beta_i,1}, \tag{10.1}$$

facilitating the representation of $n_\beta = \{0, 1, \ldots, 2^{N_\beta} - 1\}$ indistinguishable bosons on each side of the density matrix. This bit representation allows for a direct mapping of the Fock state basis onto the visible neuron layer of the restricted Boltzmann machine, analogous to the assignment of spin-1/2 systems and without further modifications to the underlying neural network structure. Here, the maximum representable boson occupation number is determined by the number of bits. When employing, e.g., a total of $N_\beta = 4$ artificial neurons as bits, $2^4$ possible Fock state configurations can be depicted by the resulting network, with the bit-encoded Fock state number given by

$$n_\beta = 2^0 \delta_{\beta_1,1} + 2^1 \delta_{\beta_2,1} + 2^2 \delta_{\beta_3,1} + 2^3 \delta_{\beta_4,1}. \tag{10.2}$$

Fig. 10.1 depicts the unfolding bit-encoded restricted Boltzmann machine, consisting of a visible layer of $2(N + N_\beta)$ sites $\boldsymbol{\sigma} = (\sigma_1, \ldots, \sigma_N, \beta_1^\sigma, \ldots, \beta_{N_\beta}^\sigma)$ and $\boldsymbol{\eta} = (\eta_1, \ldots, \eta_N, \beta_1^\eta, \ldots, \beta_{N_\beta}^\eta)$ storing the configuration of the left and right side of the density matrix and split up into $N$ neurons each representing a spin-1/2 system (orange) and $N_\beta$ neurons employed as bits to encode the boson number occupation (blue). Moreover, the network includes two auxiliary hidden layers, each featuring $M$ neurons $\boldsymbol{h}^\sigma$ and $\boldsymbol{h}^\eta$, respectively (green shapes), and an ancillary mixing layer of $K$ sites $\boldsymbol{h}^\mu$ linking the left and right side of the density matrix (red shapes). The hidden and ancillary neural network layers are once more traced

out (see Ch. 5), resulting in neural density operator elements [57–59, 72, 78]

$$\rho_{\boldsymbol{\vartheta}}(\boldsymbol{\sigma},\boldsymbol{\eta}) = \prod_{m=1}^{M}\prod_{k=1}^{K} 8\exp\left[\sum_{i=1}^{N}(a_i\sigma_i + a_i^*\eta_i) + \sum_{i=N+1}^{N+N_\beta}\left(a_i\beta_{i-N}^{\sigma} + a_i^*\beta_{i-N}^{\eta}\right)\right]$$
$$\times\cosh\left(b_m + \sum_{i=1}^{N}W_{mi}\sigma_i + \sum_{i=N+1}^{N+N_\beta}W_{mi}\beta_{i-N}^{\sigma}\right)\cosh\left(b_m^* + \sum_{i=1}^{N}W_{mi}^*\eta_i + \sum_{i=N+1}^{N+N_\beta}W_{mi}^*\beta_{i-N}^{\eta}\right)$$
$$\times\cosh\left[c_k + c_k^* + \sum_{i=1}^{N}(U_{ki}\sigma_i + U_{ki}^*\eta_i) + \sum_{i=N+1}^{N+N_\beta}\left(U_{ki}\beta_{i-N}^{\sigma} + U_{ki}^*\beta_{i-N}^{\eta}\right)\right], \tag{10.3}$$

with $\boldsymbol{\vartheta} = (\boldsymbol{a},\boldsymbol{b},\boldsymbol{c},\boldsymbol{W},\boldsymbol{U})$ denoting the set of complex training parameters which constitute the neural network degrees of freedom. They are split up into real and imaginary parts, resulting in a total of $2(N+N_\beta)+2M+K+2M(N+N_\beta)+2K(N+N_\beta)$ elements, and consist of biases $\boldsymbol{a}$ for visible neurons, $\boldsymbol{b}$ for hidden sites and $\boldsymbol{c}$ for the mixing layer, and of complex weights $\boldsymbol{W}$ and $\boldsymbol{U}$ linking the visible sites $(\boldsymbol{\sigma},\boldsymbol{\eta})$ to the hidden neurons $\boldsymbol{h}^{\sigma}$, $\boldsymbol{h}^{\eta}$ and the ancillary mixing layer $\boldsymbol{h}^{\mu}$, respectively [see Fig. 10.1].

## 10.3 Training procedure

In common master equation implementations of bosonic and hybrid quantum systems, the exponential growth of the Hilbert space dimension for rising system sizes renders an exact mapping of the density matrix increasingly expensive in the limit of large boson numbers. As discussed in previous Chapters, the neural network ansatz for open quantum systems solves this problem by estimating the density matrix $\rho$ by the neural density operator $\rho_{\boldsymbol{\vartheta}}$ [Eq. (10.3)] via iterative training of variational parameters $\boldsymbol{\vartheta}$. For the following implementation, we employ the standard Metropolis algorithm for the sampling of $N_s$ elements of configuration space, where a new sample $(\boldsymbol{\sigma},\boldsymbol{\eta}) = (\sigma_1,\ldots,\sigma_N,\beta_1^{\sigma},\ldots,\beta_{N_\beta}^{\sigma};\eta_1,\ldots,\eta_N,\beta_1^{\eta},\ldots,\beta_{N_\beta}^{\eta})$ is proposed based on the current system configuration and either accepted or rejected at a certain acceptance probability (see Ch. 5) [104].

When considering a setup comprising a number of spin-1/2 quantum systems interacting with a bosonic mode, the amount of nonzero density matrix elements is severely restricted by the properties of the spin-boson interaction. As a result, in these scenarios the unfolding steady state density matrix is often times highly sparse. Since we are only interested in the stationary system state, we make use of this condition to improve the efficiency and accuracy of the Hilbert space sampling by only drawing system configurations from the subspace of nonzero stationary state density matrix elements. Hence, during the proposition of a new sample configuration we employ a random selection rule where the left and right setting of each spin $\sigma_1,\ldots,\sigma_N,\eta_1,\ldots,\eta_N$ is flipped at a probability of 50% each. Based on the new spin configuration, a new random and bit-encoded Fock number configuration $\beta_1^{\sigma},\ldots,\beta_{N_\beta}^{\sigma},\beta_1^{\eta},\ldots,\beta_{N_\beta}^{\eta}$ is drawn, only allowing for combinations corresponding to nonzero elements of the stationary density matrix. To determine whether

to accept or reject a newly proposed sample configuration, we employ the linear acceptance function

$$A(n+1,n) = \min\left[1, \frac{\tilde{p}_{\boldsymbol{\vartheta}}(\boldsymbol{\sigma}_{n+1}, \boldsymbol{\eta}_{n+1})}{\tilde{p}_{\boldsymbol{\vartheta}}(\boldsymbol{\sigma}_n, \boldsymbol{\eta}_n)}\right], \tag{10.4}$$

where $(\boldsymbol{\sigma}_n, \boldsymbol{\eta}_n)$ denotes the current and $(\boldsymbol{\sigma}_{n+1}, \boldsymbol{\eta}_{n+1})$ the proposed Hilbert space sample. Again, we employ the stochastic reconfiguration approach [117–119] to estimate the occurrence probability of a given sample configuration $(\boldsymbol{\sigma}_n, \boldsymbol{\eta}_n)$ with $n = \{1, \ldots, N_s\}$ and system observables as statistical expectation values over the $N_s$ sample configurations drawn during each training iteration. As a result, the normalized occurrence probability is given by (see Ch. 5)

$$\tilde{p}_{\boldsymbol{\vartheta}}(\boldsymbol{\sigma}_n, \boldsymbol{\eta}_n) = \frac{|\rho_{\boldsymbol{\vartheta}}(\boldsymbol{\sigma}_n, \boldsymbol{\eta}_n)|^2}{\sum_{n=1}^{N_s} |\rho_{\boldsymbol{\vartheta}}(\boldsymbol{\sigma}_n, \boldsymbol{\eta}_n)|^2}, \tag{10.5}$$

and diagonal observables are calculated as statistical averages $\langle X(\boldsymbol{\sigma}, \boldsymbol{\sigma})\rangle \approx \langle\langle X(\boldsymbol{\sigma}, \boldsymbol{\sigma})\rangle\rangle_q$ [57–59, 117–119] with

$$\langle\langle X(\boldsymbol{\sigma}, \boldsymbol{\sigma})\rangle\rangle_q := \sum_{n=1}^{N_s} \tilde{q}_{\boldsymbol{\vartheta}}(\boldsymbol{\sigma}_n) \sum_{\boldsymbol{\xi}} X(\boldsymbol{\sigma}_n, \boldsymbol{\xi}) \frac{\rho_{\boldsymbol{\vartheta}}(\boldsymbol{\xi}, \boldsymbol{\sigma}_n)}{\rho_{\boldsymbol{\vartheta}}(\boldsymbol{\sigma}_n, \boldsymbol{\sigma}_n)}. \tag{10.6}$$

Since only diagonal observables are figures of merit in the here considered scenario, the normalized occurrence probability of diagonal system configurations

$$\tilde{q}_{\boldsymbol{\vartheta}}(\boldsymbol{\sigma}_n) = \frac{\rho_{\boldsymbol{\vartheta}}(\boldsymbol{\sigma}_n, \boldsymbol{\sigma}_n)}{\sum_{n=1}^{N_s} \rho_{\boldsymbol{\vartheta}}(\boldsymbol{\sigma}_n, \boldsymbol{\sigma}_n)} \tag{10.7}$$

is used to improve numerical efficiency: During each training iteration, $N_s$ diagonal system configurations $(\boldsymbol{\sigma}_n, \boldsymbol{\sigma}_n)$ are sampled for the calculation of diagonal observables and $N_s$ general samples $(\boldsymbol{\sigma}_n, \boldsymbol{\eta}_n)$ are drawn to determine $\tilde{p}_{\boldsymbol{\vartheta}}(\boldsymbol{\sigma}, \boldsymbol{\eta})$ for the optimization of the neural network.

The training objective is to estimate the stationary state of the considered system, given by the condition $\dot{\rho} = \mathcal{L}\rho = 0$, with $\mathcal{L}$ denoting the Liouvillian superoperator [1, 268]. For the optimization of the variational parameter set $\boldsymbol{\vartheta}$ towards this condition, we define a cost function $C(\boldsymbol{\vartheta}) = \|\mathcal{L}\rho_{\boldsymbol{\vartheta}}\|_2^2$ (see Ch. 5) [57, 59]. The variational parameters are initialized at small nonzero random values, $\vartheta_l^{(0)} \in [-0.01, 0.01]\backslash\{0\}$ and updated during each iteration $t \to t+1$ using the standard stochastic gradient descent approach,

$$\vartheta_l^{(t+1)} = \vartheta_l^{(t)} - \nu \nabla_{\vartheta_l} C[\boldsymbol{\vartheta}^{(t)}], \tag{10.8}$$

at learning rate $\nu$ [46]. The gradient of the corresponding cost function is again determined as (see Ch. 5) [57, 72]

$$\begin{aligned}
&\nabla_{\vartheta_l} C(\boldsymbol{\vartheta}) \\
&= 2\mathrm{Re}\Bigg\{ \sum_{n=1}^{N_s} \tilde{p}_{\boldsymbol{\vartheta}}(\boldsymbol{\sigma}_n, \boldsymbol{\eta}_n) \tilde{\mathcal{L}}^{\dagger}(\boldsymbol{\sigma}_n, \boldsymbol{\eta}_n) \sum_{m=1}^{N_s} \mathcal{L}(\boldsymbol{\sigma}_n, \boldsymbol{\eta}_n, \boldsymbol{\sigma}_m, \boldsymbol{\eta}_m) \frac{\boldsymbol{\rho}_{\boldsymbol{\vartheta}}(\boldsymbol{\sigma}_m, \boldsymbol{\eta}_m)}{\boldsymbol{\rho}_{\boldsymbol{\vartheta}}(\boldsymbol{\sigma}_n, \boldsymbol{\eta}_n)} O_{\vartheta_l}(\boldsymbol{\sigma}_m, \boldsymbol{\eta}_m) \\
&- \left[\sum_{n=1}^{N_s} \tilde{p}_{\boldsymbol{\vartheta}}(\boldsymbol{\sigma}_n, \boldsymbol{\eta}_n) O_{\vartheta_l}(\boldsymbol{\sigma}_n, \boldsymbol{\eta}_n)\right] \left[\sum_{n=1}^{N_s} \tilde{p}_{\boldsymbol{\vartheta}}(\boldsymbol{\sigma}_n, \boldsymbol{\eta}_n) \tilde{\mathcal{L}}^{\dagger}(\boldsymbol{\sigma}_n, \boldsymbol{\eta}_n) \tilde{\mathcal{L}}(\boldsymbol{\sigma}_n, \boldsymbol{\eta}_n)\right] \Bigg\},
\end{aligned} \tag{10.9}$$

with the estimator of the Liouvillian

$$\tilde{\mathcal{L}}(\boldsymbol{\sigma}_n, \boldsymbol{\eta}_n) := \sum_{\boldsymbol{\sigma}_m, \boldsymbol{\eta}_m} \mathcal{L}(\boldsymbol{\sigma}_n, \boldsymbol{\eta}_n, \boldsymbol{\sigma}_m, \boldsymbol{\eta}_m) \frac{\rho_{\boldsymbol{\vartheta}}(\boldsymbol{\sigma}_m, \boldsymbol{\eta}_m)}{\rho_{\boldsymbol{\vartheta}}(\boldsymbol{\sigma}_n, \boldsymbol{\eta}_n)}, \tag{10.10}$$

and logarithmic derivatives written as diagonal matrices with elements

$$[\boldsymbol{O}_{\vartheta_l}]_{\boldsymbol{\sigma}_n\boldsymbol{\eta}_n, \boldsymbol{\sigma}_n\boldsymbol{\eta}_n} = O_{\vartheta_l}(\boldsymbol{\sigma}_n, \boldsymbol{\eta}_n) = \frac{\partial[\ln \rho_{\boldsymbol{\vartheta}}(\boldsymbol{\sigma}_n, \boldsymbol{\eta}_n)]}{\partial \vartheta_l}, \tag{10.11}$$

representing the neural density operator gradients with respect to all $l$ elements of $\boldsymbol{\vartheta}$ and for a specific sample configuration $(\boldsymbol{\sigma}_n, \boldsymbol{\eta}_n)$.

## 10.4 Neural network efficiency gain

The core advantage behind the application of the restricted Boltzmann machine approach to open quantum systems is its high degree of information compression: The $2(N + N_\beta) + 2M + K + 2M(N + N_\beta) + 2K(N + N_\beta)$ variational training parameters stored in $\boldsymbol{\vartheta}$ represent the neural network degrees of freedom and only depend on the number of visible neurons $N + N_\beta$ constituting the spin-1/2 systems and the employed bits to encode the Fock state basis. In a common master equation implementation of a system featuring $d$ degrees of freedom, $d(d+1)/2$ density matrix elements must be determined to solve the system of differential equations $\dot{\boldsymbol{\rho}}(t) = \mathcal{L}\boldsymbol{\rho}(t)$ until the steady state is attained. To compare the neural network information compression to these common density matrix approaches with respect to the efficiency scaling of the Fock state basis dimension, we investigate the paradigmatic open Jaynes-Cummings model, consisting of a single spin-1/2 system interacting with a bosonic cavity mode, constituting a one-atom laser system [24]. Under the rotating wave and dipole approximation, the respective system Hamiltonian reads [324–327]

$$H/\hbar = \omega_0 \sigma^+\sigma^- + \omega_c c^\dagger c + g_0 \left(\sigma^+ c + \sigma^- c^\dagger\right), \tag{10.12}$$

where $c^\dagger$, $c$ are bosonic creation and annihilation operators and $\sigma^\pm$ denote Pauli spin operators. $\omega_0$ and $\omega_c$ refer to the spin and cavity mode frequencies and $g_0$ corresponds to the coupling strength between system and cavity mode. Moreover, the system is incoherently excited at a driving rate $\Gamma$ and subjected to incoherent decay of the bosonic mode occupation at rate $\kappa$ in a Markovian Lindblad description. As a result, the time evolution dynamics for the density operator is given by

$$\dot{\boldsymbol{\rho}}(t) = \mathcal{L}\boldsymbol{\rho}(t) = -i\,[H/\hbar, \boldsymbol{\rho}(t)] + \mathcal{D}\left[\sqrt{\kappa/2}c\right]\boldsymbol{\rho}(t) + \mathcal{D}\left[\sqrt{\Gamma/2}\sigma^+\right]\boldsymbol{\rho}(t), \tag{10.13}$$

with Lindblad dissipators [1, 268]

$$\mathcal{D}\left[\sqrt{\kappa/2}c\right]\boldsymbol{\rho}(t) = \frac{\kappa}{2}\left[2c\boldsymbol{\rho}(t)c^\dagger - \{c^\dagger c, \boldsymbol{\rho}(t)\}\right], \tag{10.14a}$$

$$\mathcal{D}\left[\sqrt{\Gamma/2}\sigma^+\right]\boldsymbol{\rho}(t) = \frac{\Gamma}{2}\left[2\sigma^+\boldsymbol{\rho}(t)\sigma^- - \{\sigma^-\sigma^+, \boldsymbol{\rho}(t)\}\right], \tag{10.14b}$$

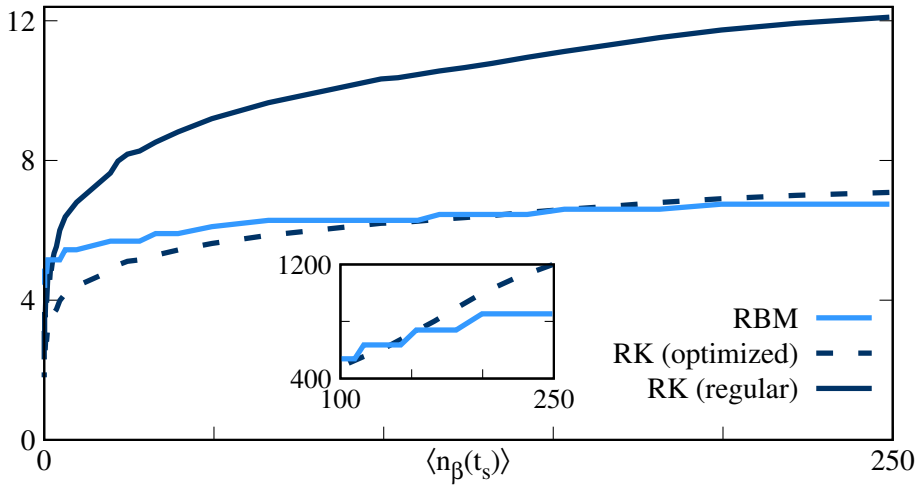


*Figure 10.2:* Required degrees of freedom to achieve numerical convergence with respect to the average stationary state boson occupation number, depicted on a logarithmic scale. The restricted Boltzmann machine implementation (solid light blue line) is compared to both a regular unoptimized master equation approach (solid dark blue line) and a maximally optimized approach with a truncated configuration space only comprising nonzero stationary state density matrix elements (dashed dark blue line). The inset shows a zoom-in on a linear scale, where the neural network implementation becomes supremely efficient.

resulting in incoherent driving and decay of system and cavity mode, respectively. In the following calculations, we employ the parameters $g_0 = 0.2\,\mathrm{ps}^{-1}$, $\Gamma = 0.4\,\mathrm{ps}^{-1}$, $\omega_0 = \omega_c$ and various bosonic dissipation rates $\kappa$. Moreover, we only consider the stationary state attained at time $t_s$, where the condition $\dot{\boldsymbol{\rho}}(t_s) = \mathcal{L}\boldsymbol{\rho}(t_s) = 0$ is fulfilled within numerical precision.

This model is chosen due to the high sparsity of the resulting stationary state density matrix, allowing for the application of a Heisenberg projector method to achieve a profound grade of optimization for the regular density matrix implementation: Using a Heisenberg operator, we project the full configuration space onto the relevant subspace consisting of only $2(d-1)$ nonzero steady state density matrix elements [1, 331]. In the here considered system, this corresponds to $2(2n_\beta^{max} - 1)$ elements with $n_\beta^{max}$ denoting the chosen upper numerical limit for the boson number occupation. While this corresponds to $2n_\beta^{max}(2n_\beta^{max} + 1)/2$ degrees of freedom in the unoptimized master equation approach, the complexity of the neural network implementation increases with the number of bits $N_\beta$ representing the Fock state basis. Here, the maximum boson number occupation is determined by $n_\beta^{max} = 2^{N_\beta} - 1$. We note that regardless of the specific implementation and parameter choices, convergence with respect to the numerical boson limit given by $n_\beta^{max}$ or $N_\beta$ must always be ensured.

Fig. 10.2 shows the required degrees of freedom to achieve numerical convergence with respect to the average steady state boson number occupation $\langle n_\beta(t_s)\rangle$, which is varied via tuning of the bosonic dissipation rate $\kappa$. The resulting numerical complexity is de-

picted on a logarithmic scale. In case of the neural network implementation, convergence is achieved for a sufficiently large number of bits $N_\beta$. At this point, statistical noise can be reduced by increasing the number of sample configurations $N_s$, further improving convergence. For the master equation approach, we assume numerical convergence once an incremental expansion of the Fock state basis yields a relative deviation of less than 0.1% in $\langle n_\beta(t_s)\rangle$. Moreover, common dynamical Runge Kutta implementations typically demand increasingly small time steps for increasing system sizes to obtain numerically convergent results. In addition, the number of density matrix elements for the solution of Eq. (10.13) scales *polynomially* with the system size, leading to a polynomial increase of complexity for increasing stationary Fock state occupations (solid dark blue line in Fig. 10.2). For a maximally optimized density matrix implementation, we exploit the sparsity of the stationary state configuration space, reducing its dimension via application of a Heisenberg projector method. As a result, the increase in complexity is reduced to scale *linearly* with the bosonic degrees of freedom (dashed dark blue line in Fig. 10.2). In the neural network approach, the required degrees of freedom scale only with the number of visible neurons $N_\beta + 1$. In our experience, it has proven more successful to increase the number of bosonic bits $N_\beta$ rather than the hidden layer densities to achieve improvements in convergence. In consequence, the solid light blue line in Fig. 10.2 depicts the neural network degrees of freedom to attain numerical convergence at fixed hidden layer densities $M/(N_\beta + 1) = K/(N_\beta + 1) = 1$, exhibiting a slow linear increase for rising stationary boson occupation numbers.

As illustrated in Fig. 10.2, the bit-encoded restricted Boltzmann machine architecture facilitates a much more efficient information compression for open hybrid systems compared to the common unoptimized master equation approach. The inset shows a zoom-in on the scaling of degrees of freedom depicted on a linear scale. In the neural network implementation, the bit encoding of Fock states leads to a stepwise increase in complexity (solid light blue line in inset). Comparable efficiency is only achieved via the maximally optimized density matrix approach, whose efficiency even surpasses the restricted Boltzmann machine implementation in the limit of low boson number occupations. Crucially, the degree of information compression in the neural network approach becomes even more effective above Fock state occupations of $\langle n_\beta(t_s)\rangle \approx 160$ (see inset). Considering the already outstanding degree of Hilbert space compression in the maximally optimized master equation implementation, the here achieved neural network efficiency is remarkable. In the following Sections, we verify the accuracy of the bit-encoded restricted Boltzmann machine and its scalability potential with respect to large boson number regime.

## 10.5 Accuracy

As an example application to confirm the accuracy of the presented neural encoding of Fock states, we consider the stationary boson number statistics $P_n(t_s)$ for the model system prescribed by Eq. (10.13), where

$$P_n(t) = \frac{1}{n!}\left\langle c^{\dagger n} c^n(t)\right\rangle - \frac{1}{n!}\sum_{m=1}^{n^{max}} \frac{(n+m)!}{m!} P_{n+m}(t) \tag{10.15}$$

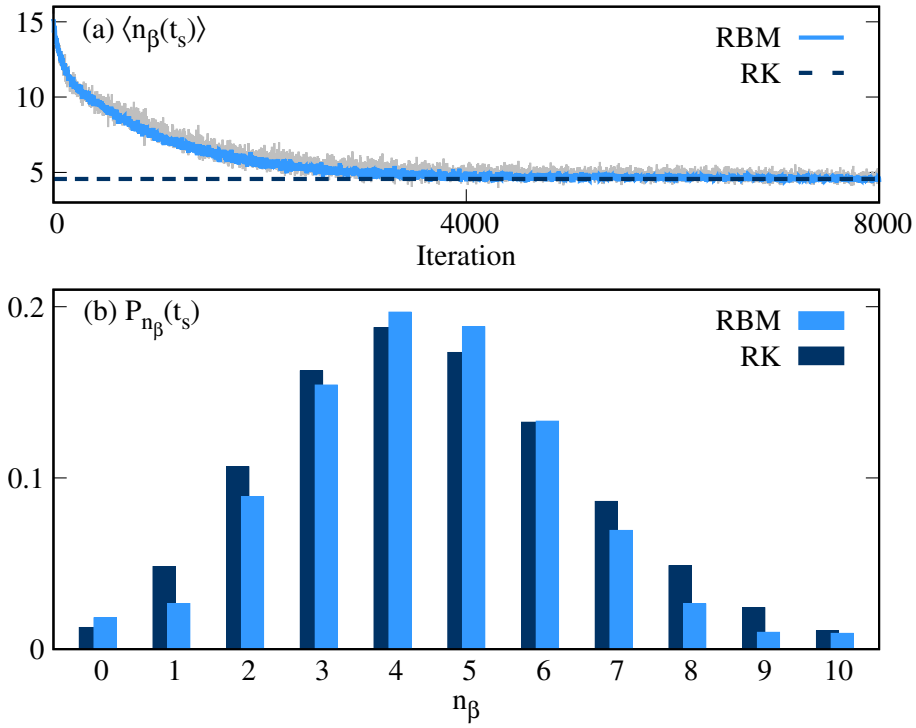


*Figure 10.3:* Demonstration of the accuracy of the bit-encoded restricted Boltzmann machine implementation of bosonic number states. (a) Mean stationary boson occupation number $\langle n_\beta \rangle (t_s)$ calculated using the neural network (solid blue line), compared to a calculation using fewer samples per iteration (solid grey line) and to the common density matrix benchmark (dashed line). (b) Stationary boson number statistics obtained from the restricted Boltzmann machine approach (light blue bars) and compared to benchmark calculations (dark blue bars).

denotes the probability of detecting $n$ bosons in the system at time $t$, calculated up to the highest included correlation degree $n^{max}$ [21, 332]. We employ a low cavity dissipation rate $\kappa = 0.04\,\mathrm{ps}^{-1}$ and choose $N_\beta = 5$ bits and hidden layer densities $M/(N_\beta + 1) = K/(N_\beta + 1) = 1$ to achieve numerical convergence in accordance to Fig. 10.2. Moreover, the presented results are obtained using $N_s = 5000$ sample configurations per iteration at a learning rate $\nu = 0.01$. In addition, as a benchmark we employ a regular master equation approach to calculate the stationary state using the same set of parameters, $n_\beta^{max} = 14$ and a time discretization $\Delta t = 0.02\,\mathrm{ps}$.

Fig. 10.3(a) depicts the estimated mean steady state of the boson number occupation $\langle n_\beta \rangle (t_s)$ over the number of neural network training iterations (solid blue line) and compared to the density matrix implementation benchmark $\langle n_\beta(t_s) \rangle \approx 4.56$ (dashed blue line), showing excellent agreement after approximately 4000 iterations. The light statistical fluctuations exhibited in the restricted Boltzmann machine solution can be further suppressed by increasing the number of training samples $N_s$: The solid grey line in Fig. 10.3(a) shows a comparison calculation using five times fewer samples, resulting in increased oscillations. Fig. 10.3(b) shows the stationary Fock state number statistics $P_{n_\beta(t_s)}$ [Eq. (10.15)] obtained

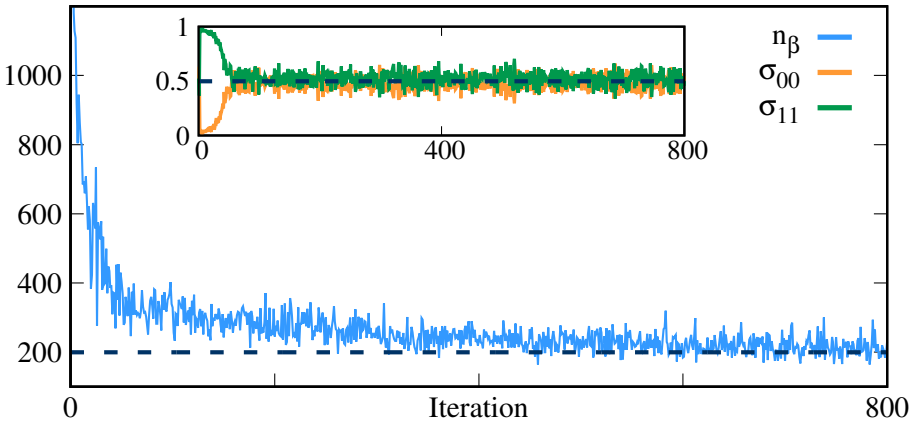


*Figure 10.4:* Demonstration of the scalability potential of the bit-encoded restricted Boltzmann machine in the limit of large boson number occupations. The solid blue line shows the average Fock state occupation number $\langle n_\beta(t_s)\rangle$ over network training iterations. The inset depicts the spin up and spin down populations of the single spin system over iterations (green and orange lines). Dashed blue lines correspond to benchmark results.

in the neural network approach (light blue bars) and compared to a benchmark density matrix implementation (dark blue bars). The two unfolding statistics are in overall very close qualitative agreement, with both their highest boson number probability located at $n_\beta = 4$. However, we note that the statistics resulting from the neural network implementation is prone to error accumulation in the boson number regime $n_\beta > 10$: In consequence of the stochastic reconfiguration method applied to the raw restricted Boltzmann machine output to calculate occurrence probabilities, the latter are afflicted by statistical deviations by design. During the evaluation of Eq. (10.15), the occurring statistical error multiplies for each increasing correlation order of $n_\beta$, leading to error propagation displayed in the form of oscillating statistics in the large occupation regime. This limits the neural network accuracy for the estimation of Fock state occupation statistics to the low boson number regime within reasonable computation times.

## 10.6 Scalability

To access the large Fock state occupation regime, we calculate the stationary state of the considered model system [Eq. (10.13)] once more using a small cavity dissipation rate $\kappa = 0.001\,\mathrm{ps}^{-1}$, yielding an average steady state occupation $\langle n_\beta(t_s)\rangle \approx 199$. In this regime, the information compression efficiency of the neural network implementation has been demonstrated to be superior even to a maximally optimized master equation implementation, as shown in Fig. 10.2. For the training of the network, $N_\beta = 13$ bits, hidden layer densities $M/(N_\beta+1) = K/(N_\beta+1) = 1$ and $N_s = 5000$ samples per iteration are employed at a learning rate $\nu = 0.003$. Even though the mean Fock state occupation number $\langle n_\beta(t_s)\rangle$ is valued well below the maximum boson number $n_\beta^{max} = 2^{N_\beta}-1$, applying fewer bits $N_\beta$ in the network leads to non-converging results, highlighting the necessity for

sufficient degrees of freedom to allow for accurate outcomes [112]. However, the supremely efficient scaling of the neural network degrees of freedom for increasing system sizes still enables high-performing calculations in this regime.

In Fig. 10.4, we show results for the average boson number occupation $\langle n_\beta(t_s)\rangle$ over training iterations (solid blue line), obtained using the restricted Boltzmann machine architecture. Strikingly, after approximately 400 iterations it already approaches the density matrix benchmark result at $\langle n_\beta(t_s)\rangle \approx 199$ (dashed blue line). The inset depicts the average stationary state spin up and spin down populations of the single spin system (green and orange lines), exhibiting very good agreement with the corresponding benchmark results (dashed blue lines). We conclude that while the required bosonic degrees of freedom by far exceed the average stationary boson occupation taken in the considered parameter setup, the amount of training iterations to achieve numerical convergence is drastically decreased for increasing visible neurons. This behavior is explained by the reduced asymmetry of the employed spin-boson interaction [Eq. (10.12)] in the regime of large Fock state occupations $n \gg 1$ where $\sqrt{n} \approx \sqrt{n+1}$, since the restricted Boltzmann machine has been shown to excel with regard to performance and convergence for the simulation of symmetric systems [72]. Moreover, the bit-encoded neural network has been demonstrated to achieve better degrees of information compression than even a maximally optimized density matrix implementation where a Heisenberg projector method has been used for optimal truncation of the corresponding Hilbert space, underlining the efficiency and performance of the bit-encoded restricted Boltzmann machine implementation of Fock states in the high boson number regime.

## 10.7 Conclusion

We have developed a neural encoding of Fock number states for the restricted Boltzmann machine architecture, expanding its capabilities from high-performing approximate mappings for open spin-1/2 systems to hybrid systems featuring bosonic degrees of freedom. Using the presented method, we have further advanced the paradigm of a universally applicable neural network architecture for the simulation of open quantum systems. Strikingly, in the limit of large boson number occupations the restricted Boltzmann machine implementation requires severely fewer degrees of freedom than regular master equation based approaches and even outperforms the information compression efficiency of a maximally optimized realization, where the corresponding configuration space has been truncated to the sparsest possible subspace via a Heisenberg projector method. We have confirmed the accuracy of the bit-encoded neural network approach for Fock states by estimating the steady state boson number statistics of a model system, yielding good qualitative agreement with comparison benchmark results. Moreover, to underline the scalability potential and performance of the presented method, we have calculated the average stationary Fock state occupation in the high boson number regime, where the information compression of the neural network has been shown to become supremely efficient. Once numerical convergence is attained by variation of the number of network degrees of freedom, it can

be further enhanced, e.g., by increasing the number of training samples or by application of adaptive sampling strategies [72].

# 11 Conclusion and outlook

In summary, in this thesis we have derived and further advanced multiple state-of-the-art theoretical open system methods and applied them to a wide variety of physical scenarios. After introducing all of the employed techniques in the first part of this thesis, the second part has focused on the emergence of dissipation-induced non-Markovian phenomena in open quantum systems:

In Chapter 6, we have predicted arising memory-critical Majorana edge correlation dynamics in a topological superconductor, facilitated by non-Markovian fermion-phonon interactions and leading to a recovery of topological properties. Aside from the considered solid-state scenarios, the observed non-Markovian information backflow is expected to also occur in realizations of ultracold quantum gases coupled to a superfluid reservoir where excitations result in the emergence of phonon interactions, or in experimental setups with intentionally induced system-reservoir interactions with a structured bosonic reservoir, as long as non-Markovian correlations can arise. We have shown that a tailored reservoir coupling can improve the stability of topological properties and even lead to their full recovery, giving rise to new prospects for the utilization and control of memory-dependent topological phenomena.

In Chapter 7, we have investigated the emergence of a non-equilibrium steady state in an optically driven $V$-type quantum emitter, exhibiting complete population inversion due to phonon-induced non-Markovian system-reservoir interactions. The observed mechanism can be exploited to create unidirectional quantum transport of carriers or excitation in an array of quantum dots, depending on the considered bidirectional interdot coupling. The reported population inversion has been shown to be robust against a wide range of perturbations and may be applied to enable carrier or excitation transport in quantum optical devices or in the context of light harvesting processes in biological systems.

In Chapter 8, we have developed an MPS-based tensor network approach for a time-discrete quantum memory in Liouville space. In combination with a tensor network implementation of real-time path integrals for continuous structured reserovirs, we have created a quasi-2D tensor network architecture to facilitate numerically exact calculations of quantum systems simultaneously coupled to two non-Markovian environments, supporting both diagonal and off-diagonal system-reservoir interactions and maintaining crucial system-reservoir and inter-reservoir entanglement information. As an example application, we have demonstrated that dynamical correlation buildup and non-Markovian interactions in between a structured phonon reservoir and time-discrete coherent photon feedback can counteract destructive interference, resulting in dynamical population trapping. The here established quasi-2D tensor network provides a numerically exact tool to gain access to the

mostly unexplored field of multiple interacting non-Markovian environments. Its performance may be further enhanced by tracing out the time-discrete memory bins after their interaction with the system, giving access to improved time discretizations. Furthermore, in future works the quasi-2D network may be advanced to a true 2D architecture using projected entangled pair states with combined reservoir memory bins to enable simulations with further improved numerical performance.

In the third part of this thesis, novel artificial neural network techniques for efficient information compression in open quantum systems have been developed and investigated. In Chapter 9, we have expanded the representational limits of established neural network implementations by deriving adaptive sampling strategies, enabling accurate and highly efficient calculations of large open quantum spin-1/2 systems with asymmetric properties. These hybrid sampling techniques open up new perspectives for the optimization and customization of the restricted Boltzmann machine architecture in a wide variety of open quantum systems, while further improving accuracy and performance.

Lastly, in Chapter 10 we have derived a neural bit encoding scheme for Fock number states in the restricted Boltzmann machine architecture to facilitate high performing calculations of hybrid systems featuring bosonic degrees of freedom. Using the presented approach, we have further advanced the paradigm of a universally applicable neural network architecture for open quantum systems beyond pure spin-1/2 setups. We have demonstrated the accuracy and scalability of the approach by estimating both the stationary state boson number statistics of a model system and the average stationary Fock state occupation in the large boson number regime. Crucially, in the high occupation limit the bit-encoded neural network requires severely fewer degrees of freedom than common density matrix based approaches and even surpasses the information compression efficiency of a maximally optimized master equation implementation, where the corresponding configuration space has been truncated to the sparsest possible subspace via a Heisenberg projector method.

# Appendices

# A Calculations: Path integral formalism

## A.1 Trace over coherent states

The trace over the reservoir is defined in terms of thermal phonon states $|n_{\boldsymbol{q}}\rangle$,

$$\mathrm{tr}_B\{\ldots\} = \prod_{\boldsymbol{q}} \sum_{n_{\boldsymbol{q}}=0}^{\infty} \langle n_{\boldsymbol{q}}| \left[\ldots\right] |n_{\boldsymbol{q}}\rangle \,, \tag{A.1}$$

which can be written in terms of unnormalized coherent states,

$$|n_{\boldsymbol{q}}\rangle = \int \frac{\mathrm{d}^2\alpha_{\boldsymbol{q}}}{\pi} |\alpha_{\boldsymbol{q}}\rangle \langle\alpha_{\boldsymbol{q}}|n_{\boldsymbol{q}}\rangle = \int \frac{\mathrm{d}^2\alpha_{\boldsymbol{q}}}{\pi} |\alpha_{\boldsymbol{q}}\rangle \sum_{m_{\boldsymbol{q}}=0}^{\infty} e^{-|\alpha_{\boldsymbol{q}}|^2/2} \frac{\alpha_{\boldsymbol{q}}^{*m_{\boldsymbol{q}}}}{\sqrt{m_{\boldsymbol{q}}!}} \langle m_{\boldsymbol{q}}|n_{\boldsymbol{q}}\rangle \,. \tag{A.2}$$

Using this representation, Eq. (A.1) takes the form

$$\begin{aligned}
\mathrm{tr}_B\{\ldots\} &= \prod_{\boldsymbol{q}} \sum_{n_{\boldsymbol{q}}=0}^{\infty} \langle n_{\boldsymbol{q}}| \, \mathbb{1}[\ldots]\mathbb{1} \, |n_{\boldsymbol{q}}\rangle \\
&= \prod_{\boldsymbol{q}} \sum_{n_{\boldsymbol{q}}=0}^{\infty} \int \frac{\mathrm{d}^2\alpha_{\boldsymbol{q}}}{\pi} \int \frac{\mathrm{d}^2\beta_{\boldsymbol{q}}}{\pi} \langle n_{\boldsymbol{q}}|\beta_{\boldsymbol{q}}\rangle \langle\beta_{\boldsymbol{q}}| \left[\ldots\right] |\alpha_{\boldsymbol{q}}\rangle \langle\alpha_{\boldsymbol{q}}|n_{\boldsymbol{q}}\rangle \\
&= \prod_{\boldsymbol{q}} \int \frac{\mathrm{d}^2\alpha_{\boldsymbol{q}}}{\pi} \int \frac{\mathrm{d}^2\beta_{\boldsymbol{q}}}{\pi} \langle\beta_{\boldsymbol{q}}| \left[\ldots\right] |\alpha_{\boldsymbol{q}}\rangle \underbrace{e^{-|\alpha_{\boldsymbol{q}}|^2/2 - |\beta_{\boldsymbol{q}}|^2/2 + \alpha_{\boldsymbol{q}}^*\beta_{\boldsymbol{q}}}}_{=\langle\alpha_{\boldsymbol{q}}|\beta_{\boldsymbol{q}}\rangle} \\
&= \prod_{\boldsymbol{q}} \int \frac{\mathrm{d}^2\alpha_{\boldsymbol{q}}}{\pi} \langle\alpha_{\boldsymbol{q}}| \left[\ldots\right] |\alpha_{\boldsymbol{q}}\rangle \,.
\end{aligned} \tag{A.3}$$

## A.2 Evaluation of Gaussian integrals

Starting from the density matrix element representation of Eq. (4.30),

$$\begin{aligned}
&\langle i_N|\,\rho_S(t)\,|i'_N\rangle = \prod_{\boldsymbol{q}} \int \frac{\mathrm{d}^2\alpha_{\boldsymbol{q}_N}}{\pi} \int \frac{\mathrm{d}^2\alpha_{\boldsymbol{q}_0}}{\pi} \int \frac{\mathrm{d}^2\beta_{\boldsymbol{q}_0}}{\pi} \sum_{i_1,\ldots,i_{N-1}=1}^{2} \sum_{i'_1,\ldots,i'_{N-1}=1}^{2} \\
&\times M_{i_N i_{N-1}} \ldots M_{i_1 i_0} M_{i'_0 i'_1} \ldots M_{i'_{N-1} i'_N} (1-\xi_{\boldsymbol{q}_0}) \langle i_0|\,\rho_S(0)\,|i'_0\rangle \\
&\times \exp\Bigg\{ -|\alpha_{\boldsymbol{q}_N}|^2 - |\alpha_{\boldsymbol{q}_0}|^2 - |\beta_{\boldsymbol{q}_0}|^2 + \xi_{\boldsymbol{q}_0}\alpha^*_{\boldsymbol{q}_0}\beta_{\boldsymbol{q}_0} + \alpha_{\boldsymbol{q}_0}\alpha^*_{\boldsymbol{q}_N} e^{-i\omega_{\boldsymbol{q}}t} + \beta^*_{\boldsymbol{q}_0}\alpha_{\boldsymbol{q}_N} e^{i\omega_{\boldsymbol{q}}t} \\
&- ig_{\boldsymbol{q}} \int_0^t \mathrm{d}\tau' \left[\alpha_{\boldsymbol{q}_0} e^{-i\omega_{\boldsymbol{q}}\tau'} + \alpha^*_{\boldsymbol{q}_N} e^{-i\omega_{\boldsymbol{q}}(t-\tau')}\right] j(\tau') - g^2_{\boldsymbol{q}} \int_0^t \mathrm{d}\tau \int_0^\tau \mathrm{d}\tau'\, e^{-i\omega_{\boldsymbol{q}}(\tau-\tau')} j(\tau) j(\tau') \\
&+ ig_{\boldsymbol{q}} \int_0^t \mathrm{d}\tau' \left[\beta^*_{\boldsymbol{q}_0} e^{i\omega_{\boldsymbol{q}}\tau'} + \alpha_{\boldsymbol{q}_N} e^{i\omega_{\boldsymbol{q}}(t-\tau')}\right] j'(\tau') - g^2_{\boldsymbol{q}} \int_0^t \mathrm{d}\tau \int_0^\tau \mathrm{d}\tau'\, e^{i\omega_{\boldsymbol{q}}(\tau-\tau')} j'(\tau) j'(\tau') \Bigg\},
\end{aligned} \tag{A.4}$$

we have yet to trace out the reservoir explicitly by carrying out the remaining three integrals. For an easier notation, we abbreviate the time-dependent integrals via

$$x := -ig_{\boldsymbol{q}} \int_0^t \mathrm{d}\tau'\, e^{-i\omega_{\boldsymbol{q}}\tau'} j(\tau'), \tag{A.5a}$$

$$x' := ig_{\boldsymbol{q}} \int_0^t \mathrm{d}\tau'\, e^{i\omega_{\boldsymbol{q}}\tau'} j'(\tau'), \tag{A.5b}$$

$$y := -ig_{\boldsymbol{q}} \int_0^t \mathrm{d}\tau'\, e^{-i\omega_{\boldsymbol{q}}(t-\tau')} j(\tau'), \tag{A.5c}$$

$$y' := ig_{\boldsymbol{q}} \int_0^t \mathrm{d}\tau'\, e^{i\omega_{\boldsymbol{q}}(t-\tau')} j'(\tau'), \tag{A.5d}$$

and extract all phonon contributions from Eq. (4.30), defining

$$\begin{aligned}
A := \int \frac{\mathrm{d}^2\alpha_{\boldsymbol{q}_N}}{\pi} \int \frac{\mathrm{d}^2\alpha_{\boldsymbol{q}_0}}{\pi} \int \frac{\mathrm{d}^2\beta_{\boldsymbol{q}_0}}{\pi} \exp\Big[&\xi_{\boldsymbol{q}_0}\alpha^*_{\boldsymbol{q}_0}\beta_{\boldsymbol{q}_0} - |\alpha_{\boldsymbol{q}_N}|^2 - |\alpha_{\boldsymbol{q}_0}|^2 - |\beta_{\boldsymbol{q}_0}|^2 \\
&+ \alpha_{\boldsymbol{q}_0}\alpha^*_{\boldsymbol{q}_N} e^{-i\omega_{\boldsymbol{q}}t} + \beta^*_{\boldsymbol{q}_0}\alpha_{\boldsymbol{q}_N} e^{i\omega_{\boldsymbol{q}}t} + \alpha_{\boldsymbol{q}_0} x + \alpha^*_{\boldsymbol{q}_N} y + \beta^*_{\boldsymbol{q}_0} x' + \alpha_{\boldsymbol{q}_N} y'\Big].
\end{aligned} \tag{A.6}$$

In the following calculations, we make use of Gaussian integrals,

$$\int_{-\infty}^{\infty} \mathrm{d}z\, e^{-\mu(z+\nu)^2} = \sqrt{\frac{\pi}{\mu}}. \tag{A.7}$$

### A.2.1 First integration

For the first integration, we define $\alpha_{\boldsymbol{q}_0} =: a + ib$ and extract all $\alpha_{\boldsymbol{q}_0}$-dependent terms from Eq. (A.6), yielding

$$\begin{aligned} B :=& \int \mathrm{d}a \int \mathrm{d}b \, \exp\left[\xi_{\boldsymbol{q}_0}\beta_{\boldsymbol{q}_0}(a-ib) - a^2 - b^2 + (a+ib)\left(x + \alpha^*_{\boldsymbol{q}_N} e^{-i\omega_{\boldsymbol{q}}t}\right)\right] \\ =& \int \mathrm{d}a \, \exp\left[-a^2 + a\left(\xi_{\boldsymbol{q}_0}\beta_{\boldsymbol{q}_0} + x + \alpha^*_{\boldsymbol{q}_N} e^{-i\omega_{\boldsymbol{q}}t}\right)\right] \\ & \int \mathrm{d}b \, \exp\left[-b^2 + ib\left(-\xi_{\boldsymbol{q}_0}\beta_{\boldsymbol{q}_0} + x + \alpha^*_{\boldsymbol{q}_N} e^{-i\omega_{\boldsymbol{q}}t}\right)\right]. \end{aligned} \tag{A.8}$$

Extending the exponential arguments by a zero addition of the form

$$-\left(a^2 - a[\ldots]\right) = -\left(a^2 - \frac{2}{2}a[\ldots] + \frac{1}{4}[\ldots]^2 - \frac{1}{4}[\ldots]^2\right) = -\left(a - \frac{1}{2}[\ldots]\right)^2 + \frac{1}{4}[\ldots]^2, \tag{A.9}$$

and making use of the Gaussian identity in Eq. (A.7), the integrals are evaluated as

$$B = \pi \exp\left[\xi_{\boldsymbol{q}_0}\beta_{\boldsymbol{q}_0}\left(x + \alpha^*_{\boldsymbol{q}_N} e^{-i\omega_{\boldsymbol{q}}t}\right)\right], \tag{A.10}$$

and Eq. (A.6) takes the form

$$\begin{aligned} A = \int \frac{\mathrm{d}^2\alpha_{\boldsymbol{q}_N}}{\pi} \int \frac{\mathrm{d}^2\beta_{\boldsymbol{q}_0}}{\pi} \exp\Big[ & -|\alpha_{\boldsymbol{q}_N}|^2 - |\beta_{\boldsymbol{q}_0}|^2 \\ & + \beta^*_{\boldsymbol{q}_0}\alpha_{\boldsymbol{q}_N} e^{i\omega_{\boldsymbol{q}}t} + \xi_{\boldsymbol{q}_0}\beta_{\boldsymbol{q}_0}\alpha^*_{\boldsymbol{q}_N} e^{-i\omega_{\boldsymbol{q}}t} + \xi_{\boldsymbol{q}_0}\beta_{\boldsymbol{q}_0}x + \alpha^*_{\boldsymbol{q}_N}y + \beta^*_{\boldsymbol{q}_0}x' + \alpha_{\boldsymbol{q}_N}y'\Big]. \end{aligned} \tag{A.11}$$

### A.2.2 Second integration

The second integral is carried out in the same fashion. We define $\beta_{\boldsymbol{q}_0} =: a + ib$ and introduce a new expression containing all $\beta_{\boldsymbol{q}_0}$-dependent terms of Eq. (A.11),

$$\begin{aligned} C :=& \int \mathrm{d}a \int \mathrm{d}b \, \exp\left[-a^2 - b^2 + (a-ib)\left(x' + \alpha_{\boldsymbol{q}_N} e^{i\omega_{\boldsymbol{q}}t}\right) + (a+ib)\left(\xi_{\boldsymbol{q}_0}x + \xi_{\boldsymbol{q}_0}\alpha^*_{\boldsymbol{q}_N} e^{-i\omega_{\boldsymbol{q}}t}\right)\right] \\ =& \int \mathrm{d}a \, \exp\left[-a^2 + a\left(x' + \alpha_{\boldsymbol{q}_N} e^{i\omega_{\boldsymbol{q}}t} + \xi_{\boldsymbol{q}_0}x + \xi_{\boldsymbol{q}_0}\alpha^*_{\boldsymbol{q}_N} e^{-i\omega_{\boldsymbol{q}}t}\right)\right] \\ & \int \mathrm{d}b \, \exp\left[-b^2 + ib\left(-x' - \alpha_{\boldsymbol{q}_N} e^{i\omega_{\boldsymbol{q}}t} + \xi_{\boldsymbol{q}_0}x + \xi_{\boldsymbol{q}_0}\alpha^*_{\boldsymbol{q}_N} e^{-i\omega_{\boldsymbol{q}}t}\right)\right]. \end{aligned} \tag{A.12}$$

The arguments of the exponential functions are once more expanded by a zero addition [Eq. (A.9)]. Afterwards, the Gaussian identity is used, yielding

$$C = \pi \exp\left[\xi_{\boldsymbol{q}_0}\left(xx' + x'\alpha^*_{\boldsymbol{q}_N} e^{-i\omega_{\boldsymbol{q}}t} + x\alpha_{\boldsymbol{q}_N} e^{i\omega_{\boldsymbol{q}}t} + |\alpha_{\boldsymbol{q}_N}|^2\right)\right], \tag{A.13}$$

and the updated expression for Eq. (A.11) reads

$$\begin{aligned} A = \int \frac{\mathrm{d}^2\alpha_{\boldsymbol{q}_N}}{\pi} \exp\Big[ & -|\alpha_{\boldsymbol{q}_N}|^2 + \alpha^*_{\boldsymbol{q}_N}y + \alpha_{\boldsymbol{q}_N}y' \\ & + \xi_{\boldsymbol{q}_0}\left(xx' + x'\alpha^*_{\boldsymbol{q}_N} e^{-i\omega_{\boldsymbol{q}}t} + x\alpha_{\boldsymbol{q}_N} e^{i\omega_{\boldsymbol{q}}t} + |\alpha_{\boldsymbol{q}_N}|^2\right)\Big]. \end{aligned} \tag{A.14}$$

### A.2.3 Third integration

For the last remaining integral, we define $\alpha_{\boldsymbol{q}_N} =: a + ib$ and perform the same operations as before, resulting in

$$A = \frac{1}{1-\xi_{\boldsymbol{q}_0}} \exp\left[\xi_{\boldsymbol{q}_0} x x' + \frac{1}{1-\xi_{\boldsymbol{q}_0}} \left(yy' + \xi_{\boldsymbol{q}_0} xy e^{i\omega_{\boldsymbol{q}} t} + \xi_{\boldsymbol{q}_0} x' y' e^{-i\omega_{\boldsymbol{q}} t} + \xi_{\boldsymbol{q}_0}^2 xx'\right)\right]. \quad \text{(A.15)}$$

As a next step, $\xi_{\boldsymbol{q}_0} = \bar{n}_{\boldsymbol{q}_0}/(1+\bar{n}_{\boldsymbol{q}_0})$ and the definitions of Eq. (A.5) are reinserted into Eq. (A.15). Together with all phonon-independent terms, the resulting expression for the density matrix elements reads

$$\begin{aligned}
\langle i_N|\,\rho_S(t)\,|i'_N\rangle = &\sum_{i_1,\ldots,i_{N-1}=1}^{2} \sum_{i'_1,\ldots,i'_{N-1}=1}^{2} M_{i_N i_{N-1}} \ldots M_{i_1 i_0} M_{i'_0 i'_1} \ldots M_{i'_{N-1} i'_N} \\
&\times \exp\left( \sum_{\boldsymbol{q}} \left\{ - g_{\boldsymbol{q}}^2 \int_0^t \mathrm{d}\tau \int_0^\tau \mathrm{d}\tau' \left[ e^{-i\omega_{\boldsymbol{q}}(\tau-\tau')} j(\tau) j(\tau') + e^{i\omega_{\boldsymbol{q}}(\tau-\tau')} j'(\tau) j'(\tau') \right] \right.\right. \\
&+ g_{\boldsymbol{q}}^2 \int_0^t \mathrm{d}\tau \int_0^t \mathrm{d}\tau'\, e^{i\omega_{\boldsymbol{q}}(\tau-\tau')} j(\tau) j'(\tau') \\
&\left.\left. - \bar{n}_{\boldsymbol{q}_0} g_{\boldsymbol{q}}^2 \int_0^t \mathrm{d}\tau \int_0^t \mathrm{d}\tau'\, e^{i\omega_{\boldsymbol{q}}(\tau-\tau')} \left[j(\tau) - j'(\tau)\right] \left[j(\tau') - j'(\tau')\right] \right\} \right) \langle i_0|\,\rho_S(0)\,|i'_0\rangle\,. \quad \text{(A.16)}
\end{aligned}$$

The argument of the exponential function is referred to as the *influence functional* $S_{inf}$ and can be further simplified for the case $g_{\boldsymbol{q}} = g_{\boldsymbol{q}}^*$ and two carrier states. Inserting $1 = [\Theta(\tau-\tau') + \Theta(\tau'-\tau)]$, the last two terms can be rewritten,

$$\int_0^t \mathrm{d}\tau \int_0^t \mathrm{d}\tau' \left[\Theta(\tau-\tau') + \Theta(\tau'-\tau)\right] [\ldots] = \int_0^t \mathrm{d}\tau \int_0^\tau \mathrm{d}\tau' \,[\ldots] + \int_0^{\tau'} \mathrm{d}\tau \int_0^t \mathrm{d}\tau' \,[\ldots]\,. \quad \text{(A.17)}$$

Substituting $\tau$ with $\tau'$ in the second term of Eq. (A.17), the influence functional can be written as

$$\begin{aligned}
S_{inf}(t) = \sum_{\boldsymbol{q}} \Bigg\{ &- g_{\boldsymbol{q}}^2 \int_0^t \mathrm{d}\tau \int_0^\tau \mathrm{d}\tau' \left[ e^{-i\omega_{\boldsymbol{q}}(\tau-\tau')} j(\tau) j(\tau') + e^{i\omega_{\boldsymbol{q}}(\tau-\tau')} j'(\tau) j'(\tau') \right] \\
&+ g_{\boldsymbol{q}}^2 \int_0^t \mathrm{d}\tau \int_0^\tau \mathrm{d}\tau' \left[ e^{i\omega_{\boldsymbol{q}}(\tau-\tau')} j(\tau) j'(\tau') + e^{-i\omega_{\boldsymbol{q}}(\tau-\tau')} j(\tau') j'(\tau) \right] \\
&- \bar{n}_{\boldsymbol{q}_0} g_{\boldsymbol{q}}^2 \int_0^t \mathrm{d}\tau \int_0^\tau \mathrm{d}\tau'\, e^{i\omega_{\boldsymbol{q}}(\tau-\tau')} \left[j(\tau) - j'(\tau)\right] \left[j(\tau') - j'(\tau')\right] \\
&- \bar{n}_{\boldsymbol{q}_0} g_{\boldsymbol{q}}^2 \int_0^t \mathrm{d}\tau \int_0^\tau \mathrm{d}\tau'\, e^{-i\omega_{\boldsymbol{q}}(\tau-\tau')} \left[j(\tau') - j'(\tau')\right] \left[j(\tau) - j'(\tau)\right] \Bigg\}. \quad \text{(A.18)}
\end{aligned}$$

Defining the reservoir autocorrelation function

$$\eta(\tau-\tau') := \sum_{\boldsymbol{q}} g_{\boldsymbol{q}}^2 \{(2\bar{n}_{\boldsymbol{q}_0}+1)\cos\left[\omega_{\boldsymbol{q}}(\tau-\tau')\right] - i \sin\left[\omega_{\boldsymbol{q}}(\tau-\tau')\right]\}, \quad \text{(A.19)}$$

we arrive at the final expression for the influence functional,

$$S_{inf}(t) = -\int_0^t \mathrm{d}\tau \int_0^\tau \mathrm{d}\tau' \, \left[j(\tau) - j'(\tau)\right] \left[\eta(\tau - \tau')j(\tau') - \eta^*(\tau - \tau')j'(\tau')\right], \tag{A.20}$$

and

$$\begin{aligned}\langle i_N | \, \rho_S(t) \, | i'_N \rangle = & \sum_{i_1,\ldots,i_{N-1}=1}^{2} \sum_{i'_1,\ldots,i'_{N-1}=1}^{2} M_{i_N i_{N-1}} \ldots M_{i_1 i_0} M_{i'_0 i'_1} \ldots M_{i'_{N-1} i'_N} \\ & \exp\left[S_{inf}(t)\right] \langle i_0 | \, \rho_S(0) \, | i'_0 \rangle \, . \end{aligned} \tag{A.21}$$

# B Calculations: Polaronic Kitaev chain

## B.1 Polaron transformation

To derive the polaron-transformed Kitaev Hamiltonian, we start from Eqs. (6.1) and (6.2), yielding the total dissipative Kitaev Hamiltonian $H_0 = H_k + H_b$,

$$\begin{aligned} H_0/\hbar = &\sum_{l=1}^{N-1} \left[ \left( -J c_l^\dagger c_{l+1} + \Delta c_l c_{l+1} \right) + \text{H.c.} \right] - \mu \sum_{l=1}^{N} c_l^\dagger c_l \\ &+ \int \mathrm{d}^3 k \ \left[ \omega_k r_{\boldsymbol{k}}^\dagger r_{\boldsymbol{k}} + \sum_{l=1}^{N} g_{\boldsymbol{k}} c_l^\dagger c_l (r_{\boldsymbol{k}}^\dagger + r_{\boldsymbol{k}}) \right]. \end{aligned} \tag{B.1}$$

As a first step, we define collective bosonic operators $R^\dagger = \int \mathrm{d}^3 k \ (g_{\boldsymbol{k}}/\omega_k) r_{\boldsymbol{k}}^\dagger$ and apply the unitary polaron transformation $H_\mathrm{p} = U_\mathrm{p} H_0 U_\mathrm{p}^{-1}$ to the dissipative Kitaev Hamiltonian via transformation matrices $U_\mathrm{p} = \exp[\sum_{l=1}^{N} c_l^\dagger c_l (R^\dagger - R)]$. To carry out the transformation, the Baker-Campbell-Hausdorff formula is applied,

$$e^X Y e^{-X} = \sum_{n=0}^{\infty} \frac{1}{n!} [X,Y]_n, \quad [X,Y]_n = [X,[X,Y]_{n-1}], \quad [X,Y]_0 = Y. \tag{B.2}$$

We start with the transformation of the first term of the dissipative Kitaev Hamiltonian,

$$\frac{1}{\hbar} U_\mathrm{p} H_{0,(i)} U_\mathrm{p}^{-1} = \sum_{n=0}^{\infty} \frac{1}{n!} \left[ \sum_{l=1}^{N} c_l^\dagger c_l (R^\dagger - R), \sum_{l'=1}^{N-1} \left[ \left( -J c_{l'}^\dagger c_{l'+1} + \Delta c_{l'} c_{l'+1} \right) + \text{H.c.} \right] \right]_n . \tag{B.3}$$

Evaluating the first four steps of the Baker-Campbell-Hausdorff formula yields

$$\begin{aligned} &\frac{1}{\hbar} u_p H_{0,(i)} u_p^{-1} = -\sum_{l=1}^{N-1} J \left( c_l^\dagger c_{l+1} + c_{l+1}^\dagger c_l \right) \\ &- \frac{1}{2}\Delta \sum_{l=1}^{N-1} \left( c_l^\dagger c_{l+1}^\dagger + c_{l+1} c_l \right) \left[ \frac{1}{2!} 2^2 (R^\dagger - R)^2 + \frac{1}{4!} 2^4 (R^\dagger - R)^4 + \dots \right] \\ &+ \frac{1}{2}\Delta \sum_{l=1}^{N-1} \left( c_l^\dagger c_{l+1}^\dagger - c_{l+1} c_l \right) \left[ \frac{1}{1!} (-2)(R^\dagger - R) + \frac{1}{3!} (-2)^3 (R^\dagger - R)^3 + \dots \right]. \end{aligned} \tag{B.4}$$

At this point, a recurrent pattern of fermionic operators can be identified and expanded into a representation of hyperbolic functions, resulting in the form

$$\frac{1}{\hbar}u_p H_{0,(i)}u_p^{-1} = \sum_{l=1}^{N-1}\Big\{ -J\left(c_l^\dagger c_{l+1} + c_{l+1}^\dagger c_l\right) - \Delta\left(c_l^\dagger c_{l+1}^\dagger + c_{l+1}c_l\right)\cosh\left[2(R-R^\dagger)\right] + \Delta\left(c_l^\dagger c_{l+1}^\dagger - c_{l+1}c_l\right)\sinh\left[2(R-R^\dagger)\right]\Big\}. \tag{B.5}$$

The transformation of the second contribution of Eq. (B.1) yields

$$\frac{1}{\hbar}u_p H_{0,(ii)}u_p^{-1} = \sum_{n=0}^{\infty}\frac{1}{n!}\left[\sum_{l=1}^{N} c_l^\dagger c_l (R^\dagger - R), -\mu\sum_{l'=1}^{N} c_{l'}^\dagger c_{l'}\right]_n = -\mu\sum_{l=1}^{N} c_l^\dagger c_l. \tag{B.6}$$

For the evaluation of the third term, the first two steps of the Baker-Campbell-Hausdorff formula are carried out explicitly. The transformation is prescribed by

$$\frac{1}{\hbar}u_p H_{0,(iii)}u_p^{-1} = \sum_{n=0}^{\infty}\frac{1}{n!}\left[\sum_{l=1}^{N}\int \mathrm{d}^3k\; c_l^\dagger c_l \frac{g_{\boldsymbol{k}}}{\omega_k}(r_{\boldsymbol{k}}^\dagger - r_{\boldsymbol{k}}), \int \mathrm{d}^3k'\; \omega_{k'} r_{\boldsymbol{k}'}^\dagger r_{\boldsymbol{k}'}\right]_n, \tag{B.7}$$

leading to

$$\frac{1}{\hbar}u_p H_{0,(iii)}u_p^{-1} = \int \mathrm{d}^3k'\;\left[\omega_{k'} r_{\boldsymbol{k}'}^\dagger r_{\boldsymbol{k}'} - \sum_{l=1}^{N} c_l^\dagger c_l g_{k'}(r_{\boldsymbol{k}'}^\dagger + r_{\boldsymbol{k}'}) + \frac{2}{2!}\sum_{l,l'=1}^{N}\frac{g_{k'}^2}{\omega_{k'}} c_l^\dagger c_l c_{l'}^\dagger c_{l'}\right]. \tag{B.8}$$

From the result of the second step, i.e., the last term in Eq. (B.8), it follows that $[\ldots]_{n\geq 3} = 0$. The transformation of the fourth term is prescribed by

$$\frac{1}{\hbar}u_p H_{0,(iv)}u_p^{-1} = \sum_{n=0}^{\infty}\frac{1}{n!}\left[\sum_{l=1}^{N}\int \mathrm{d}^3k\; c_l^\dagger c_l \frac{g_{\boldsymbol{k}}}{\omega_k}(r_{\boldsymbol{k}}^\dagger - r_{\boldsymbol{k}}), \sum_{l'=1}^{N}\int \mathrm{d}^3k'\; g_{k'} c_{l'}^\dagger c_{l'}\left(r_{\boldsymbol{k}'}^\dagger + r_{\boldsymbol{k}'}\right)\right]_n. \tag{B.9}$$

Carrying out the first step of the Baker-Campbell-Hausdorff formula results in

$$\frac{1}{\hbar}u_p H_{0,(iv)}u_p^{-1} = \sum_{l'=1}^{N}\int \mathrm{d}^3k'\;\left[g_{k'} c_{l'}^\dagger c_{l'}\left(r_{\boldsymbol{k}'}^\dagger + r_{\boldsymbol{k}'}\right) - 2\sum_{l=1}^{N}\frac{g_{k'}^2}{\omega_{k'}} c_l^\dagger c_l c_{l'}^\dagger c_{l'}\right]. \tag{B.10}$$

Again, from the last term in Eq. (B.10) it follows that $[\ldots]_{n\geq 2} = 0$.

With this, we have transformed all terms of Eq. (B.1). Adding up all partial results finally yields $H_\mathrm{p} = H_\mathrm{p,s} + H_\mathrm{p,b} + H_\mathrm{p,I}$ with

$$H_\mathrm{p,s}/\hbar = -J\sum_{l=1}^{N-1}\left(c_l^\dagger c_{l+1} + \mathrm{H.c.}\right) - \mu\sum_{l=1}^{N} c_l^\dagger c_l, \tag{B.11}$$

$$H_{\mathrm{p,I}}/\hbar = \Delta \sum_{l=1}^{N-1} \Big\{ -\left(c_l^\dagger c_{l+1}^\dagger + c_{l+1}c_l\right) \cosh\left[2(R-R^\dagger)\right] + \left(c_l^\dagger c_{l+1}^\dagger - c_{l+1}c_l\right) \sinh\left[2(R-R^\dagger)\right] \Big\}, \tag{B.12}$$

and $H_{\mathrm{p,b}}/\hbar = \int \mathrm{d}^3k\ \omega_k r_{\boldsymbol{k}}^\dagger r_{\boldsymbol{k}}$. Here we have neglected the arising polaron energy shift term

$$H_{\mathrm{shift}}/\hbar = \int \mathrm{d}^3k\ \frac{g_k^2}{\omega_k} \left(\sum_{l=1}^{N} c_l^\dagger c_l\right)^2. \tag{B.13}$$

## B.2 Franck-Condon renormalization

The polaron Hamiltonian is renormalized such that

$$\mathrm{tr}_B\{[H_{\mathrm{p,I}}, \rho(t)]\} = 0\ \forall t. \tag{B.14}$$

This is achieved via a Franck-Condon renormalization, where a zero term is added to the Hamiltonian. For the polaronic Kitaev chain, Eq. (B.14) can be fulfilled by adding the term

$$\sum_{l=1}^{N-1} \Delta(c_l^\dagger c_{l+1}^\dagger + c_{l+1}c_l)\,\langle B\rangle \tag{B.15}$$

to the interaction Hamiltonian $H_{\mathrm{p,I}}$ with a newly introduced Franck-Condon renormalization factor

$$\langle B\rangle = \mathrm{tr}\left\{\exp\left[-2(R-R^\dagger)\right]\right\} = \exp\left[-\phi(0)/2\right]. \tag{B.16}$$

In return, Eq. (B.15) is subtracted from the free contribution of the polaron Hamiltonian. Hence, the total Hamiltonian $H_p$ remains unaltered by this transformation. The Franck-Condon renormalized polaron Hamiltonians read

$$H_{\mathrm{p,s}}/\hbar = -\sum_{l=1}^{N-1} \left[\Delta\left(c_l^\dagger c_{l+1}^\dagger + c_{l+1}c_l\right)\langle B\rangle + J\left(c_l^\dagger c_{l+1} + c_{l+1}^\dagger c_l\right)\right] - \mu \sum_{l=1}^{N} c_l^\dagger c_l, \tag{B.17}$$

and

$$H_{\mathrm{p,I}}/\hbar = \Delta \sum_{l=1}^{N-1} \Big[ -\left(c_l^\dagger c_{l+1}^\dagger + c_{l+1}c_l\right)\left(\cosh\left(2(R-R^\dagger)\right) - \langle B\rangle\right) + \left(c_l^\dagger c_{l+1}^\dagger - c_{l+1}c_l\right)\sinh\left(2(R-R^\dagger)\right)\Big]. \tag{B.18}$$

## B.3 Polaron master equation

The polaron master equation is derived using standard second-order perturbation theory. The von Neumann equation is formally solved by integration and reinserted into itself. The Born approximation and the first Markov approximation are applied,

$$\rho(t-\tau) \approx \rho_S(t) \otimes \rho_B(0) \tag{B.19}$$

where indices $S$ and $B$ denote the system and environmental part of the full system density matrix $\rho(t)$, respectively. Tracing out the phononic degrees of freedom results in the non-Markovian Redfield master equation

$$\frac{\mathrm{d}}{\mathrm{d}t}\rho_S(t) = -i\left[H_{\mathrm{p,s}}, \rho_S(t)\right] - \int_0^t d\tau \mathrm{tr}_B\{[H_{\mathrm{p,I}}, [H_{\mathrm{p,I}}(-\tau), \rho_S(t) \otimes \rho_B]]\}. \tag{B.20}$$

We define collective operators

$$\begin{aligned}
X_a(t) &= -\Delta \sum_{l=1}^{N-1} \left(c_l^\dagger c_{l+1}^\dagger + c_{l+1}c_l\right), \; X_b(t) = \Delta \sum_{l=1}^{N-1} \left(c_l^\dagger c_{l+1}^\dagger - c_{l+1}c_l\right), \\
B_a(t) &= \exp\left\{2\left[R(t) - R^\dagger(t)\right]\right\} + \exp\left\{-2\left[R(t) - R^\dagger(t)\right]\right\}, \\
B_b(t) &= \exp\left\{2\left[R(t) - R^\dagger(t)\right]\right\} - \exp\left\{-2\left[R(t) - R^\dagger(t)\right]\right\},
\end{aligned} \tag{B.21}$$

and the Franck-Condon renormalized fermion-phonon interaction term of the polaron-transformed Hamiltonian takes the form

$$H_{\mathrm{p,I}}(t) = \frac{1}{2}X_a(t)\left[B_a(t) - \langle B_a\rangle\right] + \frac{1}{2}X_b(t)B_b(t). \tag{B.22}$$

Next, the integrand of Eq. (B.20) is evaluated. For a simpler notation we denote $X_{a,b}(-\tau) = X'_{a,b}$, $B_{a,b}(-\tau) = B'_{a,b}$, resulting in

$$\begin{aligned}
&[H_{\mathrm{p,I}}, [H_{\mathrm{p,I}}(-\tau), \rho]] \\
&= \left[H_{\mathrm{p,I}}, \frac{1}{2}\left[X'_aB'_a, \rho\right] + \frac{1}{2}\left[X'_bB'_b, \rho\right] - \frac{\langle B_a\rangle}{2}\left[X'_a, \rho\right]\right] \\
&= \frac{1}{2}\left[H_{\mathrm{p,I}}, \left[X'_aB'_a, \rho\right]\right] + \frac{1}{2}\left[H_{\mathrm{p,I}}, \left[X'_bB'_b, \rho\right]\right] - \frac{\langle B_a\rangle}{2}\left[H_{\mathrm{p,I}}, \left[X'_a, \rho\right]\right] \\
&= \frac{1}{4}\left[X_aB_a, \left[X'_aB'_a, \rho\right]\right] + \frac{1}{4}\left[X_bB_b, \left[X'_aB'_a, \rho\right]\right] - \frac{\langle B_a\rangle}{4}\left[X_a, \left[X'_aB'_a, \rho\right]\right] \\
&+ \frac{1}{4}\left[X_aB_a, \left[X'_bB'_b, \rho\right]\right] + \frac{1}{4}\left[X_bB_b, \left[X'_bB'_b, \rho\right]\right] - \frac{\langle B_a\rangle}{4}\left[X_a, \left[X'_bB'_b, \rho\right]\right] \\
&- \frac{\langle B_a\rangle}{4}\left[X_aB_a, \left[X'_a, \rho\right]\right] - \frac{\langle B_a\rangle}{4}\left[X_bB_b, \left[X'_a, \rho\right]\right] + \frac{\langle B_a\rangle^2}{4}\left[X_a, \left[X'_a, \rho\right]\right].
\end{aligned} \tag{B.23}$$

The most complicated terms of Eq. (B.23) are of the form $[XB,[X'B',\rho]]$. Taking the trace over the reservoir yields

$$\begin{aligned}
&\mathrm{tr}_B\Big(\,[XB,[X'B',\rho]]\,\Big)\\
&=\mathrm{tr}_B\Big(XBX'B'\rho - XB\rho X'B' - X'B'\rho XB + \rho X'B'XB\Big)\\
&= XX'\rho_S\,\langle BB'\rangle - X\rho_S X'\,\langle B'B\rangle - X'\rho_S X\,\langle BB'\rangle + \rho_S X'X\,\langle B'B\rangle\\
&= \langle BB'\rangle\,\Big(XX'\rho_S - X'\rho_S X\Big) + \langle B'B\rangle\,\Big(\rho_S X'X - X\rho_S X'\Big)\\
&= \langle BB'\rangle\,[X,X'\rho_S] - \langle B'B\rangle\,[X,\rho_S X']\,,
\end{aligned} \tag{B.24}$$

with $\langle\ldots\rangle = \mathrm{tr}_B\{\rho(t)\ldots\}$. The other contributions read

$$\begin{aligned}
\mathrm{tr}_B\Big(\,[X,[X'B',\rho]]\,\Big) &= \langle B'\rangle\,([X,X'\rho_S] - [X,\rho_S X'])\,,\\
\mathrm{tr}_B\Big(\,[XB,[X',\rho]]\,\Big) &= \langle B\rangle\,([X,X'\rho_S] - [X,\rho_S X'])\,,\\
\mathrm{tr}_B\Big(\,[X,[X',\rho]]\,\Big) &= ([X,X'\rho_S] - [X,\rho_S X'])\,.
\end{aligned} \tag{B.25}$$

It can be shown that $\langle B_a B'_b\rangle = \langle B_b B'_a\rangle = 0$. $\langle B'_a\rangle$ is calculated as

$$\begin{aligned}
\langle B'_a\rangle &= \mathrm{tr}_B\left(\rho_B\left\{e^{2[R(-\tau)-R^\dagger(-\tau)]} + e^{-2[R(-\tau)-R^\dagger(-\tau)]}\right\}\right)\\
&= 2\mathrm{tr}_B\left[\rho_B\left(1+\frac{1}{2!}\left\{2\left[R(-\tau)-R^\dagger(-\tau)\right]\right\}^2+\ldots\right)\right]\\
&= 2\mathrm{tr}_B\left(\rho_B\left\{1+\frac{1}{2!}\left[2\int \mathrm{d}^3k\;\frac{g_{\boldsymbol{k}}}{\omega_k}\left(r_{\boldsymbol{k}}e^{i\omega_k\tau} - r^\dagger_{\boldsymbol{k}}e^{-i\omega_k\tau}\right)\right]^2+\ldots\right\}\right)\\
&= 2\mathrm{tr}_B\left(\rho_B\left\{1+\frac{1}{2!}\left[-\int \mathrm{d}^3k\;|2g_{\boldsymbol{k}}/\omega_k|^2(1+2n_k)\right]+\ldots\right\}\right)\\
&= 2\mathrm{tr}_B\left(\rho_B\left\{1+\frac{1}{1!}\left[-\frac{1}{2}\int \mathrm{d}^3k\;|2g_{\boldsymbol{k}}/\omega_k|^2(1+2n_k)\right]+\ldots\right\}\right)\\
&= 2\exp\left[-\frac{1}{2}\int \mathrm{d}^3k\;|2g_{\boldsymbol{k}}/\omega_k|^2(2n_k+1)\right] = \langle B_a\rangle\,,
\end{aligned} \tag{B.26}$$

and Eq. (B.23) takes the form

$$\begin{aligned}
&\mathrm{tr}_B\left[H_{\mathrm{p,I}},\left[\tilde{H}'_{p,I},\rho_S(t)\otimes\rho_B\right]\right]\\
&= \frac{1}{4}\,\langle B_aB'_a\rangle\,[X_a,X'_a\rho_S(t)] - \frac{1}{4}\,\langle B'_aB_a\rangle\,[X_a,\rho_S(t)X'_a] + \frac{1}{4}\,\langle B_bB'_b\rangle\,[X_b,X'_b\rho_S(t)]\\
&- \frac{1}{4}\,\langle B'_bB_b\rangle\,[X_b,\rho_S(t)X'_b] - \frac{1}{4}\,\langle B_a\rangle^2\,([X_a,X'_a\rho_S(t)] - [X_a,\rho_S(t)X'_a])\,.
\end{aligned} \tag{B.27}$$

### B.3.1 Reservoir correlations

The reservoir correlations $\langle B_{a,b}B_{a,b}(-\tau)\rangle\,, \langle B_{a,b}(-\tau)B_{a,b}\rangle$ are calculated next. We require

$$\begin{aligned}
&\Big[2(R-R^\dagger), 2(R(-\tau)-R^\dagger(-\tau))\Big] \\
&= \int \mathrm{d}^3k \int \mathrm{d}^3k' \; \frac{2^2 g_{\boldsymbol{k}} g_{\boldsymbol{k}'}}{\omega_k \omega_{k'}} \left[r_{\boldsymbol{k}} - r^\dagger_{\boldsymbol{k}}, r_{\boldsymbol{k}'} e^{i\omega_{k'}\tau} - r^\dagger_{\boldsymbol{k}'} e^{-i\omega_{k'}\tau}\right] \\
&= 2i \int \mathrm{d}^3k \; |2g_{\boldsymbol{k}}/\omega_k|^2 \sin(\omega_k \tau) =: 2i\phi_s(\tau),
\end{aligned} \tag{B.28}$$

and make use of the simplified Baker-Campbell-Hausdorff formula $e^X e^Y = e^{X+Y} e^{1/2[X,Y]}$, which is valid if $[X,[X,Y]] = 0$ and $[Y,[Y,X]] = 0$. We start with the correlation $\langle B_a B_a(-\tau)\rangle$,

$$\begin{aligned}
\langle B_a B_a(-\tau)\rangle &= \mathrm{tr}_B \left\{\rho_B \left[e^{2(R-R^\dagger)} + e^{-2(R-R^\dagger)}\right]\left[e^{2[R(-\tau)-R^\dagger(-\tau)]} + e^{-2[R(-\tau)-R^\dagger(-\tau)]}\right]\right\} \\
&= \mathrm{tr}_B \Bigg\{\rho_B \Big[e^{2(R-R^\dagger)} e^{2[R(-\tau)-R^\dagger(-\tau)]} + e^{-2(R-R^\dagger)} e^{-2[R(-\tau)-R^\dagger(-\tau)]} \\
&\quad + e^{2(R-R^\dagger)} e^{-2[R(-\tau)-R^\dagger(-\tau)]} + e^{-2(R-R^\dagger)} e^{2[R(-\tau)-R^\dagger(-\tau)]}\Big]\Bigg\} \\
&= \mathrm{tr}_B \Bigg\{\rho_B \Big[e^{2[R^\dagger+R^\dagger(-\tau)]-2[R+R(-\tau)]} e^{1/2\left[2(R-R^\dagger),2(R(-\tau)-R^\dagger(-\tau))\right]} \\
&\quad + e^{-2[R^\dagger+R^\dagger(-\tau)]+2[R+R(-\tau)]} e^{1/2\left[2(R-R^\dagger),2(R(-\tau)-R^\dagger(-\tau))\right]} \\
&\quad + e^{2[R^\dagger-R^\dagger(-\tau)]-2[R-R(-\tau)]} e^{1/2\left[2(R-R^\dagger),2(R(-\tau)-R^\dagger(-\tau))\right](-1)} \\
&\quad + e^{-2[R^\dagger-R^\dagger(-\tau)]+2[R-R(-\tau)]} e^{1/2\left[2(R-R^\dagger),2(R(-\tau)-R^\dagger(-\tau))\right](-1)}\Big]\Bigg\},
\end{aligned} \tag{B.29}$$

with $e^{1/2\left[2(R-R^\dagger),2(R(-\tau)-R^\dagger(-\tau))\right]} = e^{i\phi_s(\tau)}$. Using the identity $\cosh(x) = \frac{1}{2}(e^x + e^{-x}) = 1 + \frac{x^2}{2!} + \frac{x^4}{4!} + \ldots$, Eq. (B.29) is rewritten as

$$\begin{aligned}
\langle B_a B_a(-\tau)\rangle &= 2\mathrm{tr}_B \rho_B \Bigg[\Bigg(1 + \frac{1}{2!}\left\{2\left[R^\dagger + R^\dagger(-\tau)\right] - 2\left[R + R(-\tau)\right]\right\}^2 \\
&\quad + \frac{1}{4!}\left\{2\left[R^\dagger + R^\dagger(-\tau)\right] - 2\left[R + R(-\tau)\right]\right\}^4 + \ldots\Bigg) e^{i\phi_s(\tau)} \\
&\quad + \Bigg(1 + \frac{1}{2!}\left\{2\left[R^\dagger - R^\dagger(-\tau)\right] - 2\left[R - R(-\tau)\right]\right\}^2 \\
&\quad + \frac{1}{4!}\left\{2\left[R^\dagger - R^\dagger(-\tau)\right] - 2\left[R - R(-\tau)\right]\right\}^4 + \ldots\Bigg) e^{-i\phi_s(\tau)}\Bigg].
\end{aligned} \tag{B.30}$$

We define

$$\begin{aligned}[R \pm R(-\tau)] &= \int \mathrm{d}^3k \ \frac{g_{\boldsymbol{k}}}{\omega_k}(1 \pm e^{i\omega_k\tau})r_{\boldsymbol{k}} =: \int \mathrm{d}^3k \ f_{\pm}(\boldsymbol{k})r_{\boldsymbol{k}}, \\ \left[R^\dagger \pm R^\dagger(-\tau)\right] &= \int \mathrm{d}^3k \ \frac{g_{\boldsymbol{k}}}{\omega_k}(1 \pm e^{-i\omega_k\tau})r^\dagger_{\boldsymbol{k}} =: \int \mathrm{d}^3k \ f^*_{\pm}(\boldsymbol{k})r^\dagger_{\boldsymbol{k}},\end{aligned} \tag{B.31}$$

and the first product in Eq. (B.30) takes the form

$$\begin{aligned}&\mathrm{tr}_B\left(\rho_B\left\{2\left[R^\dagger + R^\dagger(-\tau)\right] - 2\left[R + R(-\tau)\right]\right\}^2\right) \\ &= \mathrm{tr}_B\left(\rho_B\left\{2\int \mathrm{d}^3k \ \left[f^*_+(\boldsymbol{k})r^\dagger_{\boldsymbol{k}} - f_+(\boldsymbol{k})r_{\boldsymbol{k}}\right]\right\}^2\right) \\ &= 2^2\int \mathrm{d}^3k \int \mathrm{d}^3k' \ \mathrm{tr}_B\left\{\rho_B\left[-f^*_+(\boldsymbol{k})f_+(\boldsymbol{k}')r^\dagger_{\boldsymbol{k}}r_{\boldsymbol{k}'} - f_+(\boldsymbol{k})f^*_+(\boldsymbol{k}')r_{\boldsymbol{k}}r^\dagger_{\boldsymbol{k}'}\right]\right\} \\ &= -2^2\int \mathrm{d}^3k \ |f_+(\boldsymbol{k})|^2(2n_k+1).\end{aligned} \tag{B.32}$$

The next term is factorized using Wick's theorem, yielding

$$\begin{aligned}&\mathrm{tr}_B\left(\rho_B\left\{2\left[R^\dagger + R^\dagger(-\tau)\right] - 2[R + R(-\tau)]\right\}^4\right) \\ &\approx 2^4 3\int \mathrm{d}^3k \int \mathrm{d}^3k' \ |f_+(\boldsymbol{k})|^2|f_+(\boldsymbol{k}')|^2(2n_k+1)(2n_{k'}+1).\end{aligned} \tag{B.33}$$

Factorizing all terms in Eq. (B.30) in this fashion results in two exponential series, yielding

$$\begin{aligned}\langle B_aB_a(-\tau)\rangle =& 2\exp\left[-\frac{1}{2}\int \mathrm{d}^3k \ |2f_+(\boldsymbol{k})|^2(2n_k+1) + i\phi_s(\tau)\right] \\ &+2\exp\left[-\frac{1}{2}\int \mathrm{d}^3k \ |2f_-(\boldsymbol{k})|^2(2n_k+1) - i\phi_s(\tau)\right],\end{aligned} \tag{B.34}$$

with $|f_\pm(\boldsymbol{k})|^2 = |g_{\boldsymbol{k}}/\omega_k|^2[2 \pm 2\cos(\omega_k\tau)]$. The phonon number $n_k$ is modeled as a Bose distribution, resulting in $(2n_k+1) = \coth[\hbar\omega_k/(2k_BT)]$. We define the phonon correlation function

$$\phi(\tau) := \int \mathrm{d}^3k \left|\frac{2g_{\boldsymbol{k}}}{\omega_k}\right|^2\left[\coth\left(\frac{\hbar\omega_k}{2k_BT}\right)\cos(\omega_k\tau) - i\sin(\omega_k\tau)\right], \tag{B.35}$$

and arrive at the final form of the reservoir correlation

$$\langle B_aB_a(-\tau)\rangle = 4\exp[-\phi(0)]\cosh[\phi(\tau)]. \tag{B.36}$$

$\langle B_bB_b(-\tau)\rangle$ is calculated in the same fashion. The calculation of $\langle B_a(-\tau)B_a\rangle$ has already been done up to a sign in $\phi_s(\tau)$. The resulting terms read

$$\begin{aligned}\langle B_a(-\tau)B_a\rangle &= 4\exp[-\phi(0)]\cosh[\phi^*(\tau)] = \langle B_aB_a(-\tau)\rangle^*, \\ \langle B_bB_b(-\tau)\rangle &= -4\exp[-\phi(0)]\sinh[\phi(\tau)], \\ \langle B_b(-\tau)B_b\rangle &= -4\exp[-\phi(0)]\sinh[\phi^*(\tau)] = \langle B_bB_b(-\tau)\rangle^*.\end{aligned} \tag{B.37}$$

Finally, inserting the correlation functions into Eq. (B.27) yields

$$\begin{aligned}\mathrm{tr}_B\left[H_{\mathrm{p,I}},\left[H'_{\mathrm{p,I}},\rho_S(t)\otimes\rho_B\right]\right] &= \{\exp\left[-\phi(0)\right]\left(\cosh\left[\phi(\tau)\right]-1\right)\left[X_a,X'_a\rho_S(t)\right] \\ &\quad -\exp\left[-\phi(0)\right]\sinh\left[\phi(\tau)\right]\left[X_b,X'_b\rho_S(t)\right]+\mathrm{H.c.}\},\end{aligned} \tag{B.38}$$

and the polaron master equation takes the form

$$\begin{aligned}\frac{\mathrm{d}}{\mathrm{d}t}\rho_S(t) &= -i\left[H_{\mathrm{p,s}},\rho_S(t)\right]-e^{-\phi(0)}\int_0^t d\tau\{\left(\cosh\left[\phi(\tau)\right]-1\right)\left[X_a,X_a(-\tau)\rho_S(t)\right] \\ &\quad -\sinh\left[\phi(\tau)\right]\left[X_b,X_b(-\tau)\rho_S(t)\right]+\mathrm{H.c.}\}.\end{aligned} \tag{B.39}$$

## B.4 Majorana edge correlation

To investigate the fate of topological properties in the polaronic Kitaev chain, the Majorana edge correlation $\langle\theta\rangle(t)$ is calculated. In the case of an ideal Kitaev chain it is given by [143, 144]

$$\begin{aligned}&-i\left\langle\gamma_L\gamma_R\right\rangle(t)=\mathrm{tr}\{\rho(t)(c_1+c_1^\dagger)(c_N^\dagger-c_N)\} \\ &=\sum_{\{n\}}\left\langle n_1,\ldots,n_N\right|\rho(t)(c_1+c_1^\dagger)(c_N^\dagger-c_N)\left|n\right\rangle \\ &=\sum_{\{n\}}\Big[-\left\langle n_1,\ldots,n_N\right|\rho(t)\left|0,\ldots,1\right\rangle\delta_{n_1,1}\delta_{n_N,0}-\left\langle n\right|\rho(t)\left|1,\ldots,0\right\rangle\delta_{n_1,0}\delta_{n_N,1} \\ &+\left\langle n_1,\ldots,n_N\right|\rho(t)\left|1,\ldots,1\right\rangle\delta_{n_1,0}\delta_{n_N,0}+\left\langle n\right|\rho(t)\left|0,\ldots,0\right\rangle\delta_{n_1,1}\delta_{n_N,1}\Big]e^{i\pi\sum_{l=2}^{N-1}n_l} \\ &=\sum_{\{n\}}\Big[-\left\langle 1,n_2,\ldots,n_{N-1},0\right|\rho(t)\left|0,n_2,\ldots,n_{N-1},1\right\rangle \\ &-\left\langle 0,n_2,\ldots,n_{N-1},1\right|\rho(t)\left|1,n_2,\ldots,n_{N-1},0\right\rangle \\ &+\left\langle 0,n_2,\ldots,n_{N-1},0\right|\rho(t)\left|1,n_2,\ldots,n_{N-1},1\right\rangle \\ &+\left\langle 1,n_2,\ldots,n_{N-1},1\right|\rho(t)\left|0,n_2,\ldots,n_{N-1},0\right\rangle\Big]e^{i\pi\sum_{l=2}^{N-1}n_l},\end{aligned} \tag{B.40}$$

with $n_l=\{0,1\}$ and $l=\{1,\ldots,N\}$. When assuming even parity conditions, i.e., $\sum_{l=1}^{N}n_l=2\nu$, $\nu\in\mathbb{N}_0$, this yields

$$\begin{aligned}\langle\theta\rangle(t)=\sum_{\{n\}}\Big[&\left\langle 1,n_2,\ldots,n_{N-1},0\right|\rho(t)\left|0,n_2,\ldots,n_{N-1},1\right\rangle \\ &+\left\langle 0,n_2,\ldots,n_{N-1},1\right|\rho(t)\left|1,n_2,\ldots,n_{N-1},0\right\rangle \\ &+\left\langle 0,n_2,\ldots,n_{N-1},0\right|\rho(t)\left|1,n_2,\ldots,n_{N-1},1\right\rangle \\ &+\left\langle 1,n_2,\ldots,n_{N-1},1\right|\rho(t)\left|0,n_2,\ldots,n_{N-1},0\right\rangle\Big].\end{aligned} \tag{B.41}$$

In the case of odd parity conditions, $\sum_{l=1}^{N} n_l = 2\nu + 1$, $\nu \in \mathbb{N}_0$, the Jordan-Wigner phase results in negative signs,

$$\begin{aligned}\langle\theta\rangle(t) = -\sum_{\{n\}}\Big[ &\langle 1, n_2, \ldots, n_{N-1}, 0|\,\rho(t)\,|0, n_2, \ldots, n_{N-1}, 1\rangle \\ &+ \langle 0, n_2, \ldots, n_{N-1}, 1|\,\rho(t)\,|1, n_2, \ldots, n_{N-1}, 0\rangle \\ &+ \langle 0, n_2, \ldots, n_{N-1}, 0|\,\rho(t)\,|1, n_2, \ldots, n_{N-1}, 1\rangle \\ &+ \langle 1, n_2, \ldots, n_{N-1}, 1|\,\rho(t)\,|0, n_2, \ldots, n_{N-1}, 0\rangle\Big]. \end{aligned} \tag{B.42}$$

## B.5 Equations of motion

The equations of motion are stated for the system density matrix elements

$$\langle m_1, \ldots, m_N|\,\rho_S\,|n_1, \ldots, n_N\rangle(t) = \langle m|\,\rho_S\,|n\rangle(t). \tag{B.43}$$

For a shorter notation we henceforth write $\rho_S(t) = \rho(t)$. The equations of motion resulting from the first term of the polaron master equation read

$$\begin{aligned}&-i\,\langle m|\,[H_{\mathrm{p,s}}, \rho(t)]\,|n\rangle \\ &= 2i\mu \sum_{l=1}^{N-1} (m_l - n_l)\,\langle m|\,\rho(t)\,|n\rangle \\ &+ iU \sum_{l=1}^{N-1}\Big[(2n_l - 1)(2n_{l+1} - 1) - (2m_l - 1)(2m_{l+1} - 1)\Big]\,\langle m|\,\rho(t)\,|n\rangle \\ &+ iJe^{-\phi(0)/2} \sum_{l=1}^{N-1}\Big[\langle \ldots, m_l + 1, m_{l+1} + 1, \ldots|\,\rho(t)\,|n\rangle\,\delta_{m_l,0}\delta_{m_{l+1},0} \\ &+ \langle \ldots, m_l - 1, m_{l+1} - 1, \ldots|\,\rho(t)\,|n\rangle\,\delta_{m_l,1}\delta_{m_{l+1},1} \\ &- \langle m|\,\rho(t)\,|\ldots, n_l + 1, n_{l+1} + 1, \ldots\rangle\,\delta_{n_l,0}\delta_{n_{l+1},0} \\ &- \langle m|\,\rho(t)\,|\ldots, n_l - 1, n_{l+1} - 1, \ldots\rangle\,\delta_{n_l,1}\delta_{n_{l+1},1}\Big] \\ &+ iJ \sum_{l=1}^{N-1}\Big[\langle \ldots, m_l + 1, m_{l+1} - 1, \ldots|\,\rho(t)\,|n\rangle\,\delta_{m_l,0}\delta_{m_{l+1},1} \\ &+ \langle \ldots, m_l - 1, m_{l+1} + 1, \ldots|\,\rho(t)\,|n\rangle\,\delta_{m_l,1}\delta_{m_{l+1},0} \\ &- \langle m|\,\rho(t)\,|\ldots, n_l + 1, n_{l+1} - 1, \ldots\rangle\,\delta_{n_l,0}\delta_{n_{l+1},1} \\ &- \langle m|\,\rho(t)\,|\ldots, n_l - 1, n_{l+1} + 1, \ldots\rangle\,\delta_{n_l,1}\delta_{n_{l+1},0}\Big]. \end{aligned} \tag{B.44}$$

We define $G_a(\tau) := \cosh[\phi(\tau)] - 1$, $G_b(\tau) := -\sinh[\phi(\tau)]$, and

$$\chi(\tau) := G_a(\tau)\,[X_a, X_a(-\tau)\rho_S(t)] + G_b(\tau)\,[X_b, X_b(-\tau)\rho_S(t)] + \text{H.c.}. \tag{B.45}$$

The second term of the master equation then takes the form $-\exp\left[-\phi(0)\right]\int_0^t d\tau\chi(\tau)$, with

$$
\begin{aligned}
&\langle m|\,\chi(\tau)\,|n\rangle \\
&= \sum_{i=a,b}\Big[G_i(\tau)\,\langle m|\,X_iX_i(-\tau)\rho(t)\,|n\rangle - G_i(\tau)\,\langle m|\,X_i(-\tau)\rho(t)X_i\,|n\rangle \\
&+ G_i^*(\tau)\,\langle m|\,\rho(t)X_i(-\tau)X_i\,|n\rangle - G_i^*(\tau)\,\langle m|\,X_i\rho(t)X_a(-\tau)\,|n\rangle\Big] \\
&= \sum_{i=a,b}\sum_{\{s\}}\Big[G_i(\tau)\,\langle m|\,X_iX_i(-\tau)\,|s\rangle\,\langle s|\,\rho(t)\,|n\rangle - G_i(\tau)\,\langle m|\,X_i(-\tau)\,|s\rangle\,\langle s|\,\rho(t)X_i\,|n\rangle \\
&+ G_i^*(\tau)\,\langle m|\,\rho(t)\,|s\rangle\,\langle s|\,X_i(-\tau)X_i\,|n\rangle - G_i^*(\tau)\,\langle m|\,X_i\rho(t)\,|s\rangle\,\langle s|\,X_i(-\tau)\,|n\rangle\Big]. \qquad \text{(B.46)}
\end{aligned}
$$

Inserting the definitions of the system correlations $X_{a,b}$ yields

$$
\begin{aligned}
&\langle m|\,\chi(\tau)\,|n\rangle = \Delta\sum_{\{s\}}\sum_{l}\Big\{\,\langle s|\,\rho(t)\,|n\rangle \\
&\Big[-G_a(\tau)\,\langle\ldots,m_l+1,m_{l+1}+1,\ldots|\,X_a(-\tau)\,|s\rangle\,\delta_{m_l,0}\delta_{m_{l+1},0} \\
&-G_a(\tau)\,\langle\ldots,m_l-1,m_{l+1}-1,\ldots|\,X_a(-\tau)\,|s\rangle\,\delta_{m_l,1}\delta_{m_{l+1},1} \\
&+G_b(\tau)\,\langle\ldots,m_l-1,m_{l+1}-1,\ldots|\,X_b(-\tau)\,|s\rangle\,\delta_{m_l,1}\delta_{m_{l+1},1} \\
&-G_b(\tau)\,\langle\ldots,m_l+1,m_{l+1}+1,\ldots|\,X_b(-\tau)\,|s\rangle\,\delta_{m_l,0}\delta_{m_{l+1},0}\Big] \\
&+\langle m|\,\rho(t)\,|s\rangle \\
&\Big[-G_a^*(\tau)\,\langle s|\,X_a(-\tau)\,|\ldots,n_l+1,n_{l+1}+1,\ldots\rangle\,\delta_{n_l,0}\delta_{n_{l+1},0} \\
&-G_a^*(\tau)\,\langle s|\,X_a(-\tau)\,|\ldots,n_l-1,n_{l+1}-1,\ldots\rangle\,\delta_{n_l,1}\delta_{n_{l+1},1} \\
&+G_b^*(\tau)\,\langle s|\,X_b(-\tau)\,|\ldots,n_l+1,n_{l+1}+1,\ldots\rangle\,\delta_{n_l,0}\delta_{n_{l+1},0} \\
&-G_b^*(\tau)\,\langle s|\,X_b(-\tau)\,|\ldots,n_l-1,n_{l+1}-1,\ldots\rangle\,\delta_{n_l,1}\delta_{n_{l+1},1}\Big] \\
&+\langle s|\,\rho(t)\,|\ldots,n_l+1,n_{l+1}+1,\ldots\rangle\,\delta_{n_l,0}\delta_{n_{l+1},0} \\
&\Big[G_a(\tau)\,\langle m|\,X_a(-\tau)\,|s\rangle - G_b(\tau)\,\langle m|\,X_b(-\tau)\,|s\rangle\Big] \\
&+\langle s|\,\rho(t)\,|\ldots,n_l-1,n_{l+1}-1,\ldots\rangle\,\delta_{n_l,1}\delta_{n_{l+1},1} \\
&\Big[G_a(\tau)\,\langle m|\,X_a(-\tau)\,|s\rangle + G_b(\tau)\,\langle m|\,X_b(-\tau)\,|s\rangle\Big] \\
&+\langle\ldots,m_l+1,m_{l+1}+1,\ldots|\,\rho(t)\,|s\rangle\,\delta_{m_l,0}\delta_{m_{l+1},0} \\
&\Big[G_a^*(\tau)\,\langle s|\,X_a(-\tau)\,|n\rangle + G_b^*(\tau)\,\langle s|\,X_b(-\tau)\,|n\rangle\Big] \\
&+\langle\ldots,m_l-1,m_{l+1}-1,\ldots|\,\rho(t)\,|s\rangle\,\delta_{m_l,1}\delta_{m_{l+1},1} \\
&\Big[G_a^*(\tau)\,\langle s|\,X_a(-\tau)\,|n\rangle - G_b^*(\tau)\,\langle s|\,X_b(-\tau)\,|n\rangle\Big]\Big\}. \qquad \text{(B.47)}
\end{aligned}
$$

As described in Sec. 3.5, the time-dependent system correlations $X_{a,b}(-\tau)$ are expanded via the time-evolution operator $U_0(t,0) = \exp\left(-iH_{\mathrm{p,s}}t/\hbar\right)$, resulting in

$$\begin{aligned}\langle m|\, X_a(-\tau)\,|n\rangle = &-\Delta \sum_l \sum_{\{s\}} \Big[ \langle s_1,\ldots,0,0,\ldots,s_N|\, \rho_c(-\tau)\,|s_1,\ldots,1,1,\ldots,s_N\rangle \\ &+ \langle s_1,\ldots,1,1,\ldots,s_N|\, \rho_c(-\tau)\,|s_1,\ldots,0,0,\ldots,s_N\rangle \Big], \end{aligned} \tag{B.48}$$

$$\begin{aligned}\langle m|\, X_b(-\tau)\,|n\rangle = &+\Delta \sum_l \sum_{\{s\}} \Big[ \langle s_1,\ldots,0,0,\ldots,s_N|\, \rho_c(-\tau)\,|s_1,\ldots,1,1,\ldots,s_N\rangle \\ &- \langle s_1,\ldots,1,1,\ldots,s_N|\, \rho_c(-\tau)\,|s_1,\ldots,0,0,\ldots,s_N\rangle \Big], \end{aligned} \tag{B.49}$$

with $\rho_c$ the conditional density matrix.

# C Calculations: Chain of V-type emitters

## C.1 Parameters

Table C.1 shows the parameters employed for all numerical calculations in Ch. 7.

| Parameter | Single emitter | Chain (single) | Chain (all-to-all) |
|---|---|---|---|
| $\delta\epsilon$ | $-1.0\,\mathrm{meV}$ | $-1.0\,\mathrm{meV}$ | $-1.0\,\mathrm{meV}$ |
| $\hbar\Omega$ | $0.0658\,\mathrm{meV}$ | $0.0658\,\mathrm{meV}$ | $0.3291\,\mathrm{meV}$ |
| $T$ | $4\,\mathrm{K}$ | $4\,\mathrm{K}$ | $4\,\mathrm{K}$ |
| $\hbar f$ | — | $0.0658\,\mathrm{meV}$ | $0.0658\,\mathrm{meV}$ |

*Table C.1:* Parameters employed for numerical calculations of the $V$-type emitter model, including the single emitter case and the quantum dot chain with single Dexter- and Förster-type interdot couplings, as well as Dexter-type coupling between all excited states of adjacent emitters.

## C.2 Heisenberg picture: Equations of motion

The full set of Heisenberg equations of motion up to second order in phonon contributions for a single $V$-type emitter read

$$\begin{aligned}
\frac{\mathrm{d}}{\mathrm{d}t}\langle\sigma_{mn}\rangle = i\Big[&\Delta_2\left(\langle\sigma_{2n}\rangle\,\delta_{m2} - \langle\sigma_{m2}\rangle\,\delta_{n2}\right) + \Delta_3\left(\langle\sigma_{3n}\rangle\,\delta_{m3} - \langle\sigma_{m3}\rangle\,\delta_{n3}\right)\\
&+ \Omega\left(\langle\sigma_{1n}\rangle\,\delta_{m2} + \langle\sigma_{2n}\rangle\,\delta_{m1} - \langle\sigma_{m2}\rangle\,\delta_{n1} - \langle\sigma_{m1}\rangle\,\delta_{n2}\right)\\
&+ \Omega\left(\langle\sigma_{1n}\rangle\,\delta_{m3} + \langle\sigma_{3n}\rangle\,\delta_{m1} - \langle\sigma_{m3}\rangle\,\delta_{n1} - \langle\sigma_{m1}\rangle\,\delta_{n3}\right)\\
&+ \int \mathrm{d}^3k\; g_{\boldsymbol{k}}\Big(\langle\sigma_{2n}r^\dagger_{\boldsymbol{k}}\rangle\,\delta_{m2} + \langle\sigma_{3n}r^\dagger_{\boldsymbol{k}}\rangle\,\delta_{m3} - \langle\sigma_{m2}r^\dagger_{\boldsymbol{k}}\rangle\,\delta_{n2} - \langle\sigma_{m3}r^\dagger_{\boldsymbol{k}}\rangle\,\delta_{n3}\\
&+ \langle\sigma_{2n}r_{\boldsymbol{k}}\rangle\,\delta_{m2} + \langle\sigma_{3n}r_{\boldsymbol{k}}\rangle\,\delta_{m3} - \langle\sigma_{m2}r_{\boldsymbol{k}}\rangle\,\delta_{n2} - \langle\sigma_{m3}r_{\boldsymbol{k}}\rangle\,\delta_{n3}\Big)\Big],
\end{aligned} \tag{C.1}$$

$$\begin{aligned}
\frac{\mathrm{d}}{\mathrm{d}t}\langle\sigma_{mn}r_{\boldsymbol{k}}^{\dagger}\rangle &= i\Big[\Delta_2\left(\langle\sigma_{2n}r_{\boldsymbol{k}}^{\dagger}\rangle\,\delta_{m2}-\langle\sigma_{m2}r_{\boldsymbol{k}}^{\dagger}\rangle\,\delta_{n2}\right)+\Delta_3\left(\langle\sigma_{3n}r_{\boldsymbol{k}}^{\dagger}\rangle\,\delta_{m3}-\langle\sigma_{m3}r_{\boldsymbol{k}}^{\dagger}\rangle\,\delta_{n3}\right)\\
&+\Omega\left(\langle\sigma_{1n}r_{\boldsymbol{k}}^{\dagger}\rangle\,\delta_{m2}+\langle\sigma_{2n}r_{\boldsymbol{k}}^{\dagger}\rangle\,\delta_{m1}-\langle\sigma_{m2}r_{\boldsymbol{k}}^{\dagger}\rangle\,\delta_{n1}-\langle\sigma_{m1}r_{\boldsymbol{k}}^{\dagger}\rangle\,\delta_{n2}\right)\\
&+\Omega\left(\langle\sigma_{1n}r_{\boldsymbol{k}}^{\dagger}\rangle\,\delta_{m3}+\langle\sigma_{3n}r_{\boldsymbol{k}}^{\dagger}\rangle\,\delta_{m1}-\langle\sigma_{m3}r_{\boldsymbol{k}}^{\dagger}\rangle\,\delta_{n1}-\langle\sigma_{m1}r_{\boldsymbol{k}}^{\dagger}\rangle\,\delta_{n3}\right)\\
&+\omega_k\,\langle\sigma_{mn}r_{\boldsymbol{k}}^{\dagger}\rangle\\
&+g_{\boldsymbol{k}}\left(\langle r_{\boldsymbol{k}}^{\dagger}r_{\boldsymbol{k}}\rangle+1\right)\left(\langle\sigma_{2n}\rangle\,\delta_{m2}+\langle\sigma_{3n}\rangle\,\delta_{m3}\right)-g_{\boldsymbol{k}}\,\langle r_{\boldsymbol{k}}^{\dagger}r_{\boldsymbol{k}}\rangle\left(\langle\sigma_{m2}\rangle\,\delta_{n2}+\langle\sigma_{m3}\rangle\,\delta_{n3}\right)\Big],
\end{aligned}\tag{C.2}$$

$$\begin{aligned}
\frac{\mathrm{d}}{\mathrm{d}t}\langle\sigma_{mn}r_{\boldsymbol{k}}\rangle &= i\Big[\Delta_2\left(\langle\sigma_{2n}r_{\boldsymbol{k}}\rangle\,\delta_{m2}-\langle\sigma_{m2}r_{\boldsymbol{k}}\rangle\,\delta_{n2}\right)+\Delta_3\left(\langle\sigma_{3n}r_{\boldsymbol{k}}\rangle\,\delta_{m3}-\langle\sigma_{m3}r_{\boldsymbol{k}}\rangle\,\delta_{n3}\right)\\
&+\Omega\left(\langle\sigma_{1n}r_{\boldsymbol{k}}\rangle\,\delta_{m2}+\langle\sigma_{2n}r_{\boldsymbol{k}}\rangle\,\delta_{m1}-\langle\sigma_{m2}r_{\boldsymbol{k}}\rangle\,\delta_{n1}-\langle\sigma_{m1}r_{\boldsymbol{k}}\rangle\,\delta_{n2}\right)\\
&+\Omega\left(\langle\sigma_{1n}r_{\boldsymbol{k}}\rangle\,\delta_{m3}+\langle\sigma_{3n}r_{\boldsymbol{k}}\rangle\,\delta_{m1}-\langle\sigma_{m3}r_{\boldsymbol{k}}\rangle\,\delta_{n1}-\langle\sigma_{m1}r_{\boldsymbol{k}}\rangle\,\delta_{n3}\right)\\
&-\omega_k\,\langle\sigma_{mn}r_{\boldsymbol{k}}\rangle\\
&+g_{\boldsymbol{k}}\,\langle r_{\boldsymbol{k}}^{\dagger}r_{\boldsymbol{k}}\rangle\left(\langle\sigma_{2n}\rangle\,\delta_{m2}+\langle\sigma_{3n}\rangle\,\delta_{m3}\right)-g_{\boldsymbol{k}}\left(\langle r_{\boldsymbol{k}}^{\dagger}r_{\boldsymbol{k}}\rangle+1\right)\left(\langle\sigma_{m2}\rangle\,\delta_{n2}+\langle\sigma_{m3}\rangle\,\delta_{n3}\right)\Big].
\end{aligned}\tag{C.3}$$

## C.3 Polaron master equation: Derivation

Since the single $V$-type emitter is a special case of the chain of $N$ emitters, we only derive the polaron master equation for the elaborate case. In difference to the derivation of the polaron master equation for the polaronic Kitaev chain (see Appendix B), here we assume separate baths for each emitter.

### C.3.1 Polaron transformation

As a first step, the open system Hamiltonian is transformed into a polaronic frame. We apply the unitary polaron transformation $H_p = U_p H U_p^{-1}$ with

$$U_p = \exp\left[\sum_{l=0}^{N-1}\int \mathrm{d}^3k\;\frac{1}{\omega_{k_l}}\left(g_{k_l}\sigma_{22}^{l}+g_{k_l}\sigma_{33}^{l}\right)\left(r_{\boldsymbol{k}}^{\dagger}-r_{\boldsymbol{k}}\right)\right],\tag{C.4}$$

and define collective bosonic operators

$$R_l = \int \mathrm{d}^3k_l\;\frac{g_{k_l}}{\omega_{k_l}}r_{\boldsymbol{k}_l},\tag{C.5}$$

resulting in

$$U_p = \exp\Big[\sum_{l=0}^{N-1}\sum_{i=2,3}\sigma_{ii}^{l}(R_l^{\dagger}-R_l)\Big].\tag{C.6}$$

The transformation is performed via multiple applications of the Baker-Campbell-Hausdorff formula

$$e^{X}Ye^{-X} = \sum_{n=0}^{\infty}\frac{1}{n!}[X,Y]_n,\tag{C.7}$$

with $[X,Y]_n = [X,[X,Y]_{n-1}]$, $[X,Y]_0 = Y$. We start with the free electronic contribution

$$H_{el,0} = \hbar\Delta_2\sigma_{22}^l + \hbar\Delta_3\sigma_{33}^l. \tag{C.8}$$

The transformation reads

$$\frac{1}{\hbar}U_pH_{el,0}U_p^{-1} = \sum_{n=0}^{\infty}\frac{1}{n!}\left[\sum_{l=0}^{N-1}\left\{\sigma_{22}^l(R_l^\dagger - R_l) + \sigma_{33}^l(R_l^\dagger - R_l)\right\}, \sum_{l'=0}^{N-1}\left(\Delta_2\sigma_{22}^{l'} + \Delta_3\sigma_{33}^{l'}\right)\right]_n. \tag{C.9}$$

Since $U_p\sigma_{22}^lU_p^{-1} = \sigma_{22}^l$, $U_p\sigma_{33}^lU_p^{-1} = \sigma_{33}^l$, the shape of the Hamiltonian does not change. Next, we transform the electron-light interaction Hamiltonian $H_l$ with

$$\frac{1}{\hbar}U_pH_lU_p^{-1} = \sum_{n=0}^{\infty}\frac{1}{n!}\left[\sum_{l=0}^{N-1}\left\{\sigma_{22}^l(R_l^\dagger - R_l) + \sigma_{33}^l(R_l^\dagger - R_l)\right\}, \sum_{l'=0}^{N-1}\Omega\left(\sigma_{12}^{l'} + \sigma_{21}^{l'} + \sigma_{13}^{l'} + \sigma_{31}^{l'}\right)\right]_n. \tag{C.10}$$

We calculate the first three terms of the sum and identify an exponential factorization of the entire expression, resulting in

$$\frac{1}{\hbar}U_pH_lU_p^{-1} = \sum_{l=0}^{N-1}\sum_{i=2,3}\Omega\left[(\sigma_{1i}^l + \sigma_{i1}^l)\cosh(R_l^\dagger - R_l) + (\sigma_{i1}^l - \sigma_{1i}^l)\sinh(R_l^\dagger - R_l)\right]. \tag{C.11}$$

The homogeneous phonon contribution yields

$$\frac{1}{\hbar}U_pH_{ph,0}U_p^{-1} = \sum_{l=0}^{N-1}\int \mathrm{d}^3k_l\ \left[\omega_{k_l}r_{\boldsymbol{k}_l}^\dagger r_{\boldsymbol{k}_l} - \sum_{i=2,3}g_{k_l}\sigma_{ii}^l(r_{\boldsymbol{k}_l}^\dagger + r_{\boldsymbol{k}_l}) + \sum_{i=2,3}\frac{g_{k_l}^2}{\omega_{k_l}}\sigma_{ii}^l\right], \tag{C.12}$$

and the transformed electron-phonon interaction Hamiltonian is given by

$$\frac{1}{\hbar}U_pH_{el,ph}U_p^{-1} = \sum_{l=0}^{N-1}\sum_{i=2,3}\int \mathrm{d}^3k_l\ \left[g_{k_l}\sigma_{ii}^l(r_{\boldsymbol{k}_l}^\dagger + r_{\boldsymbol{k}_l}) - 2\frac{g_{k_l}^2}{\omega_{k_l}}\sigma_{ii}^l\right]. \tag{C.13}$$

Lastly, the transformation of the Dexter interdot coupling Hamiltonian yields

$$\begin{aligned}\frac{1}{\hbar}U_pH_DU_p^{-1} = \sum_{l=0}^{N-2}\Big\{&\left[f(t)\sigma_{35}^l + f^*(t)\sigma_{53}^l\right]\cosh\left[R_{l+1}^\dagger - R_{l+1} - \left(R_l^\dagger - R_l\right)\right]\\ &+\left[f^*(t)\sigma_{53}^l - f(t)\sigma_{35}^l\right]\sinh\left[R_{l+1}^\dagger - R_{l+1} - \left(R_l^\dagger - R_l\right)\right]\Big\}.\end{aligned} \tag{C.14}$$

We define $H_p = H_{p,0} + H_{p,I}$ and get the full polaron-transformed open system Hamiltonian with

$$H_{p,0}/\hbar = \sum_{l=0}^{N-1}\left(\sum_{i=2,3}\bar{\Delta}_i\sigma_{ii}^l + \int \mathrm{d}^3k_l\ \omega_{k_l}r_{\boldsymbol{k}_l}^\dagger r_{\boldsymbol{k}_l}\right), \tag{C.15}$$

and

$$H_{p,I}/\hbar = \sum_{l=0}^{N-1}\sum_{i=2,3}\Omega\left[(\sigma_{1i}^{l}+\sigma_{i1}^{l})\cosh(R_l^\dagger - R_l) + (\sigma_{i1}^{l}-\sigma_{1i}^{l})\sinh(R_l^\dagger - R_l)\right]$$
$$+\sum_{l=0}^{N-2}\Big\{\left[f(t)\sigma_{35}^{l}+f^*(t)\sigma_{53}^{l}\right]\cosh\left[R_{l+1}^\dagger - R_{l+1} - \left(R_l^\dagger - R_l\right)\right]$$
$$+\left[f^*(t)\sigma_{53}^{l}-f(t)\sigma_{35}^{l}\right]\sinh\left[R_{l+1}^\dagger - R_{l+1} - \left(R_l^\dagger - R_l\right)\right]\Big\}, \tag{C.16}$$

where we have introduced the polaron-shifted detuning

$$\bar{\Delta}_i^l = \Delta_i - \int \mathrm{d}^3k_l\ \frac{g_{k_l}^2}{\omega_{k_l}}. \tag{C.17}$$

### C.3.2 Franck-Condon renormalization

To simplify the evaluation of the upcoming polaron master equation, we renormalize the polaron interaction Hamiltonian such that

$$\mathrm{tr}_B\{[H_{p,I},\rho(t)]\} = 0. \tag{C.18}$$

We define

$$X_{+,i}^{[l]} := \left(\sigma_{1i}^{l}+\sigma_{i1}^{l}\right), \quad X_{-,i}^{[l]} := i\left(\sigma_{i1}^{l}-\sigma_{1i}^{l}\right), \tag{C.19a}$$
$$X_{+,f}^{[l]} := \left(e^{i\delta\epsilon t/\hbar}\sigma_{35}^{l}+e^{-i\delta\epsilon t/\hbar}\sigma_{53}^{l}\right), \quad X_{-,f}^{[l]} := i\left(e^{-i\delta\epsilon t/\hbar}\sigma_{53}^{l}-e^{i\delta\epsilon t/\hbar}\sigma_{35}^{l}\right), \tag{C.19b}$$
$$B_p^{[l]} := \exp\left[R_l^\dagger - R_l\right], \quad B_m^{[l]} := \exp\left[-\left(R_l^\dagger - R_l\right)\right], \tag{C.19c}$$

and

$$\bar{\Omega}_l := \Omega\mathrm{tr}\left\{B_p^{[l]}\right\} = \Omega\left\langle e^{R_l^\dagger - R_l}\right\rangle,$$
$$\bar{f}_{0l} := f_0\mathrm{tr}\left\{B_p^{[l+1]}B_m^{[l]}\right\} = f_0\left\langle e^{R_{l+1}^\dagger - R_{l+1} - (R_l^\dagger - R_l)}\right\rangle. \tag{C.20}$$

The condition in Eq. (C.18) is fulfilled by subtracting $\sum_{l=0}^{N-1}\sum_{i=2,3}\bar{\Omega}_l X_{+,i}^{[l]} + \sum_{l=0}^{N-2}\bar{f}_{0l}X_{+,f}^{[l]}$ from $H_{p,I}$ and in turn adding it to $H_{p,0}$. The Franck-Condon renormalized Hamiltonians read

$$H_{p,0}/\hbar = \sum_{l=0}^{N-1}\left[\sum_{i=2,3}\left(\bar{\Delta}_i\sigma_{ii}^{l}+\bar{\Omega}X_{+,i}^{[l]}\right)+\bar{f}_{0l}X_{+,f}^{[l]}\left[1-\delta_{l,(N-1)}\right]+\int \mathrm{d}^3k_l\ \omega_{k_l}r_{\boldsymbol{k}_l}^\dagger r_{\boldsymbol{k}_l}\right], \tag{C.21}$$

and

$$H_{p,I}/\hbar = \sum_{l=0}^{N-1}\sum_{i=2,3}\left\{X_{+,i}^{[l]}\left[\Omega\cosh\left(R_l^\dagger - R_l\right)-\bar{\Omega}_l\right]-i\Omega X_{-,i}^{[l]}\sinh\left(R_l^\dagger - R_l\right)\right\}$$
$$+\sum_{l=0}^{N-2}\Big(X_{+,f}^{[l]}\left\{f_0\cosh\left[R_{l+1}^\dagger - R_{l+1} - \left(R_l^\dagger - R_l\right)\right]-\bar{f}_{0l}\right\}$$
$$-if_0X_{-,f}^{[l]}\sinh\left[R_{l+1}^\dagger - R_{l+1} - (R_l^\dagger - R_l)\right]\Big). \tag{C.22}$$

### C.3.3 Polaron master equation

For the derivation of the polaron master equation we start from the Redfield equation,

$$\frac{\mathrm{d}}{\mathrm{d}t}\rho_S(t) = -\frac{i}{\hbar}\left[H_{p,0}, \rho_S(t)\right] - \frac{1}{\hbar^2}\int_0^t d\tau \mathrm{tr}_B\{[H_{p,I}, [H_{p,I}(-\tau), \rho_S(t)\otimes\rho_B]]\}, \tag{C.23}$$

and first evaluate the integrand $[H_{p,I}, [H_{p,I}(-\tau), \rho]]$. We define new collective bath operators in the interaction picture,

$$B_+^{[l]}(t) = \exp\left[R_l(t) - R_l^\dagger(t)\right] + \exp\left\{-\left[R_l(t) - R_l^\dagger(t)\right]\right\}, \tag{C.24a}$$
$$B_-^{[l]}(t) = \exp\left[R_l(t) - R_l^\dagger(t)\right] - \exp\left\{-\left[R_l(t) - R_l^\dagger(t)\right]\right\}, \tag{C.24b}$$

and

$$\begin{aligned} C_+^{[l]}(t) &= \exp\left\{\left[R_{l+1}(t) - R_{l+1}^\dagger(t)\right] - \left[R_l(t) - R_l^\dagger(t)\right]\right\} \\ &\quad + \exp\left\{-\left[R_{l+1}(t) - R_{l+1}^\dagger(t)\right] + \left[R_l(t) - R_l^\dagger(t)\right]\right\}, \end{aligned} \tag{C.25a}$$
$$\begin{aligned} C_-^{[l]}(t) &= \exp\left\{\left[R_{l+1}(t) - R_{l+1}^\dagger(t)\right] - \left[R_l(t) - R_l^\dagger(t)\right]\right\} \\ &\quad - \exp\left\{-\left[R_{l+1}(t) - R_{l+1}^\dagger(t)\right] + \left[R_l(t) - R_l^\dagger(t)\right]\right\}, \end{aligned} \tag{C.25b}$$

and rewrite the interaction Hamiltonian accordingly, resulting in

$$\begin{aligned} H_{p,I}(t)/\hbar = &\sum_{l=0}^{N-1}\sum_{i=2,3}\left[\frac{\Omega}{2}X_{+,i}^{[l]}(t)B_+^{[l]}(t) + i\frac{\Omega}{2}X_{-,i}^{[l]}(t)B_-^{[l]}(t) - \bar{\Omega}_l X_{+,i}^{[l]}(t)\right] \\ &+ \sum_{l=0}^{N-2}\left[\frac{f_0}{2}X_{+,f}^{[l]}(t)C_+^{[l]}(t) + i\frac{f_0}{2}X_{-,f}^{[l]}(t)C_-^{[l]}(t) - \bar{f}_{0l}X_{+,f}^{[l]}(t)\right]. \end{aligned} \tag{C.26}$$

For a simpler notation, we denote $X_i(-\tau) = X_i'$, $B(-\tau) = B'$, $C(-\tau) = C'$. The integrand is evaluated as

$$\begin{aligned} &[H_{p,I}, [H_{p,I}(-\tau), \rho]] \\ &= \sum_{l'=0}^{N-1}\sum_{i=2,3}\left[H_{p,I}, \frac{\Omega}{2}\left[X_{+,i}^{[l]\prime}B_+^{[l]\prime}, \rho\right] + i\frac{\Omega}{2}\left[X_{-,i}^{[l]\prime}B_-^{[l]\prime}, \rho\right] - \bar{\Omega}_{l'}\left[X_{+,i}^{[l]\prime}, \rho\right]\right] \\ &+ \sum_{l'=0}^{N-2}\left[H_{p,I}, \frac{f_0}{2}\left[X_{+,f}^{[l]\prime}C_+^{[l]\prime}, \rho\right] + i\frac{f_0}{2}\left[X_{-,f}^{[l]\prime}C_-^{[l]\prime}, \rho\right] - \bar{f}_{0l'}\left[X_{+,f}^{[l]\prime}, \rho\right]\right] \end{aligned}$$

$$
\begin{aligned}
&= \sum_{l,l'=0}^{N-1} \sum_{i,j=2,3} \Bigg( \frac{\Omega^2}{4} \left[ X^{[l]}_{+,j} B^{[l]}_{+}, \left[ {X^{[l']}_{+,i}}' B^{[l']}_{+}{}', \rho \right] \right] + i \frac{\Omega^2}{4} \left[ X^{[l]}_{-,j} B^{[l]}_{-}, \left[ {X^{[l']}_{+,i}}' B^{[l']}_{+}{}', \rho \right] \right] \\
&- \frac{\Omega}{2} \bar{\Omega}_l \left[ X^{[l]}_{+,j}, \left[ {X^{[l']}_{+,i}}' B^{[l']}_{+}{}', \rho \right] \right] + i \frac{\Omega^2}{4} \left[ X^{[l]}_{+,j} B^{[l]}_{+}, \left[ {X^{[l']}_{-,i}}' B^{[l']}_{-}{}', \rho \right] \right] \\
&- \frac{\Omega^2}{4} \left[ X^{[l]}_{-,j} B^{[l]}_{-}, \left[ {X^{[l']}_{-,i}}' B^{[l']}_{-}{}', \rho \right] \right] - i \frac{\Omega}{2} \bar{\Omega}_l \left[ X^{[l]}_{+,j}, \left[ {X^{[l']}_{-,i}}' B^{[l']}_{-}{}', \rho \right] \right] \\
&- \frac{\Omega}{2} \bar{\Omega}_{l'} \left[ X^{[l]}_{+,j} B^{[l]}_{+}, \left[ {X^{[l']}_{+,i}}', \rho \right] \right] - i \frac{\Omega}{2} \bar{\Omega}_{l'} \left[ X^{[l]}_{-,j} B^{[l]}_{-}, \left[ {X^{[l']}_{+,i}}', \rho \right] \right] \\
&+ \bar{\Omega}_l \bar{\Omega}_{l'} \left[ X^{[l]}_{+,j}, \left[ {X^{[l']}_{+,i}}', \rho \right] \right] \Bigg) \\
&+ \sum_{l,l'=0}^{N-1} \sum_{i=2,3} [1 - \delta_{l,(N-1)}] \Bigg( \frac{\Omega f_0}{4} \left[ X^{[l]}_{+,f} C^{[l]}_{+}, \left[ {X^{[l']}_{+,i}}' B^{[l']}_{+}{}', \rho \right] \right] + i \frac{\Omega f_0}{4} \left[ X^{[l]}_{-,f} C^{[l]}_{-}, \left[ {X^{[l']}_{+,i}}' B^{[l']}_{+}{}', \rho \right] \right] \\
&- \frac{\Omega}{2} \bar{f}_{0l} \left[ X^{[l]}_{+,f}, \left[ {X^{[l']}_{+,i}}' B^{[l']}_{+}{}', \rho \right] \right] + i \frac{\Omega f_0}{4} \left[ X^{[l]}_{+,f} C^{[l]}_{+}, \left[ {X^{[l']}_{-,i}}' B^{[l']}_{-}{}', \rho \right] \right] \\
&- \frac{\Omega f_0}{4} \left[ X^{[l]}_{-,f} C^{[l]}_{-}, \left[ {X^{[l']}_{-,i}}' B^{[l']}_{-}{}', \rho \right] \right] - i \frac{\Omega}{2} \bar{f}_{0l} \left[ X^{[l]}_{+,f}, \left[ {X^{[l']}_{-,i}}' B^{[l']}_{-}{}', \rho \right] \right] \\
&- \frac{f_0}{2} \bar{\Omega}_{l'} \left[ X^{[l]}_{+,f} C^{[l]}_{+}, \left[ {X^{[l']}_{+,i}}', \rho \right] \right] - i \frac{f_0}{2} \bar{\Omega}_{l'} \left[ X^{[l]}_{-,f} C^{[l]}_{-}, \left[ {X^{[l']}_{+,i}}', \rho \right] \right] \\
&+ \bar{f}_{0l} \bar{\Omega}_{l'} \left[ X^{[l]}_{+,f}, \left[ {X^{[l']}_{+,i}}', \rho \right] \right] \Bigg) \\
&+ \sum_{l,l'=0}^{N-1} \sum_{j=2,3} [1 - \delta_{l',(N-1)}] \Bigg( \frac{\Omega f_0}{4} \left[ X^{[l]}_{+,j} B^{[l]}_{+}, \left[ {X^{[l']}_{+,f}}' C^{[l']}_{+}{}', \rho \right] \right] + i \frac{\Omega f_0}{4} \left[ X^{[l]}_{-,j} B^{[l]}_{-}, \left[ {X^{[l']}_{+,f}}' C^{[l']}_{+}{}', \rho \right] \right] \\
&- \frac{f_0}{2} \bar{\Omega}_l \left[ X^{[l]}_{+,j}, \left[ {X^{[l']}_{+,f}}' C^{[l']}_{+}{}', \rho \right] \right] + i \frac{\Omega f_0}{4} \left[ X^{[l]}_{+,j} B^{[l]}_{+}, \left[ {X^{[l']}_{-,f}}' C^{[l']}_{-}{}', \rho \right] \right] \\
&- \frac{\Omega f_0}{4} \left[ X^{[l]}_{-,j} B^{[l]}_{-}, \left[ {X^{[l']}_{-,f}}' C^{[l']}_{-}{}', \rho \right] \right] - i \frac{f_0}{2} \bar{\Omega}_l \left[ X^{[l]}_{+,j}, \left[ {X^{[l']}_{-,f}}' C^{[l']}_{-}{}', \rho \right] \right] \\
&- \frac{\Omega}{2} \bar{f}_{0l'} \left[ X^{[l]}_{+,j} B^{[l]}_{+}, \left[ {X^{[l']}_{+,f}}', \rho \right] \right] - i \frac{\Omega}{2} \bar{f}_{0l'} \left[ X^{[l]}_{-,j} B^{[l]}_{-}, \left[ {X^{[l']}_{+,f}}', \rho \right] \right] \\
&+ \bar{\Omega}_l \bar{f}_{0l'} \left[ X^{[l]}_{+,j}, \left[ {X^{[l']}_{+,f}}', \rho \right] \right] \Bigg) \\
&+ \sum_{l,l'=0}^{N-2} \Bigg( \frac{f_0^2}{4} \left[ X^{[l]}_{+,f} C^{[l]}_{+}, \left[ {X^{[l']}_{+,f}}' C^{[l']}_{+}{}', \rho \right] \right] + i \frac{f_0^2}{4} \left[ X^{[l]}_{-,f} C^{[l]}_{-}, \left[ {X^{[l']}_{+,f}}' C^{[l']}_{+}{}', \rho \right] \right] \\
&- \frac{f_0}{2} \bar{f}_{0l} \left[ X^{[l]}_{+,f}, \left[ {X^{[l']}_{+,f}}' C^{[l']}_{+}{}', \rho \right] \right] + i \frac{f_0^2}{4} \left[ X^{[l]}_{+,f} C^{[l]}_{+}, \left[ {X^{[l']}_{-,f}}' C^{[l']}_{-}{}', \rho \right] \right] \\
&- \frac{f_0^2}{4} \left[ X^{[l]}_{-,f} C^{[l]}_{-}, \left[ {X^{[l']}_{-,f}}' C^{[l']}_{-}{}', \rho \right] \right] - i \frac{f_0}{2} \bar{f}_{0l} \left[ X^{[l]}_{+,f}, \left[ {X^{[l']}_{-,f}}' C^{[l']}_{-}{}', \rho \right] \right] \\
&- \frac{f_0}{2} \bar{f}_{0l'} \left[ X^{[l]}_{+,f} C^{[l]}_{+}, \left[ {X^{[l']}_{+,f}}', \rho \right] \right] - i \frac{f_0}{2} \bar{f}_{0l'} \left[ X^{[l]}_{-,f} C^{[l]}_{-}, \left[ {X^{[l']}_{+,f}}', \rho \right] \right] \\
&+ \bar{f}_{0l} \bar{f}_{0l'} \left[ X^{[l]}_{+,f}, \left[ {X^{[l']}_{+,f}}', \rho \right] \right] \Bigg). \qquad \text{(C.27)}
\end{aligned}
$$

The most complicated terms in Eq. (C.27) are of the form $[X_jB,[X_i'C',\rho]]$ for $i,j = \{2,3,f\}$. Taking the trace over the bath yields

$$\begin{aligned}
&\mathrm{tr}_B\{[X_jB,[X_i'C',\rho]]\}\\
&=\mathrm{tr}_B\{X_jBX_i'C'\rho - X_jB\rho X_i'C' - X_i'C'\rho X_jB + \rho X_i'C'X_jB\}\\
&=X_jX_i'\rho_S\langle BC'\rangle - X_j\rho_SX_i'\langle C'B\rangle - X_i'\rho_SX_j\langle BC'\rangle + \rho_SX_i'X_j\langle C'B\rangle\\
&=\langle BC'\rangle\left(X_jX_i'\rho_S - X_i'\rho_SX_j\right) + \langle C'B\rangle\left(\rho_SX_i'X_j - X_j\rho_SX_i'\right)\\
&=\langle BC'\rangle[X_j,X_i'\rho_S] - \langle C'B\rangle[X_j,\rho_SX_i']\,. \qquad \text{(C.28)}
\end{aligned}$$

Moreover, we have

$$\begin{aligned}
\mathrm{tr}_B\{[X_jB,[X_i'B',\rho]]\} &= \langle BB'\rangle[X_j,X_i'\rho_S] - \langle B'B\rangle[X_j,\rho_SX_i']\,,\\
\mathrm{tr}_B\{[X_j,[X_i'B_i',\rho]]\} &= \langle B_i'\rangle([X_j,X_i'\rho_S] - [X_j,\rho_SX_i'])\,,\\
\mathrm{tr}_B\{[X_jB_j,[X_i',\rho]]\} &= \langle B_j\rangle([X_j,X_i'\rho_S] - [X_j,\rho_SX_i'])\,,\\
\mathrm{tr}_B\{[X_j,[X_i',\rho]]\} &= ([X_j,X_i'\rho_S] - [X_j,\rho_SX_i'])\,. \qquad \text{(C.29)}
\end{aligned}$$

It can be shown that $\langle B_+^{[l]}B_-^{[l]\prime}\rangle = \langle B_-^{[l]}B_+^{[l]\prime}\rangle = 0\ \forall l,l'$. Since $\langle e^{R-R^\dagger}\rangle = \langle e^{-(R-R^\dagger)}\rangle$ we have

$$\langle B_+^{[l]}\rangle = 2\langle e^{R_l-R_l^\dagger}\rangle\,,\quad \langle B_-^{[l]}\rangle = 0. \qquad \text{(C.30)}$$

In the same fashion, we obtain $\langle C_+^{[l]}C_-^{[l]\prime}\rangle = \langle C_-^{[l]}C_+^{[l]\prime}\rangle = 0\ \forall l,l'$ and

$$\langle C_+^{[l]}\rangle = 2\langle e^{(R_{l+1}-R_{l+1}^\dagger)-(R_l-R_l^\dagger)}\rangle\,,\quad \langle C_-^{[l]}\rangle = 0. \qquad \text{(C.31)}$$

Lastly, this also yields $\langle B_+^{[l]}C_-^{[l]\prime}\rangle = \langle B_-^{[l]}C_+^{[l]\prime}\rangle = 0\ \forall l,l'$ and $\langle C_+^{[l]}B_-^{[l]\prime}\rangle = \langle C_-^{[l]}B_+^{[l]\prime}\rangle = 0\ \forall l,l'$. Next, we calculate $\langle B_+^{[l]\prime}\rangle$,

$$\begin{aligned}
\langle B_+^{[l]\prime}\rangle &= \mathrm{tr}_B\left\{\rho_B\left[e^{\tilde R_l-\tilde R_l{}^\dagger} + e^{-(\tilde R_l-\tilde R_l{}^\dagger)}\right]\right\}\\
&= 2\mathrm{tr}_B\left\{\rho_B\left[1+\frac{1}{2!}\left(\tilde R_l-\tilde R_l{}^\dagger\right)^2+\ldots\right]\right\}\\
&= 2\mathrm{tr}_B\left(\rho_B\left\{1+\frac{1}{2!}\left[\int \mathrm{d}^3k_l\ \frac{g_{k_l}}{\omega_{k_l}}\left(r_{\boldsymbol{k}_l}e^{i\omega_{k_l}\tau} - r_{\boldsymbol{k}_l}^\dagger e^{-i\omega_{k_l}\tau}\right)\right]^2+\ldots\right\}\right)\\
&= 2\exp\left[-\frac{1}{2}\int \mathrm{d}^3k_l\ |g_{k_l}/\omega_k|^2(2n_{k_l}+1)\right] = \langle B_+^{[l]}\rangle\,. \qquad \text{(C.32)}
\end{aligned}$$

$\langle C_+^{[l]\prime}\rangle$ is calculated analogously, resulting in

$$\begin{aligned}
\langle C_+^{[l]\prime}\rangle &= \mathrm{tr}_B\Big\{\rho_B\Big[e^{(\tilde R_{l+1}-\tilde R_{l+1}^\dagger)-(\tilde R_l-\tilde R_l^\dagger)} + e^{-(\tilde R_{l+1}-\tilde R_{l+1}^\dagger)+(\tilde R_l-\tilde R_l^\dagger)}\Big]\Big\}\\
&= 2\mathrm{tr}_B\Big\{\rho_B\Big[1+\frac{1}{2!}\left(\tilde R_{l+1}-\tilde R_{l+1}^\dagger-\tilde R_l+\tilde R_l^\dagger\right)^2+\ldots\Big]\Big\}\\
&= 2\mathrm{tr}_B\Big\{\rho_B\left[1+0+\ldots\right]\Big\} = 2 = \langle C_+^{[l]}\rangle\,. \qquad \text{(C.33)}
\end{aligned}$$

However, $[\tilde{R}_{l+1} - \tilde{R}^\dagger_{l+1} - \tilde{R}_l + \tilde{R}^\dagger_l)]^2 = 0$, and therefore all terms depending on phonon operators vanish in the expectation value. With this and Eqs. (C.30) and (C.31) we have also evaluated

$$\langle e^{(R_l - R_l^\dagger)} \rangle = \exp\left[ -\frac{1}{2} \int \mathrm{d}^3 k_l \left| \frac{g_{k_l}}{\omega_{k_l}} \right|^2 (2n_{k_l} + 1) \right], \tag{C.34}$$

and $\langle e^{(R_{l+1} - R^\dagger_{l+1}) - (R_l - R^\dagger_l)} \rangle = 1$. Moreover, it follows $\bar{f}_{0l} = f_0$.

$\mathrm{tr}_B\{[H_{p,I}, [H_{p,I}(-\tau), \rho]]\}$ now takes the form

$$\begin{aligned}
&\sum_{l,l'=0}^{N-1} \sum_{i,j=2,3} \Bigg\{ \frac{\Omega^2}{4} \left( \langle B_+^{[l]} B_+^{[l']\prime} \rangle \left[ X_{+,j}^{[l]}, X_{+,i}^{[l']\prime} \rho_S \right] - \langle B_+^{[l']\prime} B_+^{[l]} \rangle \left[ X_{+,j}^{[l]}, \rho_S X_{+,i}^{[l']\prime} \right] \right) \\
&- \frac{\Omega}{2} \bar{\Omega}_l \langle B_+^{[l']\prime} \rangle \left( \left[ X_{+,j}^{[l]}, X_{+,i}^{[l']\prime} \rho_S \right] - \left[ X_{+,j}^{[l]}, \rho_S X_{+,i}^{[l']\prime} \right] \right) \\
&- \frac{\Omega^2}{4} \left( \langle B_-^{[l]} B_-^{[l']\prime} \rangle \left[ X_{-,j}^{[l]}, X_{-,i}^{[l']\prime} \rho_S \right] - \langle B_-^{[l']\prime} B_-^{[l]} \rangle \left[ X_{-,j}^{[l]}, \rho_S X_{-,i}^{[l']\prime} \right] \right) \\
&- \frac{\Omega}{2} \bar{\Omega}_{l'} \langle B_+^{[l]} \rangle \left( \left[ X_{+,j}^{[l]}, X_{+,i}^{[l']\prime} \rho_S \right] - \left[ X_{+,j}^{[l]}, \rho_S X_{+,i}^{[l']\prime} \right] \right) \\
&+ \bar{\Omega}_l \bar{\Omega}_{l'} \left( \left[ X_{+,j}^{[l]}, X_{+,i}^{[l']\prime} \rho_S \right] - \left[ X_{+,j}^{[l]}, \rho_S X_{+,i}^{[l']\prime} \right] \right) \Bigg\} \\
&+ \sum_{l,l'=0}^{N-1} \sum_{i=2,3} [1 - \delta_{l,(N-1)}] \Bigg\{ \frac{\Omega f_0}{4} \left( \langle C_+^{[l]} B_+^{[l']\prime} \rangle \left[ X_{+,f}^{[l]}, X_{+,i}^{[l']\prime} \rho_S \right] - \langle B_+^{[l']\prime} C_+^{[l]} \rangle \left[ X_{+,f}^{[l]}, \rho_S X_{+,i}^{[l']\prime} \right] \right) \\
&- \frac{\Omega}{2} \bar{f}_{0l} \langle B_+^{[l']\prime} \rangle \left( \left[ X_{+,f}^{[l]}, X_{+,i}^{[l']\prime} \rho_S \right] - \left[ X_{+,f}^{[l]}, \rho_S X_{+,i}^{[l']\prime} \right] \right) \\
&- \frac{\Omega f_0}{4} \left( \langle C_-^{[l]} B_-^{[l']\prime} \rangle \left[ X_{-,f}^{[l]}, X_{-,i}^{[l']\prime} \rho_S \right] - \langle B_-^{[l']\prime} C_-^{[l]} \rangle \left[ X_{-,f}^{[l]}, \rho_S X_{-,i}^{[l']\prime} \right] \right) \\
&- \frac{f_0}{2} \bar{\Omega}_{l'} \langle C_+^{[l]} \rangle \left( \left[ X_{+,f}^{[l]}, X_{+,i}^{[l']\prime} \rho_S \right] - \left[ X_{+,f}^{[l]}, \rho_S X_{+,i}^{[l']\prime} \right] \right) \\
&+ \bar{f}_{0l} \bar{\Omega}_{l'} \left( \left[ X_{+,f}^{[l]}, X_{+,i}^{[l']\prime} \rho_S \right] - \left[ X_{+,f}^{[l]}, \rho_S X_{+,i}^{[l']\prime} \right] \right) \Bigg\} \\
&+ \sum_{l,l'=0}^{N-1} \sum_{j=2,3} [1 - \delta_{l',(N-1)}] \Bigg\{ \frac{\Omega f_0}{4} \left( \langle B_+^{[l]} C_+^{[l']\prime} \rangle \left[ X_{+,j}^{[l]}, X_{+,f}^{[l']\prime} \rho_S \right] - \langle C_+^{[l']\prime} B_+^{[l]} \rangle \left[ X_{+,j}^{[l]}, \rho_S X_{+,f}^{[l']\prime} \right] \right) \\
&- \frac{f_0}{2} \bar{\Omega}_l \langle C_+^{[l']\prime} \rangle \left( \left[ X_{+,j}^{[l]}, X_{+,f}^{[l']\prime} \rho_S \right] - \left[ X_{+,j}^{[l]}, \rho_S X_{+,f}^{[l']\prime} \right] \right) \\
&- \frac{\Omega f_0}{4} \left( \langle B_-^{[l]} C_-^{[l']\prime} \rangle \left[ X_{-,j}^{[l]}, X_{-,f}^{[l']\prime} \rho_S \right] - \langle C_-^{[l']\prime} B_-^{[l]} \rangle \left[ X_{-,j}^{[l]}, \rho_S X_{-,f}^{[l']\prime} \right] \right) \\
&- \frac{\Omega}{2} \bar{f}_{0l'} \langle B_+^{[l]} \rangle \left( \left[ X_{+,j}^{[l]}, X_{+,f}^{[l']\prime} \rho_S \right] - \left[ X_{+,j}^{[l]}, \rho_S X_{+,f}^{[l']\prime} \right] \right)
\end{aligned}$$

$$
\begin{aligned}
&+ \bar{\Omega}_l \bar{f}_{0l'} \left( \left[ X^{[l]}_{+,j}, {X^{[l']}_{+,f}}' \rho_S \right] - \left[ X^{[l]}_{+,j}, \rho_S {X^{[l']}_{+,f}}' \right] \right) \Bigg\} \\
&+ \sum_{l,l'=0}^{N-2} \Bigg\{ \frac{f_0^2}{4} \left( \langle C^{[l]}_{+} {C^{[l']}_{+}}' \rangle \left[ X^{[l]}_{+,f}, {X^{[l']}_{+,f}}' \rho_S \right] - \langle {C^{[l']}_{+}}' C^{[l]}_{+} \rangle \left[ X^{[l]}_{+,f}, \rho_S {X^{[l']}_{+,f}}' \right] \right) \\
&- \frac{f_0}{2} \bar{f}_{0l} \langle {C^{[l']}_{+}}' \rangle \left( \left[ X^{[l]}_{+,f}, {X^{[l']}_{+,f}}' \rho_S \right] - \left[ X^{[l]}_{+,f}, \rho_S {X^{[l']}_{+,f}}' \right] \right) \\
&- \frac{f_0^2}{4} \left( \langle C^{[l]}_{-} {C^{[l']}_{-}}' \rangle \left[ X^{[l]}_{-,f}, {X^{[l']}_{-,f}}' \rho_S \right] - \langle {C^{[l']}_{-}}' C^{[l]}_{-} \rangle \left[ X^{[l]}_{-,f}, \rho_S {X^{[l']}_{-,f}}' \right] \right) \\
&- \frac{f_0}{2} \bar{f}_{0l'} \langle C^{[l]}_{+} \rangle \left( \left[ X^{[l]}_{+,f}, {X^{[l']}_{+,f}}' \rho_S \right] - \left[ X^{[l]}_{+,f}, \rho_S {X^{[l']}_{+,f}}' \right] \right) \\
&+ \bar{f}_{0l} \bar{f}_{0l'} \left( \left[ X^{[l]}_{+,f}, {X^{[l']}_{+,f}}' \rho_S \right] - \left[ X^{[l]}_{+,f}, \rho_S {X^{[l']}_{+,f}}' \right] \right) \Bigg\}. \qquad \text{(C.35)}
\end{aligned}
$$

From $\bar{\Omega}_l = \Omega \langle e^{-(R_l - R_l^\dagger)} \rangle$, it follows

$$
\langle B^{[l]}_{+} \rangle = \frac{2\bar{\Omega}_l}{\Omega}. \qquad \text{(C.36)}
$$

Together with $\bar{f}_{0l} = f_0$ and $\langle C^{[l]}_{+} \rangle = 2$ this results in

$$
\begin{aligned}
&\mathrm{tr}_B\{[H_{p,I}, [H_{p,I}(-\tau), \rho]]\} \\
&= \sum_{l,l'=0}^{N-1} \sum_{i,j=2,3} \Bigg\{ \frac{\Omega^2}{4} \left( \langle B^{[l]}_{+} {B^{[l']}_{+}}' \rangle \left[ X^{[l]}_{+,j}, {X^{[l']}_{+,i}}' \rho_S \right] - \langle {B^{[l']}_{+}}' B^{[l]}_{+} \rangle \left[ X^{[l]}_{+,j}, \rho_S {X^{[l']}_{+,i}}' \right] \right) \\
&- \frac{\Omega^2}{4} \left( \langle B^{[l]}_{-} {B^{[l']}_{-}}' \rangle \left[ X^{[l]}_{-,j}, {X^{[l']}_{-,i}}' \rho_S \right] - \langle {B^{[l']}_{-}}' B^{[l]}_{-} \rangle \left[ X^{[l]}_{-,j}, \rho_S {X^{[l']}_{-,i}}' \right] \right) \\
&- \bar{\Omega}_l \bar{\Omega}_{l'} \left( \left[ X^{[l]}_{+,j}, {X^{[l']}_{+,i}}' \rho_S \right] - \left[ X^{[l]}_{+,j}, \rho_S {X^{[l']}_{+,i}}' \right] \right) \Bigg\} \\
&+ \sum_{l,l'=0}^{N-1} \sum_{i=2,3} [1 - \delta_{l,(N-1)}] \Bigg\{ \frac{\Omega f_0}{4} \left( \langle C^{[l]}_{+} {B^{[l']}_{+}}' \rangle \left[ X^{[l]}_{+,f}, {X^{[l']}_{+,i}}' \rho_S \right] - \langle {B^{[l']}_{+}}' C^{[l]}_{+} \rangle \left[ X^{[l]}_{+,f}, \rho_S {X^{[l']}_{+,i}}' \right] \right) \\
&- \frac{\Omega f_0}{4} \left( \langle C^{[l]}_{-} {B^{[l']}_{-}}' \rangle \left[ X^{[l]}_{-,f}, {X^{[l']}_{-,i}}' \rho_S \right] - \langle {B^{[l']}_{-}}' C^{[l]}_{-} \rangle \left[ X^{[l]}_{-,f}, \rho_S {X^{[l']}_{-,i}}' \right] \right) \\
&- f_0 \bar{\Omega}_{l'} \left( \left[ X^{[l]}_{+,f}, {X^{[l']}_{+,i}}' \rho_S \right] - \left[ X^{[l]}_{+,f}, \rho_S {X^{[l']}_{+,i}}' \right] \right) \Bigg\} \\
&+ \sum_{l,l'=0}^{N-1} \sum_{j=2,3} [1 - \delta_{l',(N-1)}] \Bigg\{ \frac{\Omega f_0}{4} \left( \langle B^{[l]}_{+} {C^{[l']}_{+}}' \rangle \left[ X^{[l]}_{+,j}, {X^{[l']}_{+,f}}' \rho_S \right] - \langle {C^{[l']}_{+}}' B^{[l]}_{+} \rangle \left[ X^{[l]}_{+,j}, \rho_S {X^{[l']}_{+,f}}' \right] \right) \\
&- \frac{\Omega f_0}{4} \left( \langle B^{[l]}_{-} {C^{[l']}_{-}}' \rangle \left[ X^{[l]}_{-,j}, {X^{[l']}_{-,f}}' \rho_S \right] - \langle {C^{[l']}_{-}}' B^{[l]}_{-} \rangle \left[ X^{[l]}_{-,j}, \rho_S {X^{[l']}_{-,f}}' \right] \right) \\
&- \bar{\Omega}_l f_0 \left( \left[ X^{[l]}_{+,j}, {X^{[l']}_{+,f}}' \rho_S \right] - \left[ X^{[l]}_{+,j}, \rho_S {X^{[l']}_{+,f}}' \right] \right) \Bigg\}
\end{aligned}
$$

$$
\begin{aligned}
&+\sum_{l,l'=0}^{N-2}\Bigg\{\frac{f_0^2}{4}\left(\langle C_+^{[l]}C_+^{[l']\prime}\rangle\left[X_{+,f}^{[l]},X_{+,f}^{[l']\prime}\rho_S\right]-\langle C_+^{[l']\prime}C_+^{[l]}\rangle\left[X_{+,f}^{[l]},\rho_S X_{+,f}^{[l']\prime}\right]\right)\\
&-\frac{f_0^2}{4}\left(\langle C_-^{[l]}C_-^{[l']\prime}\rangle\left[X_{-,f}^{[l]},X_{-,f}^{[l']\prime}\rho_S\right]-\langle C_-^{[l']\prime}C_-^{[l]}\rangle\left[X_{-,f}^{[l]},\rho_S X_{-,f}^{[l']\prime}\right]\right)\\
&-f_0^2\left(\left[X_{+,f}^{[l]},X_{+,f}^{[l']\prime}\rho_S\right]-\left[X_{+,f}^{[l]},\rho_S X_{+,f}^{[l']\prime}\right]\right)\Bigg\}. \qquad \text{(C.37)}
\end{aligned}
$$

### Bath correlations

In the upcoming calculations of the bath correlations, we require

$$
\left[R_l-R_l^\dagger,\tilde{R}_{l'}(-\tau)-\tilde{R}_{l'}^\dagger(-\tau)\right]=2i\int \mathrm{d}^3k_l\ (g_{k_l}^2/\omega_{k_l}^2)\sin(\omega_{k_l}\tau)=:2i\phi_s(\tau), \qquad \text{(C.38)}
$$

and apply the simplified Baker-Campbell-Hausdorff formula $e^Xe^Y=e^{X+Y}e^{1/2[X,Y]}$, which is valid if $[X,[X,Y]]=0$ and $[Y,[Y,X]]=0$. The first reservoir correlation is evaluated as

$$
\begin{aligned}
&\langle B_+^{[l]}B_+^{[l']}(-\tau)\rangle=\mathrm{tr}_B\Big\{\rho_B\Big[e^{(R_l-R_l^\dagger)}+e^{-(R_l-R_l^\dagger)}\Big]\Big[e^{(\tilde{R}_{l'}-\tilde{R}_{l'}^\dagger)}+e^{-(\tilde{R}_{l'}-\tilde{R}_{l'}^\dagger)}\Big]\Big\}\\
&=\mathrm{tr}_B\Big\{\rho_B\Big[e^{(R_l^\dagger+\tilde{R}_{l'}^\dagger)-(R_l+\tilde{R}_{l'})}e^{1/2\left[(R_l-R_l^\dagger),(\tilde{R}_{l'}-\tilde{R}_{l'}^\dagger)\right]}\\
&+e^{-(R_l^\dagger+\tilde{R}_{l'}^\dagger)+(R_l+\tilde{R}_{l'})}e^{1/2\left[(R_l-R_l^\dagger),(\tilde{R}_{l'}-\tilde{R}_{l'}^\dagger)\right]}+e^{(R_l^\dagger-\tilde{R}_{l'}^\dagger)-(R_l-\tilde{R}_{l'})}e^{1/2\left[(R_l-R_l^\dagger),(\tilde{R}_{l'}-\tilde{R}_{l'}^\dagger)\right](-1)}\\
&+e^{-(R_l^\dagger-\tilde{R}_{l'}^\dagger)+(R_l-\tilde{R}_{l'})}e^{1/2\left[(R_l-R_l^\dagger),(\tilde{R}_{l'}-\tilde{R}_{l'}^\dagger)\right](-1)}\Big]\Big\}, \qquad \text{(C.39)}
\end{aligned}
$$

with $e^{1/2\left[(R_l-R_l^\dagger),(\tilde{R}_{l'}-\tilde{R}_{l'}^\dagger)\right]}=e^{i\phi_s(\tau)}$, leading to

$$
\begin{aligned}
&\langle B_+^{[l]}B_+^{[l']}(-\tau)\rangle\\
&=2\mathrm{tr}_B\rho_B\Big(\Big\{1+\frac{1}{2!}\left[\left(R_l^\dagger+\tilde{R}_{l'}^\dagger\right)-\left(R_l+\tilde{R}_{l'}\right)\right]^2+\frac{1}{4!}\left[\left(R_l^\dagger+\tilde{R}_{l'}^\dagger\right)-\left(R_l+\tilde{R}_{l'}\right)\right]^4+\dots\Big\}e^{i\phi_s(\tau)}\\
&+\Big\{1+\frac{1}{2!}\left[\left(R_l^\dagger-\tilde{R}_{l'}^\dagger\right)-\left(R_l-\tilde{R}_{l'}\right)\right]^2+\frac{1}{4!}\left[\left(R_l^\dagger-\tilde{R}_{l'}^\dagger\right)-\left(R_l-\tilde{R}_{l'}\right)\right]^4+\dots\Big\}e^{-i\phi_s(\tau)}\Big), \qquad \text{(C.40)}
\end{aligned}
$$

with

$$
\begin{aligned}
R_l\pm\tilde{R}_{l'}(-\tau)&=\int \mathrm{d}^3k_l\ \frac{g_{k_l}}{\omega_{k_l}}r_{\boldsymbol{k}_l}\pm\int \mathrm{d}^3k_l'\ \frac{g_{k_{l'}}}{\omega_{k_{l'}}}e^{i\omega_{k_{l'}}\tau}r_{k_{l'}},\\
R_l^\dagger\pm\tilde{R}_{l'}^\dagger(-\tau)&=\int \mathrm{d}^3k_l\ \frac{g_{k_l}}{\omega_{k_l}}r_{\boldsymbol{k}_l}^\dagger\pm\int \mathrm{d}^3k_l'\ \frac{g_{k_{l'}}}{\omega_{k_{l'}}}e^{-i\omega_{k_{l'}}\tau}r_{k_{l'}}^\dagger. \qquad \text{(C.41)}
\end{aligned}
$$

Hence, we arrive at

$$\begin{aligned}
&\mathrm{tr}_B\Big\{\tilde{\rho}_B\left[(R_l^\dagger+\tilde{R}_{l'}^\dagger)-(R_l+\tilde{R}_{l'})\right]^2\Big\}\\
&=-\int \mathrm{d}^3k_l\ \frac{g_{k_l}^2}{\omega_{k_l}^2}\left[(2n_{k_l}+1)+n_{k_l}e^{i\omega_{k_l}\tau}+(n_{k_l}+1)e^{-i\omega_{k_l}\tau}\right]\\
&-\int \mathrm{d}^3k_l'\ \frac{g_{k_{l'}}^2}{\omega_{k_{l'}}^2}\left[(2n_{k_{l'}}+1)+n_{k_{l'}}e^{-i\omega_{k_{l'}}\tau}+(n_{k_{l'}}+1)e^{i\omega_{k_{l'}}\tau}\right]\\
&=-\int \mathrm{d}^3k_l\ \frac{g_{k_l}^2}{\omega_{k_l}^2}\left\{(2n_{k_l}+1)\left[2+2\cos\left(\omega_{k_l}\tau\right)\right]\right\}. \qquad \text{(C.42)}
\end{aligned}$$

In the last step we have assumed identical baths. Since all that remains are complex numbers and the sums over $k_l$ and $k_{l'}$ contain the same elements, they can be summarized in a single sum. We factorize the next term using Wick's theorem and arrive at

$$\begin{aligned}
&\mathrm{tr}_B\left\{\tilde{\rho}_B\left[\left(R_l^\dagger+\tilde{R}_{l'}^\dagger\right)-\left(R_l+\tilde{R}_{l'}\right)\right]^4\right\}\\
&\approx 3\Bigg(-\int \mathrm{d}^3k_l\ \frac{g_{k_l}^2}{\omega_{k_l}^2}\left\{(2n_{k_l}+1)[1+\cos\left(\omega_{k_l}\tau\right)]-\sin\left(\omega_{k_l}\tau\right)\right\}\\
&-\int \mathrm{d}^3k_l'\ \frac{g_{k_{l'}}^2}{\omega_{k_{l'}}^2}\left\{(2n_{k_{l'}}+1)[1+\cos\left(\omega_{k_{l'}}\tau\right)]+\sin\left(\omega_{k_{l'}}\tau\right)\right\}\Bigg)\\
&\Bigg(-\int \mathrm{d}^3k_{l2}\ \frac{g_{k_{l2}}^2}{\omega_{k_{l2}}^2}\left\{(2n_{k_{l2}}+1)[1+\cos\left(\omega_{k_{l2}}\tau\right)]-\sin\left(\omega_{k_{l2}}\tau\right)\right\}\\
&-\int \mathrm{d}^3k_{l2}'\ \frac{g_{k_{l2'}}^2}{\omega_{k_{l2'}}^2}\left\{(2n_{k_{l2'}}+1)[1+\cos\left(\omega_{k_{l2'}}\tau\right)]+\sin\left(\omega_{k_{l2'}}\tau\right)\right\}\Bigg)\\
&=3\int \mathrm{d}^3k_l\ \int \mathrm{d}^3k_l'\ \frac{g_{k_l}^2}{\omega_{k_l}^2}\frac{g_{k_{l'}}^2}{\omega_{k_{l'}}^2}\Big\{(2n_{k_l}+1)[2+2\cos\left(\omega_{k_l}\tau\right)](2n_{k_{l'}}+1)[2+2\cos\left(\omega_{k_{l'}}\tau\right)]\\
&+(2n_{k_l}+1)[2+2\cos\left(\omega_{k_l}\tau\right)]\sin\left(\omega_{k_{l'}}\tau\right)-(2n_{k_{l'}}+1)[2+2\cos\left(\omega_{k_{l'}}\tau\right)]\sin\left(\omega_{k_l}\tau\right)\Big\}. \qquad \text{(C.43)}
\end{aligned}$$

In total, we get

$$\begin{aligned}
\langle B_+^{[l]}B_+^{[l']}(-\tau)\rangle &= 2\exp\left[-\frac{1}{2}\int \mathrm{d}^3k\ \left|f_+^l\right|^2(2n_k+1)+i\phi_s(\tau)\right]\\
&+2\exp\left[-\frac{1}{2}\int \mathrm{d}^3k\ \left|f_-^l\right|^2(2n_k+1)-i\phi_s(\tau)\right], \qquad \text{(C.44)}
\end{aligned}$$

with

$$\left|f_\pm^l\right|^2=\frac{g_{k_l}^2}{\omega_{k_l}^2}\left[2\pm 2\cos\left(\omega_k\tau\right)\right]. \qquad \text{(C.45)}$$

Moreover, we have assumed the reservoir in a thermal equilibrium state, allowing for its description in terms of a Bose distribution, $n_{k_l} = 1/(e^{\hbar\omega_{k_l}/k_BT} - 1)$, resulting in

$$(2n_{k_l} + 1) = \coth\left(\frac{\hbar\omega_{k_l}}{2k_BT}\right). \tag{C.46}$$

Inserting Eqs. (C.45) and (C.46) into Eq. (C.44) and making use of the definition $\phi_s(\tau)$ [Eq. (C.38)] yields the final expression for the bath correlation

$$\begin{aligned}\langle B_{+,j}B_{+,i}(-\tau)\rangle = 4\exp\left[-\int \mathrm{d}^3k_l\ \frac{g_{k_l}^2}{\omega_{k_l}^2}\coth\left(\frac{\hbar\omega_{k_l}}{2k_BT}\right)\right]\\ \times\cosh\left\{\int \mathrm{d}^3k_l\ \frac{g_{k_l}^2}{\omega_{k_l}^2}\left[\cos\left(\omega_{k_l}\tau\right)\coth\left(\frac{\hbar\omega_{k_l}}{2k_BT}\right) - i\sin(\omega_{k_l}\tau)\right]\right\}.\end{aligned} \tag{C.47}$$

We define the reservoir correlation function

$$\phi(\tau) := \int \mathrm{d}^3k_l\ \frac{g_{k_l}^2}{\omega_k^2}\left[\coth\left(\frac{\hbar\omega_{k_l}}{2k_BT}\right)\cos\left(\omega_{k_l}\tau\right) - i\sin(\omega_{k_l}\tau)\right], \tag{C.48}$$

and finally arrive at

$$\langle B_+^{[l]}B_+^{[l']}(-\tau)\rangle = 4\exp\left[-\phi(0)\right]\cosh\left[\phi(\tau)\right]. \tag{C.49}$$

$\langle B_-^{[l]}B_-^{[l']}(-\tau)\rangle$ is calculated in the same fashion. The calculation of $\langle B_+^{[l']}(-\tau)B_+^{[l]}\rangle$ has already been done up to a sign in $\phi_s(\tau)$. The resulting terms read

$$\begin{aligned}\langle B_+^{[l']}(-\tau)B_+^{[l]}\rangle &= 4\exp\left[-\phi(0)\right]\cosh\left[\phi^*(\tau)\right] = \langle B_+^{[l]}B_+^{[l']}(-\tau)\rangle^*,\\ \langle B_-^{[l]}B_-^{[l']}(-\tau)\rangle &= -4\exp\left[-\phi(0)\right]\sinh\left[\phi(\tau)\right],\\ \langle B_-^{[l']}(-\tau)B_-^{[l]}\rangle &= -4\exp\left[-\phi(0)\right]\sinh\left[\phi^*(\tau)\right] = \langle B_-^{[l]}B_-^{[l']}(-\tau)\rangle^*.\end{aligned} \tag{C.50}$$

We still have to calculate correlations including $C^{[l]}$. In the upcoming calculations, we require

$$\left[\left(R_{l+1} - R_{l+1}^\dagger\right) - \left(R_l - R_l^\dagger\right), \left(\tilde{R}_{l'+1} - \tilde{R}_{l'+1}^\dagger\right) - \left(\tilde{R}_{l'} - \tilde{R}_{l'}^\dagger\right)\right] = 0, \tag{C.51}$$

and

$$\left[\left(R_{l+1} - R_{l+1}^\dagger\right) - \left(R_l - R_l^\dagger\right), \left(\tilde{R}_{l'} - \tilde{R}_{l'}^\dagger\right)\right] = 0. \tag{C.52}$$

Again we make use of the simplified Baker-Campbell-Hausdorff formula $e^Xe^Y = e^{X+Y}e^{1/2[X,Y]}$, which is valid if $[X,[X,Y]] = 0$ and $[Y,[Y,X]] = 0$. The next reservoir correlation is evaluated as

$$\begin{aligned}\langle C_+^{[l]}C_+^{[l']}(-\tau)\rangle = \mathrm{tr}_B\Big\{\rho_B\Big[&e^{(R_{l+1}+\tilde{R}_{l'+1})-(R_{l+1}^\dagger+\tilde{R}_{l'+1}^\dagger)+(R_l^\dagger+\tilde{R}_{l'}^\dagger)-(R_l+\tilde{R}_{l'})}\\ &+ e^{(R_{l+1}-\tilde{R}_{l'+1})-(R_{l+1}^\dagger-\tilde{R}_{l'+1}^\dagger)+(R_l^\dagger-\tilde{R}_{l'}^\dagger)-(R_l-\tilde{R}_{l'})}\\ &+ e^{-(R_{l+1}-\tilde{R}_{l'+1})+(R_{l+1}^\dagger-\tilde{R}_{l'+1}^\dagger)-(R_l^\dagger-\tilde{R}_{l'}^\dagger)+(R_l-\tilde{R}_{l'})}\\ &+ e^{-(R_{l+1}+\tilde{R}_{l'+1})+(R_{l+1}^\dagger+\tilde{R}_{l'+1}^\dagger)-(R_l^\dagger+\tilde{R}_{l'}^\dagger)+(R_l+\tilde{R}_{l'})}\Big]\Big\}.\end{aligned} \tag{C.53}$$

Once again the series expansion of the cosh function is used, resulting in

$$\begin{aligned}
&\mathrm{tr}_B\Big\{\tilde{\rho}_B\Big[\Big(R_{l+1}+\tilde{R}_{l'+1}\Big)-\Big(R^\dagger_{l+1}+\tilde{R}^\dagger_{l'+1}\Big)+\Big(R^\dagger_l+\tilde{R}^\dagger_{l'}\Big)-\Big(R_l+\tilde{R}_{l'}\Big)\Big]^2\Big\}\\
&=-\int \mathrm{d}^3k_l\ \frac{g^2_{k_l}}{\omega^2_{k_l}}\Big[(2n_{k_l}+1)+n_{k_l}e^{i\omega_{k_l}\tau}+(n_{k_l}+1)e^{-i\omega_{k_l}\tau}\Big]\\
&-\int \mathrm{d}^3k'_l\ \frac{g^2_{k_{l'}}}{\omega^2_{k_{l'}}}\Big[(2n_{k_{l'}}+1)+n_{k_{l'}}e^{-i\omega_{k_{l'}}\tau}+(n_{k_{l'}}+1)e^{i\omega_{k_{l'}}\tau}\Big]\\
&+\int \mathrm{d}^3k_l\ \frac{g^2_{k_l}}{\omega^2_{k_l}}\Big[(2n_{k_l}+1)+n_{k_l}e^{i\omega_{k_l}\tau}+(n_{k_l}+1)e^{-i\omega_{k_l}\tau}\Big]\\
&+\int \mathrm{d}^3k'_l\ \frac{g^2_{k_{l'}}}{\omega^2_{k_{l'}}}\Big[(2n_{k_{l'}}+1)+n_{k_{l'}}e^{-i\omega_{k_{l'}}\tau}+(n_{k_{l'}}+1)e^{i\omega_{k_{l'}}\tau}\Big]=0.
\end{aligned}\tag{C.54}$$

Analogous to before, we find

$$\Big[\Big(R_{l+1}+\tilde{R}_{l'+1}\Big)-\Big(R^\dagger_{l+1}+\tilde{R}^\dagger_{l'+1}\Big)+\Big(R^\dagger_l+\tilde{R}^\dagger_{l'}\Big)-\Big(R_l+\tilde{R}_{l'}\Big)\Big]^2=0,\tag{C.55}$$

resulting in

$$\langle C^{[l]}_+C^{[l']}_+(-\tau)\rangle=\langle C^{[l']}_+(-\tau)C^{[l]}_+\rangle=\mathrm{tr}_B\{\rho_B(2+2)\}=4.\tag{C.56}$$

Applying the same treatment to $\langle C^{[l]}_-C^{[l']}_-(-\tau)\rangle$ results in

$$\langle C^{[l]}_-C^{[l']}_-(-\tau)\rangle=\langle C^{[l']}_-(-\tau)C^{[l]}_-\rangle=0.\tag{C.57}$$

Due to the structure of the reservoir correlations, we once again find $\langle C_+C_-\rangle=\langle C_-C_+\rangle=0$.

We still have to calculate the mixed bath contributions $\langle CB\rangle$ and $\langle BC\rangle$:

$$\begin{aligned}
&\langle C^{[l]}_+B^{[l']}_+(-\tau)\rangle\\
&=\mathrm{tr}_B\Big\{\rho_B\Big[e^{(R_{l+1}-R^\dagger_{l+1})+(R^\dagger_l+\tilde{R}^\dagger_{l'})-(R_l+\tilde{R}_{l'})}+e^{(R_{l+1}-R^\dagger_{l+1})+(R^\dagger_l-\tilde{R}^\dagger_{l'})-(R_l-\tilde{R}_{l'})}\\
&+e^{-(R_{l+1}-R^\dagger_{l+1})-(R^\dagger_l-\tilde{R}^\dagger_{l'})+(R_l-\tilde{R}_{l'})}+e^{-(R_{l+1}-R^\dagger_{l+1})-(R^\dagger_l+\tilde{R}^\dagger_{l'})+(R_l+\tilde{R}_{l'})}\Big]\Big\}.
\end{aligned}\tag{C.58}$$

Using the series expansion of the cosh function yields

$$\begin{aligned}
&\mathrm{tr}_B\Big\{\tilde{\rho}_B\Big[\Big(R_{l+1}-R^\dagger_{l+1}\Big)+\Big(R^\dagger_l+\tilde{R}^\dagger_{l'}\Big)-\Big(R_l+\tilde{R}_{l'}\Big)\Big]^2\Big\}\\
&=\int \mathrm{d}^3k_l+1\ \frac{g^2_{k_{l+1}}}{\omega^2_{k_{l+1}}}\Big[n_{k_{l+1}}e^{i\omega_{k_{l+1}}\tau}+(n_{k_{l+1}}+1)e^{-i\omega_{k_{l+1}}\tau}\Big]\\
&-\int \mathrm{d}^3k_l\ \frac{g^2_{k_l}}{\omega^2_{k_l}}\Big[n_{k_l}e^{i\omega_{k_l}\tau}+(n_{k_l}+1)e^{-i\omega_{k_l}\tau}\Big]-\int \mathrm{d}^3k'_l\ \frac{g^2_{k_{l'}}}{\omega^2_{k_{l'}}}\Big(2n_{k_{l'}}+1\Big)\\
&=-\int \mathrm{d}^3k_l\ \frac{g^2_{k_l}}{\omega^2_{k_l}}(2n_{k_l}+1).
\end{aligned}\tag{C.59}$$

In a completely analogous calculation, we obtain

$$\mathrm{tr}_B\left\{\tilde{\rho}_B\left[\left(R_{l+1}-R_{l+1}^\dagger\right)+\left(R_l^\dagger-\tilde{R}_{l'}^\dagger\right)-\left(R_l-\tilde{R}_{l'}\right)\right]^2\right\}=-\int \mathrm{d}^3k_l\ \frac{g_{k_l}^2}{\omega_{k_l}^2}(2n_{k_l}+1). \quad \text{(C.60)}$$

Following the same steps as before, this results in

$$\langle C_+^{[l]}B_+^{[l']}(-\tau)\rangle=\langle B_+^{[l']}(-\tau)C_+^{[l]}\rangle=4\exp\left[-\frac{1}{2}\phi(0)\right]. \quad \text{(C.61)}$$

The other mixed reservoir contribution is evaluated as

$$\begin{aligned}&\langle C_+^{[l']}(-\tau)B_+^{[l]}\rangle\\&=\mathrm{tr}_B\Big\{\rho_B\Big[e^{(\tilde{R}_{l'+1}-\tilde{R}_{l'+1}^\dagger)+(\tilde{R}_{l'}^\dagger+R_l^\dagger)-(\tilde{R}_{l'}+R_l)}+e^{(\tilde{R}_{l'+1}-\tilde{R}_{l'+1}^\dagger)+(\tilde{R}_{l'}^\dagger-R_l^\dagger)-(\tilde{R}_{l'}-R_l)}\\&+e^{-(\tilde{R}_{l'+1}-\tilde{R}_{l'+1}^\dagger)-(\tilde{R}_{l'}^\dagger-R_l^\dagger)+(\tilde{R}_{l'}-R_l)}+e^{-(\tilde{R}_{l'+1}-\tilde{R}_{l'+1}^\dagger)-(\tilde{R}_{l'}^\dagger+R_l^\dagger)+(\tilde{R}_{l'}+R_l)}\Big]\Big\}. \quad \text{(C.62)}\end{aligned}$$

Again, we employ the series expansion of the cosh function, resulting in

$$\mathrm{tr}_B\left\{\tilde{\rho}_B\left[\left(\tilde{R}_{l'+1}-\tilde{R}_{l'+1}^\dagger\right)+\left(\tilde{R}_{l'}^\dagger+R_l^\dagger\right)-\left(\tilde{R}_{l'}+R_l\right)\right]^2\right\}=-\int \mathrm{d}^3k_l\ \frac{g_{k_l}^2}{\omega_{k_l}^2}(2n_{k_l}+1), \quad \text{(C.63)}$$

and

$$\mathrm{tr}_B\left\{\tilde{\rho}_B\left[\left(\tilde{R}_{l'+1}-\tilde{R}_{l'+1}^\dagger\right)+\left(\tilde{R}_{l'}^\dagger-R_l^\dagger\right)-\left(\tilde{R}_{l'}-R_l\right)\right]^2\right\}=-\int \mathrm{d}^3k_l\ \frac{g_{k_l}^2}{\omega_{k_l}^2}(2n_{k_l}+1). \quad \text{(C.64)}$$

Following the same steps as before, this leads to

$$\langle C_+^{[l']}(-\tau)B_+^{[l]}\rangle=\langle B_+^{[l]}C_+^{[l']}(-\tau)\rangle=4\exp\left[-\frac{1}{2}\phi(0)\right]. \quad \text{(C.65)}$$

The remaining contributions are given by

$$\begin{aligned}\langle C_-^{[l]}B_-^{[l']}(-\tau)\rangle&=\langle B_-^{[l']}(-\tau)C_-^{[l]}\rangle=0,\\\langle C_-^{[l']}(-\tau)B_-^{[l]}\rangle&=\langle B_-^{[l]}C_-^{[l']}(-\tau)\rangle=0, \quad \text{(C.66)}\end{aligned}$$

and all mixed contributions of the form $\langle B_+C_-\rangle$, $\langle B_-C_+\rangle$ are once again zero.

### Resulting master equation

Making use of $\bar{\Omega} = \Omega \exp(-\phi(0)/2)$, $\bar{f}_0 = f_0$, and inserting the correlation functions into Eq. (B.27) yields the final result

$$
\begin{aligned}
&\mathrm{tr}_B\{[H_{p,I},[H_{p,I}(-\tau),\rho]]\} \\
&= \sum_{l,l'=0}^{N-1}\sum_{i,j=2,3} \Omega^2 e^{-\phi(0)} \Big\{ (\cosh[\phi(\tau)]-1)\left[X^{[l]}_{+,j}, X^{[l']\prime}_{+,i}\rho_S\right] - (\cosh[\phi^*(\tau)]-1)\left[X^{[l]}_{+,j}, \rho_S X^{[l']\prime}_{+,i}\right] \\
&+ \sinh[\phi(\tau)]\left[X^{[l]}_{-,j}, X^{[l']\prime}_{-,i}\rho_S\right] - \sinh[\phi^*(\tau)]\left[X^{[l]}_{-,j}, \rho_S X^{[l']\prime}_{-,i}\right] \Big\} \\
&+ \sum_{l,l'=0}^{N-1}\sum_{i=2,3}\left[1-\delta_{l,(N-1)}\right]\Big\{\Omega f_0 e^{-\phi(0)/2}\left(\left[X^{[l]}_{+,f}, X^{[l']\prime}_{+,i}\rho_S\right] - \left[X^{[l]}_{+,f}, \rho_S X^{[l']\prime}_{+,i}\right]\right) \\
&- \Omega f_0 e^{-\phi(0)/2}\left(\left[X^{[l]}_{+,f}, X^{[l']\prime}_{+,i}\rho_S\right] - \left[X^{[l]}_{+,f}, \rho_S X^{[l']\prime}_{+,i}\right]\right)\Big\} \\
&+ \sum_{l,l'=0}^{N-1}\sum_{j=2,3}\left[1-\delta_{l',(N-1)}\right]\Big\{\Omega f_0 e^{-\phi(0)/2}\left(\left[X^{[l]}_{+,j}, X^{[l']\prime}_{+,f}\rho_S\right] - \left[X^{[l]}_{+,j}, \rho_S X^{[l']\prime}_{+,f}\right]\right) \\
&- \Omega f_0 e^{-\phi(0)/2}\left(\left[X^{[l]}_{+,j}, X^{[l']\prime}_{+,f}\rho_S\right] - \left[X^{[l]}_{+,j}, \rho_S X^{[l']\prime}_{+,f}\right]\right)\Big\} \\
&+ \sum_{l,l'=0}^{N-2}\Big\{f_0^2\left(\left[X^{[l]}_{+,f}, X^{[l']\prime}_{+,f}\rho_S\right] - \left[X^{[l]}_{+,f}, \rho_S X^{[l']\prime}_{+,f}\right]\right) \\
&- f_0^2\left(\left[X^{[l]}_{+,f}, X^{[l']\prime}_{+,f}\rho_S\right] - \left[X^{[l]}_{+,f}, \rho_S X^{[l']\prime}_{+,f}\right]\right)\Big\} \\
&= \sum_{l,l'=0}^{N-1}\sum_{i,j=2,3} \Omega^2 e^{-\phi(0)} \Big\{ (\cosh[\phi(\tau)]-1)\left[X^{[l]}_{+,j}, X^{[l']\prime}_{+,i}\rho_S\right] \\
&- (\cosh[\phi^*(\tau)]-1)\left[X^{[l]}_{+,j}, \rho_S X^{[l']\prime}_{+,i}\right] \\
&+ \sinh[\phi(\tau)]\left[X^{[l]}_{-,j}, X^{[l']\prime}_{-,i}\rho_S\right] - \sinh[\phi^*(\tau)]\left[X^{[l]}_{-,j}, \rho_S X^{[l']\prime}_{-,i}\right] \Big\},
\end{aligned}
\tag{C.67}
$$

and the master equation takes the form

$$
\begin{aligned}
\frac{\mathrm{d}}{\mathrm{d}t}\rho_S(t) &= -\frac{i}{\hbar}\left[H_{p,0},\rho_S(t)\right] - \frac{\bar{\Omega}^2}{\hbar^2}\sum_{l,l'=0}^{N-1}\sum_{i,j=2,3} \\
&\times \int_0^t d\tau \left\{ G_+(\tau)\left[X^{[l]}_{+,j}, X^{[l']\prime}_{+,i}\rho_S\right] + G_-(\tau)\left[X^{[l]}_{-,j}, X^{[l']\prime}_{-,i}\rho_S\right] + \mathrm{H.c.}\right\},
\end{aligned}
\tag{C.68}
$$

with

$$G_+(\tau) = \cosh\left[\phi(\tau)\right] - 1, \tag{C.69a}$$
$$G_-(\tau) = \sinh\left[\phi(\tau)\right], \tag{C.69b}$$
$$\phi(\tau) = \int \mathrm{d}^3 k_l \, \frac{g_{k_l}^2}{\omega_{k_l}^2} \left[\coth\left(\frac{\hbar\omega_{k_l}}{2k_B T}\right)\cos(\omega_{k_l}\tau) - i\sin(\omega_{k_l}\tau)\right], \tag{C.69c}$$

and

$$X_{+,i}^{[l]}(t) = \left[\sigma_{1i}^l(t) + \sigma_{i1}^l(t)\right], \tag{C.70a}$$
$$X_{-,i}^{[l]}(t) = i\left[\sigma_{i1}^l(t) - \sigma_{1i}^l(t)\right], \tag{C.70b}$$

where $\sigma_{mn}^l = \sigma_{(m+3l)(n+3l)}$.

## C.4 Polaron master equation: Equations of motion

### C.4.1 Single V-type emitter

The polaron master equation for a single $V$-type emitter reads

$$\begin{aligned}\frac{\mathrm{d}}{\mathrm{d}t}\rho_S(t) &= -\frac{i}{\hbar}\left[H_{p,0}, \rho_S(t)\right] \\ &- \frac{\bar{\Omega}^2}{\hbar^2}\sum_{i,j=2,3}\int_0^t d\tau \sum_{s=\pm}\left\{G_s(\tau)\left[X_{s,j}, X_{s,i}(-\tau)\rho_S(t)\right] + \text{H.c.}\right\},\end{aligned} \tag{C.71}$$

with

$$X_{+,i}(\tau) = \left[\sigma_{1i}(\tau) + \sigma_{i1}(\tau)\right], \tag{C.72a}$$
$$X_{-,i}(\tau) = i\left[\sigma_{i1}(\tau) - \sigma_{1i}(\tau)\right], \tag{C.72b}$$
$$\bar{\Omega} = \Omega\exp\left[-\phi(0)/2\right]. \tag{C.72c}$$

We calculate the equations of motion for all density matrix elements $\rho_{mn} := \langle m|\,\rho_S\,|n\rangle$. For a shorter notation, we denote $\langle m|\,X_{l,i}(-\tau)\,|n\rangle =: X_{l,i}^{mn}(-\tau)$. The resulting equations of motion read

$$\begin{aligned}\frac{\mathrm{d}}{\mathrm{d}t}\rho_{mn} &= \sum_{i=2,3}\left[i\bar{\Delta}_i^l\left(\rho_{mi}\delta_{ni} - \rho_{in}\delta_{mi}\right) + i\bar{\Omega}(\rho_{m1}\delta_{ni} + \rho_{mi}\delta_{n1} - \rho_{in}\delta_{m1} - \rho_{1n}\delta_{mi})\right] \\ &- \frac{\bar{\Omega}^2}{\hbar^2}\sum_{i,j=2,3}\int_0^t d\tau\,\langle m|\,\chi^{ij}(\tau)\,|n\rangle,\end{aligned} \tag{C.73}$$

where

$$\begin{aligned}
\langle m|\,\chi^{ij}(\tau)\,|n\rangle = \sum_{q=1}^{3}\Big(&\rho_{qn}\Big\{\Big[G_+^{ij}(\tau)X_{+,j}^{iq}(-\tau) - iG_-^{ij}(\tau)X_{-,j}^{iq}(-\tau)\Big]\delta_{m1}\\
&+\Big[G_+^{ij}(\tau)X_{+,j}^{1q}(-\tau) + iG_-^{ij}(\tau)X_{-,j}^{1q}(-\tau)\Big]\delta_{mi}\Big\}\\
&+\rho_{mq}\Big\{\Big[G_+^{ij*}(\tau)X_{+,j}^{q1}(-\tau) - iG_-^{ij*}(\tau)X_{-,j}^{q1}(-\tau)\Big]\delta_{ni}\\
&+\Big[G_+^{ij*}(\tau)X_{+,j}^{qi}(-\tau) + iG_-^{ij*}(\tau)X_{-,j}^{qi}(-\tau)\Big]\delta_{n1}\Big\}\\
&+\rho_{q1}\Big[-G_+^{ij}(\tau)X_{+,j}^{mq}(-\tau) + iG_-^{ij}(\tau)X_{-,j}^{mq}(-\tau)\Big]\delta_{ni}\\
&+\rho_{qi}\Big[-G_+^{ij}(\tau)X_{+,j}^{mq}(-\tau) - iG_-^{ij}(\tau)X_{-,j}^{mq}(-\tau)\Big]\delta_{n1}\\
&+\rho_{1q}\Big[-G_+^{ij*}(\tau)X_{+,j}^{qn}(-\tau) - iG_-^{ij*}(\tau)X_{-,j}^{qn}(-\tau)\Big]\delta_{mi}\\
&+\rho_{iq}\Big[-G_+^{ij*}(\tau)X_{+,j}^{qn}(-\tau) + iG_-^{ij*}(\tau)X_{-,j}^{qn}(-\tau)\Big]\delta_{m1}\Big).
\end{aligned} \tag{C.74}$$

### C.4.2 Chain of V-type emitters

The equations of motion resulting from Eq. (C.68) are given by

$$\begin{aligned}
\frac{\mathrm{d}}{\mathrm{d}t}\rho_{mn} = &\sum_{l=0}^{N-1}\sum_{i=2,3}\Big\{i\bar{\Delta}_i^l\Big[\rho_{m(i+3l)}\delta_{n,(i+3l)} - \rho_{(i+3l)n}\delta_{m,(i+3l)}\Big]\\
&+i\bar{\Omega}\Big[\rho_{m(1+3l)}\delta_{n,(i+3l)} + \rho_{m(i+3l)}\delta_{n,(1+3l)} - \rho_{(i+3l)n}\delta_{m,(1+3l)} - \rho_{(1+3l)n}\delta_{m,(i+3l)}\Big]\\
&-\frac{\bar{\Omega}^2}{\hbar^2}\int_0^t d\tau\,\langle m|\,\chi_l^{ij}(\tau)\,|n\rangle\Big\} + i\sum_{l=0}^{N-2}\Big\{f(t)\Big[\rho_{m(5+3l)}\delta_{n,(3+3l)} - \rho_{(3+3l)n}\delta_{m,(5+3l)}\Big]\\
&+f^*(t)\Big[\rho_{m(3+3l)}\delta_{n,(5+3l)} - \rho_{(5+3l)n}\delta_{m,(3+3l)}\Big]\Big\},
\end{aligned} \tag{C.75}$$

where

$$\begin{aligned}
\langle m|\,\chi_l^{ij}(\tau)\,|n\rangle = \sum_{l'=0}^{N-1}\sum_{q=1}^{3}\Big(&\rho_{qn}\\
&\times\Big\{\Big[G_+(\tau)\,\langle i+3l|\,X_{+,j}^{[l']}(-\tau)\,|q+3l\rangle - iG_-(\tau)\,\langle i+3l|\,X_{-,j}^{[l']}(-\tau)\,|q+3l\rangle\Big]\delta_{m,(1+3l)}\\
&+\Big[G_+(\tau)\,\langle 1+3l|\,X_{+,j}^{[l']}(-\tau)\,|q+3l\rangle + iG_-(\tau)\,\langle 1+3l|\,X_{-,j}^{[l']}(-\tau)\,|q+3l\rangle\Big]\delta_{m,(i+3l)}\Big\}\\
&+\rho_{mq}\Big\{\Big[G_+^*(\tau)\,\langle q+3l|\,X_{+,j}^{[l']}(-\tau)\,|1+3l\rangle - iG_-^*(\tau)\,\langle q+3l|\,X_{-,j}^{[l']}(-\tau)\,|1+3l\rangle\Big]\delta_{n,(i+3l)}\\
&+\Big[G_+^*(\tau)\,\langle q+3l|\,X_{+,j}^{[l']}(-\tau)\,|i+3l\rangle + iG_-^*(\tau)\,\langle q+3l|\,X_{-,j}^{[l']}(-\tau)\,|i+3l\rangle\Big]\delta_{n,(1+3l)}\Big\}\\
&+\rho_{q1}\Big[-G_+(\tau)\,\langle m|\,X_{+,j}^{[l']}(-\tau)\,|q+3l\rangle + iG_-(\tau)\,\langle m|\,X_{-,j}^{[l']}(-\tau)\,|q+3l\rangle\Big]\delta_{n,(i+3l)}\\
&+\rho_{qi}\Big[-G_+(\tau)\,\langle m|\,X_{+,j}^{[l']}(-\tau)\,|q+3l\rangle - iG_-(\tau)\,\langle m|\,X_{-,j}^{[l']}(-\tau)\,|q+3l\rangle\Big]\delta_{n,(1+3l)}
\end{aligned}$$

$$+\rho_{1q}\Big[-G_{+}^{*}(\tau)\left\langle q+3l\right|X_{+,j}^{[l']}(-\tau)\left|n\right\rangle - iG_{-}^{*}(\tau)\left\langle q+3l\right|X_{-,j}^{[l']}(-\tau)\left|n\right\rangle\Big]\delta_{m,(i+3l)}$$
$$+\rho_{iq}\Big[-G_{+}^{*}(\tau)\left\langle q+3l\right|X_{+,j}^{[l']}(-\tau)\left|n\right\rangle + iG_{-}^{*}(\tau)\left\langle q+3l\right|X_{-,j}^{[l']}(-\tau)\left|n\right\rangle\Big]\delta_{m,(1+3l)}\Big). \quad \text{(C.76)}$$

For the solution of the resulting integro-differential equation, we employ the time-evolution operator $U_0(t,0) = \exp(-iH_{p,0}t/\hbar)$ to calculate the time-dependent system correlations, yielding

$$\begin{aligned}\left\langle m\right|X_{+,i}^{[l']}(-\tau)\left|n\right\rangle &= \sum_{q=1}^{3N}\Big[\left\langle q\right|\rho_c(-\tau)\left|i+3l'\right\rangle\delta_{q,(1+3l')} + \left\langle q\right|\rho_c(-\tau)\left|1+3l'\right\rangle\delta_{q,(i+3l')}\Big]\\ &= \left\langle 1+3l'\right|\rho_c(-\tau)\left|i+3l'\right\rangle + \left\langle i+3l'\right|\rho_c(-\tau)\left|1+3l'\right\rangle, \end{aligned} \quad \text{(C.77)}$$

and

$$\begin{aligned}\left\langle m\right|X_{-,i}^{[l']}(-\tau)\left|n\right\rangle &= i\sum_{q=1}^{3N}\Big[\left\langle q\right|\rho_c(-\tau)\left|i+3l'\right\rangle\delta_{q,(1+3l')} - \left\langle q\right|\rho_c(-\tau)\left|1+3l'\right\rangle\delta_{q,(i+3l')}\Big]\\ &= i\Big(\left\langle 1+3l'\right|\rho_c(-\tau)\left|i+3l'\right\rangle - \left\langle i+3l'\right|\rho_c(-\tau)\left|1+3l'\right\rangle\Big), \end{aligned} \quad \text{(C.78)}$$

with $\rho_c$ the conditional density matrix.

# Bibliography


[1] H. P. Breuer and F. Petruccione, *The theory of open quantum systems* (Oxford University Press, Oxford, 2002).

[2] Heinz-Peter Breuer, Elsi-Mari Laine, Jyrki Piilo, and Bassano Vacchini, "Colloquium: Non-markovian dynamics in open quantum systems," Rev. Mod. Phys. **88**, 021002 (2016).

[3] Inés de Vega and Daniel Alonso, "Dynamics of non-markovian open quantum systems," Rev. Mod. Phys. **89**, 015001 (2017).

[4] Bi-Heng Liu, Li Li, Yun-Feng Huang, Chuan-Feng Li, Guang-Can Guo, Elsi-Mari Laine, Heinz-Peter Breuer, and Jyrki Piilo, "Experimental control of the transition from markovian to non-markovian dynamics of open quantum systems," Nature Physics **7**, 931 (2011).

[5] Bi-Heng Liu, Dong-Yang Cao, Yun-Feng Huang, Chuan-Feng Li, Guang-Can Guo, Elsi-Mari Laine, Heinz-Peter Breuer, and Jyrki Piilo, "Photonic realization of nonlocal memory effects and non-markovian quantum probes," Scientific Reports **3**, 1781 (2013).

[6] Daniel M. Reich, Nadav Katz, and Christiane P. Koch, "Exploiting non-markovianity for quantum control," Scientific Reports **5**, 12430 (2015).

[7] M. M. Wolf, J. Eisert, T. S. Cubitt, and J. I. Cirac, "Assessing non-markovian quantum dynamics," Phys. Rev. Lett. **101**, 150402 (2008).

[8] Ching-Kit Chan, Guin-Dar Lin, Susanne F. Yelin, and Mikhail D. Lukin, "Quantum interference between independent reservoirs in open quantum systems," Phys. Rev. A **89**, 042117 (2014).

[9] Jun Jing and Ting Yu, "Non-markovian relaxation of a three-level system: Quantum trajectory approach," Phys. Rev. Lett. **105**, 240403 (2010).

[10] P. Kaer, P. Lodahl, A.-P. Jauho, and J. Mork, "Microscopic theory of indistinguishable single-photon emission from a quantum dot coupled to a cavity: The role of non-markovian phonon-induced decoherence," Phys. Rev. B **87**, 081308 (2013).

[11] Victor V. Kozlov, Yuri Rostovtsev, and Marlan O. Scully, "Inducing quantum coherence via decays and incoherent pumping with application to population trapping, lasing without inversion, and quenching of spontaneous emission," Phys. Rev. A **74**, 063829 (2006).

[12] T. M. Stace, A. C. Doherty, and S. D. Barrett, "Population inversion of a driven two-level system in a structureless bath," Phys. Rev. Lett. **95**, 106801 (2005).

[13] P. Kaer, T. R. Nielsen, P. Lodahl, A.-P. Jauho, and J. Mørk, "Non-markovian model of photon-assisted dephasing by electron-phonon interactions in a coupled quantum-dot–cavity system," Phys. Rev. Lett. **104**, 157401 (2010).

[14] S. Weiler, A. Ulhaq, S. M. Ulrich, D. Richter, M. Jetter, P. Michler, C. Roy, and S. Hughes, "Phonon-assisted incoherent excitation of a quantum dot and its emission properties," Phys. Rev. B **86**, 241304 (2012).

[15] Emil V. Denning, Jake Iles-Smith, Niels Gregersen, and Jesper Mork, "Phonon effects in quantum dot single-photon sources," Opt. Mater. Express **10**, 222–239 (2020).

[16] Erik Stock, Matthias-Rene Dachner, Till Warming, Andrei Schliwa, Anatol Lochmann, Axel Hoffmann, Aleksandr I. Toropov, Askhat K. Bakarov, Ilya A. Derebezov, Marten Richter, Vladimir A. Haisler, Andreas Knorr, and Dieter Bimberg, "Acoustic and optical phonon scattering in a single in(ga)as quantum dot," Phys. Rev. B **83**, 041304 (2011).

[17] S. Hughes, P. Yao, F. Milde, A. Knorr, D. Dalacu, K. Mnaymneh, V. Sazonova, P. J. Poole, G. C. Aers, J. Lapointe, R. Cheriton, and R. L. Williams, "Influence of electron-acoustic phonon scattering on off-resonant cavity feeding within a strongly coupled quantum-dot cavity system," Phys. Rev. B **83**, 165313 (2011).

[18] A. Thoma, P. Schnauber, M. Gschrey, M. Seifried, J. Wolters, J.-H. Schulze, A. Strittmatter, S. Rodt, A. Carmele, A. Knorr, T. Heindel, and S. Reitzenstein, "Exploring dephasing of a solid-state quantum emitter via time- and temperature-dependent hong-ou-mandel experiments," Phys. Rev. Lett. **116**, 033601 (2016).

[19] Yumian Su, Dieter Bimberg, Andreas Knorr, and Alexander Carmele, "Collective light emission revisited: Reservoir induced coherence," Phys. Rev. Lett. **110**, 113604 (2013).

[20] Julia Kabuss, Alexander Carmele, Marten Richter, and Andreas Knorr, "Microscopic equation-of-motion approach to the multiphonon assisted quantum emission of a semiconductor quantum dot," Phys. Rev. B **84**, 125324 (2011).

[21] Julia Kabuss, Alexander Carmele, Marten Richter, Weng W Chow, and Andreas Knorr, "Inductive equation of motion approach for a semiconductor qd-qed: Coherence induced control of photon statistics," physica status solidi (b) **248**, 872 (2011).

[22] A. Naesby, T. Suhr, P. T. Kristensen, and J. Mørk, "Influence of pure dephasing on emission spectra from single photon sources," Phys. Rev. A **78**, 045802 (2008).

[23] Antoine Reigue, Jake Iles-Smith, Fabian Lux, Léonard Monniello, Mathieu Bernard, Florent Margaillan, Aristide Lemaitre, Anthony Martinez, Dara P. S. McCutcheon, Jesper Mørk, Richard Hostein, and Valia Voliotis, "Probing electron-phonon interaction through two-photon interference in resonantly driven semiconductor quantum dots," Phys. Rev. Lett. **118**, 233602 (2017).

[24] Sören Kreinberg, Tomislav Grbešić, Max Strauß, Alexander Carmele, Monika Emmerling, Christian Schneider, Sven Höfling, Xavier Porte, and Stephan Reitzenstein, "Quantum-optical spectroscopy of a two-level system using an electrically driven micropillar laser as a resonant excitation source," Light: Science & Applications **7**, 41 (2018).

[25] Florian A. Y. N. Schröder, David H. P. Turban, Andrew J. Musser, Nicholas D. M. Hine, and Alex W. Chin, "Tensor network simulation of multi-environmental open quantum dynamics via machine learning and entanglement renormalisation," Nature Communications **10**, 1062 (2019).

[26] I. A. Luchnikov, S. V. Vintskevich, H. Ouerdane, and S. N. Filippov, "Simulation complexity of open quantum dynamics: Connection with tensor networks," Phys. Rev. Lett. **122**, 160401 (2019).

[27] I. A. Luchnikov, S. V. Vintskevich, D. A. Grigoriev, and S. N. Filippov, "Machine learning non-markovian quantum dynamics," Phys. Rev. Lett. **124**, 140502 (2020).

[28] A. Vagov, M. D. Croitoru, V. M. Axt, P. Machnikowski, and T. Kuhn, "Dynamics of quantum dots with strong electron phonon coupling: Correlation expansion vs. path integrals," physica status solidi (b) **248**, 839–842 (2011).

[29] M. Glässl, A. Vagov, S. Lüker, D. E. Reiter, M. D. Croitoru, P. Machnikowski, V. M. Axt, and T. Kuhn, "Long-time dynamics and stationary nonequilibrium of an optically driven strongly confined quantum dot coupled to phonons," Phys. Rev. B **84**, 195311 (2011).

[30] R. P. Feynman and A. R. Hibbs, *Quantum Mechanics and Path Integrals* (McGraw-Hill College, New York, 1965).

[31] Ulrich Weiss, *Quantum Dissipative Systems* (World Scientific, Singapore, 2011).

[32] A.O. Caldeira and A.J. Leggett, "Path integral approach to quantum Brownian motion," Physica A: Statistical Mechanics and its Applications **121**, 587–616 (1983).

[33] A. Vagov, M. D. Croitoru, M. Glässl, V. M. Axt, and T. Kuhn, "Real-time path integrals for quantum dots: Quantum dissipative dynamics with superohmic environment coupling," Phys. Rev. B **83**, 094303 (2011).

[34] M. Glässl, A. M. Barth, and V. M. Axt, "Proposed robust and high-fidelity preparation of excitons and biexcitons in semiconductor quantum dots making active use of phonons," Phys. Rev. Lett. **110**, 147401 (2013).

[35] A. M. Barth, A. Vagov, and V. M. Axt, "Path-integral description of combined hamiltonian and non-hamiltonian dynamics in quantum dissipative systems," Phys. Rev. B **94**, 125439 (2016).

[36] M. Cosacchi, M. Cygorek, F. Ungar, A. M. Barth, A. Vagov, and V. M. Axt, "Path-integral approach for nonequilibrium multitime correlation functions of open quantum systems coupled to markovian and non-markovian environments," Phys. Rev. B **98**, 125302 (2018).

[37] Nancy Makri and Dmitrii E. Makarov, "Tensor propagator for iterative quantum time evolution of reduced density matrices. i. theory," The Journal of Chemical Physics **102**, 4600–4610 (1995).

[38] Nancy Makri and Dmitrii E. Makarov, "Tensor propagator for iterative quantum time evolution of reduced density matrices. II. numerical methodology," The Journal of Chemical Physics **102**, 4611–4618 (1995).

[39] Ulrich Schollwöck, "The density-matrix renormalization group in the age of matrix product states," Annals of Physics **326**, 96–192 (2011).

[40] Román Orús, "A practical introduction to tensor networks: Matrix product states and projected entangled pair states," Annals of Physics **349**, 117–158 (2014).

[41] Guifré Vidal, "Efficient classical simulation of slightly entangled quantum computations," Phys. Rev. Lett. **91**, 147902 (2003).

[42] Guifré Vidal, "Efficient simulation of one-dimensional quantum many-body systems," Phys. Rev. Lett. **93**, 040502 (2004).

[43] J.I. Cirac, D. Pérez-García, N. Schuch, and F. Verstraete, "Matrix product density operators: Renormalization fixed points and boundary theories," Annals of Physics **378**, 100–149 (2017).

[44] Sandra C. Kuhn and Marten Richter, "Combined tensor network/cluster expansion method using logic gates: Illustrated for (bi)excitons by a single-layer $mos_2$ model system," Phys. Rev. B **99**, 241301 (2019).

[45] Sandra C. Kuhn and Marten Richter, "Tensor network strategies for calculating biexcitons and trions in monolayer two-dimensional materials beyond the ground state," Phys. Rev. B **101**, 075302 (2020).

[46] Maria Schuld and Francesco Petruccione, *Supervised Learning with Quantum Computers* (Springer, Cham, 2018).

[47] Giuseppe Carleo and Matthias Troyer, "Solving the quantum many-body problem with artificial neural networks," Science **355**, 602 (2017).

[48] Dong-Ling Deng, Xiaopeng Li, and S. Das Sarma, "Machine learning topological states," Phys. Rev. B **96**, 195145 (2017).

[49] Dong-Ling Deng, Xiaopeng Li, and S. Das Sarma, "Quantum entanglement in neural network states," Phys. Rev. X **7**, 021021 (2017).

[50] Ivan Glasser, Nicola Pancotti, Moritz August, Ivan D. Rodriguez, and J. Ignacio Cirac, "Neural-network quantum states, string-bond states, and chiral topological states," Phys. Rev. X **8**, 011006 (2018).

[51] Giacomo Torlai and Roger G. Melko, "Latent space purification via neural density operators," Phys. Rev. Lett. **120**, 240503 (2018).

[52] Giacomo Torlai, Guglielmo Mazzola, Juan Carrasquilla, Matthias Troyer, Roger Melko, and Giuseppe Carleo, "Neural-network quantum state tomography," Nature Physics **14**, 447 (2018).

[53] Markus Schmitt and Markus Heyl, "Quantum many-body dynamics in two dimensions with artificial neural networks," Phys. Rev. Lett. **125**, 100503 (2020).

[54] Heiko Burau and Markus Heyl, "Unitary long-time evolution with quantum renormalization groups and artificial neural networks," arXiv:2009.04473 (2020).

[55] Yusuke Nomura, Andrew S. Darmawan, Youhei Yamaji, and Masatoshi Imada, "Restricted boltzmann machine learning for solving strongly correlated quantum systems," Phys. Rev. B **96**, 205152 (2017).

[56] Nobuyuki Yoshioka and Ryusuke Hamazaki, "Constructing neural stationary states for open quantum many-body systems," Phys. Rev. B **99**, 214306 (2019).

[57] Filippo Vicentini, Alberto Biella, Nicolas Regnault, and Cristiano Ciuti, "Variational neural-network ansatz for steady states in open quantum systems," Phys. Rev. Lett. **122**, 250503 (2019).

[58] Michael J. Hartmann and Giuseppe Carleo, "Neural-network approach to dissipative quantum many-body dynamics," Phys. Rev. Lett. **122**, 250502 (2019).

[59] Alexandra Nagy and Vincenzo Savona, "Variational quantum monte carlo method with a neural-network ansatz for open quantum systems," Phys. Rev. Lett. **122**, 250501 (2019).

[60] Adrián A. Budini, "Quantum non-markovian processes break conditional past-future independence," Phys. Rev. Lett. **121**, 240401 (2018).

[61] Philip Taranto, Felix A. Pollock, Simon Milz, Marco Tomamichel, and Kavan Modi, "Quantum markov order," Phys. Rev. Lett. **122**, 140401 (2019).

[62] Felix A. Pollock, César Rodríguez-Rosario, Thomas Frauenheim, Mauro Paternostro, and Kavan Modi, "Operational markov condition for quantum processes," Phys. Rev. Lett. **120**, 040405 (2018).

[63] Felix A. Pollock, César Rodríguez-Rosario, Thomas Frauenheim, Mauro Paternostro, and Kavan Modi, "Non-markovian quantum processes: Complete framework and efficient characterization," Phys. Rev. A **97**, 012127 (2018).

[64] Li Li, Michael J.W. Hall, and Howard M. Wiseman, "Concepts of quantum non-markovianity: A hierarchy," Physics Reports **759**, 1–51 (2018).

[65] C.-F. Li, G.-C. Guo, and J. Piilo, "Non-markovian quantum dynamics: What does it mean?" EPL (Europhysics Letters) **127**, 50001 (2019).

[66] Javier del Pino, Florian A. Y. N. Schröder, Alex W. Chin, Johannes Feist, and Francisco J. Garcia-Vidal, "Tensor network simulation of non-markovian dynamics in organic polaritons," Phys. Rev. Lett. **121**, 227401 (2018).

[67] Sofia Arranz Regidor, Gavin Crowder, Howard Carmichael, and Stephen Hughes, "Modelling quantum light-matter interactions in waveguide-qed with retardation and a time-delayed feedback: matrix product states versus a space-discretized waveguide model," arXiv:2011.12205 (2020).

[68] Emil V. Denning, Matias Bundgaard-Nielsen, and Jesper Mørk, "Optical signatures of electron-phonon decoupling due to strong light-matter interactions," Phys. Rev. B **102**, 235303 (2020).

[69] Oliver Kaestle, Yue Sun, Ying Hu, and Alexander Carmele, "Memory-critical dynamical buildup of phonon-dressed majorana fermions," Phys. Rev. B **102**, 245115 (2020).

[70] Oliver Kaestle, Emil Vosmar Denning, Jesper Mørk, Andreas Knorr, and Alexander Carmele, "Unidirectional quantum transport in optically driven $v$-type quantum dot chains," Phys. Rev. B **103**, 115418 (2021).

[71] Oliver Kaestle, Regina Finsterhoelzl, Andreas Knorr, and Alexander Carmele, "Continuous and time-discrete non-markovian system-reservoir interactions: Dissipative coherent quantum feedback in liouville space," Phys. Rev. Research **3**, 023168 (2021).

[72] Oliver Kaestle and Alexander Carmele, "Sampling asymmetric open quantum systems for artificial neural networks," Phys. Rev. B **103**, 195420 (2021).

[73] Oliver Kaestle and Alexander Carmele, "Efficient bit encoding of neural networks for fock states," Phys. Rev. A **103**, 062409 (2021).

[74] A. J. Leggett, S. Chakravarty, A. T. Dorsey, Matthew P. A. Fisher, Anupam Garg, and W. Zwerger, "Dynamics of the dissipative two-state system," Rev. Mod. Phys. **59**, 1–85 (1987).

[75] A. Strathearn, P. Kirton, D. Kilda, J. Keeling, and B. W. Lovett, "Efficient non-markovian quantum dynamics using time-evolving matrix product operators," Nature Communications **9**, 3322 (2018).

[76] Mathias R. Jørgensen and Felix A. Pollock, "Exploiting the causal tensor network structure of quantum processes to efficiently simulate non-markovian path integrals," Phys. Rev. Lett. **123**, 240602 (2019).

[77] Dominic Gribben, Aidan Strathearn, Jake Iles-Smith, Dainius Kilda, Ahsan Nazir, Brendon W. Lovett, and Peter Kirton, "Exact quantum dynamics in structured environments," Phys. Rev. Research **2**, 013265 (2020).

[78] Giuseppe Carleo, Ignacio Cirac, Kyle Cranmer, Laurent Daudet, Maria Schuld, Naftali Tishby, Leslie Vogt-Maranto, and Lenka Zdeborová, "Machine learning and the physical sciences," Rev. Mod. Phys. **91**, 045002 (2019).

[79] Tom Vieijra, Corneel Casert, Jannes Nys, Wesley De Neve, Jutho Haegeman, Jan Ryckebusch, and Frank Verstraete, "Restricted boltzmann machines for quantum states with non-abelian or anyonic symmetries," Phys. Rev. Lett. **124**, 097201 (2020).

[80] Alexander Carmele and Stephan Reitzenstein, "Non-Markovian features in semiconductor quantum optics: quantifying the role of phonons in experiment and theory," Nanophotonics **8**, 655–683 (2019).

[81] M. O. Scully and M. S. Zubairy, *Quantum Optics* (Cambridge University Press, Cambridge, 1997).

[82] G. S. Agarwal, *Quantum Optics* (Cambridge University Press, Cambridge, 2013).

[83] Ulf Leonhardt, "Quantum-state tomography and discrete wigner function," Phys. Rev. Lett. **74**, 4101–4105 (1995).

[84] Ulf Leonhardt, "Discrete wigner function and quantum-state tomography," Phys. Rev. A **53**, 2998–3013 (1996).

[85] Matthias Christandl and Renato Renner, "Reliable quantum state tomography," Phys. Rev. Lett. **109**, 120403 (2012).

[86] Amro Dodin, Timur Tscherbul, Robert Alicki, Amar Vutha, and Paul Brumer, "Secular versus nonsecular redfield dynamics and fano coherences in incoherent excitation: An experimental proposal," Phys. Rev. A **97**, 013421 (2018).

[87] Ross Manson, Kaushik Roy-Choudhury, and Stephen Hughes, "Polaron master equation theory of pulse-driven phonon-assisted population inversion and single-photon emission from quantum-dot excitons," Phys. Rev. B **93**, 155423 (2016).

[88] Chee Kong Lee, Jeremy Moix, and Jianshu Cao, "Accuracy of second order perturbation theory in the polaron and variational polaron frames," The Journal of Chemical Physics **136**, 204120 (2012).

[89] Dara P S McCutcheon and Ahsan Nazir, "Quantum dot Rabi rotations beyond the weak exciton–phonon coupling regime," New Journal of Physics **12**, 113042 (2010).

[90] Seogjoo Jang, Yuan-Chung Cheng, David R. Reichman, and Joel D. Eaves, "Theory of coherent resonance energy transfer," The Journal of Chemical Physics **129**, 101104 (2008).

[91] Avinash Kolli, Ahsan Nazir, and Alexandra Olaya-Castro, "Electronic excitation dynamics in multichromophoric systems described via a polaron-representation master equation," The Journal of Chemical Physics **135**, 154112 (2011).

[92] Hung-Tzu Chang, Pan-Pan Zhang, and Yuan-Chung Cheng, "Criteria for the accuracy of small polaron quantum master equation in simulating excitation energy transfer dynamics," The Journal of Chemical Physics **139**, 224112 (2013).

[93] Pavel P. Aseev, Pasquale Marra, Peter Stano, Jelena Klinovaja, and Daniel Loss, "Degeneracy lifting of Majorana bound states due to electron-phonon interactions," Phys. Rev. B **99**, 205435 (2019).

[94] G. Goldstein and C. Chamon, "Decay rates for topological memories encoded with Majorana fermions," Phys. Rev. B **84**, 205109 (2011).

[95] A. A. Abrikosov, L. P. Gorkov, and I. E. Dzialoshinskii, *Quantum Field Theoretical Methods in Statistical Physics* (Pergamon, New York, 1965).

[96] G. D. Mahan, *Many-Particle Physics* (Kluwer Academic/Plenum, New York, 2000).

[97] J. Förstner, C. Weber, J. Danckwerts, and A. Knorr, "Phonon-Assisted Damping of Rabi Oscillations in Semiconductor Quantum Dots," Phys. Rev. Lett. **91**, 127401 (2003).

[98] Alexander Carmele, Andreas Knorr, and Frank Milde, "Stabilization of photon collapse and revival dynamics by a non-Markovian phonon bath," New Journal of Physics **15**, 105024 (2013).

[99] Alois Würger, "Strong-coupling theory for the spin-phonon model," Phys. Rev. B **57**, 347–361 (1998).

[100] I. Wilson-Rae and A. Imamoğlu, "Quantum dot cavity-qed in the presence of strong electron-phonon interactions," Phys. Rev. B **65**, 235311 (2002).

[101] Torsten Fließbach, *Quantenmechanik* (Springer, Berlin, Heidelberg, 2018).

[102] A. Strathearn, B. W. Lovett, and P. Kirton, "Efficient real-time path integrals for non-Markovian spin-boson models," New Journal of Physics **19**, 093009 (2017).

[103] A. Pathak, *Elements of Quantum Computation and Quantum Communication* (Taylor & Francis, Boca Raton, 2013).

[104] Nicholas Metropolis, Arianna W. Rosenbluth, Marshall N. Rosenbluth, Augusta H. Teller, and Edward Teller, "Equation of state calculations by fast computing machines," The Journal of Chemical Physics **21**, 1087 (1953).

[105] Christian P. Robert and George Casella, *Monte Carlo Statistical Methods* (Springer, New York, 2004).

[106] N. G. van Kampen, *Stochastic Processes in Physics and Chemistry*, third edition ed. (Elsevier, New York, 2007).

[107] Roger G. Melko, Giuseppe Carleo, Juan Carrasquilla, and J. Ignacio Cirac, "Restricted boltzmann machines in quantum physics," Nature Physics **15**, 887 (2019).

[108] Mohammad H. Amin, Evgeny Andriyash, Jason Rolfe, Bohdan Kulchytskyy, and Roger Melko, "Quantum boltzmann machine," Phys. Rev. X **8**, 021050 (2018).

[109] Chang Yu Hsieh, Qiming Sun, Shengyu Zhang, and Chee Kong Lee, "Unitary-coupled restricted boltzmann machine ansatz for quantum simulations," npj Quantum Information **7**, 19 (2021).

[110] Rongxin Xia and Sabre Kais, "Quantum machine learning for electronic structure calculations," Nature Communications **9**, 4195 (2018).

[111] Daniel Alcalde Puente and Ilya M. Eremin, "Convolutional restricted boltzmann machine aided monte carlo: An application to ising and kitaev models," Phys. Rev. B **102**, 195148 (2020).

[112] Dan Sehayek, Anna Golubeva, Michael S. Albergo, Bohdan Kulchytskyy, Giacomo Torlai, and Roger G. Melko, "Learnability scaling of quantum states: Restricted boltzmann machines," Phys. Rev. B **100**, 195125 (2019).

[113] Jian Cui, J. Ignacio Cirac, and Mari Carmen Bañuls, "Variational matrix product operators for the steady state of dissipative quantum systems," Phys. Rev. Lett. **114**, 220601 (2015).

[114] Hendrik Weimer, "Variational principle for steady states of dissipative quantum many-body systems," Phys. Rev. Lett. **114**, 040402 (2015).

[115] Giuseppe Carleo, Yusuke Nomura, and Masatoshi Imada, "Constructing exact representations of quantum many-body systems with deep neural networks," Nature Communications **9**, 5322 (2018).

[116] W. K. Hastings, "Monte carlo sampling methods using markov chains and their applications," Biometrika **57**, 97 (1970).

[117] Sandro Sorella, "Green function monte carlo with stochastic reconfiguration," Phys. Rev. Lett. **80**, 4558 (1998).

[118] Sandro Sorella, Michele Casula, and Dario Rocca, "Weak binding between two aromatic rings: Feeling the van der waals attraction by quantum monte carlo methods," The Journal of Chemical Physics **127**, 014105 (2007).

[119] Federico Becca and Sandro Sorella, *Quantum Monte Carlo Approaches for Correlated Systems* (Cambridge University Press, Cambridge, 2017).

[120] N. Lindner, G. Refael, and V. Galitski, "Floquet topological insulator in semiconductor quantum wells," Nature Physics **7**, 490 (2011).

[121] Takuya Kitagawa, Matthew A. Broome, Alessandro Fedrizzi, Mark S. Rudner, Erez Berg, Ivan Kassal, Alán Aspuru-Guzik, Eugene Demler, and Andrew G. White, "Observation of topologically protected bound states in photonic quantum walks," Nature Communications **3**, 882 (2012).

[122] Gregor Jotzu, Michael Messer, Rémi Desbuquois, Martin Lebrat, Thomas Uehlinger, Daniel Greif, and Tilman Esslinger, "Experimental realization of the topological haldane model with ultracold fermions," Nature **515**, 237 (2014).

[123] David Aasen, Michael Hell, Ryan V. Mishmash, Andrew Higginbotham, Jeroen Danon, Martin Leijnse, Thomas S. Jespersen, Joshua A. Folk, Charles M. Marcus, Karsten Flensberg, and Jason Alicea, "Milestones toward majorana-based quantum computing," Phys. Rev. X **6**, 031016 (2016).

[124] Ying Hu, Peter Zoller, and Jan Carl Budich, "Dynamical buildup of a quantized hall response from nontopological states," Phys. Rev. Lett. **117**, 126803 (2016).

[125] Jan Carl Budich, Ying Hu, and Peter Zoller, "Helical floquet channels in 1d lattices," Phys. Rev. Lett. **118**, 105302 (2017).

[126] N. Fläschner, D. Vogel, M. Tarnowski, B. S. Rem, D.-S. Lühmann, M. Heyl, J. C. Budich, L. Mathey, and K. Sengstock, "Observation of dynamical vortices after quenches in a system with topology," Nature Physics **14**, 265 (2018).

[127] Matthias Tarnowski, F. Nur Ünal, Nick Fläschner, Benno S. Rem, André Eckardt, Klaus Sengstock, and Christof Weitenberg, "Measuring topology from dynamics by obtaining the chern number from a linking number," Nature Communications **10**, 1728 (2019).

[128] Markus Heyl, "Dynamical quantum phase transitions: a review," Reports on Progress in Physics **81**, 054001 (2018).

[129] Wei Sun, Chang-Rui Yi, Bao-Zong Wang, Wei-Wei Zhang, Barry C. Sanders, Xiao-Tian Xu, Zong-Yao Wang, Joerg Schmiedmayer, Youjin Deng, Xiong-Jun Liu, Shuai Chen, and Jian-Wei Pan, "Uncover topology by quantum quench dynamics," Phys. Rev. Lett. **121**, 250403 (2018).

[130] Bo Song, Chengdong He, Sen Niu, Long Zhang, Zejian Ren, Xiong-Jun Liu, and Gyu-Boong Jo, "Observation of nodal-line semimetal with ultracold fermions in an optical lattice," Nature Physics **15**, 911 (2019).

[131] Lin Zhang, Long Zhang, Sen Niu, and Xiong-Jun Liu, "Dynamical classification of topological quantum phases," Science Bulletin **63**, 1385–1391 (2018).

[132] Zheng Shi, Piet W Brouwer, Karsten Flensberg, Leonid I Glazman, and Felix von Oppen, "Long distance coherence of majorana wires," arXiv:2002.01539 (2020).

[133] James W McIver, Benedikt Schulte, F-U Stein, Toru Matsuyama, Gregor Jotzu, Guido Meier, and Andrea Cavalleri, "Light-induced anomalous hall effect in graphene," Nature Physics **16**, 38–41 (2020).

[134] Andreas Elben, Jinlong Yu, Guanyu Zhu, Mohammad Hafezi, Frank Pollmann, Peter Zoller, and Benoît Vermersch, "Many-body topological invariants from randomized measurements in synthetic quantum matter," Science advances **6**, 3666 (2020).

[135] M. S. Rudner and L. S. Levitov, "Topological transition in a non-hermitian quantum walk," Phys. Rev. Lett. **102**, 065703 (2009).

[136] Sebastian Diehl, Enrique Rico, Mikhail A. Baranov, and Peter Zoller, "Topology by dissipation in atomic quantum wires," Nature Physics **7**, 971 (2011).

[137] Diego Rainis and Daniel Loss, "Majorana qubit decoherence by quasiparticle poisoning," Phys. Rev. B **85**, 174533 (2012).

[138] Manuel J. Schmidt, Diego Rainis, and Daniel Loss, "Decoherence of majorana qubits by noisy gates," Phys. Rev. B **86**, 085414 (2012).

[139] Matteo Ippoliti, Matteo Rizzi, Vittorio Giovannetti, and Leonardo Mazza, "Quantum memories with zero-energy majorana modes and experimental constraints," Phys. Rev. A **93**, 062325 (2016).

[140] L. Mazza, M. Rizzi, M. D. Lukin, and J. I. Cirac, "Robustness of quantum memories based on Majorana zero modes," Phys. Rev. B **88**, 205142 (2013).

[141] C-E Bardyn, M A Baranov, C V Kraus, E Rico, A İmamoğlu, P Zoller, and S Diehl, "Topology by dissipation," New Journal of Physics **15**, 085001 (2013).

[142] Fabio L. Pedrocchi and David P. DiVincenzo, "Majorana braiding with thermal noise," Phys. Rev. Lett. **115**, 120402 (2015).

[143] Ying Hu, Zi Cai, Mikhail A. Baranov, and Peter Zoller, "Majorana fermions in noisy Kitaev wires," Phys. Rev. B **92**, 165118 (2015).

[144] Alexander Carmele, Markus Heyl, Christina Kraus, and Marcello Dalmonte, "Stretched exponential decay of Majorana edge modes in many-body localized Kitaev chains under dissipation," Phys. Rev. B **92**, 195107 (2015).

[145] Jan Carl Budich, Peter Zoller, and Sebastian Diehl, "Dissipative preparation of chern insulators," Phys. Rev. A **91**, 042117 (2015).

[146] Victor V. Albert, Barry Bradlyn, Martin Fraas, and Liang Jiang, "Geometry and response of lindbladians," Phys. Rev. X **6**, 041031 (2016).

[147] Zongping Gong, Sho Higashikawa, and Masahito Ueda, "Zeno hall effect," Phys. Rev. Lett. **118**, 200401 (2017).

[148] Simon Lieu, Max McGinley, and Nigel R. Cooper, "Tenfold way for quadratic lindbladians," Phys. Rev. Lett. **124**, 040401 (2020).

[149] Yuval Oreg, Gil Refael, and Felix von Oppen, "Helical Liquids and Majorana Bound States in Quantum Wires," Phys. Rev. Lett. **105**, 177002 (2010).

[150] Piet W. Brouwer, Mathias Duckheim, Alessandro Romito, and Felix von Oppen, "Probability Distribution of Majorana End-State Energies in Disordered Wires," Phys. Rev. Lett. **107**, 196804 (2011).

[151] V. Mourik, K. Zuo, S. M. Frolov, S. R. Plissard, E. P. A. M. Bakkers, and L. P. Kouwenhoven, "Signatures of majorana fermions in hybrid superconductor-semiconductor nanowire devices," Science **336**, 1003–1007 (2012).

[152] Leonid P. Rokhinson, Xinyu Liu, and Jacek K. Furdyna, "The fractional a.c. Josephson effect in a semiconductor–superconductor nanowire as a signature of Majorana particles," Nature Physics **8**, 795 (2012).

[153] Anindya Das, Yuval Ronen, Yonatan Most, Yuval Oreg, Moty Heiblum, and Hadas Shtrikman, "Zero-bias peaks and splitting in an Al–InAs nanowire topological superconductor as a signature of Majorana fermions," Nature Physics **8**, 887 (2012).

[154] Stevan Nadj-Perge, Ilya K. Drozdov, Jian Li, Hua Chen, Sangjun Jeon, Jungpil Seo, Allan H. MacDonald, B. Andrei Bernevig, and Ali Yazdani, "Observation of Majorana fermions in ferromagnetic atomic chains on a superconductor," Science **346**, 602–607 (2014).

[155] H. O. H. Churchill, V. Fatemi, K. Grove-Rasmussen, M. T. Deng, P. Caroff, H. Q. Xu, and C. M. Marcus, "Superconductor-nanowire devices from tunneling to the multichannel regime: Zero-bias oscillations and magnetoconductance crossover," Phys. Rev. B **87**, 241401 (2013).

[156] A. D. K. Finck, D. J. Van Harlingen, P. K. Mohseni, K. Jung, and X. Li, "Anomalous Modulation of a Zero-Bias Peak in a Hybrid Nanowire-Superconductor Device," Phys. Rev. Lett. **110**, 126406 (2013).

[157] Valla Fatemi, Sanfeng Wu, Yuan Cao, Landry Bretheau, Quinn D. Gibson, Kenji Watanabe, Takashi Taniguchi, Robert J. Cava, and Pablo Jarillo-Herrero, "Electrically tunable low-density superconductivity in a monolayer topological insulator," Science **362**, 926–929 (2018).

[158] Antonio Fornieri, Alexander M. Whiticar, F. Setiawan, Elías Portolés, Asbjørn C. C. Drachmann, Anna Keselman, Sergei Gronin, Candice Thomas, Tian Wang, Ray Kallaher, Geoffrey C. Gardner, Erez Berg, Michael J. Manfra, Ady Stern, Charles M. Marcus, and Fabrizio Nichele, "Evidence of topological superconductivity in planar josephson junctions," Nature **569**, 89–92 (2019).

[159] Hechen Ren, Falko Pientka, Sean Hart, Andrew T. Pierce, Michael Kosowsky, Lukas Lunczer, Raimund Schlereth, Benedikt Scharf, Ewelina M. Hankiewicz, Laurens W. Molenkamp, Bertrand I. Halperin, and Amir Yacoby, "Topological superconductivity in a phase-controlled josephson junction," Nature **569**, 93–98 (2019).

[160] A Yu Kitaev, "Unpaired Majorana fermions in quantum wires," Physics-Uspekhi **44**, 131–136 (2001).

[161] Ari M. Turner, Frank Pollmann, and Erez Berg, "Topological phases of one-dimensional fermions: An entanglement point of view," Phys. Rev. B **83**, 075102 (2011).

[162] Lukasz Fidkowski and Alexei Kitaev, "Effects of interactions on the topological classification of free fermion systems," Phys. Rev. B **81**, 134509 (2010).

[163] Jason Alicea, Yuval Oreg, Gil Refael, Felix von Oppen, and Matthew P. A. Fisher, "Non-Abelian statistics and topological quantum information processing in 1D wire networks," Nature Physics **7**, 412–417 (2011).

[164] Roman M. Lutchyn, Tudor D. Stanescu, and S. Das Sarma, "Search for Majorana Fermions in Multiband Semiconducting Nanowires," Phys. Rev. Lett. **106**, 127001 (2011).

[165] Zhida Song, Zhong Fang, and Chen Fang, "$(d-2)$-Dimensional Edge States of Rotation Symmetry Protected Topological States," Phys. Rev. Lett. **119**, 246402 (2017).

[166] Xie Chen, Zheng-Cheng Gu, Zheng-Xin Liu, and Xiao-Gang Wen, "Symmetry-Protected Topological Orders in Interacting Bosonic Systems," Science **338**, 1604–1606 (2012).

[167] Yi-Zhuang You and Cenke Xu, "Symmetry-protected topological states of interacting fermions and bosons," Phys. Rev. B **90**, 245120 (2014).

[168] T. Senthil, "Symmetry-protected topological phases of quantum matter," Annual Review of Condensed Matter Physics **6**, 299–324 (2015).

[169] Chetan Nayak, Steven H. Simon, Ady Stern, Michael Freedman, and Sankar Das Sarma, "Non-Abelian anyons and topological quantum computation," Rev. Mod. Phys. **80**, 1083–1159 (2008).

[170] A.Yu. Kitaev, "Fault-tolerant quantum computation by anyons," Annals of Physics **303**, 2–30 (2003).

[171] Frank Wilczek, "Majorana returns," Nature Physics **5**, 614 (2009).

[172] Ady Stern, "Non-Abelian states of matter," Nature **464**, 187 (2010).

[173] Sankar Das Sarma, Michael Freedman, and Chetan Nayak, "Majorana zero modes and topological quantum computation," npj Quantum Information **1**, 15001 (2015).

[174] C.W.J. Beenakker, "Search for Majorana Fermions in Superconductors," Annual Review of Condensed Matter Physics **4**, 113–136 (2013).

[175] Masatoshi Sato and Satoshi Fujimoto, "Topological phases of noncentrosymmetric superconductors: Edge states, Majorana fermions, and non-Abelian statistics," Phys. Rev. B **79**, 094504 (2009).

[176] Masatoshi Sato and Yoichi Ando, "Topological superconductors: a review," Reports on Progress in Physics **80**, 076501 (2017).

[177] Martin Leijnse and Karsten Flensberg, "Introduction to topological superconductivity and Majorana fermions," Semiconductor Science and Technology **27**, 124003 (2012).

[178] Christina V. Kraus, Marcello Dalmonte, Mikhail A. Baranov, Andreas M. Läuchli, and P. Zoller, "Majorana Edge States in Atomic Wires Coupled by Pair Hopping," Phys. Rev. Lett. **111**, 173004 (2013).

[179] Jason Alicea, "New directions in the pursuit of Majorana fermions in solid state systems," Reports on Progress in Physics **75**, 076501 (2012).

[180] Liang Fu and C. L. Kane, "Superconducting Proximity Effect and Majorana Fermions at the Surface of a Topological Insulator," Phys. Rev. Lett. **100**, 096407 (2008).

[181] Jay D. Sau, Roman M. Lutchyn, Sumanta Tewari, and S. Das Sarma, "Generic New Platform for Topological Quantum Computation Using Semiconductor Heterostructures," Phys. Rev. Lett. **104**, 040502 (2010).

[182] Roman M. Lutchyn, Jay D. Sau, and S. Das Sarma, "Majorana Fermions and a Topological Phase Transition in Semiconductor-Superconductor Heterostructures," Phys. Rev. Lett. **105**, 077001 (2010).

[183] Liang Jiang, Takuya Kitagawa, Jason Alicea, A. R. Akhmerov, David Pekker, Gil Refael, J. Ignacio Cirac, Eugene Demler, Mikhail D. Lukin, and Peter Zoller, "Majorana Fermions in Equilibrium and in Driven Cold-Atom Quantum Wires," Phys. Rev. Lett. **106**, 220402 (2011).

[184] C V Kraus, S Diehl, P Zoller, and M A Baranov, "Preparing and probing atomic Majorana fermions and topological order in optical lattices," New Journal of Physics **14**, 113036 (2012).

[185] A. Bühler, N. Lang, C.V. Kraus, G. Möller, S.D. Huber, and H.P. Büchler, "Majorana modes and p-wave superfluids for fermionic atoms in optical lattices," Nature Communications **5**, 4504 (2014).

[186] Matthieu C. Dartiailh, Takis Kontos, Benoit Douçot, and Audrey Cottet, "Direct Cavity Detection of Majorana Pairs," Phys. Rev. Lett. **118**, 126803 (2017).

[187] Junying Shen, Jian Lyu, Jason Z. Gao, Ying-Ming Xie, Chui-Zhen Chen, Changwoo Cho, Omargeldi Atanov, Zhijie Chen, Kai Liu, Yajian J. Hu, King Yau Yip, Swee K. Goh, Qing Lin He, Lei Pan, Kang L. Wang, Kam Tuen Law, and Rolf Lortz, "Spectroscopic fingerprint of chiral Majorana modes at the edge of a quantum anomalous Hall insulator/superconductor heterostructure," Proceedings of the National Academy of Sciences **117**, 238–242 (2020).

[188] Zhenyu Wang, Jorge Olivares Rodriguez, Lin Jiao, Sean Howard, Martin Graham, G. D. Gu, Taylor L. Hughes, Dirk K. Morr, and Vidya Madhavan, "Evidence for dispersing 1D Majorana channels in an iron-based superconductor," Science **367**, 104–108 (2020).

[189] Naoyuki Shibata and Hosho Katsura, "Dissipative spin chain as a non-Hermitian Kitaev ladder," Phys. Rev. B **99**, 174303 (2019).

[190] Ying Hu and Mikhail A. Baranov, "Effects of gapless bosonic fluctuations on Majorana fermions in an atomic wire coupled to a molecular reservoir," Phys. Rev. A **92**, 053615 (2015).

[191] C.-E. Bardyn, M. A. Baranov, E. Rico, A. İmamoğlu, P. Zoller, and S. Diehl, "Majorana Modes in Driven-Dissipative Atomic Superfluids with a Zero Chern Number," Phys. Rev. Lett. **109**, 130402 (2012).

[192] C.-E. Bardyn and A. İmamoğlu, "Majorana-like Modes of Light in a One-Dimensional Array of Nonlinear Cavities," Phys. Rev. Lett. **109**, 253606 (2012).

[193] Chun-Xiao Liu, Jay D. Sau, and S. Das Sarma, "Role of dissipation in realistic Majorana nanowires," Phys. Rev. B **95**, 054502 (2017).

[194] Yizhen Huang, Alejandro M. Lobos, and Zi Cai, "Dissipative Majorana Quantum Wires," Science **21**, 241–248 (2019).

[195] Bo Song, Long Zhang, Chengdong He, Ting Fung Jeffrey Poon, Elnur Hajiyev, Shanchao Zhang, Xiong-Jun Liu, and Gyu-Boong Jo, "Observation of symmetry-protected topological band with ultracold fermions," Science Advances **4**, 4748 (2018).

[196] Christina Knapp, Torsten Karzig, Roman M. Lutchyn, and Chetan Nayak, "Dephasing of Majorana-based qubits," Phys. Rev. B **97**, 125404 (2018).

[197] Jan Carl Budich, Stefan Walter, and Björn Trauzettel, "Failure of protection of Majorana based qubits against decoherence," Phys. Rev. B **85**, 121405 (2012).

[198] F. Grusdt, N. Y. Yao, D. Abanin, M. Fleischhauer, and E. Demler, "Interferometric measurements of many-body topological invariants using mobile impurities," Nature Communications **7**, 11994 (2016).

[199] A. Camacho-Guardian, N. Goldman, P. Massignan, and G. M. Bruun, "Dropping an impurity into a chern insulator: A polaron view on topological matter," Phys. Rev. B **99**, 081105 (2019).

[200] Gian Luca Giorgi, Stefano Longhi, Albert Cabot, and Roberta Zambrini, "Quantum probing topological phase transitions by non-markovianity," Annalen der Physik **531**, 1900307 (2019).

[201] A. Ricottone, M. S. Rudner, and W. A. Coish, "Topological transition of a non-markovian dissipative quantum walk," arXiv:2003.00350 (2020).

[202] Mackillo Kira and Stephan W Koch, *Semiconductor quantum optics* (Cambridge University Press, Cambridge, 2011).

[203] Volkhard May and Oliver Kühn, *Charge and energy transfer dynamics in molecular systems* (John Wiley & Sons, Weinheim, 2008).

[204] Michael A Stroscio and Mitra Dutta, *Phonons in nanostructures* (Cambridge University Press, Cambridge, 2001).

[205] Birgit Krummheuer, Vollrath Martin Axt, and Tilmann Kuhn, "Theory of pure dephasing and the resulting absorption line shape in semiconductor quantum dots," Phys. Rev. B **65**, 195313 (2002).

[206] Nikolett Német, Scott Parkins, Andreas Knorr, and Alexander Carmele, "Stabilizing quantum coherence against pure dephasing in the presence of time-delayed coherent feedback at finite temperature," Phys. Rev. A **99**, 053809 (2019).

[207] D. E. Reiter, T. Kuhn, and V. M. Axt, "Distinctive characteristics of carrier-phonon interactions in optically driven semiconductor quantum dots," Advances in Physics: X **4**, 1655478 (2019).

[208] Max Strauß, Alexander Carmele, Julian Schleibner, Marcel Hohn, Christian Schneider, Sven Höfling, Janik Wolters, and Stephan Reitzenstein, "Wigner time delay induced by a single quantum dot," Phys. Rev. Lett. **122**, 107401 (2019).

[209] Emil V. Denning, Jake Iles-Smith, and Jesper Mork, "Quantum light-matter interaction and controlled phonon scattering in a photonic fano cavity," Phys. Rev. B **100**, 214306 (2019).

[210] Woochul Kim, "Strategies for engineering phonon transport in thermoelectrics," J. Mater. Chem. C **3**, 10336–10348 (2015).

[211] Shiyun Xiong, Kimmo Sääskilahti, Yuriy A. Kosevich, Haoxue Han, Davide Donadio, and Sebastian Volz, "Blocking phonon transport by structural resonances in alloy-based nanophononic metamaterials leads to ultralow thermal conductivity," Phys. Rev. Lett. **117**, 025503 (2016).

[212] Alexander A. Balandin, "Nanophononics: Phonon engineering in nanostructures and nanodevices," Journal of Nanoscience and Nanotechnology **5**, 1015–1022 (2005).

[213] Alexander A. Balandin, Evghenii P. Pokatilov, and D. L. Nika, "Phonon engineering in hetero- and nanostructures," Journal of Nanoelectronics and Optoelectronics **2**, 140–170 (2007).

[214] E. M. Stoudenmire, Jason Alicea, Oleg A. Starykh, and Matthew P.A. Fisher, "Interaction effects in topological superconducting wires supporting Majorana fermions," Phys. Rev. B **84**, 014503 (2011).

[215] Sylvain Nascimbène, "Realizing one-dimensional topological superfluids with ultracold atomic gases," Journal of Physics B: Atomic, Molecular and Optical Physics **46**, 134005 (2013).

[216] Cássio Sozinho Amorim, Kazuto Ebihara, Ai Yamakage, Yukio Tanaka, and Masatoshi Sato, "Majorana braiding dynamics in nanowires," Phys. Rev. B **91**, 174305 (2015).

[217] Per-Lennart Ardelt, Lukas Hanschke, Kevin A. Fischer, Kai Müller, Alexander Kleinkauf, Manuel Koller, Alexander Bechtold, Tobias Simmet, Jakob Wierzbowski, Hubert Riedl, Gerhard Abstreiter, and Jonathan J. Finley, "Dissipative preparation of the exciton and biexciton in self-assembled quantum dots on picosecond time scales," Phys. Rev. B **90**, 241404 (2014).

[218] A. M. Barth, S. Lüker, A. Vagov, D. E. Reiter, T. Kuhn, and V. M. Axt, "Fast and selective phonon-assisted state preparation of a quantum dot by adiabatic undressing," Phys. Rev. B **94**, 045306 (2016).

[219] Yanwen Wu, I. M. Piper, M. Ediger, P. Brereton, E. R. Schmidgall, P. R. Eastham, M. Hugues, M. Hopkinson, and R. T. Phillips, "Population inversion in a single ingaas quantum dot using the method of adiabatic rapid passage," Phys. Rev. Lett. **106**, 067401 (2011).

[220] Emmanuel Paspalakis, Sofia Evangelou, and Andreas F. Terzis, "Control of excitonic population inversion in a coupled semiconductor quantum dot–metal nanoparticle system," Phys. Rev. B **87**, 235302 (2013).

[221] C. Roy and S. Hughes, "Influence of electron–acoustic-phonon scattering on intensity power broadening in a coherently driven quantum-dot–cavity system," Phys. Rev. X **1**, 021009 (2011).

[222] S Hughes and H J Carmichael, "Phonon-mediated population inversion in a semiconductor quantum-dot cavity system," New Journal of Physics **15**, 053039 (2013).

[223] A. Metelmann and A. A. Clerk, "Nonreciprocal photon transmission and amplification via reservoir engineering," Phys. Rev. X **5**, 021025 (2015).

[224] J. H. Quilter, A. J. Brash, F. Liu, M. Glässl, A. M. Barth, V. M. Axt, A. J. Ramsay, M. S. Skolnick, and A. M. Fox, "Phonon-assisted population inversion of a single InGaAs/GaAs quantum dot by pulsed laser excitation," Phys. Rev. Lett. **114**, 137401 (2015).

[225] S. E. Thomas, M. Billard, N. Coste, S. C. Wein, Priya, H. Ollivier, O. Krebs, L. Tazaïrt, A. Harouri, A. Lemaitre, I. Sagnes, C. Anton, L. Lanco, N. Somaschi, J. C. Loredo, and P. Senellart, "Efficient source of indistinguishable single-photons based on phonon-assisted excitation," arXiv:2007.04330 (2020).

[226] J. Houmark, T. R. Nielsen, J. Mørk, and A.-P. Jauho, "Comparison of electromagnetically induced transparency schemes in semiconductor quantum dot structures: Impact of many-body interactions," Phys. Rev. B **79**, 115420 (2009).

[227] D. Barettin, J. Houmark, B. Lassen, M. Willatzen, T. R. Nielsen, J. Mørk, and A.-P. Jauho, "Optical properties and optimization of electromagnetically induced transparency in strained inas/gaas quantum dot structures," Phys. Rev. B **80**, 235304 (2009).

[228] Q. Q. Wang, A. Muller, M. T. Cheng, H. J. Zhou, P. Bianucci, and C. K. Shih, "Coherent control of a v-type three-level system in a single quantum dot," Phys. Rev. Lett. **95**, 187404 (2005).

[229] C.W.J. Beenakker and H. van Houten, "Quantum transport in semiconductor nanostructures," in *Semiconductor Heterostructures and Nanostructures*, Solid State Physics, Vol. 44, edited by Henry Ehrenreich and David Turnbull (Academic Press, San Diego, 1991).

[230] S. A. Crooker, J. A. Hollingsworth, S. Tretiak, and V. I. Klimov, "Spectrally resolved dynamics of energy transfer in quantum-dot assemblies: Towards engineered energy flows in artificial materials," Phys. Rev. Lett. **89**, 186802 (2002).

[231] S. Machida, M. Matsuo, K. Fujiwara, J. R. Folkenberg, and J. M. Hvam, "Dynamics of unidirectional phonon-assisted transport of photoexcited carriers in step-graded $\mathrm{in}_x(\mathrm{al}_{0.17}\mathrm{ga}_{0.83})_{1-x}\mathrm{As}/\mathrm{al}_{0.17}\mathrm{ga}_{0.83}\mathrm{As}$ multiple quantum wells," Phys. Rev. B **67**, 205322 (2003).

[232] S. Sangu, K. Kobayashi, A. Shojiguchi, T. Kawazoe, and M. Ohtsu, "Excitation energy transfer and population dynamics in a quantum dot system induced by optical near-field interaction," Journal of Applied Physics **93**, 2937–2945 (2003).

[233] Siyuan Lu and Anupam Madhukar, "Nonradiative resonant excitation transfer from nanocrystal quantum dots to adjacent quantum channels," Nano Letters **7**, 3443–3451 (2007).

[234] R. E. Chandler, A. J. Houtepen, J. Nelson, and D. Vanmaekelbergh, "Electron transport in quantum dot solids: Monte carlo simulations of the effects of shell filling, coulomb repulsions, and site disorder," Phys. Rev. B **75**, 085325 (2007).

[235] Rita C. Iotti, Emanuele Ciancio, and Fausto Rossi, "Quantum transport theory for semiconductor nanostructures: A density-matrix formulation," Phys. Rev. B **72**, 125347 (2005).

[236] Marten Richter, Kwang Jun Ahn, Andreas Knorr, Andrei Schliwa, Dieter Bimberg, Mohamed El-Amine Madjet, and Thomas Renger, "Theory of excitation transfer in coupled nanostructures – from quantum dots to light harvesting complexes," physica status solidi (b) **243**, 2302–2310 (2006).

[237] Lorenzo Cupellini, Stefano Caprasecca, Ciro A. Guido, Frank Müh, Thomas Renger, and Benedetta Mennucci, "Coupling to charge transfer states is the key to modulate the optical bands for efficient light harvesting in purple bacteria," The Journal of Physical Chemistry Letters **9**, 6892–6899 (2018).

[238] Rémi Métivier, Fabian Nolde, Klaus Müllen, and Thomas Basché, "Electronic excitation energy transfer between two single molecules embedded in a polymer host," Phys. Rev. Lett. **98**, 047802 (2007).

[239] David M. Leitner and Hari Datt Pandey, "Quantum bottlenecks and unidirectional energy flow in molecules," Annalen der Physik **527**, 601–609 (2015).

[240] Xiao Zheng, JunYan Luo, Jinshuang Jin, and YiJing Yan, "Complex non-markovian effect on time-dependent quantum transport," The Journal of Chemical Physics **130**, 124508 (2009).

[241] Patrick Rebentrost, Masoud Mohseni, Ivan Kassal, Seth Lloyd, and Alán Aspuru-Guzik, "Environment-assisted quantum transport," New Journal of Physics **11**, 033003 (2009).

[242] W. Z. Shangguan, T. C. Au Yeung, Y. B. Yu, and C. H. Kam, "Quantum transport in a one-dimensional quantum dot array," Phys. Rev. B **63**, 235323 (2001).

[243] Matthias-René Dachner, Ermin Malic, Marten Richter, Alexander Carmele, Julia Kabuss, Alexander Wilms, Jeong-Eun Kim, Gregor Hartmann, Janik Wolters, Uwe Bandelow, and Andreas Knorr, "Theory of carrier and photon dynamics in quantum dot light emitters," physica status solidi (b) **247**, 809–828 (2010).

[244] R V N Melnik and M Willatzen, "Bandstructures of conical quantum dots with wetting layers," Nanotechnology **15**, 1–8 (2003).

[245] K. J. Ahn, J. Förstner, and A. Knorr, "Resonance fluorescence of semiconductor quantum dots: Signatures of the electron-phonon interaction," Phys. Rev. B **71**, 153309 (2005).

[246] Ermin Malic and Andreas Knorr, *Graphene and carbon nanotubes: Ultrafast optics and relaxation dynamics* (Wiley-VCH, Weinheim, 2013).

[247] Weng W. Chow and Frank Jahnke, "On the physics of semiconductor quantum dots for applications in lasers and quantum optics," Progress in Quantum Electronics **37**, 109–184 (2013).

[248] D E Reiter, T Kuhn, M Glässl, and V M Axt, "The role of phonons for exciton and biexciton generation in an optically driven quantum dot," Journal of Physics: Condensed Matter **26**, 423203 (2014).

[249] J. Schilp, T. Kuhn, and G. Mahler, "Electron-phonon quantum kinetics in pulse-excited semiconductors: Memory and renormalization effects," Phys. Rev. B **50**, 5435–5447 (1994).

[250] Fausto Rossi and Tilmann Kuhn, "Theory of ultrafast phenomena in photoexcited semiconductors," Rev. Mod. Phys. **74**, 895–950 (2002).

[251] Jens Förstner, Carsten Weber, Juliane Danckwerts, and Andreas Knorr, "Phonon-induced damping of rabi oscillations in semiconductor quantum dots," physica status solidi (b) **238**, 419–422 (2003).

[252] D. L. Dexter, "A theory of sensitized luminescence in solids," The Journal of Chemical Physics **21**, 836–850 (1953).

[253] Judith F. Specht, Andreas Knorr, and Marten Richter, "Two-dimensional spectroscopy: An approach to distinguish förster and dexter transfer processes in coupled nanostructures," Physical Review B **91**, 155313 (2015).

[254] L. Brusaferri, S. Sanguinetti, E. Grilli, M. Guzzi, A. Bignazzi, F. Bogani, L. Carraresi, M. Colocci, A. Bosacchi, P. Frigeri, and S. Franchi, "Thermally activated carrier transfer and luminescence line shape in self-organized InAs quantum dots," Applied Physics Letters **69**, 3354–3356 (1996).

[255] S. Sanguinetti, M. Padovani, M. Gurioli, E. Grilli, M. Guzzi, A. Vinattieri, M. Colocci, P. Frigeri, and S. Franchi, "Carrier transfer and photoluminescence quenching in InAs/GaAs multilayer quantum dots," Applied Physics Letters **77**, 1307–1309 (2000).

[256] G. G. Tarasov, Yu. I. Mazur, Z. Ya. Zhuchenko, A. Maaßdorf, D. Nickel, J. W. Tomm, H. Kissel, C. Walther, and W. T. Masselink, "Carrier transfer in self-assembled coupled InAs/GaAs quantum dots," Journal of Applied Physics **88**, 7162–7170 (2000).

[257] Yu. I. Mazur, X. Wang, Z. M. Wang, G. J. Salamo, M. Xiao, and H. Kissel, "Photoluminescence study of carrier transfer among vertically aligned double-stacked InAs/GaAs quantum dot layers," Applied Physics Letters **81**, 2469–2471 (2002).

[258] Yu. I. Mazur, Zh. M. Wang, G. G. Tarasov, Min Xiao, G. J. Salamo, J. W. Tomm, V. Talalaev, and H. Kissel, "Interdot carrier transfer in asymmetric bilayer inas/gaas quantum dot structures," Applied Physics Letters **86**, 063102 (2005).

[259] Yu. I. Mazur, V. G. Dorogan, E. Marega, G. G. Tarasov, D. F. Cesar, V. Lopez-Richard, G. E. Marques, and G. J. Salamo, "Mechanisms of interdot coupling in (in,ga)as/GaAs quantum dot arrays," Applied Physics Letters **94**, 123112 (2009).

[260] J. Bhattacharyya, S. Zybell, S. Winnerl, M. Helm, M. Hopkinson, L. R. Wilson, and H. Schneider, "In-plane interdot carrier transfer in InAs/GaAs quantum dots," Applied Physics Letters **100**, 152101 (2012).

[261] Ignacio Piquero-Zulaica, Jorge Lobo-Checa, Ali Sadeghi, Zakaria M. Abd El-Fattah, Chikahiko Mitsui, Toshihiro Okamoto, Rémy Pawlak, Tobias Meier, Andrés Arnau, J. Enrique Ortega, Jun Takeya, Stefan Goedecker, Ernst Meyer, and Shigeki Kawai, "Precise engineering of quantum dot array coupling through their barrier widths," Nature Communications **8**, 787 (2017).

[262] Elżbieta Zipper, Marcin Kurpas, and Maciej M Maśka, "Wave function engineering in quantum dot–ring nanostructures," New Journal of Physics **14**, 093029 (2012).

[263] Jacob Hastrup, Lorenzo Leandro, and Nika Akopian, "All-optical charging and charge transport in quantum dots," Scientific Reports **10**, 14911 (2020).

[264] Th. Förster, "Zwischenmolekulare energiewanderung und fluoreszenz," Ann. Phys. **437**, 55–75 (1948).

[265] Aaron R. Clapp, Igor L. Medintz, and Hedi Mattoussi, "Förster resonance energy transfer investigations using quantum-dot fluorophores," ChemPhysChem **7**, 47–57 (2006).

[266] Emil Rozbicki and Paweł Machnikowski, "Quantum kinetic theory of phonon-assisted excitation transfer in quantum dot molecules," Phys. Rev. Lett. **100**, 027401 (2008).

[267] Paweł Machnikowski and Emil Rozbicki, "Phonon-assisted excitation transfer in quantum dot molecules: from quantum kinetics to transfer rates," physica status solidi (b) **246**, 320–324 (2009).

[268] Shaul Mukamel, *Principles of nonlinear optical spectroscopy* (Oxford University Press, New York, 1995).

[269] J. Förstner, K.J. Ahn, J. Danckwerts, M. Schaarschmidt, I. Waldmüller, C. Weber, and A. Knorr, "Light propagation- and many-particle-induced non-lorentzian lineshapes in semiconductor nanooptics," physica status solidi (b) **234**, 155–165 (2002).

[270] Tadashi Kawazoe, Kiyoshi Kobayashi, Jungshik Lim, Yoshihito Narita, and Motoichi Ohtsu, "Direct observation of optically forbidden energy transfer between CuCl quantum cubes via near-field optical spectroscopy," Phys. Rev. Lett. **88**, 067404 (2002).

[271] K. Kobayashi, S. Sangu, A. Shojiguchi, T. Kawazoe, K. Kitahara, and M. Ohtsu, "Excitation dynamics in a three-quantum dot system driven by optical near-field interaction: towards a nanometric photonic device," Journal of Microscopy **210**, 247–251 (2003).

[272] Suguru Sangu, Kiyoshi Kobayashi, Akira Shojiguchi, and Motoichi Ohtsu, "Logic and functional operations using a near-field optically coupled quantum-dot system," Physical Review B **69**, 115334 (2004).

[273] Arata Sato, Fujio Minami, and Kiyoshi Kobayashi, "Spin and excitation energy transfer in a quantum-dot pair system through optical near-field interactions," Physica E: Low-dimensional Systems and Nanostructures **40**, 313–316 (2007).

[274] K. Nishibayashi, T. Kawazoe, M. Ohtsu, K. Akahane, and N. Yamamoto, "Observation of interdot energy transfer between InAs quantum dots," Applied Physics Letters **93**, 042101 (2008).

[275] Luqi Yuan, Shanshan Xu, and Shanhui Fan, "Achieving nonreciprocal unidirectional single-photon quantum transport using the photonic aharonov-bohm effect," Opt. Lett. **40**, 5140–5143 (2015).

[276] Qian Lin and Shanhui Fan, "Light guiding by effective gauge field for photons," Phys. Rev. X **4**, 031031 (2014).

[277] V. Peano, C. Brendel, M. Schmidt, and F. Marquardt, "Topological phases of sound and light," Phys. Rev. X **5**, 031011 (2015).

[278] Vittorio Peano, Martin Houde, Florian Marquardt, and Aashish A. Clerk, "Topological quantum fluctuations and traveling wave amplifiers," Phys. Rev. X **6**, 041026 (2016).

[279] Miguel A. Bandres, Mikael C. Rechtsman, and Mordechai Segev, "Topological photonic quasicrystals: Fractal topological spectrum and protected transport," Phys. Rev. X **6**, 011016 (2016).

[280] A. V. Poshakinskiy and A. N. Poddubny, "Optomechanical kerker effect," Phys. Rev. X **9**, 011008 (2019).

[281] Sahand Mahmoodian, Giuseppe Calajó, Darrick E. Chang, Klemens Hammerer, and Anders S. Sørensen, "Dynamics of many-body photon bound states in chiral waveguide qed," Phys. Rev. X **10**, 031011 (2020).

[282] Hannes Pichler and Peter Zoller, "Photonic circuits with time delays and quantum feedback," Phys. Rev. Lett. **116**, 093601 (2016).

[283] Pierre-Olivier Guimond, Hannes Pichler, Arno Rauschenbeutel, and Peter Zoller, "Chiral quantum optics with v-level atoms and coherent quantum feedback," Phys. Rev. A **94**, 033829 (2016).

[284] P-O Guimond, M Pletyukhov, H Pichler, and P Zoller, "Delayed coherent quantum feedback from a scattering theory and a matrix product state perspective," Quantum Science and Technology **2**, 044012 (2017).

[285] Aidan Strathearn, *Modelling Non-Markovian Quantum Systems Using Tensor Networks* (Springer, Cham, 2020).

[286] A. Kshetrimayum, M. Rizzi, J. Eisert, and R. Orús, "Tensor network annealing algorithm for two-dimensional thermal states," Phys. Rev. Lett. **122**, 070502 (2019).

[287] D. Tamascelli, A. Smirne, J. Lim, S. F. Huelga, and M. B. Plenio, "Efficient simulation of finite-temperature open quantum systems," Phys. Rev. Lett. **123**, 090402 (2019).

[288] Regina Finsterhölzl, Manuel Katzer, Andreas Knorr, and Alexander Carmele, "Using matrix-product states for open quantum many-body systems: Efficient algorithms for markovian and non-markovian time-evolution," Entropy **22**, 984 (2020).

[289] Regina Finsterhölzl, Manuel Katzer, and Alexander Carmele, "Nonequilibrium non-markovian steady states in open quantum many-body systems: Persistent oscillations in heisenberg quantum spin chains," Phys. Rev. B **102**, 174309 (2020).

[290] Giuseppe Calajó, Yao-Lung L. Fang, Harold U. Baranger, and Francesco Ciccarello, "Exciting a bound state in the continuum through multiphoton scattering plus delayed quantum feedback," Phys. Rev. Lett. **122**, 073601 (2019).

[291] Gavin Crowder, Howard Carmichael, and Stephen Hughes, "Quantum trajectory theory of few-photon cavity-qed systems with a time-delayed coherent feedback," Phys. Rev. A **101**, 023807 (2020).

[292] Zhihai Wang, Tuomas Jaako, Peter Kirton, and Peter Rabl, "Supercorrelated radiance in nonlinear photonic waveguides," Phys. Rev. Lett. **124**, 213601 (2020).

[293] Alexander Carmele, Nikolett Nemet, Victor Canela, and Scott Parkins, "Pronounced non-markovian features in multiply excited, multiple emitter waveguide qed: Retardation induced anomalous population trapping," Phys. Rev. Research **2**, 013238 (2020).

[294] U. Dorner and P. Zoller, "Laser-driven atoms in half-cavities," Phys. Rev. A **66**, 023816 (2002).

[295] Julia Kabuss, Dmitry O. Krimer, Stefan Rotter, Kai Stannigel, Andreas Knorr, and Alexander Carmele, "Analytical study of quantum-feedback-enhanced rabi oscillations," Phys. Rev. A **92**, 053801 (2015).

[296] Alexander Carmele, Scott Parkins, and Andreas Knorr, "Quantum-optical realization of an ornstein-uhlenbeck-type process via simultaneous action of white noise and feedback," Phys. Rev. A **102**, 033712 (2020).

[297] Arne L. Grimsmo, "Time-delayed quantum feedback control," Phys. Rev. Lett. **115**, 060402 (2015).

[298] M. A. Wilson, P. Bushev, J. Eschner, F. Schmidt-Kaler, C. Becher, R. Blatt, and U. Dorner, "Vacuum-field level shifts in a single trapped ion mediated by a single distant mirror," Phys. Rev. Lett. **91**, 213602 (2003).

[299] G. Hétet, L. Slodička, M. Hennrich, and R. Blatt, "Single atom as a mirror of an optical cavity," Phys. Rev. Lett. **107**, 133002 (2011).

[300] I.-C. Hoi, A. F. Kockum, L. Tornberg, A. Pourkabirian, G. Johansson, P. Delsing, and C. M. Wilson, "Probing the quantum vacuum with an artificial atom in front of a mirror," Nature Physics **11**, 1045–1049 (2015).

[301] Anatoly A. Svidzinsky, Jonathan S. Ben-Benjamin, Stephen A. Fulling, and Don N. Page, "Excitation of an atom by a uniformly accelerated mirror through virtual transitions," Phys. Rev. Lett. **121**, 071301 (2018).

[302] Kisa Barkemeyer, Regina Finsterhölzl, Andreas Knorr, and Alexander Carmele, "Revisiting quantum feedback control: Disentangling the feedback-induced phase from the corresponding amplitude," Advanced Quantum Technologies **3**, 1900078 (2019).

[303] Francois Dubin, Daniel Rotter, Manas Mukherjee, Carlos Russo, Jürgen Eschner, and Rainer Blatt, "Photon correlation versus interference of single-atom fluorescence in a half-cavity," Phys. Rev. Lett. **98**, 183003 (2007).

[304] A.W. Glaetzle, K. Hammerer, A.J. Daley, R. Blatt, and P. Zoller, "A single trapped atom in front of an oscillating mirror," Optics Communications **283**, 758–765 (2010).

[305] Alexander Carmele, Julia Kabuss, Franz Schulze, Stephan Reitzenstein, and Andreas Knorr, "Single photon delayed feedback: A way to stabilize intrinsic quantum cavity electrodynamics," Phys. Rev. Lett. **110**, 013601 (2013).

[306] Hannes Pichler, Soonwon Choi, Peter Zoller, and Mikhail D. Lukin, "Universal photonic quantum computation via time-delayed feedback," Proceedings of the National Academy of Sciences **114**, 11362–11367 (2017).

[307] Tomaž Prosen, "Open $xxz$ spin chain: Nonequilibrium steady state and a strict bound on ballistic transport," Phys. Rev. Lett. **106**, 217206 (2011).

[308] Marko Žnidarič, "A matrix product solution for a nonequilibrium steady state of an XX chain," Journal of Physics A: Mathematical and Theoretical **43**, 415004 (2010).

[309] Marko Žnidarič, "Spin transport in a one-dimensional anisotropic heisenberg model," Phys. Rev. Lett. **106**, 220601 (2011).

[310] D. Karevski, V. Popkov, and G. M. Schütz, "Exact matrix product solution for the boundary-driven lindblad $xxz$ chain," Phys. Rev. Lett. **110**, 047201 (2013).

[311] Marko Žnidarič, Antonello Scardicchio, and Vipin Kerala Varma, "Diffusive and subdiffusive spin transport in the ergodic phase of a many-body localizable system," Phys. Rev. Lett. **117**, 040601 (2016).

[312] Leon Droenner and Alexander Carmele, "Boundary-driven heisenberg chain in the long-range interacting regime: Robustness against far-from-equilibrium effects," Phys. Rev. B **96**, 184421 (2017).

[313] Manuel Katzer, Willy Knorr, Regina Finsterhölzl, and Alexander Carmele, "Long-range interaction in an open boundary-driven heisenberg spin lattice: A far-from-equilibrium transition to ballistic transport," Phys. Rev. B **102**, 125101 (2020).

[314] Hannu Wichterich, Markus J. Henrich, Heinz-Peter Breuer, Jochen Gemmer, and Mathias Michel, "Modeling heat transport through completely positive maps," Phys. Rev. E **76**, 031115 (2007).

[315] V. Popkov, D. Karevski, and G. M. Schütz, "Driven isotropic heisenberg spin chain with arbitrary boundary twisting angle: Exact results," Phys. Rev. E **88**, 062118 (2013).

[316] Zi Cai and Thomas Barthel, "Algebraic versus exponential decoherence in dissipative many-particle systems," Phys. Rev. Lett. **111**, 150403 (2013).

[317] Tomaž Prosen and Marko Žnidarič, "Matrix product simulations of non-equilibrium steady states of quantum spin chains," Journal of Statistical Mechanics: Theory and Experiment **2009**, P02035 (2009).

[318] Tomaž Prosen, "Matrix product solutions of boundary driven quantum chains," Journal of Physics A: Mathematical and Theoretical **48**, 373001 (2015).

[319] Xiansong Xu, Chu Guo, and Dario Poletti, "Interplay of interaction and disorder in the steady state of an open quantum system," Phys. Rev. B **97**, 140201 (2018).

[320] J. J. Mendoza-Arenas, M. Žnidarič, V. K. Varma, J. Goold, S. R. Clark, and A. Scardicchio, "Asymmetry in energy versus spin transport in certain interacting disordered systems," Phys. Rev. B **99**, 094435 (2019).

[321] Vladislav Popkov, Tomaž Prosen, and Lenart Zadnik, "Inhomogeneous matrix product ansatz and exact steady states of boundary-driven spin chains at large dissipation," Phys. Rev. E **101**, 042122 (2020).

[322] Song Cheng, Jing Chen, and Lei Wang, "Information perspective to probabilistic modeling: Boltzmann machines versus born machines," Entropy **20**, 583 (2018).

[323] Hidemaro Suwa and Synge Todo, "Markov chain monte carlo method without detailed balance," Phys. Rev. Lett. **105**, 120603 (2010).

[324] Bruce W. Shore and Peter L. Knight, "The jaynes-cummings model," Journal of Modern Optics **40**, 1195 (1993).

[325] R. R. Puri and G. S. Agarwal, "Collapse and revival phenomena in the jaynes-cummings model with cavity damping," Phys. Rev. A **33**, 3610 (1986).

[326] Marten Richter, Alexander Carmele, Anna Sitek, and Andreas Knorr, "Few-photon model of the optical emission of semiconductor quantum dots," Phys. Rev. Lett. **103**, 087407 (2009).

[327] Michael Gegg, Alexander Carmele, Andreas Knorr, and Marten Richter, "Superradiant to subradiant phase transition in the open system dicke model: dark state cascades," New Journal of Physics **20**, 013006 (2018).

[328] Alex Neville, Chris Sparrow, Raphaël Clifford, Eric Johnston, Patrick M. Birchall, Ashley Montanaro, and Anthony Laing, "Classical boson sampling algorithms with superior performance to near-term experiments," Nature Physics **13**, 1153 (2017).

[329] Iris Agresti, Niko Viggianiello, Fulvio Flamini, Nicolò Spagnolo, Andrea Crespi, Roberto Osellame, Nathan Wiebe, and Fabio Sciarrino, "Pattern recognition techniques for boson sampling validation," Phys. Rev. X **9**, 011013 (2019).

[330] Carolin Lüders, Matthias Pukrop, Elena Rozas, Christian Schneider, Sven Höfling, Jan Sperling, Stefan Schumacher, and Marc Aßmann, "Quantifying quantum coherence in polariton condensates," arXiv:2103.03033 (2021).

[331] Eugen Fick, *Einführung in die Grundlagen der Quantentheorie* (Aula-Verlag, Wiesbaden, 1988).

[332] Julia Kabuss, Alexander Carmele, Tobias Brandes, and Andreas Knorr, "Optically driven quantum dots as source of coherent cavity phonons: A proposal for a phonon laser scheme," Phys. Rev. Lett. **109**, 054301 (2012).

# Selbständigkeitserklärung

Hiermit erkläre ich, dass ich die vorliegende Arbeit selbständig und eigenhändig sowie ohne unerlaubte fremde Hilfe und ausschließlich unter Verwendung der aufgeführten Quellen und Hilfsmittel angefertigt habe.

Berlin, 5. Mai 2021

Oliver Kästle

# Danksagung

Mein erster Dank gilt meinem Doktorvater Prof. Andreas Knorr, der diese Arbeit erst ermöglicht hat und mich in den letzten Jahren stets in allen Bereichen nach Kräften unterstützt und inspiriert hat. Mein herzlicher Dank geht zudem an Prof. Peter Rabl für die Übernahme des Zweitgutachtens sowie an Prof. Ulrike Woggon für die Übernahme des Vorsitzes des Promotionsausschusses.

Besonders möchte ich meinem Betreuer und Bürokollegen Dr. Alexander Carmele danken, ohne den es die vorliegende Arbeit in dieser Form nicht gäbe. Sein Forscherdrang, seine Erkenntniswut und sein Streben nach neuen theoretischen Fertigkeiten haben mich jeden Tag aufs neue inspiriert und stetig wachsen lassen. Sein Vertrauen in mich und unsere enorm produktive Zusammenarbeit haben die letzten zwei Jahre zu einer außergewöhnlichen und prägenden Zeit in meinem Leben gemacht, an die ich mich sehr gerne erinnern werde. Gemeinsam haben wir die Fesseln der Physik hinter uns gelassen und sind in neue Zeitalter aufgebrochen.

Mein großer Dank gebührt außerdem meinen Co-Autoren: Prof. Andreas Knorr, Dr. Alexander Carmele und Dr. Regina Finsterhölzl danke ich für eine immer konstruktive und schöne Zusammenarbeit. Außerdem danke ich Prof. Ying Hu und Yue Sun für viele lehrreiche Diskussionen über topologische Systeme und eine tolle Kollaboration. Ebenso möchte ich Prof. Jesper Mørk und Dr. Emil Denning für unsere gelungene Zusammenarbeit und zahlreiche impulsgebende Diskussionen im Bereich der Halbleiter danken. Bedanken möchte ich mich außerdem bei Dr. Marten Richter, der mich in meiner Zeit als Masterstudent betreute und in die Welt der Informationskompression einführte. Auch dadurch ist diese Arbeit zu dem geworden, was sie ist.

Weiterhin möchte ich mich herzlich bei der gesamten AG Knorr dafür bedanken, dass sie die letzten Jahre mit unzählbaren Konferenzen, Seminaren, Kaffee- und Mittagspausen und einer immer netten Atmosphäre zu einer der schönsten Zeiten in meinem Leben gemacht hat. Insbesondere möchte ich mich bei Florian Katsch, Sebastian Franke und Dominik Christiansen bedanken, die mir immer zur Seite standen und zu engen Freunden geworden sind. Mein Dank geht außerdem an Malte Selig und Irena Koschinski für schöne und unterhaltsame Mittagsrunden.

Meinen Eltern möchte ich herzlich danken, dass sie mir dieses Studium ermöglicht haben und immer zu mir und meinen Interessen standen. Auch meiner Schwester Nikola und ihrem Verlobten Steve danke ich, dass sie in all der Zeit stets ein offenes Ohr für mich hatten. Zuletzt und vor allen anderen bedanke ich mich bei Tina – dafür, dass sie in diesen turbulenten Jahren immer für mich da war und an mich geglaubt hat. Und weil das Leben mit ihr jeden Tag ein neues Wunder ist.